

**Numerical Study of the Effect of Winglets on a Horizontal
Axis Wind Turbine Performance**

By

Ali M. Farhan

Submitted in accordance with the requirements for the degree of
Doctor of Philosophy

The University of Leeds
School of Chemical and Process Engineering

September 2018

Declaration

The candidate confirms that the work submitted is his own, except where work which has formed part of jointly authored publications has been included. The contribution of the candidate and the other authors to this work has been explicitly indicated below. The candidate confirms that appropriate credit has been given within the thesis where reference has been made to the work of others.

Journal publications:

1- **A. Farhan**, A. Hassanpour, A. Burns and Y. Ghaffari Motlagh

“Numerical Study of Effect of Winglet Planform on a Horizontal Axis Wind Turbine Performance”. Published, Available online
<https://doi.org/10.1016/j.renene.2018.08.017>, 10 August 2018, Renewable Energy.

2- **A. Farhan**, A. Hassanpour, A. Burns and Y. Ghaffari Motlagh

“Numerical Investigation of the Effect of Winglet Airfoil on Performance of a Horizontal-Axis Wind Turbine”. Under preparation for submission, Renewable energy.

Conferences paper:

1- **A. Farhan**, A. Hassanpour, A. Burns and Y. Ghaffari Motlagh

“Numerical Study of Effect of Winglet Planform on a Horizontal Axis Wind Turbine Performance”. In: *Proceedings of the 25th UKACM Conference on Computational Mechanics 12 – 13 April 2017, University of Birmingham, United Kingdom.*

This copy has been supplied on the understanding that it is copyright material and that no quotation from the thesis may be published without proper acknowledgment.

© 2018 The University of Leeds and Ali M. Farhan

Acknowledgements

My first thanks will be dedicated to the God Almighty who supported me throughout my PhD study. Without this support, this study would not have been completed.

I would like to express my deepest gratitude to my supervisors, Dr Ali Hassanpour and Dr Alan Burns who have always been scientific advisors to me through their valuable comments.

I also thank my dear parents for supporting me throughout my study. I would like to thank my dear wife who always supports me, her love, patience and support that have always been my strength. Thank you to my sons Mohammed, Ruqayah, Hassanana, and Zienelabdeen.

Thank you to my sponsor (The Ministry of Higher Education and Scientific Research in Iraq – University of Al-Qadisiyah) for granting me the opportunity to carry out my PhD at the University of Leeds.

For all my friends in the school, thank you all for your valuable support and I was really lucky to work with wonderful friends like you.

Abstract

With increasing demand in producing clean and pollution free energy, special attention has been paid to wind turbines and improving their performance. Reducing the effect of wingtip vortices on the wind turbine performance can be achieved by using winglets which work to weaken the impact of wingtip vortices by diffusing them away from the blade tips. The general trend of the literature has considered winglets as diffusers of the wingtip vortices. However, extending the span of the turbine rotor by attaching winglet could improve the potential of a rotor to capture more kinetic energy from moving air. Accordingly, the winglet planform and airfoil play vital roles in wind turbines performance.

The present work reports on the study of the effect of winglet planform and winglet airfoil on the wind turbine performance using Computational Fluid Dynamics (CFD) tools. The National Renewable Energy Laboratory (NREL) phase VI rotor is used as a baseline rotor and the CFD results are validated with the experimental data in terms of torque, pressure and normal force coefficients for different wind speeds.

In this study, two turbulence models are used, which are the SST $k-\omega$ and the Spalart-Allmaras models, which can be used to predict the properties of the fluid flow in the computational domain. Both of the models show a good match of the numerical results when compared to the experimental data, at a range of low wind speeds from 5m/s to 8m/s, due to the absence of stalled flow. At higher wind speeds of 10m/s, the SST $k-\omega$ model shows a better match between the calculated torque and the experimental measurements. Consequentially, the SST $k-\omega$ model is implemented to predict the behaviour of fluid flow in all the CFD calculations in the present study.

The aerodynamic behaviour of two winglet planforms is investigated. These are rectangular and elliptical winglets to increase the NREL phase VI rotor performance. The performances of four winglet configurations are assessed when compared to the baseline power, at the range of wind speeds from 5m/s to 25m/s. The configurations are obtained by changing the winglet planforms and airfoils using the S809 and PSU 94-097 airfoils.

In this regard, the elliptical planform causes a minimizing of the wingtip vortices, more than the rectangular planform, due to the reduction of the elliptical tip by 75% when compared to the rectangular tip. A rectangular planform shows a better performance than the elliptical planform in percentages of power increase. The highest percentage in the power

increase is achieved by attaching the rectangular planform that tilted by a cant angle of 45° and extended by 15cm. This improvement is slightly more than 9%, at the range of low wind speeds from 5m/s to 10m/s, since the flow is almost attached.

Considering the effect of winglet airfoil, the study reports that, choosing a suitable winglet airfoil is mainly dependent on the aerodynamic coefficients of the selected airfoil, such as lift coefficient (C_l), drag coefficient (C_d) and moment coefficient (C_m). For this purpose, a preliminary analysis is conducted using the Xfoil code to predict the aerodynamic coefficients of selected airfoils (S801, S803, S805A and S806A airfoils). The S806A and S805A airfoils are chosen to create two different configurations. The 3D calculations show more increase in the NREL phase VI power is achieved by attaching the configuration that created using the S806A airfoil, since this airfoil has less drag coefficient.

Table of Contents

Declaration	ii
Acknowledgements	iii
Abstract	iv
List of Figures	ix
List of Tables	xv
List of Abbreviations	xvii
Nomenclature	xviii
Greek letters	xx
Chapter 1 : Introduction	1
1.1 Introduction	1
1.2 Wind Turbine.....	1
1.3 Aim of thesis.....	5
1.4 Thesis outline	6
Chapter 2 : Aerodynamics of Horizontal Axis Wind Turbine	8
2.1 Introduction	8
2.2 Actuator Disc model	10
2.3 Angular Momentum Theory	14
2.4 Blade-Element Theory (BET)	15
2.5 Blade Element Momentum Theory (BEM).....	18
2.6 Vortex Models	21
2.7 Computational Fluid Dynamic (CFD).....	23
2.8 Airfoil and general concepts of aerodynamics.....	23
2.9 Wind turbine airfoil.....	26
2.10 Three-dimensional effects on wind turbine blade	27
2.11 Three-dimensional flow behind of wind turbines	28
2.12 Wingtip vortices.....	29
2.13 Winglets	31
2.14 Winglet parameters	31
2.15 Literature review of the winglet effects on the horizontal axis wind turbine performance	33
2.16 The contributions of this thesis to enhance the literature review	46
2.17 Summary.....	47
Chapter 3 : Governing Equations and Computational Fluid Dynamics	48

3.1 Introduction	48
3.2 Governing Equations.....	48
3.2.1 Conservation of mass (Continuity equation)	49
3.2.2 Conservation of momentum.....	49
3.3 CFD modelling process	52
3.4 Solution methods.....	54
3.4.1 Pressure-Based Solver.....	55
3.5 The nature of turbulence	57
3.5.1 Turbulent flow near a wall.....	59
3.6 Turbulence models.....	61
3.6.1 Direct numerical simulations	61
3.6.2 Large eddy simulations.....	62
3.6.3 Turbulence Models of Reynolds Average Navier-Stokes Equations (RANS)	62
3.6.4 Concept of the eddy viscosity	64
3.6.5 The Spalart–Allmaras model.....	65
3.6.6 The $k - \varepsilon$ model	66
3.6.7 The $k - \omega$ model	67
3.6.8 The SST $k-\omega$ (shear stress transport) model	68
3.7 Assessment of the turbulence models' performance for HAWT applications	70
3.8 Conclusion	73
Chapter 4 : Validation of Baseline Case (NREL Phase VI Rotor).....	74
4.1 Introduction	74
4.2 Experimental Data and Real Rotor Description.....	74
4.3 Rotor geometry.....	78
4.4 Calculations of the aerodynamic force coefficients.....	80
4.5 Computational fluid domain.....	82
4.6 Mesh generation.....	83
4.7 Reynolds Number calculations.....	85
4.8 Boundary conditions.....	86
4.8.1 Inlet boundary conditions.....	87
4.8.2 Outlet boundary conditions	88
4.8.3 No-slip wall conditions	88
4.9 Solver settings.....	88
4.10 Effect of the normal wall distance.....	89
4.11 Grid independence study	90
4.12 Numerical results.....	91

4.13 Pressure and normal force coefficients	96
4.14 Conclusions.....	106
Chapter 5 : The Effect of Winglet Planform on the Performance of Wind Turbine.....	108
5.1 Introduction	108
5.2 Winglet function.....	108
5.3 Winglet configurations	109
5.4 Winglet numerical results	111
5.4.1 Assessment of configuration 1	116
5.4.2 Assessment of configuration 2.....	120
5.4.3 Assessment of configuration 3.....	122
5.4.4 Assessment of configuration 4.....	125
5.5 Aerodynamic influences of the winglet parameters on its performance	126
5.6 Sectional flow and surface wall shear streamlines	127
5.7 Pressure coefficient distributions.....	131
5.8 Normal force coefficients and thrust force.....	136
5.9 Conclusions.....	139
Chapter 6 : The Effect of Winglet Airfoil on the Wind Turbine Performance.....	141
6.1 Introduction	141
6.2 Requirements of the winglet airfoil design.....	141
6.3 Aerodynamic solver.....	142
6.4 Preliminary analysis of the selective airfoils	146
6.5 Winglet configurations	148
6.6 Pressure and normal force coefficient distributions	149
6.7 Sectional flow and surface wall shear streamlines	155
6.8 Power and Thrust Force.....	162
6.9 Winglet airfoil requirements.....	166
6.10 Conclusions.....	167
Chapter 7 : Conclusions and Recommended Future Work.....	168
7.1 Conclusions.....	168
7.2 Future work	170
References	171
Appendix-A.....	181
Appendix-B.....	184

List of Figures

Figure 1-1 View of the wind turbine, (A) horizontal axis wind turbine, (B) vertical axis wind turbine (Hau, 2013).....	2
Figure 1-2 Global wind energy production by region(GWEC, 2017).....	3
Figure 1-3 Design considerations for a wind turbine (Sant, 2007).	4
Figure 2-1 Actuator disc model of a rotor (Manwell <i>et al.</i> , 2010).....	11
Figure 2-2 Betz turbine operating parameters (Manwell <i>et al.</i> , 2010).	13
Figure 2-3 Stream tube with wake rotation (Manwell <i>et al.</i> , 2010).	14
Figure 2-4 Schematic of blade elements (Ingram, 2005).	16
Figure 2-5 Velocity components analysis (Burton <i>et al.</i> , 2001).	16
Figure 2-6 Relationships between the forces, angles and velocities of the blade element theory (Manwell <i>et al.</i> , 2010).	17
Figure 2-7 Classical BEM model with different correction factors (Tang, 2012).	20
Figure 2-8 Schematic of blade modelling in the lifting line method (Abedi, 2016).	22
Figure 2-9 Schematic of the blade and wake flow (Abedi <i>et al.</i> , 2013).	23
Figure 2-10 Airfoil terminologies (Manwell <i>et al.</i> , 2010).	25
Figure 2-11 Aerodynamic drag and lift forces on stationary airfoil (Manwell <i>et al.</i> , 2010).....	26
Figure 2-12 Pressure non-equalization between lower and upper blade surfaces (Anderson 2010).	28
Figure 2-13 3D-dimensional effects on the blade (Anderson 2010).....	28
Figure 2-14 Schematic of vortex sheet (Thomson, 1966).	28
Figure 2-15 Vortex sheet behind the wind turbine rotor (Branlard, 2011).	29
Figure 2-16 Wingtip vortices in different engineering applications (Giuni, 2013).	30
Figure 2-17 Flow visualization of the wind turbine wingtip vortices (Vermeer <i>et al.</i> , 2003).....	30
Figure 2-18 Winglet parameters (Maughmer, 2006).	32
Figure 2-19 Tip extensions and winglet configurations studied by Ariffudin <i>et al.</i> (2016).	34
Figure 2-20 Winglet configurations studied by Elfarra <i>et al.</i> (2014).	35
Figure 2-21Turbulence generating grids used by Al-Abadi (2014).....	36
Figure 3-1 Schematic of the CFD structure codes (Tu <i>et al.</i> , 2012).....	53
Figure 3-2 Flowchart of the various flow physics in CFD (Tu <i>et al.</i> , 2012)....	54

Figure 3-3 Schematic solution of the segregated and coupled algorithm (Fluent, 2013).	56
Figure 3-4 Spectral energy analysis (Versteeg and Malalasekera, 2007).....	59
Figure 3-5 Near-wall layers (Fluent, 2013).....	60
Figure 3-6 Schematic of the near-wall treatment in Ansys-Fluent (Fluent, 2013).	61
Figure 3-7 Common turbulence models classifications (Almohammadi, 2014).	64
Figure 4-1 The NREL phase VI rotor in the NASA – Ames wind tunnel (Hand <i>et al.</i> , 2001).....	75
Figure 4-2 Rotor chord distributions (Hand <i>et al.</i> , 2001).	75
Figure 4-3 Twist angle distributions(Hand <i>et al.</i> , 2001).....	76
Figure 4-4 View of the NREL Phase VI blade.	78
Figure 4-5 Airfoil cross sections of the baseline blade.	79
Figure 4-6 Rotor blade parts (Hand <i>et al.</i> , 2001).	79
Figure 4-7 Illustration of: A- Original Blade, B- Modified blade.	79
Figure 4-8 Pressure taps and five- hole probe locations (Hand <i>et al.</i> , 2001).	80
Figure 4-9 Schematic of aerodynamic force coefficients (Hand <i>et al.</i> , 2001).	81
Figure 4-10 Side view of the computational domain.	82
Figure 4-11 Front view of the computational domain.	83
Figure 4-12 View of the unstructured mesh of the stationary domain.	84
Figure 4-13 View of the unstructured mesh of the rotating domain and blade.	84
Figure 4-14 View of the boundary conditions of the problem.	87
Figure 4-15 y^+ contours for pressure and suction sides.	90
Figure 4-16 Effect of grid refinement on the computed torque.....	91
Figure 4-17 Comparison of measured and computed torque values.	93
Figure 4-18 Pressure contours and streamlines predicted by the Spalart- Allmaras model at 8m/s.	94
Figure 4-19 Pressure contours and streamlines predicted by the SST k- ω model at 8 m/s.	94
Figure 4-20 Pressure contours and streamlines predicted by the Spalart- Allmaras model at 9 m/s.	95
Figure 4-21 Pressure contours and streamlines predicted by the SST k- ω model at 9m/s.	95
Figure 4-22 Pressure contours and streamlines predicted by the SST k- ω model at 19m/s.	96

Figure 4-23 Comparison of measured and computed thrust force.....	96
Figure 4-24 Comparisons of measured and computed pressure coefficients at 5m/s.....	99
Figure 4-25 Comparisons of measured and computed pressure coefficients at 7m/s.....	100
Figure 4-26 Comparisons of measured and computed pressure coefficients at 15m/s.....	101
Figure 4-27 Comparisons of measured and computed pressure coefficients at 25m/s.....	102
Figure 4-28 Comparison of measured and computed normal force coefficients at 5m/s.....	103
Figure 4-29 Comparison of measured and computed normal force coefficients at 7m/s.....	103
Figure 4-30 Comparison of measured and computed normal force coefficients at 15m/s.....	103
Figure 4-31 Comparison of measured and computed normal force coefficients at 25m/s.....	104
Figure 4-32 Velocity contours and streamlines at 5m/s.....	104
Figure 4-33 Velocity contours and streamlines at 7m/s.....	104
Figure 4-34 Velocity contours and streamlines at 15m/s.....	105
Figure 4-35 Velocity contours and streamlines at 25m/s.....	105
Figure 4-36 Surface streamlines along the suction side of the baseline blade.	106
Figure 5-1 View of: A- Baseline blade, B- Baseline blade with winglet.....	109
Figure 5-2 View of: A- Rectangular planform, B- Elliptical planform.....	110
Figure 5-3 Illustration of: A-Schematic of the S809 airfoil, B- Schematic of the PSU 94-097 airfoil.....	111
Figure 5-4 Comparison of measured and predicted power.....	112
Figure 5-5 Comparison of calculated power using configuration 1 (cant angle of 90°).....	117
Figure 5-6 Streamlines around configuration 1 at a wind speed of 15m/s. .	118
Figure 5-7 Comparison of calculated power using configuration 1 (cant angle of 45°).....	118
Figure 5-8 Comparison of pressure contours between baseline blade and configuration 1.....	119
Figure 5-9 Comparison of pressure contours between baseline blade and configuration 1, at the spanwise section of 95%.....	120
Figure 5-10 Comparison of pressure contours between baseline blade and configuration 1, at the spanwise section of 98%.....	120

Figure 5-11 Comparison of calculated power between configuration 1 and 2, at a cant angle of 45° and height of 15cm.	122
Figure 5-12 Comparison of calculated power between configuration 1 and configuration 3.	123
Figure 5-13 Comparison of pressure contours between baseline blade and the configurations (1, 3).	124
Figure 5-14 Comparison of pressure contours between baseline blade and the configurations (1, 3).	124
Figure 5-15 comparison of pressure contours between baseline blade and the configurations (1, 3).	125
Figure 5-16 Comparison of calculated power between configuration 1 and 4 at a cant angle of 45° and height of =15cm.	126
Figure 5-17 Comparison of velocity contours and sectional flow streamlines between baseline blade and configurations 1 and 3 at 7m/s.	128
Figure 5-18 Comparison of velocity contours and sectional flow streamlines between baseline blade and configurations 1 and 3 at 15m/s.	129
Figure 5-19 Comparison of surface wall shear streamlines between the baseline blade and configurations 1 and 3 at 7m/s.	129
Figure 5-20 Comparison of surface wall shear streamlines between the baseline blade and configurations 1 and 3 at 15 m/s.	130
Figure 5-21 View of the tip vorticities of the baseline blade and configurations (1, 3) at 7m/s.	130
Figure 5-22 Comparison of tip flow streamlines between baseline blade and configurations 1 and 3 at 7m/s.	131
Figure 5-23 Comparison of sectional flow streamlines between baseline blade and configurations 1 and 3 at 15m/s.	131
Figure 5-24 Comparisons of computed pressure coefficients at 7m/s between the baseline and configurations 1 and 3.	133
Figure 5-25 Comparisons of computed pressure coefficients at 10 m/s between baseline and configurations 1 and 3.	134
Figure 5-26 Comparisons of computed pressure coefficients at 25m/s between baseline and configurations 1 and 3.	135
Figure 5-27 Comparison of normal force coefficients between baseline blade and configurations (1, 3) at 7m/s.	137
Figure 5-28 Comparison of normal force coefficients between baseline blade and configurations (1, 3) at 10m/s.	137
Figure 5-29 Comparison of normal force coefficients between baseline blade and configurations (1, 3) at 25m/s.	137

Figure 5-30 Comparison of baseline blade thrust force and configuration 1.	138
Figure 5-31 Percentage of increase in power and thrust force of configuration1.	139
Figure 6-1 Experimental lift coefficient for the S809 airfoil (Jonkman, 2003).	142
Figure 6-2 Comparison of measured and calculated lift coefficients of the S809 airfoil.....	144
Figure 6-3 Comparison of measured and calculated lift and drag coefficients of the S809 airfoil.....	144
Figure 6-4 Comparison of measured and calculated moment coefficients of the S809 airfoil.....	145
Figure 6-5 Calculated performance ratios (C_l / C_d) of the S809 airfoil.....	145
Figure 6-6 Comparison of lift coefficients between S809 and selected airfoils.	146
Figure 6-7 Comparison of drag coefficients between S809 and selected airfoils.	147
Figure 6-8 Comparison of moment coefficients between S809 and selected airfoils.	147
Figure 6-9 Comparison of performance ratio (C_l / C_d) between S809 and selected airfoils.....	147
Figure 6-10 Schematic of: A- S805A airfoil, B- S806A airfoil.	148
Figure 6-11 View of: A- Baseline tip, B-Configuration of A1 and.....	148
Figure 6-12 Comparisons of computed pressure coefficients between the baseline blade and configurations (A1 and B1) at 7m/s.....	151
Figure 6-13 Comparisons of computed pressure coefficients between the baseline blade and configurations (A1 and B1) at 10m/s.....	152
Figure 6-14 Comparisons of computed pressure coefficients between the baseline blade and configurations (A1 and B1) at 15m/s.....	153
Figure 6-15 Comparison of normal force coefficients between the baseline blade and configurations (A1, B1) at 7m/s.....	154
Figure 6-16 Comparison of normal force coefficients between the baseline blade and configurations (A1, B1) at 10m/s.....	154
Figure 6-17 Comparison of normal force coefficients between the baseline blade and configurations (A1, B1) at 15m/s.....	154
Figure 6-18 Comparison of velocity contours and sectional flow streamlines between the baseline blade and configurations (A1, B1) at 7m/s.	156
Figure 6-19 Comparison of velocity contours and sectional flow streamlines between the baseline blade and configurations (A1, B1) at 15m/s.	156

Figure 6-20 Comparison of pressure contours between baseline blade and configurations (A1 and B1) at 7m/s.	157
Figure 6-21 Comparison of pressure contours between baseline blade and configurations (A1 and B1) at 15m/s.	157
Figure 6-22 Comparison of pressure contours between baseline blade and configurations (A1 and B1 at section of 95%) at 7m/s.	158
Figure 6-23 Comparison of pressure contours between baseline blade and configurations (A1 and B1 at section of 98%) at 7m/s.	158
Figure 6-24 Comparison of pressure contours between baseline blade and configurations (A1 and B1 at section of 95%) at 15m/s.	159
Figure 6-25 Comparison of pressure contours between baseline blade and configurations (A1 and B1 at section of 98%) at 15m/s.	159
Figure 6-26 Comparison of surface wall shear streamlines between the baseline blade and configurations (A1 and B1) at 7m/s.....	160
Figure 6-27 Comparison of surface wall shear streamlines between baseline blade and configurations (A1 and B1) at 15m/s.....	160
Figure 6-28 Comparison of pressure contours and sectional flow streamlines between baseline blade and configurations (A1 and B1) at 7 m/s.	161
Figure 6-29 Comparison of the pressure contours and sectional flow streamlines between baseline blade and configurations (A1 and B1) at 15m/s.....	161
Figure 6-30 Comparison of calculated power between baseline blade and configurations (1, A1 and B1).	163
Figure 6-31 Comparison of pressure coefficients between baseline and configurations (1, A1, B1) at section of 95%.....	164
Figure 6-32 Comparison of pressure coefficients between baseline blade and configurations (1, A1, B1) at section of 98%.....	165
Figure 6-33 Comparison of calculated thrust force between baseline blade and configurations (1, A1 and B1).	165
Figure A-1 Aerodynamic characteristics of the S809 airfoil for $Re = 1.000.000$ (Somers, 1997).....	181
Figure A-2 Aerodynamic characteristics of the PSU 94-09 (Maughmer et al., 2002).	181

List of Tables

Table 1-1 Top ten wind power production countries(GWEC, 2017).....	3
Table 2-1 Shows the definitions of the airfoil terminologies.	25
Table 2-2 NREL aerofoils and their applications (Tangler and Somers, 1995).	27
Table 2-3 Winglet parameters studied by Gupta and Amano (2012).	38
Table 2-4 Winglets’ parameters used by Gertz (2011).	38
Table 2-5 Winglets’ parameters according to the study of Johansen and Sørensen (2007).....	40
Table 2-6 Winglets parameters according to the study of Johansen and Sørensen (2006).....	41
Table 2-7 The summary of advantages and limitations of literature.....	42
Table 3-1 k- ϵ model constants.	67
Table 3-2 Wilcox’s and Menter’s constants.....	70
Table 4-1 NREL phase VI rotor specifications (Hand et al., 2001).....	76
Table 4-2 Local chord and twisted angles distributions along the NREL phase VI rotor (Hand et al., 2001).	77
Table 4-3 Mesh specification of the stationary domain.	84
Table 4-4 Mesh specification of the rotating domain.....	85
Table 4-5 Reynolds numbers at the root and blade tip blade.....	86
Table 4-6 Measured rotating velocity of the rotor and air properties.....	88
Table 4-7 Comparison of measured and computed torque.....	92
Table 5-1 Winglet configurations parameters.	110
Table 5-2 Percentage of increase/decrease in power and thrust force for the configuration 1 (Rectangular/S809) at a cant angle of 90°	112
Table 5-3 Percentage of increase/decrease in power and thrust force for the configuration 1 (Rectangular/S809) at a cant angle of 45°	113
Table 5-4 Percentage of increase/decrease in power and thrust force for the configuration 2 (Rectangular/PSU 94-097) at a cant angle of 90°	113
Table 5-5 Percentage of increase/decrease in power and thrust force for the configuration 2 (Rectangular/PSU 94-097) at a cant angle of 45°	114
Table 5-6 Percentage of increase/decrease in power and thrust force for the configuration 3 (Elliptical/S809) at a cant angle of 90°	114
Table 5-7 Percentage of increase/decrease in power and thrust force for the configuration 3 (Elliptical/S809) at a cant angle of 45°	115
Table 5-8 Percentage of increase/decrease in power and thrust force for the configuration 4 (Elliptical/ PSU 94-097) at a cant angle of 90°	115

Table 5-9 Percentage of increase/decrease in power and thrust force for the configuration 4 (Elliptical/ PSU 94-097) at a cant angle of 45°.	116
Table 6-1 Values of n_{crit} for different applications.....	143
Table 6-2 Percentages of the power increase and thrust force using the configurations (1, A1 and B1).	163
Table A-1 S809 airfoil coordinates (NREL, 2016).	182
Table A-2 PSU 94-097 airfoil coordinates(Maughmer <i>et al.</i> , 2002).....	183
Table B-1 Polar file for the S809 airfoil.	184
Table B-2 Polar file for the S801 airfoil.	185
Table B-3 Polar file for the S803 airfoil.	186
Table B-4 Polar file for the S805A airfoil.	187
Table B-5 Polar file for the S806A airfoil.	188

List of Abbreviations

2D	Two-dimensional
3D	Three-dimensional
AEP	Annual energy production
AOA	Angle of Attack
BEM	Blade Element Momentum Theory
BET	Blade Element Theory
CFD	Computational Fluid Dynamics
COE	Minimum cost of energy
DNS	Direct numerical simulation
FDM	Finite difference method
FEM	Finite element method
GWEC	Global wind energy council
HAWT	Horizontal axis wind turbine
INS	Indirect numerical simulation
L.E	Leading edge
LES	Large Eddy Simulation
MRF	Multiple Reference Frame
NACA	National advisory committee for aeronautics
NREL	National Renewable Energy Laboratory
PISO	Pressure implicit with splitting of operators
RANS	Reynolds Averaged Navier-Stokes
RSM	Reynolds Stress Model
SA	Spalart-Allmaras
SGS	Subgrid-scale
SIMPLE	Semi implicit method for pressure linked equations
SIMPLEC	Semi implicit method for pressure linked equations consistent
SST	Shear Stress Transport
T.E	Trailing edge
VAWT	Vertical axis wind turbine
VM	Vortex Models
WECS	Wind energy conversion system

Nomenclature

A, A_{rotor}	Rotor disc area (m^2)
a	Axial induction factor
a'	Tangential induction factor
B	Number of blades
C_d	Drag coefficient
C_l	Lift coefficient
C_l/C_d	Performance ratio
C_N	Normal force coefficient
C_p	Power coefficient
C_p	Pressure coefficient
C_{Pmax}	Maximum theoretical power coefficient (Betz limit)
C_T, C_{TQ}	Torque Coefficient
C_T	Tangential force coefficient
C_{TH}	Thrust coefficient
c	Airfoil or blade chord length (m)
C_m	Moment coefficient
c_r	Wing root chord (m)
c_t	Wing tip chord (m)
$C1$	Winglet root chord (m)
$C2$	Winglet tip chord (m)
D, F_D	Drag force (N)
E	Kinetic energy (J)
F	Thrust force (N), Prandtl's factor
F_N	Normal force (N)
F_t, F_T	Tangential force (N)
h	Winglet height (m)
L, F_L	Lift force (N)

l	Turbulence length scale (m)
K	Turbulent kinetic energy (m^2/s^2)
\dot{m}	Mass flow rate through rotor disc (kg/s)
P	Theoretical power (W), Numerical power (W)
P_{actual}	Actual power (W)
p	Pressure (Pa)
\bar{p}	Mean component of pressure (Pa)
\acute{p}	Fluctuating component of pressure (Pa)
R	Rotor radius (m)
Re	Reynolds number
Re_{η}	Kolmogorov Reynolds number
r	Annular stream tube (m)
$S_{Mx,My \text{ and } Mz}$	Body forces per unit in the x, y and z-direction
T	Theoretical rotor torque (N.m)
T	Thrust force, used in Actuator Disc model (N)
T	Numerical torque (N.m)
T_{actual}	Actual torque (N.m)
t	Time (s)
$U, V \text{ and } W$	Mean components of velocity (m/s)
U_{rel}	Relative wind velocity (m/s)
\mathbf{u}	Velocity vector (m/s)
$u, v \text{ and } w$	Velocity components (m/s)
$u', v' \text{ and } w'$	Fluctuating components of velocity (m/s)
u_t	Friction velocity (m/s)
u_{η}	Kolmogorov velocity scale (m/s)
V_{∞}	Wind velocity (m/s)
v	Air volume (m^3)
V_{∞}	Velocity at infinity (m/s)
x, y, z	Cartesian coordinates (m)
$y+$	Non-dimensional normal wall distance
y	Normal distance from the wall (m)

Greek letters

α	Angle of attack (degrees)
δ_{ij}	Kronecker delta
Γ	Circulation (m^2/s)
ε	Dissipation rate of energy (m^2/s^3)
η	Kolmogorov length scale (m)
φ	Angle of relative wind (degrees)
θ_p	Section pitch angle (degrees)
λ	Tip speed ratio
λ_r	Local speed ratio
μ_t	Dynamic turbulent viscosity ($\text{kg}/\text{m}\cdot\text{s}$)
μ	Dynamic viscosity ($\text{kg}/\text{m}\cdot\text{s}$)
ν	Kinematic viscosity (m^2/s)
ρ	Air Density (kg/m^3)
σ'	Local solidity
τ_{ij}	Reynolds Stress tensor (N/m^2)
τ_w	Wall shear stress ($\text{kg}/\text{m}\cdot\text{s}^2$)
τ_η	Kolmogorov time scale (s)
ω	Specific energy dissipation rate (1/s)
ω	Wind turbine rotating speed (rpm)
ω	Angular velocity of the air flow in the wake (rad/s)
Ω	Rotor angular velocity (rad/s)

Chapter 1 : Introduction

1.1 Introduction

Global energy demands have increased dramatically due to technological advances and a growing global population. Currently, fossil fuels are the main source of energy that covers energy demands around the world. As a result of pollution, global warming, and the oil crisis in 1972, alternative fuel has begun to be explored. Many countries have funded research relating to solar, wind, water, biofuel and geothermal energy, with a view to reducing global dependence on fossil fuel. Wind energy has shown great potential as a renewable resource to support global demands and reduce pollution and global warming.

Wind energy is clean, free, friendly, and sustainable; these features make it reliable and promising.

1.2 Wind Turbine

A wind turbine is generally considered the largest rotational machine on Earth. It converts the kinetic energy from wind into electricity. The modern wind turbine has been mainly developed based on the windmill, which was historically used for grinding grain and pumping water (Mathew, 2006).

Wind turbines are classified, depending on their axis of rotation, into two types: a horizontal axis wind turbine (HAWT) and vertical axis wind turbine (VAWT). The HAWT rotates on a horizontal axis, which is parallel to the wind flow direction, as shown in Figure 1-1A. It is the most common type of wind turbine, which is utilised for efficiently extracting kinetic energy from moving air. However, complex components are required, such as a yaw mechanism, in order to keep a HAWT towards the wind direction. In addition, a gearbox and generator should be placed over the tower of a HAWT, which makes it more expensive (Mathew, 2006).

In contrast, VAWTs rotate on a vertical axis, as shown in Figure 1-1B. They convert kinetic energy to electricity from any direction of the moving air; hence the yaw system is eliminated in this device. Further, the generator and the gearbox can be placed on a ground which makes it more economical than HAWT.

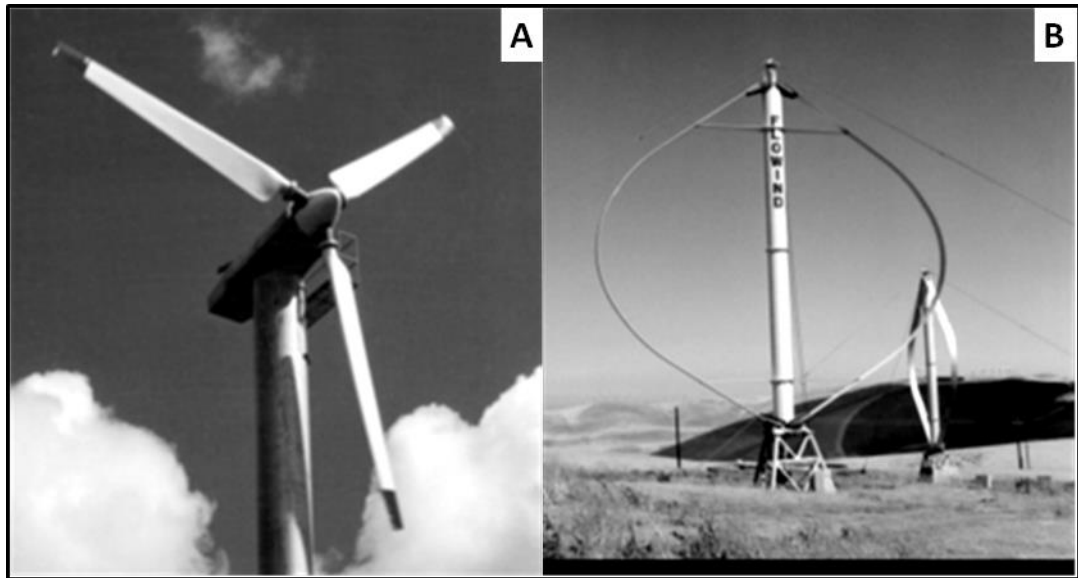


Figure 1-1 View of the wind turbine, (A) horizontal axis wind turbine, (B) vertical axis wind turbine (Hau, 2013).

Wind energy is one of the most important sources of renewable energy, which is predicted to provide 20% of global electricity by the year 2030. The number of countries that will be met their energy demands by installing new wind plants should increase in the years to come as shown in Figure 1-2. In addition, clearly shows that most global wind energy has been produced in Asia, which was 203.6 GW in 2016 and is set to increase to 357.1 GW in 2021 (GWEC, 2017).

GWEC (2017) reported the ranking of the 10 most prolific countries in the world that employ wind energy to support their national demands for 2017, as shown in Table 1-1. China is the largest country in the world, and accounts for 35% of the wind energy producing world production. Germany tops the five European countries that use wind energy to produce electricity.

The Table 1-1 shows that wind power production in the UK does not exceed 3% of the global production.

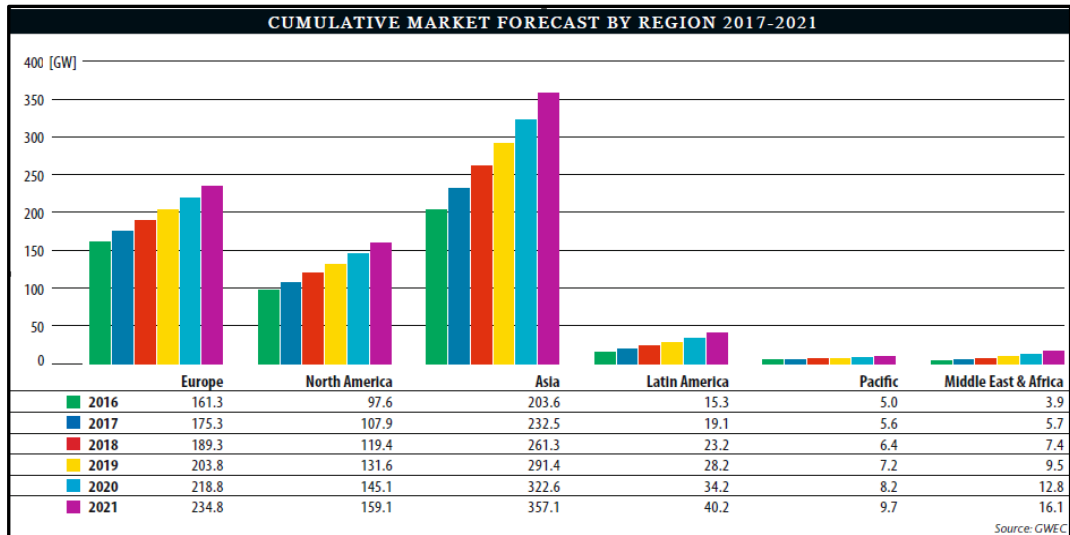


Figure 1-2 Global wind energy production by region(GWEC, 2017).

Table 1-1 Top ten wind power production countries(GWEC, 2017).

Country	MW	% Share
China	188,232	35
USA	89,077	17
Germany	56,132	10
India	32,848	6
Spain	23,170	4
United Kingdom	18,872	3
France	13,759	3
Brazil	12,763	2
Canada	12,239	2
Italy	9,479	2
Rest of the world	83,008	15
Total Top 10	456,572	85
World Total	539,581	100

In the early stages of their development, wind turbines were designed based on helicopter blade airfoil shapes, because no sophisticated wind turbine models existed. Recently, different engineering designs have played an important role in predicting aerodynamic parameters, which affect the interaction and relationship between wind and the wind turbine.

Successful wind turbine design should aim to increase output power, decrease overall costs, and increase the lifespan of a wind turbine. These aims would reduce the minimum cost of energy (COE), as shown in Figure 1-3 (Sant, 2007). Basically, there are three main complementary models that have been frequently used to design wind turbines. First, there is the aerodynamic model, which calculates aerodynamic characteristics, for example, the forces and the annual energy production (AEP) which defines the total amount of output power that produced over a year (Burton *et al.*, 2001), with a view to obtain a rotor shape and operation conditions. Second, there is the structure model, which is responsible for finding loads and the generated stresses on the bearing parts. Third, there is the cost model, which focuses mainly on the manufacturing cost of the wind energy conversion system (WECS).

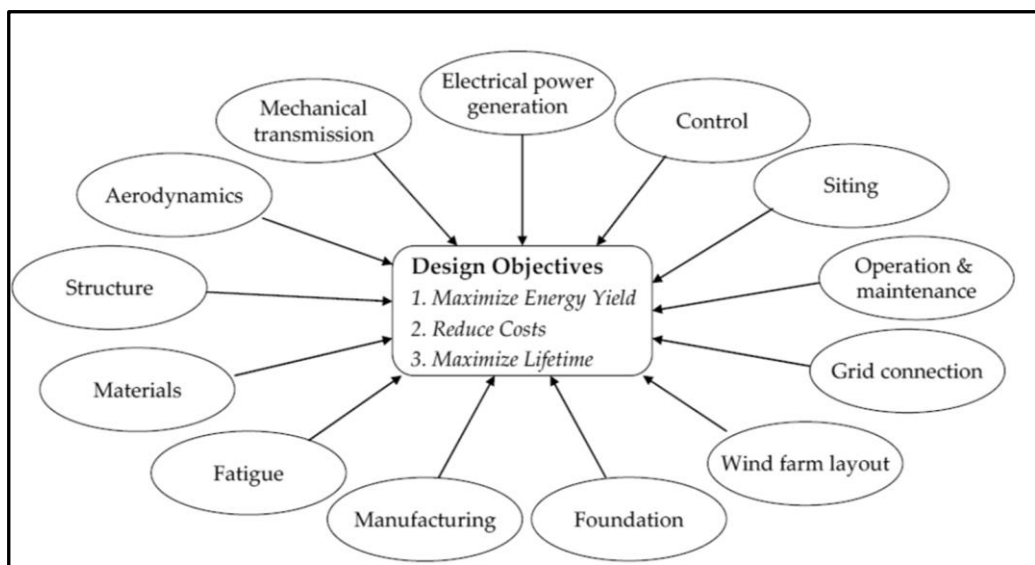


Figure 1-3 Design considerations for a wind turbine (Sant, 2007).

The aerodynamic model is considered the most important model, and works as a vital designer to minimise the COE as much as possible by determining the geometric optimization, such as the blade diameter, blade shape, and the aerodynamic angles. Vermeer *et al.* (2003) define aerodynamics as a science with the responsibility for ascertaining the interaction and relationship between wind and the wind turbine structure. It might therefore be concluded that the aerodynamic model tends to achieve three goals: the highest power

coefficient, the highest energy yield, and the lowest blade loads (Robison *et al.*, 1995).

1.3 Aim of thesis

Winglets are aerodynamic extensions that are added at the blade tip of wind turbines for the purpose of increasing in their output power. Winglets provide a flow field that weakens the spanwise flow generated due to the pressure non-equalization between the upper and lower blade surfaces. Winglets have been studied in literature as attached extensions implemented to reduce the impact of the wingtip vortices. However, attaching winglets to blade tip causes an extension in the span of the turbine rotor and that supplements its potential to capture more kinetic energy from the moving air. Accordingly, an efficient winglet should be designed with the least wetted area in order to avoid the effect of the profile drag, which has a significant impact on winglet performance.

The main objective of this study is to aerodynamically investigate the influence of attaching winglets on wind turbine performance. The objective is established by employing the CFD method and turbulence models to model the fluid flow around a wind turbine. The NREL phase VI rotor has been chosen as a baseline case for validating the numerical results in terms of torque, pressure, and normal force coefficient distributions.

Quantitative studies of winglets, to improve wind turbine output power are limited. Additionally, winglets that were modelled by studying the influence of one or two parameters led to poor performance in improving wind turbine production. The winglet parameters that are most frequently studied are cant angle, twisted angle and winglet height. The winglet planform and airfoil that significantly affect wind turbine performance have been not studied. Both (winglet planform and airfoil) play an important role in increasing or decreasing the extraction of more available energy from the moving air.

Accordingly, the performances of two different winglet planforms, namely, rectangular and elliptical, have been examined to increase the output power of a horizontal axis wind turbine. In addition, the aerodynamic influence of the winglet airfoil has been investigated by analysing the airfoil coefficients, such as lift, drag and moment coefficient in 2D.

1.4 Thesis outline

The thesis consists of seven chapters, which are briefly outlined below.

Chapter one includes a general introduction to wind energy, which is followed by an explanation of the main classifications of wind turbines. Further, a global perspective of wind energy production is included in this chapter, along with predictions for the next five years.

In chapter two, the main aerodynamic models that predict the flow field around wind turbines are discussed. This comparative discussion presents the main advantages and disadvantages of each model. In addition, the chapter includes a discussion of the aerodynamic background of winglets and the most important winglet parameters which affect wind turbine performance. The winglet literature is discussed at the end of this chapter.

Chapter three discusses the fundamentals of the governing equations of the fluid flow, which are used for predicting wind turbine performance. Further, the most important turbulence models are discussed, followed by a discussion of the most common turbulence models that are employed to calculate wind turbine power. This chapter also focuses on the Reynolds Averaged Navier-Stokes models (RANS), which have been frequently used for their reasonable results.

In chapter four, The NREL phase VI is presented as a baseline case, and is used to validate the numerical results that are obtained by implementing the SST $k-\omega$ (Shear Stress Transport) and S-A (Spalart-Allmaras) turbulence models. The validation is conducted by comparing the numerical results with the experimental data in terms of torque, pressure and force coefficients, in addition to the thrust force.

The numerical results of the NREL phase VI improvements (due to attaching different winglet planforms) are presented in chapter five. These results include percentages of increases/decreases in output power and thrust force. In this thesis, four winglet configurations are investigated by changing winglet planform, winglet airfoil, winglet height and cant angle.

It is argued that a winglet airfoil plays an important role in increasing/decreasing wind turbine performance. A preliminary aerodynamic analysis is implemented in chapter six, which is used for studying the effect of the airfoil characteristics on winglet performance. Four thin airfoils are aerodynamically examined in 2D, by comparing their aerodynamic coefficients with the S809 airfoil. Finally, The NREL phase VI power is

calculated by employing two selected airfoils, which have the lowest drag coefficients.

Finally, chapter seven presents the conclusions of this thesis, along with recommendations for future work.

Chapter 2 : Aerodynamics of Horizontal Axis Wind Turbine

2.1 Introduction

A wind turbine's performance is mainly affected by the interaction and relationship between the wind turbine and fluid flow. Aerodynamics is one of the branches of fluid dynamics engineering, which investigates how kinetic energy in the wind is efficiently converted into mechanical rotational motion, and ultimately, into electricity. Wind turbines are driven by several different complicated factors such as wind speed, wind direction, turbulent fluctuations and stalled flow. Until now, an efficient model with the potential for predicting all aerodynamic conditions that are associated with wind turbine operations has not been forthcoming (Hansen, 2015). In early attempts, aerodynamicists depended mainly on various limited methods, such as field testing and wind tunnel experiments, which require both time and effort. Accordingly, uncertainty in the results has often been expected, due to the complexity of the flow, such as the effects of a rotational flow, turbulence and vortices.

The purpose of a wind turbine is to convert the kinetic energy of the moving air into mechanical or electrical energy. The efficient conversion of the available energy in wind into a useful form depends mainly on the interaction between the wind turbine rotor and the wind streams (Mathew, 2006; Leishman, 2002). Hence, extracting the maximum power from the wind is the main objective of wind turbine design. Aerodynamic models have been developed based on the fundamental principles which describe the process of wind energy conversion. These principles can be summarised in the following equations.

The kinetic energy of the air stream available for the wind turbine is calculated from the following equation:

$$E = \frac{1}{2} \rho v V_{\infty}^2 \quad (2.1)$$

And, the energy per unit time, which is a theoretical power, can be given as follows:

$$P = \frac{1}{2} \rho A V_{\infty}^3 \quad (2.2)$$

Where,

E : Kinetic energy (J).

ρ : Air density (kg/m^3).

v : Air volume (m^3).

V_{∞} : Wind velocity (m/s).

A : cross sectional area of a rotor (m^2).

P : Theoretical power (W).

Hence, air density, wind velocity and the area of the wind turbine rotor are the most important factors that affect the power available. Among them, wind velocity has a remarkable influence due to its cubic relationship with power. In addition, the power available is indirectly affected by atmospheric conditions, due to changes in air density, air temperature, and air pressure. In reality, when the wind stream passes a wind turbine, the turbine rotor extracts a part of the kinetic energy, and the rest is carried away by the leaving air. Therefore, a wind turbine does not have the capability to completely convert all the theoretical power available. The power coefficient (C_p) is usually used to evaluate the efficiency of a wind turbine in converting kinetic energy to a useful form. Thus, the power coefficient is defined as the ratio of the power that is extracted by the rotor to the theoretical power available in the wind stream.

The C_p can be calculated using the following equation:

$$C_p = \frac{2P_{actual}}{\rho A V_{\infty}^3} \quad (2.3)$$

The power coefficient of a wind turbine is affected by factors such the blade arrangement, and the blade profile (etc.). Therefore, these factors are the main objective of wind turbine design, with a view to achieve a maximum power coefficient.

The thrust force that acts on the wind turbine rotor (F) is given by the following expression:

$$F = \frac{1}{2} \rho A_{rotor} V_{\infty}^2 \quad (2.4)$$

The theoretical rotor torque (T) can be expressed as:

$$T = \frac{1}{2} \rho A_{rotor} V_{\infty}^2 R \quad (2.5)$$

The torque coefficient is the ratio between the actual torque to the theoretical torque, as follows:

$$\text{Torque Coefficient}(C_T) = \frac{2T_{actual}}{\rho A_{rotor} V_{\infty}^2 R} \quad (2.6)$$

In addition, the tip speed ratio (λ) is an important factor that significantly affects the power and torque coefficients. It is defined as the ratio of speed of the blade tip to the free wind stream speed. Hence:

$$\lambda = \frac{\Omega R}{V_{\infty}} \quad (2.7)$$

It can also be expressed in terms of the power coefficient and torque coefficient, as follows:

$$\lambda = \frac{C_P}{C_T} \quad (2.8)$$

A number of aerodynamic models have been developed, based on the aforementioned principles, with a view to describe how a wind turbine extracts the mechanical energy from the kinetic energy of the wind. These models are discussed in the following sections.

2.2 Actuator Disc model

The actuator disc model is a simple model that has been used to predict the aerodynamic behaviour of the flow field around a wind turbine by considering the energy extraction process. It is based on a linear momentum theory, and determines the ideal power, thrust and influence of the rotor on the local wind field. The model assumes a control volume, wherein its boundaries are delimited by the surface of a stream tube and the airflow moves through the two cross-sections, as shown in Figure 2-1. The actuator disc depicts the wind turbine rotor, which creates a discontinuity of air pressure in the stream tube. A number of assumptions are considered to simplify the model, which are detailed below (Manwell *et al.*, 2010).

- The fluid flow is incompressible, inviscid, has a steady state and is homogeneous.
- There are an infinite number of blades.
- There is no rotational far field flow.
- The static pressure of the far upstream and downstream of the rotor is equal to the ambient static pressure.
- The thrust force over the disc (rotor area) is uniform.

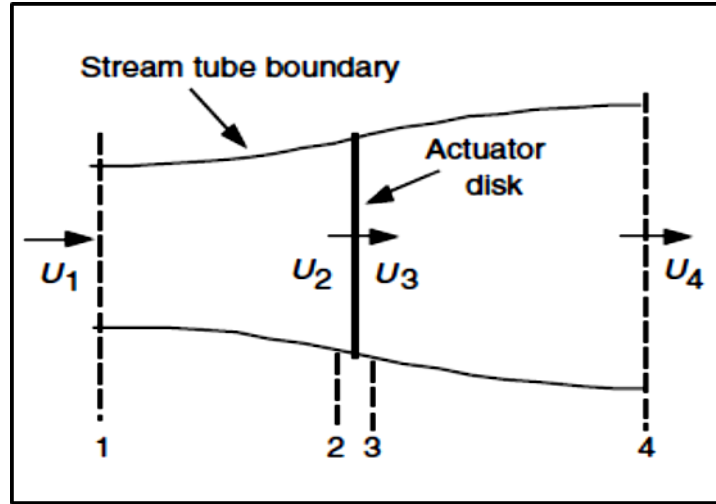


Figure 2-1 Actuator disc model of a rotor (Manwell *et al.*, 2010).

The mass flow must be equal in all the stream tube's sections, as result of the law of mass conservation. Thus, the flow is assumed to have a steady-state and is incompressible:

$$(AU)_1 = (AU)_4 = \dot{m} \quad (2.9)$$

A is the cross-sectional area, U is the air velocity and the numbers of the cross-sections are indicated by the subscripts.

The Bernoulli equation can be applied to the upstream and downstream of the disk without work, as follows:

For the stream tube upstream of the disc:

$$p_1 + \frac{1}{2}\rho U_1^2 = p_2 + \frac{1}{2}\rho U_2^2 \quad (2.10)$$

And, the stream tube downstream of the disc:

$$p_3 + \frac{1}{2}\rho U_3^2 = p_4 + \frac{1}{2}\rho U_4^2 \quad (2.11)$$

The rotor thrust is equal and opposite to the rate of change of the momentum. Thus, the thrust can be calculated as follows:

$$T = U_1 (\rho AU)_1 - U_4 (\rho AU)_4 \quad (2.12)$$

By substituting equation (2.9) into equation (2.12), therefore:

$$T = \dot{m}(U_1 - U_4) \quad (2.13)$$

Thrust can also be determined as the pressure difference between the two rotor sides, as follows:

$$T = A_2(p_2 - p_3) \quad (2.14)$$

Considering the assumptions that the pressures in the far upstream and far downstream are equal ($p_1 = p_4$), there is no change in the air velocity

across the rotor, which means ($U_2 = U_3$). The term ($p_2 - p_3$) can be solved using equations (2.10) and (2.11), and substituting the result in the equation (2.14). The thrust can be calculated in terms of the velocities in the following equation:

$$T = \frac{1}{2} \rho A_2 (U_1^2 - U_4^2) \quad (2.15)$$

By equating equation (2.15) with (2.13) and substituting that the mass flow rate is equal to $A_2 U_2$, the result is as below:

$$U_2 = \frac{U_1 + U_4}{2} \quad (2.16)$$

This means the wind velocity at the rotor plane is equal to the average of the wind speeds of upstream and downstream.

The axial induction factor (a) is defined as:

$$a = \frac{U_1 - U_2}{U_1} \quad (2.17)$$

Then,

$$U_2 = U_1(1 - a) \quad (2.18)$$

$$U_4 = U_1(1 - 2a) \quad (2.19)$$

The output power of the rotor can be obtained by the thrust times the velocity rotor, as follows:

$$P = T * U_2 \quad (2.20)$$

Therefore,

$$P = \frac{1}{2} \rho A_2 (U_1^2 - U_4^2) U_2 = \frac{1}{2} \rho A_2 U_2 (U_1 + U_4) (U_1 - U_4) \quad (2.21)$$

By substituting U_2 and U_4 from equations (2.18) and (2.19), replacing A_2 by A , U_1 by U , hence, the output power is given by the following equation:

$$P = \frac{1}{2} \rho A U^3 4a (1 - a)^2 \quad (2.22)$$

Usually, the C_p (power coefficient) represents the performance of the wind turbine rotor, and is calculated as follows:

$$C_p = \frac{P}{\frac{1}{2} \rho U^3 A} = \frac{\text{Rotor power}}{\text{Power in the wind}} \quad (2.23)$$

The C_p in terms of the axial induction factor (a) is obtained by substituting equation (2.22) in (2.23), as follows:

$$C_p = 4a(1 - a)^2 \quad (2.24)$$

The maximum theoretical power coefficient is shown in Figure 2-2. It can be obtained by taking the derivative of equation (2.24) with respect to (a) and equal it to zero, thus yielding $a = \frac{1}{3}$ and the $C_{Pmax} = \frac{16}{27} = 0.5926$.

0.5926 is the maximum power coefficient that can be obtained by an ideal turbine, and is known as the Betz limit.

Similarly, to find the axial thrust on the disc in terms of the axial induction factor (a), both equations (2.18) and (2.19) were substituted in equation (2.15) to obtain the following equation:

$$T = \frac{1}{2} \rho A U^2 [4a(1 - a)] \quad (2.25)$$

Similar to the power coefficient, the thrust coefficient (C_T) can be written as follows:

$$C_T = \frac{T}{\frac{1}{2} \rho U^2 A} = \frac{\text{Thrust force}}{\text{Dynamic force}} \quad (2.26)$$

And by substituting equation (2.25) in equation (2.26), the C_T is given in terms of the axial induction factor in the following equation:

$$C_T = 4a(1 - a) \quad (2.27)$$

Figure 2-2 shows the maximum value of the C_T for an ideal wind turbine is 1.0 when $a=0.5$ and has a value of $\frac{8}{9}$ at $C_{pmax}=0.5926$ when $a=1/3$.

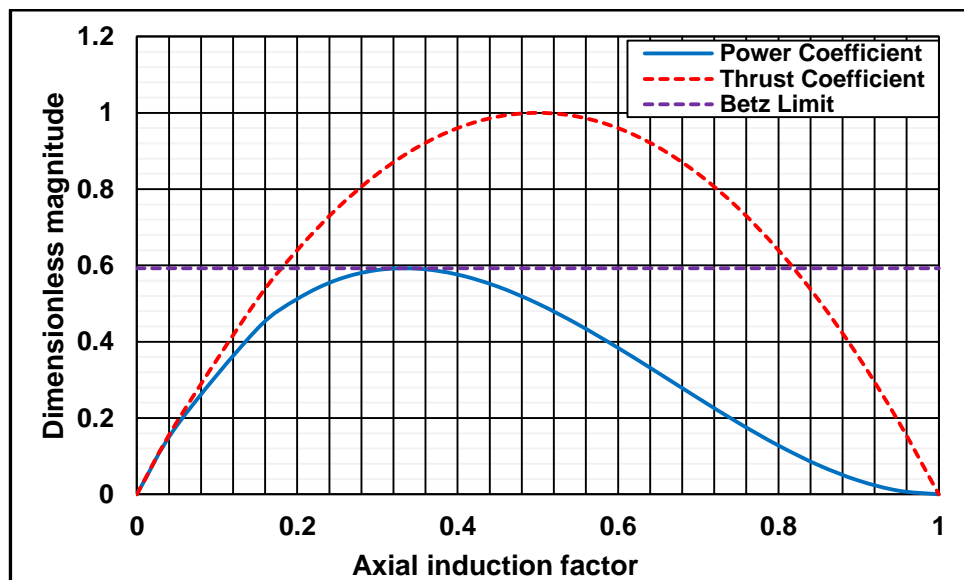


Figure 2-2 Betz turbine operating parameters (Manwell *et al.*, 2010).

However, the following effects lead to a decrease in the C_{pmax} :

- The rotational flow behind the rotor.
- Tip losses.

- Finite number of blades.
- Friction forces calculations (non-zero drag force).

2.3 Angular Momentum Theory

The main deficiency of the linear momentum theory is that it assumes there is no rotational flow at the wake flow. However, the wake flow has a rotation speed in the opposite direction of the rotor as consequence of the reaction of the rotor torque, which is achieved by the air passing through the rotor (Manwell *et al.*, 2010). Thus, the wake flow gains angular momentum behind the turbine rotor, which in turn means the air particles have velocity components in a tangential and axial direction. The tangential induction factor (a') is used to express the change in the tangential component. An annular stream tube, which has a radius (r) and radial width (dr) is used to determine the variations of both induced velocity components, as illustrated in Figure 2-3. The pressure, wake rotation and induction factors can be expressed as a function of radius.

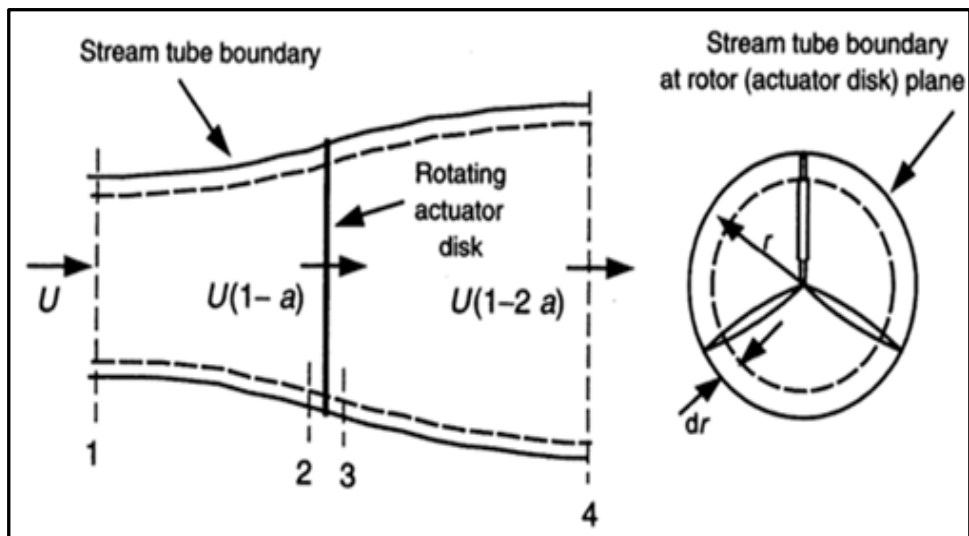


Figure 2-3 Stream tube with wake rotation (Manwell *et al.*, 2010).

In this model, the resulting thrust on an annular element is given as follows:

$$dT = (p_2 - p_3)dA = \left[\rho \left(\Omega + \frac{1}{2} \omega \right) \omega r^2 \right] 2\pi r dr \quad (2.28)$$

Where,

dA : A cross-sectional area of the element equals $2\pi r dr$ (m^2).

Ω : The angular velocity of the turbine rotor (rad/s).

ω : The angular velocity of the air flow in the wake (rad/s).

The angular induction factor a' is defined as:

$$a' = \frac{\omega}{2\Omega} \quad (2.29)$$

When the model considers the wake rotation, the thrust becomes:

$$dT = 4a'(1 + a')\frac{1}{2}\rho\Omega^2r^22\pi r dr \quad (2.30)$$

Note that based on the linear momentum analysis, the thrust equation can be rearranged to calculate the thrust force on an annular cross-section, as follows:

$$dT = 4a(1 - a)\rho U^2\pi r dr \quad (2.31)$$

Equating the equation (2.30) and (2.31) yields:

$$\frac{a(1-a)}{a'(1+a')} = \frac{\Omega^2r^2}{U^2} = \lambda_r^2 \quad (2.32)$$

Where, λ_r is the local speed ratio, it is obtained from the following equation:

$$\lambda_r = \frac{\Omega r}{U} = \frac{\lambda r}{R} \quad (2.33)$$

In this model, the torque can be equal to the rate of change of angular momentum of the air passing through the ring. Hence,

Torque=mass flow rate X change of tangential velocity X radius

$$dQ = dm(\omega r)(r) = (\rho U_2 2\pi r dr)(\omega r)(r) \quad (2.34)$$

The following torque expression can be reduced when substituting

$U_2 = U(1 - a)$ and $a' = \omega/2\Omega$ in the equation (2.34):

$$dQ = 4a'(1 - a)\frac{1}{2}\rho U\Omega r^2 2\pi r dr \quad (2.35)$$

And,

The power at each element is obtained by:

$$dP = \Omega dQ \quad (2.36)$$

2.4 Blade-Element Theory (BET)

The Blade Element Theory (BET) is used to predict wind turbine performance by dividing the rotor into a sufficient number of elements in the spanwise direction, as shown in Figure 2-4 (Ingram, 2005). The BET assumes that, there are no aerodynamic interactions between the blade elements. In addition, the generated forces are solely determined by each element using the local flow conditions, and using the lift and drag coefficients. Figure 2-5 shows that the velocity components of each element are determined in terms of wind speed, flow induction factors and rotor rotational speed. The

relationships between the forces, angles and velocities of the blade element are shown in Figure 2-6. BET depends on the known airfoil coefficients such lift coefficient (C_l) and drag coefficient (C_d) that were measured in the wind tunnel to calculate the aerodynamic forces of each element (Burton *et al.*, 2001).

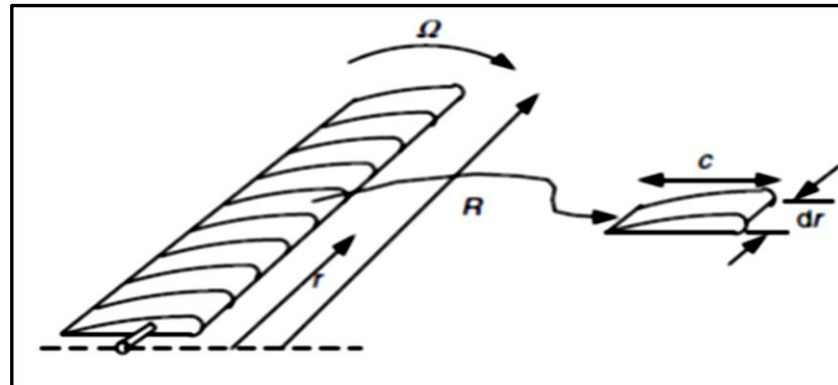


Figure 2-4 Schematic of blade elements (Ingram, 2005).

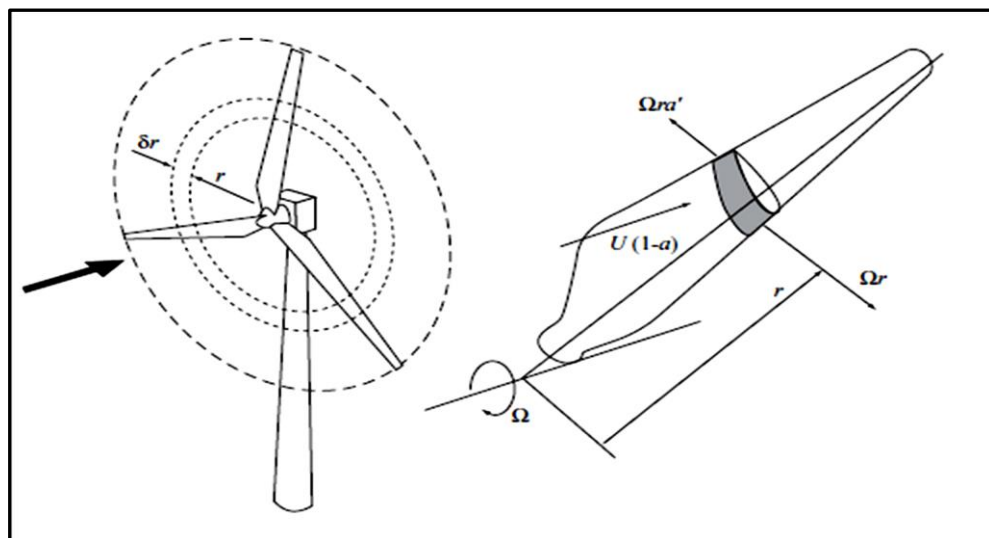


Figure 2-5 Velocity components analysis (Burton *et al.*, 2001).

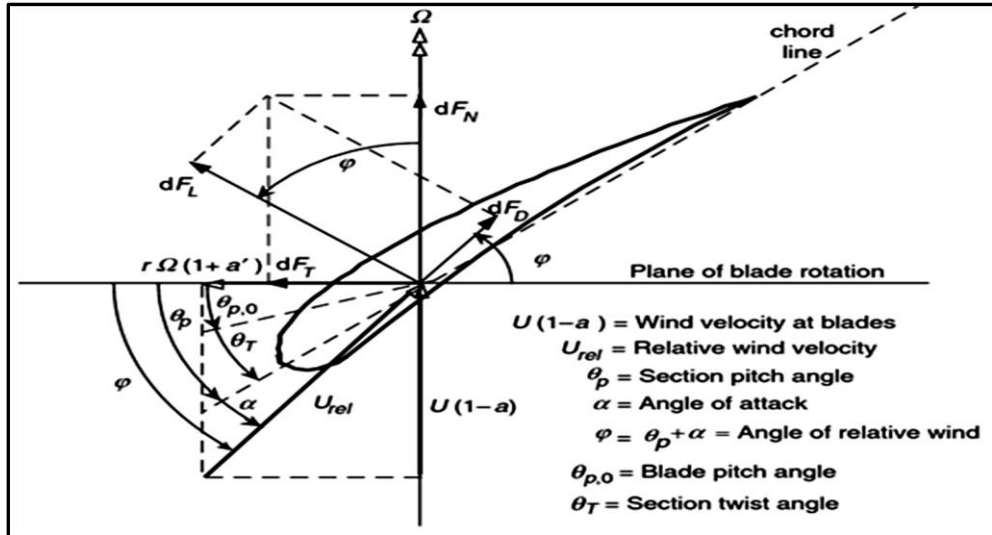


Figure 2-6 Relationships between the forces, angles and velocities of the blade element theory (Manwell *et al.*, 2010).

The following expressions can be obtained from Figure 2-6:

$$\varphi = \theta_p + \alpha \quad (2.37)$$

$$\tan\varphi = \frac{U(1-a)}{\Omega r(1+a')} = \frac{1-a}{(1+a')\lambda_r} \quad (2.38)$$

$$U_{rel} = \frac{U(1-a)}{\sin\varphi} \quad (2.39)$$

$$dF_L = \frac{1}{2} C_l \rho U_{rel}^2 c dr \quad (2.40)$$

$$dF_D = \frac{1}{2} C_d \rho U_{rel}^2 c dr \quad (2.41)$$

Hence,

The normal and tangential forces are given as follows:

$$dF_N = dF_L \cos\varphi + dF_D \sin\varphi \quad (2.42)$$

$$dF_T = dF_L \sin\varphi - dF_D \cos\varphi \quad (2.43)$$

Therefore,

The following equations are used to obtain the differential thrust force and torque respectively, when the rotor has B blades:

$$dF_N = \frac{1}{2} B \rho U_{rel}^2 (C_l \cos\varphi + C_d \sin\varphi) c dr \quad (2.44)$$

$$dQ = B r dF_T \quad (2.45)$$

$$dQ = \frac{1}{2} B \rho U_{rel}^2 (C_l \sin\varphi - C_d \cos\varphi) c r dr \quad (2.46)$$

2.5 Blade Element Momentum Theory (BEM)

The Blade Element Momentum theory (BEM) is the most common model that is frequently used to predict the aerodynamic behaviour around a wind turbine (Lanzafame and Messina, 2007; Moriarty and Hansen, 2005). The BEM method is a computationally cheaper model when compared with more sophisticated methods, such the CFD codes (Ingram, 2005; Vermeer *et al.*, 2003). BEM has been widely used in different codes, such AeroDyn and WT_Pref, to assess the optimal design of wind turbines (Moriarty and Hansen, 2005). BEM is a hybrid model that combines the Momentum Theory and the Blade Element Theory (BET). The BEM solves the thrust and torque equations that are obtained using the BET and Momentum Theory, iteratively. The BEM model calculations begin by guessing the values of the induction flow factors (a) and (a') with a view to determine the forces on each element independently. The following approach has been utilised by the BEM to design and analyse wind turbines (Manwell *et al.*, 2010):

From axial momentum theory, the thrust force is given as follows:

$$dT = 4a(1 - a)\rho U^2 \pi r dr \quad (2.31)$$

And, from angular momentum theory, the torque can be determined using the following equation:

$$dQ = 4a'(1 - a)\rho U \Omega \pi r^3 dr \quad (2.35)$$

Considering the Blade Element Theory, the normal force and torque are found respectively as follows:

$$dF_N = \frac{1}{2} B \rho U_{rel}^2 (C_l \cos \varphi + C_d \sin \varphi) c dr \quad (2.44)$$

$$dQ = \frac{1}{2} B \rho U_{rel}^2 (C_l \sin \varphi - C_d \cos \varphi) c r dr \quad (2.46)$$

By substituting U_{rel} from equation (2.39) and $\sigma' = \frac{Bc}{2\pi r}$ which is the local solidity, the equations (2.44) and (2.46) can be written as:

$$dF_N = \sigma' \pi \rho \frac{U^2 (1-a)^2}{\sin^2 \varphi} (C_l \cos \varphi + C_d \sin \varphi) r dr \quad (2.47)$$

$$dQ = \sigma' \pi \rho \frac{U^2 (1-a)^2}{\sin^2 \varphi} (C_l \sin \varphi - C_d \cos \varphi) r^2 dr \quad (2.48)$$

By equating the torque equations (2.35) and (2.48), which are given by the angular momentum and BET, with set $C_d = 0$ (for airfoils with low drag coefficients (Manwell *et al.*, 2010)), the following expression can be obtained:

$$\frac{a'}{(1-a)} = \frac{\sigma' C_l}{(4\lambda_r \sin\varphi)} \quad (2.49)$$

Similarly, the following expression can be given when equating the normal force equations (2.31) and (2.47):

$$\frac{a}{(1-a)} = \frac{\sigma' C_l \cos\varphi}{(4\sin^2\varphi)} \quad (2.50)$$

The iterative steps are as follows:

- Initially, guess values of a and a' .
- Calculate the relative wind angle (φ) using equation (2.38).
- Calculate the angle of attack using equation (2.37) and then determine C_l and C_d .
- Update values of a and a' using equations (2.49) and (2.50).

The above process is repeated until a tolerance between the new values of a and a' with the previous ones is accepted. Once the induction factors have been determined, the overall rotor power coefficient can be obtained from the following expression:

$$C_P = \left(\frac{8}{\lambda^2}\right) \int_{\lambda_h}^{\lambda} \lambda_r^3 a' (1-a) \left[1 - \left(\frac{C_d}{C_l}\right) \cot\varphi\right] d\lambda_r \quad (2.51)$$

The tip losses are considered big challenges that can cause uncertainty in the results. The tip losses are generated due to the pressure difference that is generated between the suction and pressure sides on the rotor. Accordingly, moving air tends to flow around the rotor tip, from the lower side to the upper side that reduces the lift force and the power production (James *et al.*, 2009). Therefore, a number of correction factors are used to improve the classical BEM analysis, such the Prandtl's factor (F) (Carcangiu, 2008). This factor (F) relates the number of blades, angle of the relative wind and the position on the blade as the following expression:

$$F = \left(\frac{2}{\pi}\right) \cos^{-1} \left[\exp \left(- \left\{ \frac{((B/2)[1-(r/R)])}{(r/R)\sin\varphi} \right\} \right) \right] \quad (2.52)$$

Therefore, the force equations which are obtained using momentum theory can be included by factor F, as follows:

$$dT = 4Fa(1-a)\rho U^2 \pi r dr \quad (2.53)$$

$$dQ = 4Fa'(1-a)\rho U \Omega \pi r^3 dr \quad (2.54)$$

And, the equations (2-49) and (2-50) can be rewritten to include the F factor, as follows:

$$\frac{a'}{(1-a)} = \frac{\sigma' C_l}{(4F\lambda_r \sin\varphi)} \quad (2.55)$$

$$\frac{a}{(1-a)} = \frac{\sigma' C_l \cos\varphi}{(4F \sin^2\varphi)} \quad (2.56)$$

Hence, the overall rotor power coefficient is given in the following expression:

$$C_P = \left(\frac{8}{\lambda^2}\right) \int_{\lambda_h}^{\lambda} F \lambda_r^3 a' (1-a) \left[1 - \left(\frac{C_d}{C_l}\right) \cot\varphi\right] d\lambda_r \quad (2.57)$$

Moreover, for heavy loaded conditions, when the axial induction factor is greater than 0.5, the classical BEM theory fails to accurately predict the wind velocity in the far wake flow due to the existing turbulence and recirculation flow (Manwell *et al.*, 2010). In this state, the BEM predicts the wake flow velocity as a negative value, which is unreasonable (Burton *et al.*, 2001). Figure 2-7 shows the deficiency of the BEM in matching the experimental data of the thrust coefficient (Buhl Jr, 2005). Hence, the classical BEM theory involves a number of empirical models, such as the Glauert, Burton and Wilson etc., with a view to improve the relationship between the thrust coefficient and axial induction factor (*a*) (Tang, 2012).

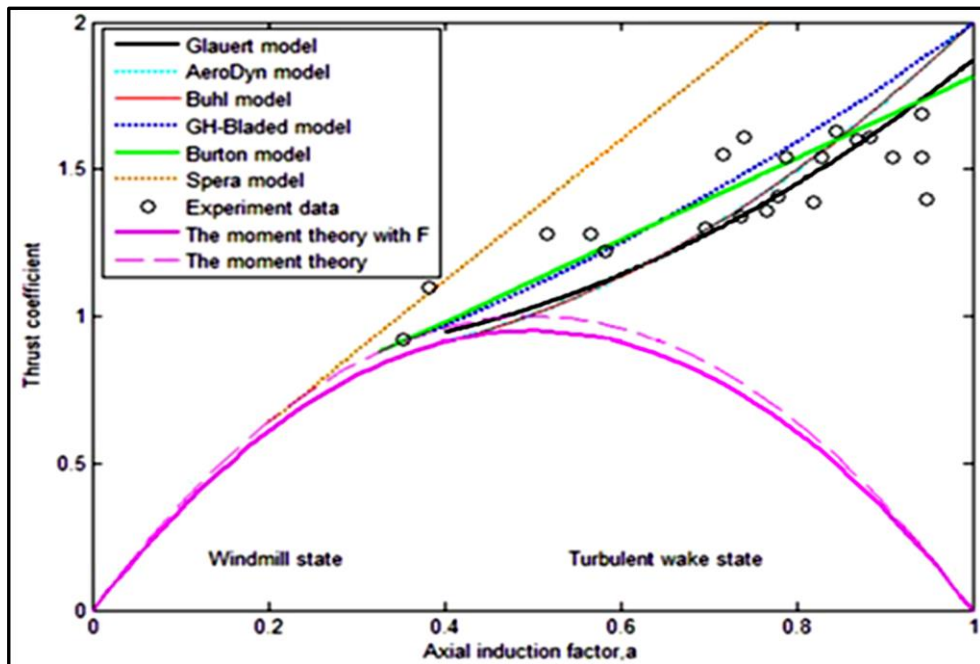


Figure 2-7 Classical BEM model with different correction factors (Tang, 2012).

From Figure 2-7, although the measurements used show a very wide scatter, all the correction models show a good predictions when compared with the measurements except the Sepra model. In addition, Figure 2-7 shows four models, namely, the Glauert model, the GH-Bladed model, the Burton model and the Sepra are well tangential to the predictions of the classical BEM theory without consideration of the tip-hub loss factor. However, these models are disconnected with the BEM predictions when the tip-hub loss factor is considered. Thus, this gap with the modified BEM predications may cause instability in calculations when a computer programme is implemented to iterate for a new induction factor (Pratumnopharat, 2012). Hence, Buhl Jr (2005) derived a new modification to the Glauert model for eliminating the numerical instability including the tip-loss factor to calculate the elemental thrust coefficient.

Furthermore, the BEM method predicts the element forces, depending on the lift and drag coefficients that were experimentally obtained from the 2D flow in a wind tunnel. It is proven that, due to the dynamic stall effects, the aerodynamic coefficients are significantly affected as result of the rotational effects (Lindenburg, 2003). Zhang (2013) reported that the BEM fails to match the measured shaft torque when the wind speed is higher than 7 m/s due to the dominant rotational effects. In the stall conditions, the rotor is more efficient in producing power that is predicted using models based on two-dimensional airfoil characteristics (Snel *et al.*, 1993; Wood, 1991). In general, the major drawback of the model is that is largely corrected depending on the empirical corrections which are not always available (Vermeer *et al.*, 2003).

2.6 Vortex Models

The Vortex models are a more sophisticated approach than the BEM versions, and have the potential to model the aerodynamic blade forces and the wake flow. They were implemented early to predict the aerodynamic forces and wake flow for helicopter rotors (Kocurek and Tangler, 1977; Landgrebe, 1972) and later used for wind turbines (Gupta, 2006). The Vortex models assume that, the flow around wind turbines is inviscid, incompressible and non-rotational, they can be modelled for predicting the wind turbines' performance. Unlike BEM, Vortex models represent a wind turbine by the number of finite blades in addition to the influence of the vortices, which can be considered in its calculations (Abedi, 2011). According to the Vortex models, the wind turbine blade is modelled by a lifting line or lifting surface and the wake is modelled by trailing horseshoe vortices.

The lifting line is based on the Prandtl's lifting line theory, where the blade is divided into a number of sections. It is restricted to a blade that has an aspect ratio greater than 1, and it can also be used for planar, slender or slightly curved blades (Van, 2001). Each section is modelled by a straight vortex filament of constant strength (Γ), as shown in Figure 2-8. The blade is replaced by a bound vortex, which is located at 1/4 of the chord line along the spanwise of a blade, and the trailing vortices are modelled by horseshoe vortices, as shown in Figure 2-9.

For each blade element, the lift force can be determined using the Kutta-Jukowski theory, as follows:

$$L = \rho V_{\infty} \times \Gamma \quad (2.58)$$

These methods need the previous knowledge of the aerodynamic tables for C_l , C_d for predicting wind turbine performance. However, these methods do not have the potential to predict the flow separation, particularly at high wind speeds of up to 12 m/s. Also, these methods need the aerodynamic table values for C_l and C_d (Leishman, 2002). Furthermore, it assumes the flow is inviscid (negligible viscosity) (Abedi, 2011).

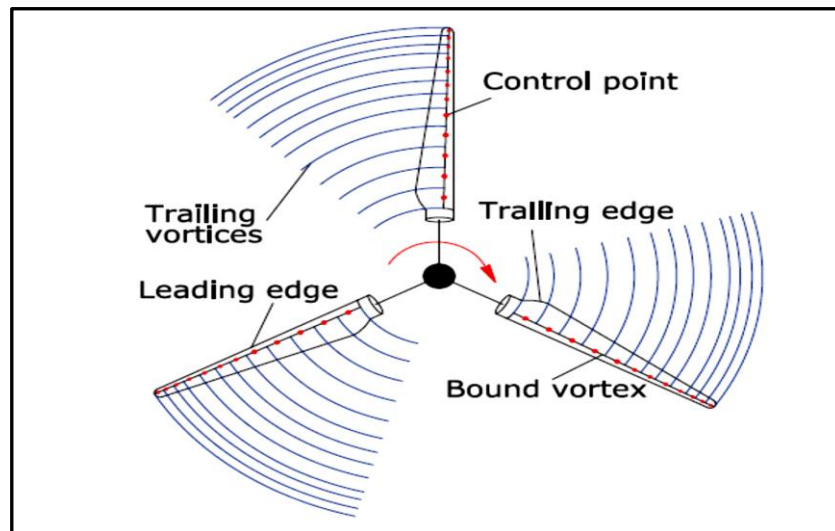


Figure 2-8 Schematic of blade modelling in the lifting line method (Abedi, 2016).

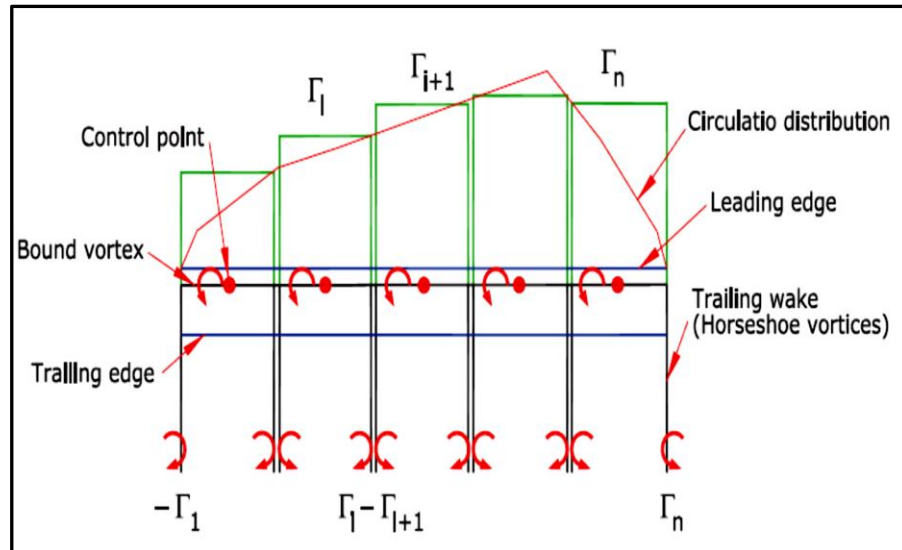


Figure 2-9 Schematic of the blade and wake flow (Abedi *et al.*, 2013).

2.7 Computational Fluid Dynamic (CFD)

CFD methods have become an attractive approach in diverse engineering fields, given that they can solve the Navier-Stokes (N-S) equations. The CFD methods have the potential to effectively describe the flow behaviour as laminar, transitional or turbulent flow. In addition, the CFD tools can represent the output results of streamlines, pressure and velocity contours as a real flow in a computational domain, without the need of previously reported C_l and C_d values. Consequently, comprehensive details that describe the flow field through the computational domain can be obtained, particularly for 3D effects (Gupta, 2006; Xu and Sankar, 2000). However, when compared to the BEM and VM methods, the CFD technique is more expensive demands due to the need for computational resources and large memory requirements. Additionally, the turbulence and separation flow associated with CFD methods are still the most challenges that limit the CFD use to predict the aerodynamic forces accurately (Leishman, 2002). In the present study, the CFD approach will be discussed in more detail in the next chapters.

2.8 Airfoil and general concepts of aerodynamics

The wind turbine output is directly related to the turbine rotor, which is mainly responsible for the generation of the aerodynamic forces, depending on the airfoil profile. The aerodynamic performance of an airfoil is mainly affected by a number of parameters, which are detailed in Figure 2-10. Their definitions are summarised in Table 2-1. Airfoil surface is divided into two sides: the upper surface is called the suction side and lower is the pressure side. The

interaction between the airfoil and flow field produces different pressure and velocity distributions on both airfoil surfaces. Accordingly, aerodynamic forces (lift and drag) and moment are generated along a rotor, and finally contribute to the wind turbine rotation, as shown in Figure 2-11. The lift and drag forces are defined as follows (Hansen, 2015):

- 1- Lift force (L): Perpendicular force in the direction of the wind stream is generated as a result of unequal pressure on the upper and lower airfoil sides, and it is used to rotate the wind turbine.
- 2- Drag force (D): Parallel force on the wind stream generates as a result of both the viscous friction forces and unequal pressure on the two airfoil surfaces.

And, the following expressions are used to determine the lift and drag force respectively:

$$L = \frac{1}{2} C_l \rho U^2 c \quad (2.59)$$

$$D = \frac{1}{2} C_d \rho U^2 c \quad (2.60)$$

Where,

L : Lift force (N).

D : Drag force (N).

C_l : Lift coefficient.

C_d : Drag coefficient.

ρ : Air Density (kg/m^3).

U : Undisturbed wind velocity (m/s).

c : Chord length (m).

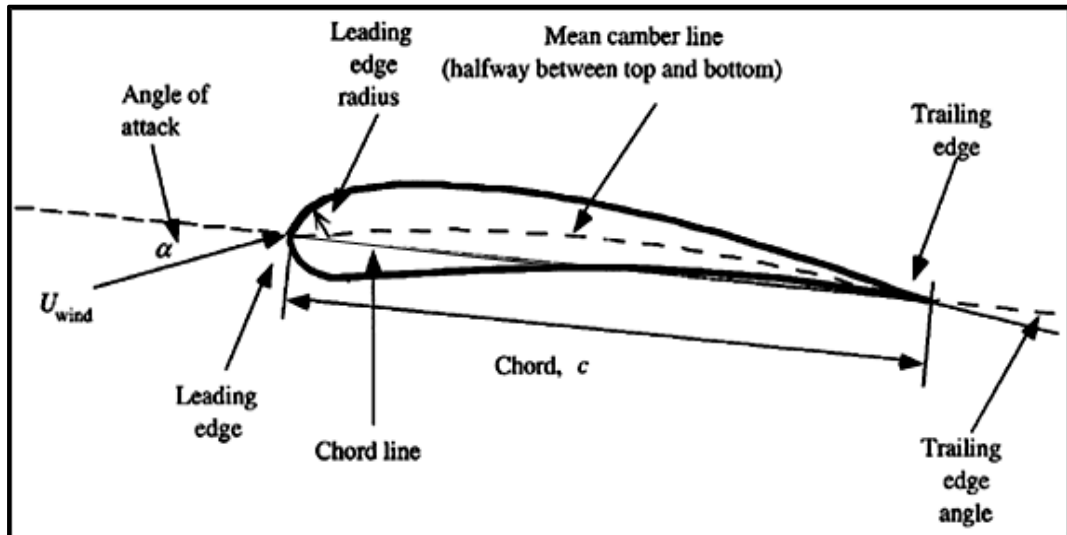


Figure 2-10 Airfoil terminologies (Manwell *et al.*, 2010).

Table 2-1 Shows the definitions of the airfoil terminologies.

Terms	Definitions
Angle of attack	The angle which the airfoil is hit by the free stream wind.
Camber	The distance between the chord line and the mean camber line.
Mean camber line	The halfway line between the upper and lower curvature from T.E to L.E.
Chord	The length of the line joining the trailing edge and the leading edge.
Chord line	The line joining the trailing edge and the leading edge.
Leading edge	The frontal curvature that faces the free stream wind.
Leading edge radius	The radius of the curvature of the leading edge.
Maximum thickness	The maximum distance between the airfoil's lower and the upper surface.
Trailing edge	The edge at the rear of airfoils.

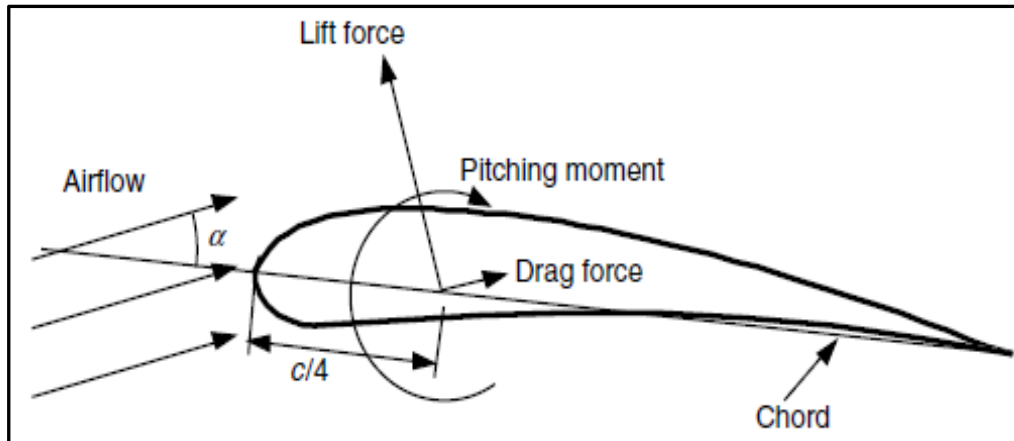


Figure 2-11 Aerodynamic drag and lift forces on stationary airfoil (Manwell *et al.*, 2010).

2.9 Wind turbine airfoil

Over the past decade, aeronautical knowledge was employed for designing wind turbine blades, because there is a similarity between them. Hence, wind turbine rotors were constructed using different available airfoil series, such as NACA 44XX, NACA 23XXXX and NACA 63XXX, which were designed for aircraft use.

However, it has been proven that all these series are sensitive to roughness effects yielding losses in the annual energy production (AEP), in particular, in the stall-regulated rotors (Tangler, 1990). One major disadvantage of the roughness effects is that the aerodynamic performance of an airfoil deteriorates remarkably as a result of the lift coefficient, which decreases as the drag coefficient is increased resulting in deterioration of the wind turbine performance (White *et al.*, 2011; Jasinski *et al.*, 1998).

Wind turbines operate in different operation conditions; therefore, it is necessary to design airfoils that are adapted to wind turbine conditions. Consequently, engineering efforts are focused on finding sophisticated wind turbine airfoils. The most important development in this field was achieved by the NREL and Airfoil Incorporated in 1984. Different airfoils were experimentally tested and designed using the Eppler code for the HAWT (Tangler and Somers, 1995).

This work produced 9 different airfoil families, which have 25 airfoils that were categorised corresponding to a blade length and generator size, as shown in Table 2-2. Additionally, each airfoil family consists of a root, primary and tip blade airfoil, in order to address the needs of stall-regulated, variable-pitch and variable wind turbines. In this effort, the roughness factor was considered for all airfoils with a view to avoid increasing the drag coefficient

due to ice, dust and the accumulation of insect debris (Tangler and Somers, 1995).

Table 2-2 NREL aerofoils and their applications (Tangler and Somers, 1995).

Blade Length(m)	Generator (KW)	Aerofoil thickness	Airfoil Family (root-----tip)			
1-5	2-20	Thick		S823		S822
5-10	20-150	Thin		S804	S801	S803
5-10	20-150	Thin	S808	S807	S805A	S806A
5-10	20-150	Thick		S821	S819	S820
10-15	150-400	Thick	S815	S814	S809	S810
10-15	150-400	Thick	S815	S814	S812	S813
10-15	150-400	Thick	S815	S814	S825	S826
15-25	400-1000	Thick		S818	S816	S817
15-25	400-1000	Thick		S818	S827	S828

2.10 Three-dimensional effects on wind turbine blade

It is understood that the airfoil shape causes a pressure difference between the upper and lower airfoil surface in 2D. Consequently, when three-dimensional blades are considered, the pressure non-equalization occurs at the wind turbine blade tip. The reason behind this phenomenon is that the air on the lower blade surface (high pressure) tends to move around the blade tip and join with the air on the upper blade surface (low pressure), as shown in Figure 2-12 (Anderson 2010). As result of the pressure non-equalization, two different spanwise air motions are generated over the lower and upper blade surfaces and a spanwise velocity component is introduced. On the low-pressure surface, the spanwise velocity component directs away from the blade tip whereas, it moves towards the blade tip on the high-pressure surface, as shown in Figure 2-13. As a result, trailing vortices are generated, which are similar to a sheet containing a number of the vortex filaments, as shown in Figure 2-14.

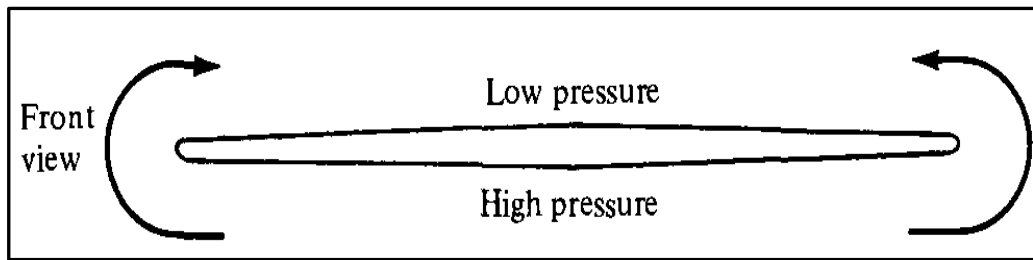


Figure 2-12 Pressure non-equalization between lower and upper blade surfaces (Anderson 2010).

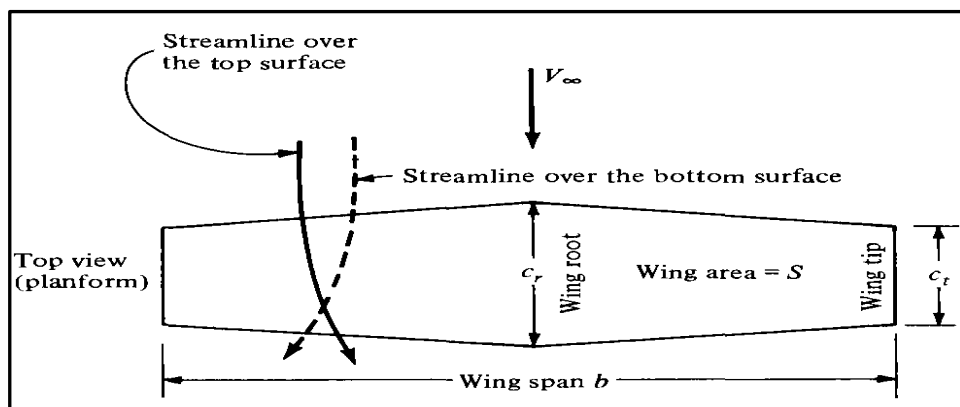


Figure 2-13 3D-dimensional effects on the blade (Anderson 2010).

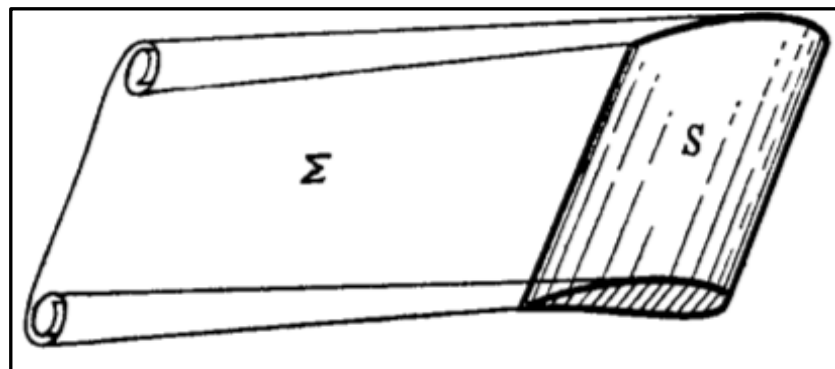


Figure 2-14 Schematic of vortex sheet (Thomson, 1966).

2.11 Three-dimensional flow behind of wind turbines

The vortex system consists of three types of vortices: the vortex sheet generates a helical path behind the rotor and the root vortices, which is created at the blade root as a linear path. In addition, the tip vortices, which are generated at the blade tip, as shown in Figure 2-15 (Hansen, 2015). Two velocity components are induced by the vortex system on a wind turbine. An axial velocity component is produced in opposition to the flow direction and

obtained using the axial induction factor. In addition, a tangential velocity component is induced in opposition to the rotation of the rotor and specified using the tangential induction factor.

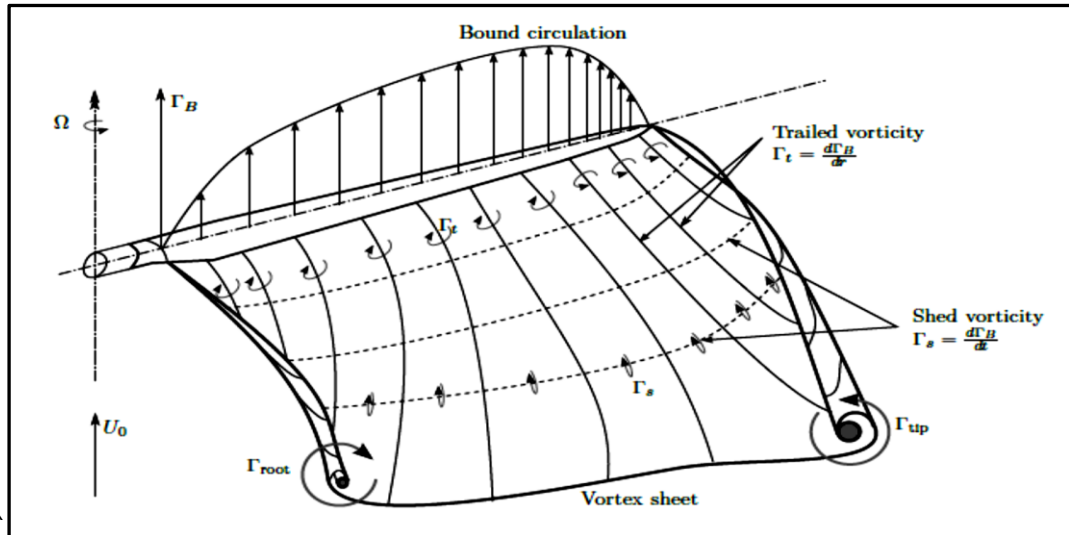


Figure 2-15 Vortex sheet behind the wind turbine rotor (Branlard, 2011).

2.12 Wingtip vortices

Wingtip vortices are common problems when studying the aerodynamics of fixed or rotating wings. They are easily observed in engineering applications, for instance, in airplane wings, helicopter blades, marine propellers, wind turbine blades and cars, as shown in Figure 2-16 (Giuni, 2013). Wingtip vortices have different influences corresponding to different engineering applications, therefore, a number of researchers have studied these effects (Park *et al.*, 2009; Arndt, 2002).

Concerning wind turbines, the wingtip vortices are inevitable as result of the 3D rotating effects. Consequently, the performance of a wind turbine is affected by the tip vortices, which are also a major source of noise and vibration. Vermeer *et al.* (2003) stated that, studying the properties of wingtip vortex is significant in improving the aerodynamic wind turbine's performance. Hence, the earlier research was experimentally conducted, using the flow visualisation to study the physical evolution of the wingtip vortices in the near wake flow (Alfredsson and Dahlberg, 1979). In their study, the wingtip vortices were observed as a sectional view when the smoke was inserted into flow using an external nozzle, as shown in Figure 2-17a. Meanwhile, they showed as a helix trace if the smoke is ejected into the flow from the blade tip, as shown in Figure 2-17b.

In addition, the tip vortex properties, for instance, the vortex spiral twist angle and the strength of the tip vortex have been experimentally studied by (Whale *et al.*, 2000; Vermeer, 1994). Further, other tip vortex properties, such as the transport velocity of the tip vortex, propagation speed and the travelling time have been investigated by a number of studies, as reviewed by (Vermeer *et al.*, 2003).

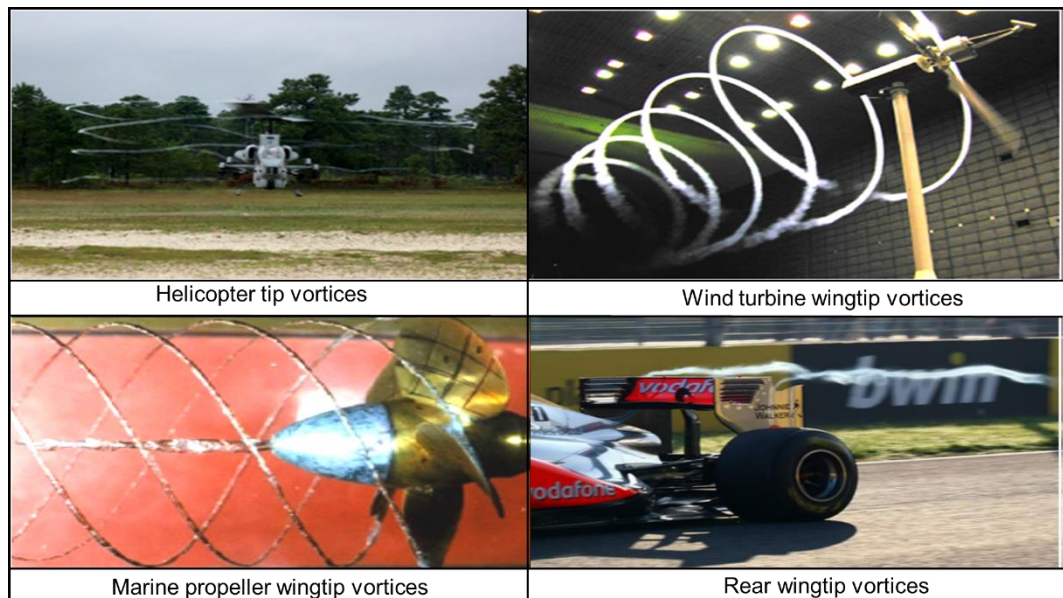


Figure 2-16 Wingtip vortices in different engineering applications (Giuni, 2013).

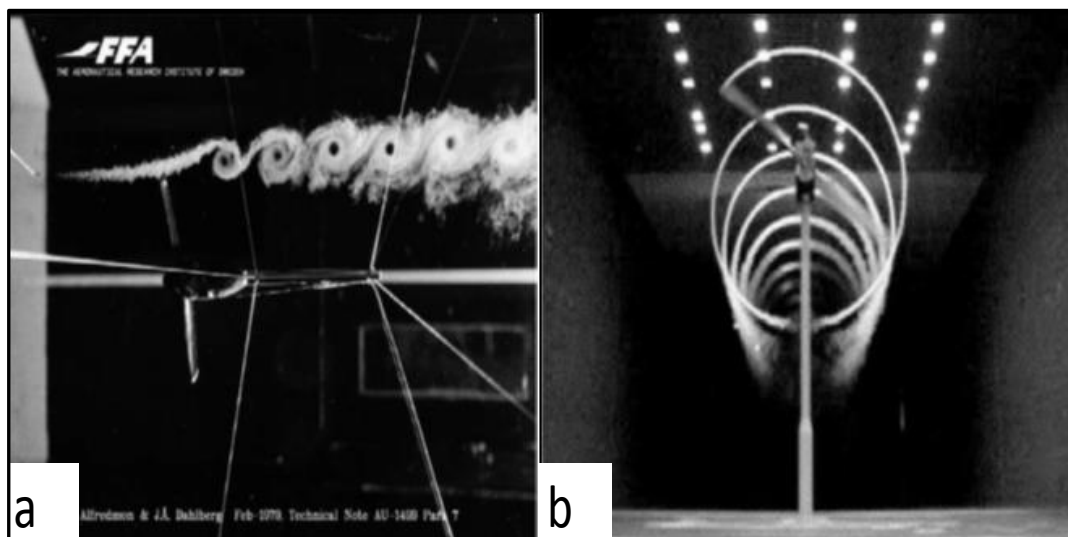


Figure 2-17 Flow visualization of the wind turbine wingtip vortices (Vermeer *et al.*, 2003).

2.13 Winglets

Winglets have been recommended as a successful solution for reducing the impact of the wingtip vortices. Winglets are defined as aerodynamic extensions that attach to the wing or blade tip to reduce the induced drag force, by diffusing the wingtip vortices toward the winglet tip. Winglets date back to 1897, but were not a topic of research until Whitcomb (1976) who investigated the winglet's effect on reducing the induced drag force. Whitcomb (1976) reported that aircraft efficiency can be improved by more than 7% by attaching nearly vertical fins to the KC-135A wing (Smith *et al.*, 2001). Winglets have been widely investigated for non-rotating wings, such as aeroplanes and sail-planes, using different winglet shapes (Prabhakar and Ohri, 2014). Gall and Smith (1987) stated that attaching winglets to biplane wings improved their performance by 13%, due to increasing the lift-curve slope and maximising the lift coefficient. For more detail, Berens (2008) provides a comprehensive review on using different winglets to improve non-rotating wings.

2.14 Winglet parameters

The pioneering work carried out by Whitcomb in 1976 is regarded as the first successful attempt to determine the outline of effective winglet design. He observed that the vertical surfaces that attached at wings tip perform efficiently in case of producing significant side forces which were overlooked in the most of the previous studies (Whitcomb, 1976).

However, Whitcomb's work was followed by Maughmer, who focused on the most effective parameters of winglet performance. The Maughmer's investigation depended on the earlier work conducted by Heyson *et al.* (1977) and Vandam and Roskam (1983). These studies investigated the influence of winglet parameters on aerodynamic load distribution on winglet/wing combinations, compared with the tip extension. Their results showed that the aerodynamic benefits from winglets are greater than the tip extensions in improving efficiency; also, the most important winglet parameters that play a significant role have been fixed such as toe, cant, sweep, twist angles and winglet length.

Maughmer has led a research group at the Pennsylvania State University since the 1980s, where extensive research works were experimentally and analytically carried out on sail-plane winglets (Maughmer, 2002). These efforts have become aspirational for all winglet designers of different applications. According to Heyson *et al.* (1977); Vandam and Roskam (1983)

and Maughmer (2003), the most important winglet parameters were established for improving the winglet performance. They stated that the winglet height, planform shape, sweep, twist, toe and cant angles should be investigated with a view to establish the optimum winglet design. In addition, Maughmer (2003) outlined a significant result, which explains that for each operating condition, there is only one optimisation characteristic for winglet/wing combination.

Moreover, it should be noted that the winglet has a different function than a wing. Thus, it requires a design to specify an airfoil for achieving its goal (Maughmer *et al.*, 2002). Hence, the winglet airfoils, with other winglet parameters (winglet height, sweep, twist, toe and cant angles) together use important parameters to shape the final planform, as shown in Figure 2-18. The following are the most common winglet parameters that have been investigated:

- Height.
- Sweep angle.
- Cant angle.
- Curvature radius.
- Toe angle.
- Twist angle.

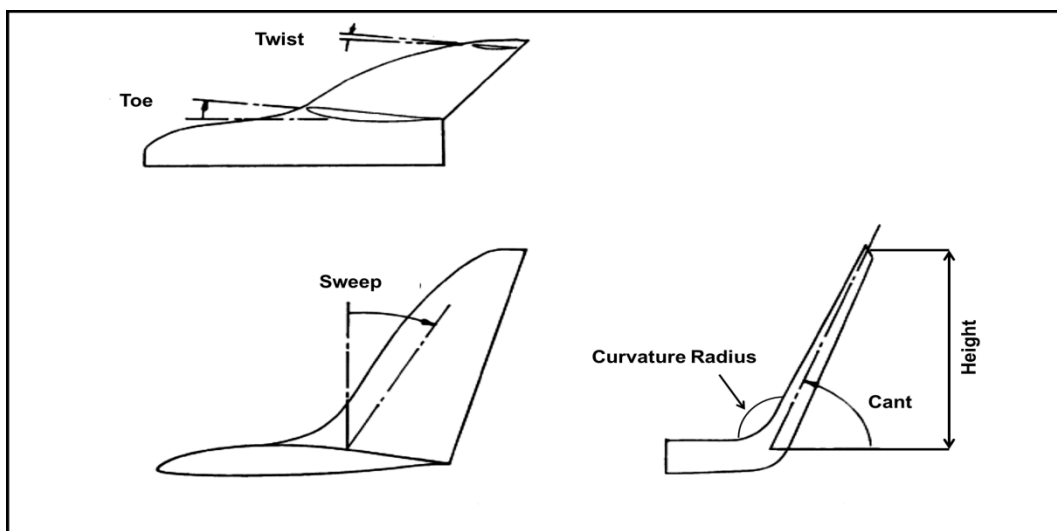


Figure 2-18 Winglet parameters (Maughmer, 2006).

However, by comparison, the investigation on the winglets' benefits in the rotating wings, particularly in wind turbines, is more limited than the studies that have been conducted on non-rotating wings (Al-Abadi, 2014; Gertz, 2011; Gaunaa and Johansen, 2007).

Finally, the following section is a summary of studies which investigate the influence of the winglet on a HAWT.

2.15 Literature review of the winglet effects on the horizontal axis wind turbine performance

Ariffudin *et al.* (2016) implemented the CFD method for studying the aerodynamic performance of two winglet configurations (upwind and downwind), compared to a sword and swept tip extension as shown in Figure 2-19. The tip extension configurations had a length of 20mm; meanwhile, both winglets were tilted by 83° towards the upwind and downwind by extending the original blade by 20 mm. All CFD computations were conducted in steady-state conditions and the SST k- ω turbulence model was used to solve RANS equations.

The results showed that both the tip extensions perform better than winglet configurations (upwind and downwind) to improve the wind turbine production in terms of the power coefficient. At tip speed ratios less than 4.5, the sword and swept tips produced average percentage increases in the power coefficient by 7.3% and 9.1% respectively, when compared with the baseline blade. However, the sword and swept tips caused reductions in power coefficient by 20% and 20.1% respectively at the tip speed ratios higher than 4.5.

In contrast, at tip speed ratios less than 3.5, the upwind and downwind winglets slightly improve the average percentage increase in power coefficient by 1.8% and 3.5% respectively. However, the reductions in the average percentage of power coefficient were obtained by 11.5% and 19% due to attaching the upwind and downwind winglets respectively, at the tip speed ratios higher than 3.5.

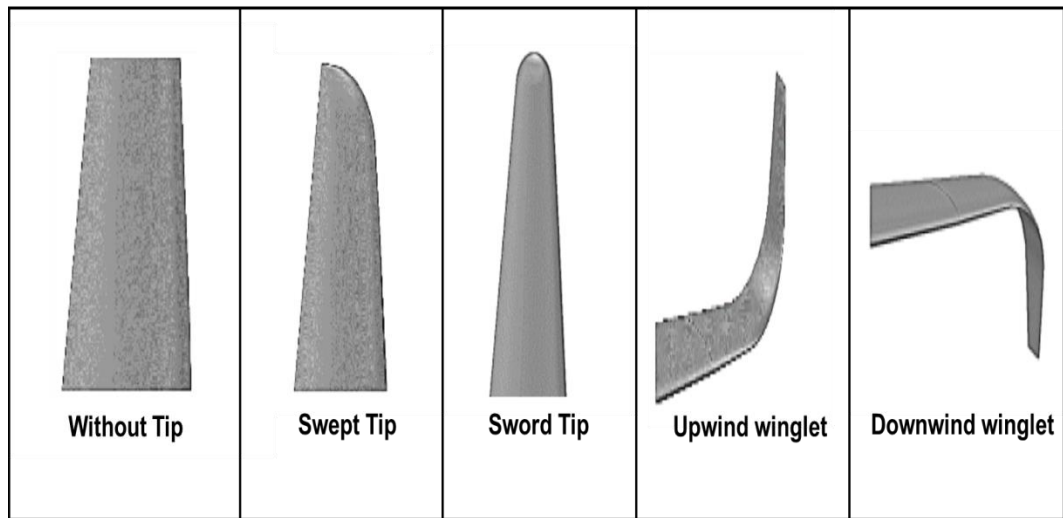


Figure 2-19 Tip extensions and winglet configurations studied by Ariffudin *et al.* (2016).

Elfarrar *et al.* (2014) used the CFD approach to investigate the aerodynamic winglet effects on the NREL phase VI performance. In this study, four winglet configurations were created by extending the blade tip 1.5% of the baseline blade radius towards pressure side, suction side, tangentially leading-edge side and tangentially trailing edge side as shown in Figure 2-20. In addition, the aerodynamic effects of the cant and twist angles are considered to improve winglet functionality. Four different turbulence models, namely, standard $k - \varepsilon$ (Lauder-Sharma), Spalart-Allmaras, $k - \varepsilon$ (Yang-Shih) and Shear Stress Transport (SST $k - \omega$) were used for validating the numerical results comprising of the experimental data.

An improvement in the power output was obtained by attaching the winglet configuration, which is tilted towards the suction side by a 45° cant angle and 2° twist angle. The percentage of increase in the power output was less than 5% at wind speeds from 5 m/s to 9 m/s, and was increased to around 10% at moderate wind speeds between 11 m/s to 15 m/s. However, due to the NREL phase VI is stalled regulated, the improvement sharply dropped to around 1% at wind speeds greater than 17 m/s.

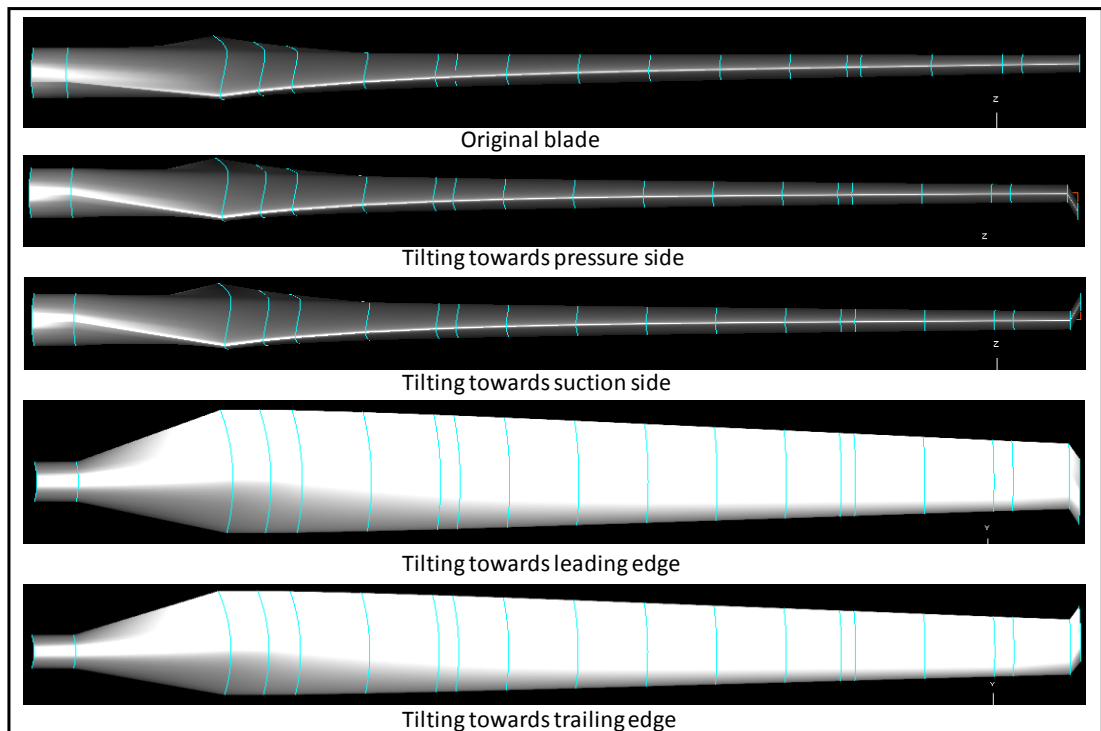


Figure 2-20 Winglet configurations studied by Elfarra *et al.* (2014).

Ali (2014) examined the effect of winglet position (upwind and downwind) on small wind turbine performance, both experimentally and numerically. Both winglet configurations were extended by 44.2 mm from the blade tip and were tilted by 45° by using the SG6051 airfoil. The experimental results showed that, the maximum power coefficient was measured to be 0.48 as a result of adding the upwind winglet, whereas the baseline produced 0.45. In contrast, the downwind winglet caused a drop in the maximum power coefficient from 0.45 (baseline) to 0.41.

In addition, the experimental improvements were achieved numerically using the CFD approach. The numerical analysis was carried out using Ansys CFX and the SST $k-\omega$ model was used to solve the governing flow equations. A slight improvement was occurred in power coefficient at the tip speed ratios less than 4 due to using the upwind winglet. However, this improvement increases to the maximum value of 0.42, when compared to 0.40 (baseline) at tip speed ratio of 4.2. Meanwhile, the downwind winglet caused a sharp reduction in the power coefficient at all tip speed ratios.

Al-Abadi (2014) experimentally investigated the influence of turbulence intensity on the power coefficient, tip vortex and the wake flow. In his study, a comparative analysis was conducted, in order to investigate the effect of the turbulence intensity and the functionality of downwind winglet on wind turbine performance in terms of the power coefficient. Two different turbulence

generating grids were implemented, namely, the fine grids, in order to generate a moderate turbulence intensity of 0.025 and the coarse grids for generating a high turbulence intensity up to 0.114 as shown in Figure 2-21. The results demonstrated that the influence of the turbulence intensity in both cases (low and high turbulence intensity) was more efficient than the winglet used to improve the power coefficient. The superiority of the turbulence increase in both cases was established at the tip speed ratio range from 3.5 to 6.

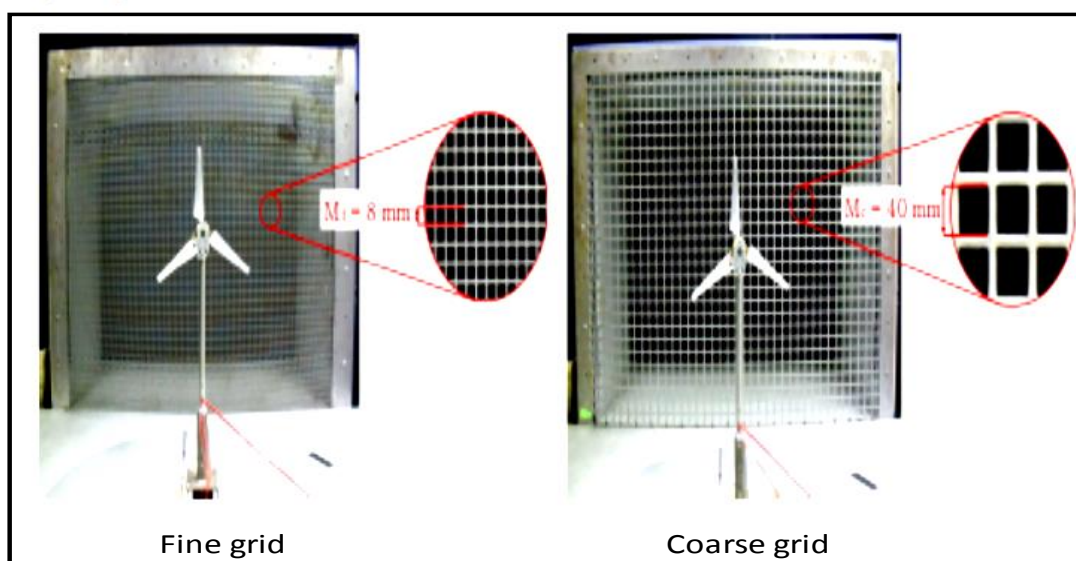


Figure 2-21 Turbulence generating grids used by Al-Abadi (2014).

Elfarrar *et al.* (2014) implemented a genetic algorithm and the CFD approach to investigate the influence of the cant and twist angles on winglet performance. The NREL phase VI was used as a baseline to validate the numerical results in terms of the power output versus wind speeds, the chordwise pressure coefficient distributions and the force coefficients. All winglet configurations were pointed towards the suction side, whilst keeping the winglet height at 1.5% of the baseline blade length.

The CFD approach was conducted in wind speeds of 5 m/s, 7m/s and 9m/s to study effect of the 24 winglet configurations that were created by varying the twist angle from -2° to 5° and three cant angles (45° , 68° and 89°). Meanwhile, a genetic algorithm was implemented to optimise the winglet configurations at the wind speeds of 5 m/s, 7 m/s and 9 m/s. The optimised results showed that the numerical torque increased by 11.7%, 9.0% and 8.0% at wind speeds of 5 m/s, 7m/s and 9m/s, respectively, when compared to the baseline torque. These improvements were obtained due to attaching the winglet that was twisted by 2° and tilted by 84° cant angle. Consequently,

an average increase in the power output was 9%, at a wind speed range from 5m/s to 25 m/s.

(Saravanan *et al.*, 2013) experimentally investigated the winglet influence on a small horizontal axis wind turbine that was used in a remote area where the grid electricity is weak. The main goal of this study was to improve small wind turbine performance and reduce the self-starting requirement. Two winglet parameters were tested in their study, namely, the winglet height and curvature radius. The winglet height was chosen to be 2% and 4% of the baseline blade radius which has 140mm length, whereas the curvature radius was 12.5% and 25% of the winglet height, whilst keeping the cant angle at 75° towards the suction side. The experiments were carried out at the range of wind speeds from 4.74 m/s to 13.42m/s, which corresponds to the tip speed ratio from 1.5 to 4. The results showed that the winglet performance increased with the winglet height directly and inversely with the winglet curvature radius.

Hence, the most effective winglet was achieved by 4% of the winglet height and 12.5% of the curvature radius. This configuration increases the power coefficient to 12.8% at a tip speed ratio of 1.91, when compared to the baseline blade. Further, the initial starting velocity of a wind turbine was decreased to 2.8 m/s when compared to the baseline blade, which starts at a velocity of 4.7 m/s. However, the configuration shows ineffective performance to improve the power coefficient at tip speed ratios higher than 3.0 with a significant violent vibration. The same result was obtained numerically by implementing the CFD approach that was conducted by Saravanan (2013).

Gupta and Amano (2012) investigated the influence of the winglet height and cant angle on wind turbine performance in terms of the output power, numerically. The RANS equations were solved in steady-state conditions using the Spalart-Allmaras turbulence model. Table 2-3 shows the winglet parameters that were studied. All the winglet configurations were tilted towards the pressure side, using the NACA4412 airfoil.

Numerical comparisons were conducted in terms of the output power between the original wind turbine model and the modifications at the range of wind speeds between 7 m/s and 19 m/s. The study shows that the power increase is directly proportional to the winglet height and the greatest increase in output power is 20%, which was achieved due to attaching configuration 4.

Table 2-3 Winglet parameters studied by Gupta and Amano (2012).

Winglet configuration	Cant angle (°)	Winglet height% (of the rotor radius=10 m)
Configuration 1	90	2
Configuration 2	90	4
Configuration 3	45	2
Configuration 4	45	4

Gertz (2011) tested two different winglets, which are the Gertz and Maniaci winglets experimentally. Further, the numerical predications of the Maniaci performance using the VM method which conducted by Maniaci (2013) is included in his study. Both winglets were created using the PSU 94-097 airfoil that was tested experimentally to be a suitable winglet airfoil which could improve sail-planes' performance. Both winglets were pointed by a 90° cant angle and the winglet height was 8% of the baseline blade which has 1440mm length toward the suction side. The parameters of both winglets are summarised in Table 2-4. The winglet parameters were taken from the author's observations of the previous literature and Maughmer's previous recommendations. The study showed that Maniaci and Gertz's winglets increased the power output by 5%, at a wind speed between 6.5 m/s to 9.5 m/s when compared to the baseline case. However, the wind turbine output decreased beyond of this wind speed range.

Table 2-4 Winglets' parameters used by Gertz (2011).

Winglet name	Planform	Root chord ratio	Tip chord ratio	Twist (°)	Toe (°)
Maniaci	Rectangular with taper	0.95	0.79	3.5	-3
Gertz	elliptical	1.0	0.34	-0.5	-0.5

Congedo and De Giorgi (2008) reported on the effect of winglet curvature radius on wind turbine performance, numerically. The NACA 63-430 and FFA-W3-301 airfoils were used for constructing the wind turbine rotor, which has a diameter of 52m. Towards the suction side, two winglet configurations were created by changing the winglet curvature radius to 25% and 50% of the winglet height, whilst keeping both the configurations' heights at 2% of the rotor radius. The computations were carried out at a wind speed equal to 7m/s, using the CFD approach. The flow was assumed to be in a steady-state condition and the turbulent viscosity was modelled using the SST k- ω turbulence model. The results showed that a slight improvement in the mechanical power was obtained due to attaching both configurations. The improvement was 1.7% and 1.6% of the mechanical power due to changing the winglet curvature radius by 25% and 50% of the winglet height, respectively.

Johansen and Sørensen (2007) offered different winglet parameters that were numerically studied, such as the winglet height, curvature radius, sweep and the twist angles, as summarised in Table 2-5. All the winglet configurations were bent towards the suction side and the computations were calculated at a wind speed equal to 8m/s. The EllipSys3D and the SST k- ω turbulence model were used for solving the RANS equations in the steady-state conditions. The results showed that an increase in the twist angle from 0° to 8° led to a slight increase in the mechanical power (around 1.6%) and thrust (around 1.9%). Further, no significant increase in the mechanical power or thrust was observed when the curvature radius was equal to 100% of the winglet height, or when increasing the sweep angle from 0° to 30°. The most significant result in this work was that the mechanical power was increased by 2.77%, by attaching the W 9, which has a height of 4% of the baseline blade.

Table 2-5 Winglets' parameters according to the study of Johansen and Sørensen (2007).

Winglet name	Winglet height (%radius)	Curvature radius (%winglet height)	Sweep angle(°)	Twist angle(°)
W1	2	50	0	0.0
W2	2	50	0	2.0
W3	2	50	0	4.0
W4	2	50	0	8.0
W5	2	100	0	0.0
W6	2	100	0	4.0
W7	2	25	0	4.0
W8	2	25	30	4.0
W9	4	12.5	0	4.0
W10	1	50	0	4.0

Johansen and Sørensen (2006) investigated the aerodynamic effect of the five winglet configurations on the turbine's mechanical power and the thrust force. In their study, the winglet configurations were designed according to changes of the winglet airfoil, twist angle and the winglet position, as shown in Table 2-6. The winglets' height and cant angle were kept at 1.5% of the rotor radius and 90° , respectively. The computations were carried out using the EllipSys3D solver and the SST k- ω turbulence model to solve the governing flow equations at wind speeds of 6, 8.5, 10 and 12m/s. The results show that all the configurations caused a slight increase of around 1.5% in the mechanical power and thrust force, when compared to the baseline blade. However, the greatest increase was achieved due to attaching configuration 5, which was bent toward the suction side. The increase in mechanical power was 1.71%, at a wind speed 10 m/s.

Table 2-6 Winglets parameters according to the study of Johansen and Sørensen (2006).

Winglet no.	airfoil	Twist angle ($^\circ$)	Winglet position
Winglet 1	NACA 64-018	0	Pressure side
Winglet 2	NACA 64-518	-2	Pressure side
Winglet 3	NACA 64-518	-5	Pressure side
Winglet 4	NACA 64-518	+3	Pressure side
Winglet 5	NACA 64-518	-2	Suction side

Finally, the advantages and limitations of the previous studies are summarised in the following table.

Table 2-7 The summary of advantages and limitations of literature.

Authors	Winglet Planform	Advantages
Ariffudin <i>et al.</i> (2016). (Numerical/CFD)	Rectangular	1. A comparative study between the influence of winglet position (upwind and downwind) and blade tip extensions (sword and swept) at different tip speed ratios.
		Limitations
		1. The effects of winglet parameters are not studied leads to a poor in the winglet performance. 2. The winglet height and cant angle implemented in the study are not enough for having a significant increase in the power coefficient. 3. The numerical computations without validation.
Elfarrar <i>et al.</i> (2014). (Numerical/CFD)	Rectangular	Advantages
		1. Studying the influence of winglet position on its performance at different wind speeds. 2. Studying the influence of cant angle (45°, 90°) and twist angle (0°, 2°) at different wind speeds.
		Limitations
		1. Winglet length effect is not studied results a poor winglet performance in low and high wind speeds. 2. Viscous forces are not considered due to implementing a value of y^+ equals 7.
Ali (2014). (Experimental and numerical/CFD).	Rectangular	Advantages
		1. Studying the influence of winglet positions (upwind and downwind) on its performance. 2. Predicting the winglet performance at a cant angle of 45°.
		Limitations
		1. The effect of winglet length is not studied results to poor performances in both winglet configurations at low tip speed ratios.

Authors	Winglet Planform	Advantages
Al-Abadi (2014). (Experimental study).	-	1. Studying the influence of turbulence level to increase a wind turbine performance comparing to a winglet function.
		Limitations
		1. A winglet design is simple and the effects of the winglet parameters were not implemented.
Elfarra <i>et al.</i> (2014). (Numerical/Genetic algorithm and CFD).	Rectangular	Advantages
		1. A genetic algorithm and CFD method are implemented to study the effects of cant angles (45°, 68° and 89°) and twist angles (-2° to 5°) on winglet performance.
		Limitations
		1. Effect of winglet height is not investigated. 2. Viscous forces are not considered due to using a value of y+ equals of 7. 3. The effect of separation flow is not considered in Genetic algorithm calculations.
Saravanan <i>et al.</i> (2013). (Experimental and numerical/CFD).	Rectangular	Advantages
		1. Studying the influence of winglet height and curvature radius to reduce the self-starting requirement of a small wind turbine.
		Limitations
		1. The best configuration shows ineffective performance at tip speed ratios higher than 3.0 due to using small winglet height.

Authors	Winglet Planform	Advantages
Gupta and Amano (2012). (Numerical/CFD).	Rectangular	1. Studying the influence of winglet height and cant angle on a winglet performance.
		Limitations
		1. Using the Spalart-Allmaras model which is known inaccurate to capture separation flow at high velocity and the viscous effects are not considered due to implementing a value of y^+ equals 6.5. 2. Numerical results without validation.
Gertz (2011). (Experimental and numerical/ VM method).	Rectangular and elliptical	Advantages
		1. A comparative study between the performances of rectangular with taper and elliptical winglets. 2. Implementing the PSU 94-097 winglet airfoil to create the winglet planform.
		Limitations
		1. The experimental limitation is that the effects of winglet parameters are not studied since they are chosen from a literature. 2. The stall flow is not modelled in the numerical predictions of Maniaci performance due to implementing the VM method.
Congedo and De Giorgi (2008). (Numerical/CFD).	Rectangular	Advantages
		1. Studying the influence of winglet curvature radius on a winglet performance.
		Limitations
		1. Studying the winglet performance was conducted at a wind speed of 7 m/s. However, an effective winglet design needs to test the winglet performance at a wide range of wind speeds. 2. One winglet parameter was predicted (winglet curvature radius) led to a poor winglet performance. A successful winglet design requires an optimising of more than two parameters, particularly, cant angle and winglet length. 3. The numerical results were conducted without validation.

Authors	Winglet Planform	Advantages
<p>Johansen and Sørensen (2007). (Numerical/CFD).</p>	<p>Rectangular</p>	<p>1. Studying the influence of four winglet parameters (winglet height, curvature radius, sweep and twist angles).</p>
		<p>Limitations</p>
		<p>1. The study was carried out at a wind speed 8 m/s, whereas an effective winglet design requires an investigation of a wide range of wind speeds. 2. The effect of cant angle is not considered leads to eliminate the potential of winglet length to a significant increase in a mechanical power. 3. The numerical results were conducted without validation.</p>
<p>Johansen and Sørensen (2006). (Numerical/CFD).</p>	<p>Rectangular</p>	<p>Advantages</p>
		<p>1. The effect of winglet airfoil, twist angle and winglet position were investigated to improve the winglet performance.</p>
		<p>Limitations</p>
<p>1. The effects of winglet height and cant angle were not considered in the study. Accordingly, the winglet configurations show poor performances. 2. The numerical results were conducted without validation.</p>		

2.16 The contributions of this thesis to enhance the literature review

According to the literature, the first successful application of the winglet was implemented to improve sail-plane performance by Maughmer and Kunz (1998), which has been regarded as the guideline for an effective winglet design for rotating and non-rotating wings. Thereby, different types of winglet planform, such as spiroid, blended, elliptical, semi-circular, split-tip and multi-winglets were investigated experimentally and numerically on aeroplanes. The numerical and experimental studies that investigated the influence of winglets were limited in wind turbines field. Additionally, the rectangular winglet planform dominated in the numerical wind turbine studies. However, three key points can be noted from the previous studies, as outlined in the following points:

- 1- As previously mentioned, there is a unique optimum design of winglet, which is related to the aerodynamic wing specifications and the flow conditions, such turbulence and stalled flow (Maughmer, 2003). The literature trend is to study of winglet performance at one wind speed, or by employing limited winglet parameters. Thereby, winglet functionality shows a slight increase or reduction in the wind turbine production as presented in the investigations that conducted by Ariffudin *et al.* (2016); Ali (2014); Congedo and De Giorgi (2008); Johansen and Sørensen (2007).
- 2- The effect of the winglet planform has not been comprehensively studied. Although, the study was conducted in the literature experimentally by Gertz (2011). The limitation of this study is that the effects of winglet parameters were not investigated since they were implemented by the author's observation of the best winglet design in literature. Further, the study involves of the predictions of the rectangular winglet performance using the VM method which does not model the effect of stall flow. However, winglet is defined as an aerodynamic extension which attaches to the blade tip. Accordingly, the optimum winglet parameters supplement the potential of turbine rotor to capture more kinetic energy. Furthermore, an uncertainty of the performance of rectangular winglet is expected due to the stall flow is not modelled in the VM method.
- 3- The winglet airfoil effect has not been investigated, considering it plays an important role in generating lift force, which enhances the winglet performance, as recommended by (Whitcomb, 1976).

Hence, the following points outline the present study's contributions:

- 1- The CFD method is employed to study the winglet performance in a wide range of wind speeds at different flow conditions such as attached and stalled flow. In chapter four, the NREL phase VI is chosen to validate the numerical results in terms of torque, thrust force, pressure coefficient distributions and the normal force coefficients.
- 2- Chapter five presents the effect of the winglet planform since it increases in the projection area of a wind turbine rotor and leads to greater interaction between the wind turbine rotor and the moving air. This aim shall be achieved by implementing the rectangular and elliptical winglet planform.
- 3- The effect of winglet airfoil, which is implemented to create the winglet planform, shall be studied in chapter six. Initially, two airfoils are employed to generate a winglet planform, namely, the S809 and PSU 94-097 airfoils. Then, a preliminary aerodynamic analysis is introduced by implementing four thin airfoils which are the S801, S803, S805A and S806A airfoils, with a view to choosing a successful winglet airfoil.

2.17 Summary

The aerodynamic fundamentals have been introduced to predict a wind turbines' performance. In addition, the chapter has included the most common aerodynamic models that are frequently implemented within the wind turbines field, such the blade element momentum theory, vortex methods and CFD methods. Among of these methods, the features of the BEM methods are discussed in detail, given that they are well known in the field of industrial applications, and reasons why they are not considered in the present study have been presented.

In addition, the chapter presents the aerodynamic background of the vortices system associated with wind turbine operation. Winglets are discussed as one solution towards reducing the impacts of vortices. Unlike rotating wings, winglets are extensively investigated in a non-rotating wing.

Finally, the chapter introduces the previous numerical and experimental studies, which investigate different winglet parameters. Winglet performance is still poor in improving wind turbine production, as shown in the extant literature. The weak points of the previous studies are also addressed in this chapter.

Chapter 3 : Governing Equations and Computational Fluid Dynamics

3.1 Introduction

The considerable developments of computational hardware resources have attracted a number of researchers towards implementing CFD methods to predict the aerodynamic characteristics of wind turbines. The CFD approaches are considered robust tools to model real fluid flow behaviour in the engineering applications, including wind turbines. Unlike the BEM and VM methods, the CFD approaches have the potential to predict wind turbine performance, without the need for any previous experimental data. Moreover, it possesses powerful graphical tools to visualise the flow field variables, such velocity, and pressure, similar to reality. Furthermore, the CFD is more of an appropriate tool for model turbulent flow around a wind turbine than BEM and VM, with a view to capture a separated flow that occurs at moderate and high wind speeds. Therefore, the CFD approach was chosen to model the fluid flow around a wind turbine and winglet, in this study.

3.2 Governing Equations

The main function of the CFD approach is to solve the governing equations that represent the fluid flow motion, whilst considering the viscosity effect. These equations are known as the Navier-Stokes equations, which are based on the conservation of mass, momentum and energy, as defined below (Anderson, 2001).

- 1- The fluid mass is conserved (Continuity equation).
- 2- The rate of change of the momentum is equal to the sum of the forces acting on a fluid particle (Newton's second law).
- 3- The rate of change of the energy is equal to the sum of the rate of heat addition to the rate of work done on a fluid particle (First law of thermodynamics).

Hence, the mathematical forms of the governing equations are provided in further detail below.

3.2.1 Conservation of mass (Continuity equation)

In Cartesian coordinates, the continuity equation is written as follows:

$$\frac{\partial \rho}{\partial t} + \frac{\partial(\rho u)}{\partial x} + \frac{\partial(\rho v)}{\partial y} + \frac{\partial(\rho w)}{\partial z} = 0 \quad (3.1)$$

Or in short terms:

$$\frac{\partial \rho}{\partial t} + \text{div}(\rho \mathbf{u}) = 0 \quad (3.2)$$

Where ρ refers to fluid density, t is time, and \mathbf{u} represents the velocity vector. The equation (3.2) is an unsteady and three-dimensional mass conservation at a point in a compressible fluid. The first term denotes the rate of change in time of the density (mass per unit volume), whereas the second term is a net flow of mass out of the fluid element, and also is known as the convective term.

In the case of an incompressible fluid flow, where the density is a constant, the equation (3.2) becomes as follows:

$$\text{div } \mathbf{u} = 0 \quad (3.3)$$

or

$$\frac{\partial u}{\partial x} + \frac{\partial v}{\partial y} + \frac{\partial w}{\partial z} = 0 \quad (3.4)$$

3.2.2 Conservation of momentum

The conservation of momentum is stated by Newton's second law. These equations are given as follows.

$$\rho \frac{Du}{Dt} = \frac{\partial(-p + \tau_{xx})}{\partial x} + \frac{\partial \tau_{yx}}{\partial y} + \frac{\partial \tau_{zx}}{\partial z} + S_{Mx} \quad (3.5)$$

$$\rho \frac{Dv}{Dt} = \frac{\partial \tau_{xy}}{\partial x} + \frac{\partial(-p + \tau_{yy})}{\partial y} + \frac{\partial \tau_{zy}}{\partial z} + S_{My} \quad (3.6)$$

$$\rho \frac{Dw}{Dt} = \frac{\partial \tau_{xz}}{\partial x} + \frac{\partial \tau_{yz}}{\partial y} + \frac{\partial(-p + \tau_{zz})}{\partial z} + S_{Mz} \quad (3.7)$$

Where

\mathbf{u} = velocity vector.

u , v and w = components of the velocity in the x , y and z -direction respectively.

p = pressure.

τ 's = the normal and shear stresses that effect the 3D fluid particle.

S_{Mx} , S_{My} and S_{Mz} = body forces in the x, y and z-direction.

The above set of partial differential equations is known as the continuity and momentum equations, which are suitable for many engineering applications, including wind turbines. It should be noted that due to the small effect of the energy equation on the fluid flow around the wind turbines leads to neglect it from the mathematical models (no heat source and no large changes in fluid temperature around wind turbines).

For a Newtonian fluid, the viscous stresses are proportional to the rates of deformation. Consequently, the nine viscous stresses can be written as follows:

$$\tau_{xx} = 2\mu \frac{\partial u}{\partial x} + \lambda \operatorname{div} \mathbf{u} \quad (3.8a)$$

$$\tau_{yy} = 2\mu \frac{\partial v}{\partial y} + \lambda \operatorname{div} \mathbf{u} \quad (3.8b)$$

$$\tau_{zz} = 2\mu \frac{\partial w}{\partial z} + \lambda \operatorname{div} \mathbf{u} \quad (3.8c)$$

$$\tau_{xy} = \tau_{yx} = \mu \left(\frac{\partial u}{\partial y} + \frac{\partial v}{\partial x} \right) \quad (3.8d)$$

$$\tau_{xz} = \tau_{zx} = \mu \left(\frac{\partial u}{\partial z} + \frac{\partial w}{\partial x} \right) \quad (3.8e)$$

$$\tau_{yz} = \tau_{zy} = \mu \left(\frac{\partial v}{\partial z} + \frac{\partial w}{\partial y} \right) \quad (3.8f)$$

Where

μ = The proportional constant to relate stresses to the linear deformations.

λ = The proportional constant to relate stresses to the volumetric deformation.

By substitution, the equations (3.8) in equations (3.5), (3.6) and (3.7) yields the Navier-Stokes equations, as follows:

$$\rho \frac{Du}{Dt} = -\frac{\partial p}{\partial x} + \frac{\partial}{\partial x} \left[2\mu \frac{\partial u}{\partial x} + \lambda \operatorname{div} \mathbf{u} \right] + \frac{\partial}{\partial y} \left[\mu \left(\frac{\partial u}{\partial y} + \frac{\partial v}{\partial x} \right) \right] + \frac{\partial}{\partial z} \left[\mu \left(\frac{\partial u}{\partial z} + \frac{\partial w}{\partial x} \right) \right] + S_{Mx} \quad (3.9)$$

$$\rho \frac{Dv}{Dt} = -\frac{\partial p}{\partial y} + \frac{\partial}{\partial x} \left[\mu \left(\frac{\partial u}{\partial y} + \frac{\partial v}{\partial x} \right) \right] + \frac{\partial}{\partial y} \left[2\mu \frac{\partial v}{\partial y} + \lambda \operatorname{div} \mathbf{u} \right] + \frac{\partial}{\partial z} \left[\mu \left(\frac{\partial v}{\partial z} + \frac{\partial w}{\partial y} \right) \right] + S_{My} \quad (3.10)$$

$$\rho \frac{Dw}{Dt} = -\frac{\partial p}{\partial z} + \frac{\partial}{\partial x} \left[\mu \left(\frac{\partial u}{\partial z} + \frac{\partial w}{\partial x} \right) \right] + \frac{\partial}{\partial y} \left[\mu \left(\frac{\partial v}{\partial z} + \frac{\partial w}{\partial y} \right) \right] + \frac{\partial}{\partial z} \left[2\mu \frac{\partial w}{\partial z} + \lambda \operatorname{div} \mathbf{u} \right] + S_{Mz} \quad (3.11)$$

Due to the large variety of numbers of temporal and spatial turbulent scales that are associated with turbulent flow, the numbers of the turbulent scales

are reduced by using the Reynolds decomposition, which replaces the flow variables by the sum of a mean and fluctuating component. Hence,

$$\left. \begin{aligned} \mathbf{u} &= \mathbf{U} + \mathbf{u}' \\ u &= U + u' \\ v &= V + v' \\ w &= W + w' \\ p &= P + p' \end{aligned} \right\} \quad (3.12)$$

Where

\mathbf{U}, U, V, W, P = mean values.

$\mathbf{u}', u', v', w', p'$ = fluctuating values.

By substituting equations (3.12) in equations (3.3), (3.9), (3.10) and (3.11), this yields the continuity equation for the mean flow and the Reynolds Averaged Navier Stokes (RANS), as follows:

$$\text{div } \mathbf{U} = 0 \quad (3.13)$$

$$\frac{\partial U}{\partial t} + \text{div}(U\mathbf{U}) = -\frac{1}{\rho} \frac{\partial P}{\partial x} + \nu \text{div}(\text{grad}(U)) + \frac{1}{\rho} \left[\frac{\partial(-\rho \overline{u'^2})}{\partial x} + \frac{\partial(-\rho \overline{u'v'})}{\partial y} + \frac{\partial(-\rho \overline{u'w'})}{\partial z} \right] \quad (3.14)$$

$$\frac{\partial V}{\partial t} + \text{div}(V\mathbf{U}) = -\frac{1}{\rho} \frac{\partial P}{\partial y} + \nu \text{div}(\text{grad}(V)) + \frac{1}{\rho} \left[\frac{\partial(-\rho \overline{v'u'})}{\partial x} + \frac{\partial(-\rho \overline{v'^2})}{\partial y} + \frac{\partial(-\rho \overline{v'w'})}{\partial z} \right] \quad (3.15)$$

$$\frac{\partial W}{\partial t} + \text{div}(W\mathbf{U}) = -\frac{1}{\rho} \frac{\partial P}{\partial z} + \nu \text{div}(\text{grad}(W)) + \frac{1}{\rho} \left[\frac{\partial(-\rho \overline{w'u'})}{\partial x} + \frac{\partial(-\rho \overline{w'v'})}{\partial y} + \frac{\partial(-\rho \overline{w'^2})}{\partial z} \right] \quad (3.16)$$

Nine extra stress terms have been added to the RANS due to the turbulence flow (turbulent fluctuations). These are known as the Reynolds stress tensor as follows:

$$\overline{u'_i u'_j} = \begin{bmatrix} \overline{u'u'} & \overline{u'v'} & \overline{u'w'} \\ \overline{v'u'} & \overline{v'v'} & \overline{v'w'} \\ \overline{w'u'} & \overline{w'v'} & \overline{w'w'} \end{bmatrix} \quad (3.17)$$

Where the three normal stresses are expressed as follows:

$$\tau_{xx} = -\rho \overline{u'^2}, \quad \tau_{yy} = -\rho \overline{v'^2}, \quad \tau_{zz} = -\rho \overline{w'^2} \quad (3.18)$$

And, three shear stresses are represented by the following expressions:

$$\tau_{xy} = \tau_{yx} = -\rho \overline{u'v'}, \quad \tau_{xz} = \tau_{zx} = -\rho \overline{u'w'}, \quad \tau_{yz} = \tau_{zy} = -\rho \overline{v'w'} \quad (3.19)$$

Boussinesq suggested that there is an analogy between the Reynolds stresses and Newton's law of viscosity. Accordingly, there is a linear relationship between the Reynolds stresses and the velocity gradients.

Turbulence models must be used to compute the Reynolds stresses and close equations (3.13), (3.14), (3.15) and (3.16). The turbulence models and the Boussinesq assumption will be discussed later in this chapter.

3.3 CFD modelling process

There are several different CFD codes available in the markets that fulfil the requirements of different engineering applications. However, most of the codes implement the same structure towards achieving their objectives. The CFD structure is divided into the pre-processor, solver and post-processor, as shown Figure 3-1. The most important stages in the CFD structure are the pre-processor and solver, which both play a significant role in the solution accuracy. The process of CFD modelling begins with creating a 2D or 3D geometry, which reflects the physical boundaries of the studied case.

The next step is to discretize the computational model, by including the objective geometry to numbers of cells, where the governing equations can be solved. The predicted results of the computational domain are largely sensitive to the size of the mesh cells. Although there are no existing rules to generate an appropriate mesh for each engineering case, it is recommended for testing the grid-independence until the convergence of the numerical results is obtained. Hence, the grid generation process is the most important and time-consuming element of the CFD process (Hirsch, 2007).

Further, the physical flow class of the studied case should be clearly defined if it belongs to the dependent or independent time. On the other hand, a consideration of the near wall effects play an important role in predicting the mean flow field variables, such as velocity, pressure and temperature. In short, all the physical properties of the flow case should be clearly defined in order to accurately reproduce the numerical case as closely as possible to reality. Figure 3-2 shows the most common characteristics of the physical flow, which are required for setting up the CFD models. In addition, the material properties and boundary conditions can be determined in the pre-processor stage (Tu *et al.*, 2012).

Like the pre-processor, the selected solver affects the numerical accuracy and convergence of the CFD results. Generally, most of the CFD packages consist of two stages of obtaining the final numerical solutions. The first stage is known as the discretization stage, wherein the partial differential equations are converted into a system of discretised algebraic equations. There are common discretised schemes for this purpose, such the finite difference method (FDM), finite volume method (FVM), and the finite element method (FEM) (Tu *et al.*, 2012). The distinguishing feature of the finite volume method is its ability to be implemented with structured and unstructured mesh in different shapes and sizes. Accordingly, FVM is employed in most of the

CFD codes for solving the Navier-Stoke equations in complex fluid flow problems.

The second stage involves the numerical algorithms that are used in the CFD package in order to obtain the numerical solutions for the system of algebraic equations. Towards this purpose, a number of iterative methods are developed and employed in the CFD codes, such as the SIMPLE, SIMPLEC and PISO algorithms (Versteeg and Malalasekera, 2007).

The post-processor is dedicated in many CFD packages to graphically analysing the numerical solutions. It provides different tools to visualize results in the computational domain in 2D or 3D, including an animation view of the dynamic solutions. The post-processor also includes:

- Visualizing the geometry with/without a grid.
- 2D contours or 3D isosurface plots.
- Vector plots and streamlines.
- Animations.

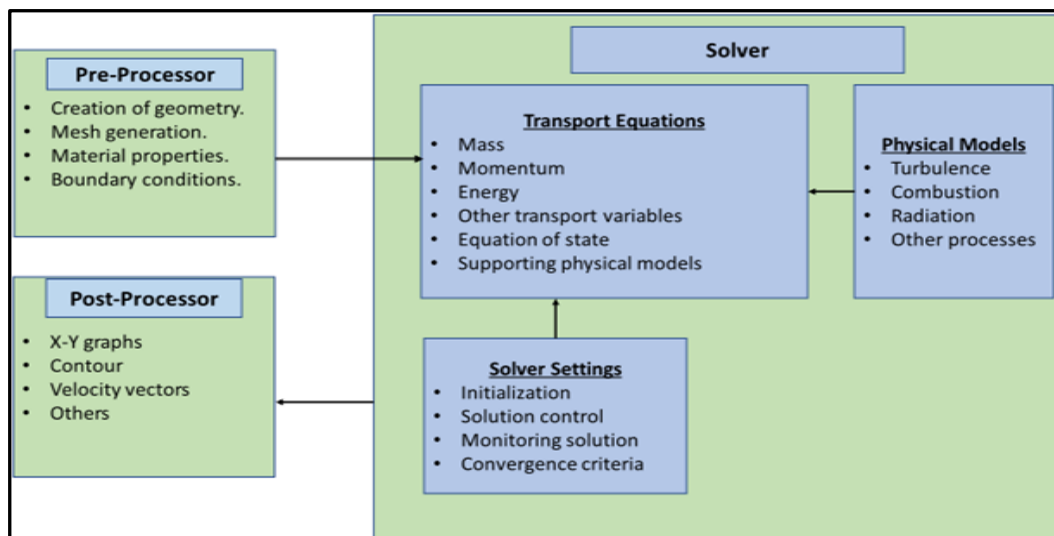


Figure 3-1 Schematic of the CFD structure codes (Tu *et al.*, 2012).

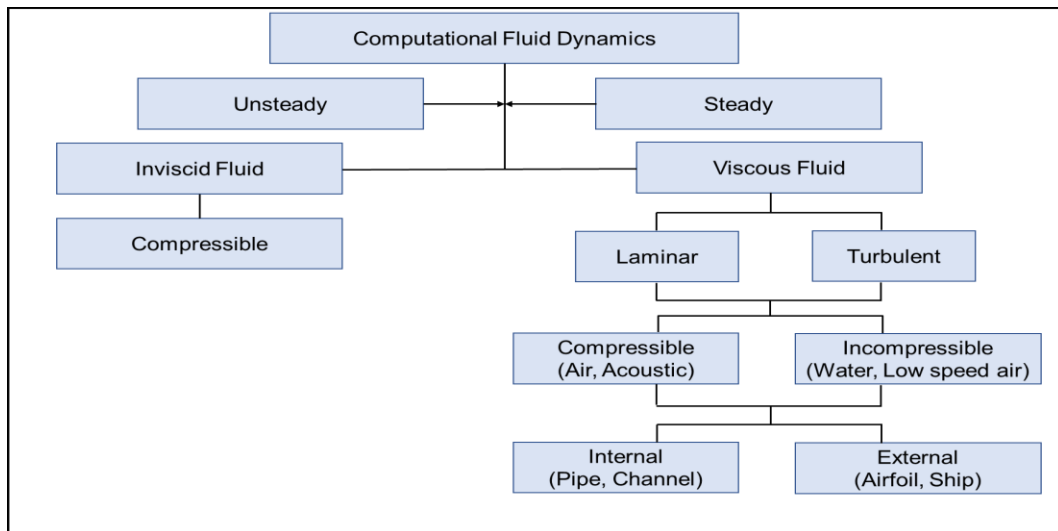


Figure 3-2 Flowchart of the various flow physics in CFD (Tu *et al.*, 2012).

3.4 Solution methods

In the present study, all the computations were performed using the ANSYS FLUENT version 17.0 which is one of the famous CFD commercial software has been implemented to solve the RANS equations in the wind turbines field. The ANSYS FLUENT is based on the control volume technique to convert the partial differential equations to algebraic equations, which can be handled numerically. The ANSYS FLUENT includes two different numerical solver algorithms, which are divided into two categories: the pressure-based solver and the density-based solver. Generally speaking, the pressure-based solver was developed to be an appropriate approach for low-speed incompressible applications, while the density-based solver was employed efficiently for high-speed compressible flows. The two solvers are implemented in the ANSYS FLUENT, with a view to solving the continuity and momentum equations in addition to the energy, turbulence and other scalars. Both algorithms calculate the velocity field by solving the momentum equations. However, in the density-based solver, the density field is obtained from the continuity equation and the pressure field can be found from the equation of state (Fluent, 2013).

In contrast, the pressure-based solver determines the pressure field by using a pressure correction equation, which can be derived by manipulating the continuity and momentum equations (Tu *et al.*, 2012). Accordingly, the pressure-based solver was chosen in this study due to a wind turbine operates at low wind speeds and the Mach number is less than 0.3, which can be considered an incompressible flow (Mathew, 2006).

3.4.1 Pressure-Based Solver

In the ANSYS FLUENT, a segregated algorithm and coupled algorithm are two available solution approaches, which belong to the class of the pressure-based solver. In the segregated algorithm, the flow governing equations are solved one after another to determine the solution variables, such as u, v, w, p, K, ω and so on (sequentially). The advantage of this approach is that it is economical in memory requirements, due to the fact that the discretised equations need only to be saved in the memory one at a time. However, the slowness of the solution convergence is the main downside of this approach, since the governing equations are solved in a segregated manner.

On the other hand, a coupled system of the governing equations involves the momentum equations, and the pressure-based continuity equation can be solved by the pressure-based coupled algorithm. Hence, the solution convergence is improved when compared to the segregated algorithm. However, the coupled approach needs greater memory requirements of about 1.5-2 times that of the segregated approach needs (Fluent, 2013). Figure 3-3 shows the differences between the schematic solution of the segregated and coupled algorithm. Considering the memory requirements, the steady-state conditions can be applied to solve the governing equations. Hence, the segregated pressure-based solver has been utilized in all the computations in this study.

In ANSYS FLUENT version 17.0, 3 types of segregated algorithm are available, namely, the SIMPLE, SIMPLER and PISO approach. They have been developed to overcome the solution problem of the non-linearity of the Navier-Stokes equations (Tu *et al.*, 2012). Essentially, they are based on guesswork and the correct procedure of the pressure calculations. The SIMPLE (Semi-Implicit for Pressure Linked Equations) was originally introduced by Patankar and Spalding (1972). The SIMPLE starts by guessing an initial value of the field pressure, in order to solve the discretised momentum equations. Then, the field velocity components can be obtained. The pressure field is iteratively corrected until the solution convergence is obtained by enforcing the continuity equation in the numerical algorithm resulting from the pressure and velocity coupling (Versteeg and Malalasekera, 2007). The SIMPLE consistent (SIMPLER) algorithm was developed by Van Doornal and Raithby in 1984, with a view to enhance the SIMPLE algorithm by using different flux correction expression on the cell face (Fluent, 2013). However, In 1986, Pressure-Implicit with Splitting of

Operators (PISO) was presented by Issa (Versteeg and Malalasekera, 2007). The PISO algorithm employs two additional corrections, namely, the neighbour (or momentum) and skewness corrections, in order to overcome the limitations of the SIMPLE and SIMPLER algorithms (Fluent, 2013).

Since the present study is conducted as steady state-conditions, the SIMPLE is an appropriate chosen to solve pressure-velocity coupling.

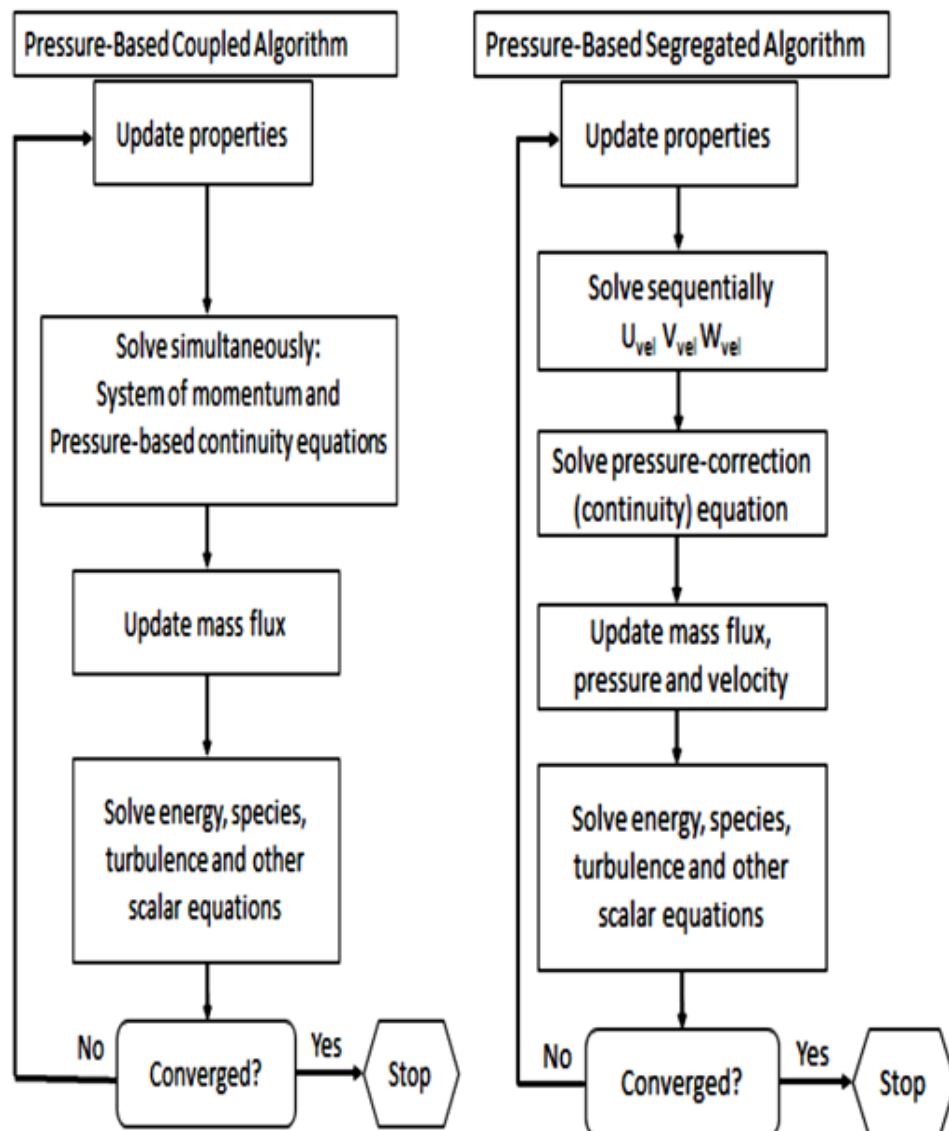


Figure 3-3 Schematic solution of the segregated and coupled algorithm (Fluent, 2013).

3.5 The nature of turbulence

Turbulence is an irregular phenomenon, where the flow behaviour is characterised as random and chaotic due to significant and irregular variations in the velocity field, and other flow properties in both space and time (Versteeg and Malalasekera, 2007). Turbulence is a complicated flow, due to the fact that it is always associated with the rotational, three-dimensional and time-dependent factors (Celik, 1999). The ability of the turbulent flow to transport effectively (mass and heat) and mix fluids is considered an interesting feature in different engineering applications. Turbulence exists in a majority of the fluid applications (Hoffmann and Chiang, 2000), such as the mixing of fuel and air in engines (automobiles, boiler, and furnaces) (Pope, 2001), pollutants (Kim and Patel, 2000) and wind turbine operation (Nilsson, 2015).

Turbulent flow is recognised by the Reynolds number, which is used to measure the ratio between inertia forces to viscous forces. It is observed experimentally that, the turbulent flow occurs at the Reynolds number higher than a critical value (Re_{crit}) which is used to categorise the flow behaviour into laminar, transition and turbulent flow regime. The turbulence structure composes of a wide range of length scales known as turbulent eddies. In the main flow, the turbulent eddies are divided into large turbulent eddies and small eddies, as corresponding to their length scale sizes and frequency (Versteeg and Malalasekera, 2007).

The largest eddies acquire their energy from the mean flow, by a process known as vortex stretching. The large eddies have a Reynolds number that is not very different in magnitude than the mean flow (Versteeg and Malalasekera, 2007). Hence, they are only dominated by the inertia forces, and thus they show an anisotropic behaviour, unlike the smallest eddies that are considered to possess an isotropic structure due to the viscous effects. According to the spectral analysis of the kinetic energy, shown in Figure 3-4, the peaks of energy are measured at a low wave-number, which means that the larger eddies carry most energy of the flow compared to the smallest eddies, which have the lowest energy content.

Between the largest and the smallest eddies, the kinetic energy is handed down progressively in a process that is known as the energy cascade. The energy cascade is considered an inviscid process at the large scales, until the viscous effect dissipates and converts the energy into thermal internal energy at the smallest scale (Pope, 2001). The slope of $-5/3$ indicates the

inertial sub range, where the energy is transferred through eddies that have scales large enough to be anisotropic eddies and small enough to be affected by the viscous effects.

Kolmogorov argues that the scales of the smallest eddies, such as length, velocity and time, can be uniquely determined by the kinematic viscosity (ν) and the dissipation rate of energy (ε). Hence, the cascade energy is handed down progressively from large eddies to smaller, until the Reynolds number is approximately equal to one and the smallest scales are determined as follows:

$$\eta \equiv \left(\nu^3 / \varepsilon \right)^{1/4} \quad (3.20)$$

$$u_\eta \equiv (\varepsilon \nu)^{1/4} \quad (3.21)$$

$$\tau_\eta \equiv (\nu / \varepsilon)^{1/2} \quad (3.22)$$

$$Re_\eta \equiv \eta u_\eta / \nu = 1 \quad (3.23)$$

Where,

η : Kolmogorov length scale (m).

ν : Kinematic viscosity (m²/s).

ε : Dissipation rate of energy (m²/s³).

u_η : Kolmogorov velocity scale (m/s).

τ_η : Kolmogorov time scale (s).

Re_η : Kolmogorov Reynolds number.

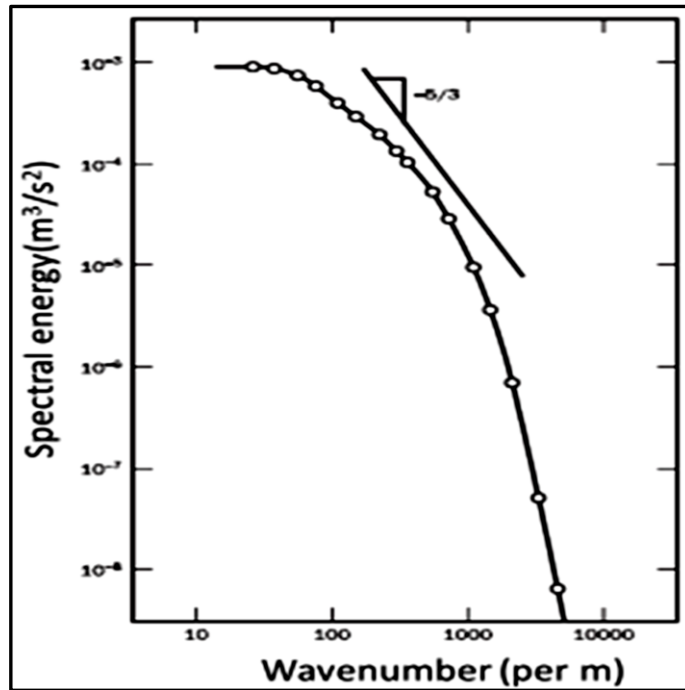


Figure 3-4 Spectral energy analysis (Versteeg and Malalasekera, 2007).

3.5.1 Turbulent flow near a wall

Turbulent flows are influenced by the wall presence in most engineering applications. Obviously, the mean fluid velocity is reduced to zero on a wall due to the friction effects, which are known as no-slip conditions (Fluent, 2013). Consequently, the wall effects must be considered in the turbulence models when successfully reproducing the turbulent flow.

The experimental efforts have reported that the near-wall region can be categorized into three layers, as shown in Figure 3-5. The inner layer is called a viscous sub-layer, where the viscous force is a dominant effect on momentum and heat or mass transfer. The fully-turbulent layer or log-law region identifies the outer region of the boundary layers, where turbulence significantly affects the flow parameters. The middle region is known as the buffer layer (or blending region), where both the turbulence and viscosity are important (Fluent, 2013).

Therefore, the flow field variables are affected by the near wall regions according to the impact of the viscosity and turbulence role in each region. Hence, a non-dimensional normal wall distance (y^+) is commonly used for distinguishing between the wall regions (Wilcox, 1993). In the context of CFD, the y^+ is used to determine how a coarse or fine mesh is required for accounting for the wall effects that play an important role in choosing the turbulence model.

From Figure 3-5, the wall regions corresponding to the y^+ value can be classified as follows:

- 1- Viscous sub-layer: $y^+ < 5$ (the velocity profile is linear, and the viscous stress dominates).
- 2- Buffer layer or blending region: $5 < y^+ < 60$ (both the viscous stress and turbulence are important).
- 3- Fully turbulent or log-law region: $y^+ > 60$ (turbulence dominates).

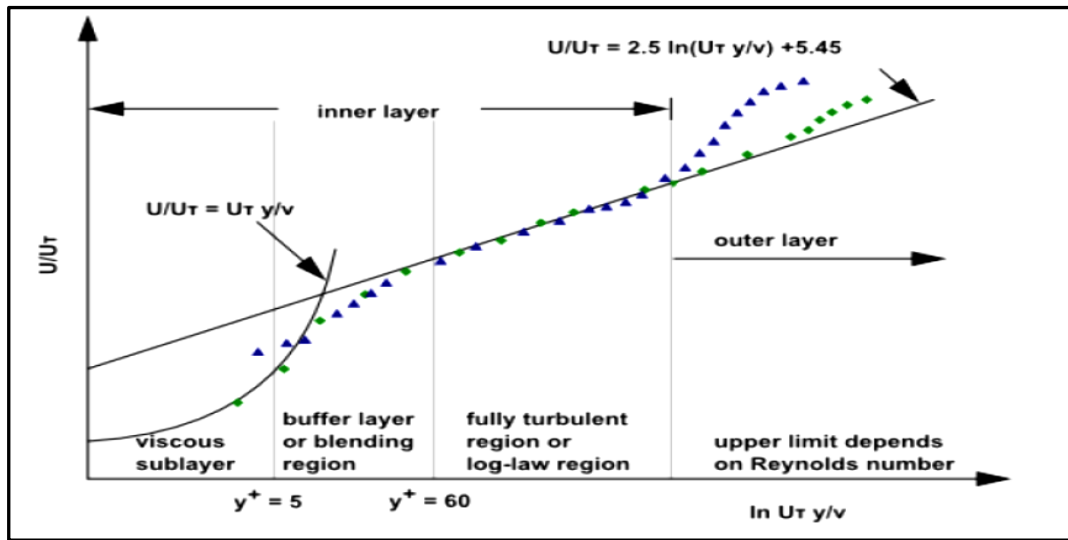


Figure 3-5 Near-wall layers (Fluent, 2013).

The y^+ value can be determined as follows:

$$y^+ = \frac{u_t y}{\nu} \quad (3.24)$$

Where, y refers to the normal distance from the wall to the wall-adjacent cell, ν is the kinematic viscosity and u_t is the friction velocity, which can be calculated as follows:

$$u_t = \sqrt{\frac{\tau_w}{\rho}} \quad (3.25)$$

Where, τ_w is the wall shear stress, ρ is the fluid density at the wall (Hoffmann and Chiang, 2000).

In ANSYS Fluent, there are different approaches to modelling the effects of the wall regions. The first approach implements semi-empirical formulas, which are known as wall functions, as a bridge between the wall and the fully-turbulent region (the viscous sub-layer and the buffer layer are not resolved). The wall function approach supplements the turbulence models to account for the wall effect without any modification.

In contrast, the second approach requires modifying the turbulence model to resolve the viscosity-affected region by mesh the way to the wall, including the viscous sub-layer. Figure 3-6 depicts the differences between the two approaches to model the viscosity-affected region (Fluent, 2013).

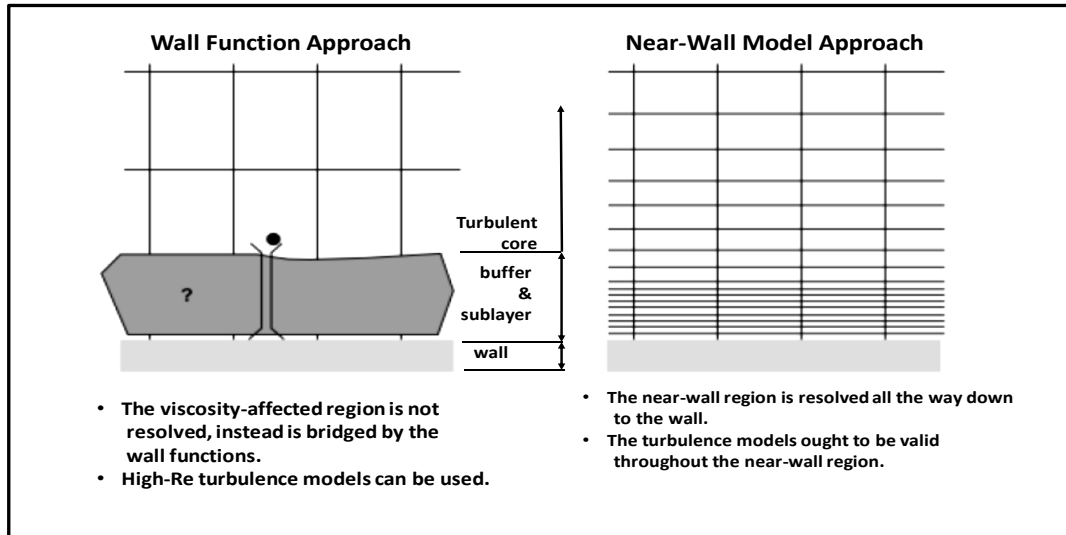


Figure 3-6 Schematic of the near-wall treatment in Ansys-Fluent (Fluent, 2013).

3.6 Turbulence models

Turbulence is considered an important phenomenon in relation to engineering flows, due to its complexity and presence within industrial applications. Hence, most engineering fields, including the wind turbines community, have developed a number of turbulence models that vary in complexity and accuracy. Basically, there are two numerical approaches that reproduce turbulence, namely, the direct numerical simulation (DNS), or the indirect numerical simulation (INS).

3.6.1 Direct numerical simulations

The DNS is considered a precise method, due to the fact that it can faithfully reproduce the whole range of the spatial and temporal scales of the turbulence (Coleman and Sandberg, 2010). In short, the structure of the turbulence from the largest eddies to the smallest eddies (Kolmogorove scales) are computed. A comparison with the conventional CFD approaches, the DNS provides more complete knowledge of the variations of the flow properties within the simulation period. In engineering applications, the DNS is restricted, since it must use a domain large enough to include the largest eddies, and the grid spacing must be fine enough to fully resolve the Kolmogorove scales. In case of homogeneous turbulence, which is the simplest form of turbulence, the computational cost of DNS increases steeply

as the cube of the Reynolds number (Re^3) (Gatski *et al.*, 1996). Consequently, its application is limited only to flows that have a low or moderate Reynolds number (Pope, 2001).

3.6.2 Large eddy simulations

The INS consists of two approaches, namely, the large eddy simulation (LES) and the RANS approach. The LES is a technique in which the largest scales of motion are represented explicitly, whereas the smaller ones are modelled (Gatski *et al.*, 1996). The LES is three dimensional and time-dependent, and thus has been employed to model unsteady flow applications, which include stalled or wake flows. The essential concept of LES is that the large and medium scales are mainly responsible for the most turbulent transport process, unlike the smaller scales, which are less important and can be modelled. Furthermore, unlike the small eddies, which tend to be isotropic and universal, the large eddies are determined depending on the geometry and the boundary conditions of the flow (Versteeg and Malalasekera, 2007). Since the smaller scales are modelled in LES, the computational model is prepared using a much coarser mesh and larger time-steps than DNS, which must reproduce the Kolmogorov scales. Hence, the LES has lower computational cost when compared to DNS (Irtaza, 2009).

The LES employs a filtering operation to decompose the turbulent properties, such the velocity or pressure fields, into the sum of a filtered component and a residual component (subgrid-scale SGS). The filtered components are derived from the Navier-Stokes equations to represent the LES continuity and momentum equations. Like the Reynolds stresses, the subgrid-scale stresses are produced due to the filtered Navier-Stokes equations and they must be modelled (Versteeg and Malalasekera, 2007).

3.6.3 Turbulence Models of Reynolds Average Navier-Stokes Equations (RANS)

The RANS equations are regarded as the oldest and most popular methods, which date back to the late 19th century when Reynolds (1895) reported on his work on turbulence (Celik, 1999). The RANS equations are based on the Reynolds decomposition that separates the physical flow properties into a mean value and its fluctuation value. The Reynolds stresses are extra terms which appear in the RANS equations, due to the interactions between different turbulent fluctuations. The Reynolds stresses are determined by a number of turbulence models, which are grounded on either employing the

turbulent viscosity concept or directly using the Reynolds stress model (RSM) (Pope, 2001). The turbulence models are classified according to the number of equations that are necessary for resolving the Reynolds stresses. Three equations are commonly used for this purpose, which include turbulent kinetic energy (K), kinetic energy dissipation rate (ϵ) or the specific energy dissipation rate (ω).

The two-equation models have been shown to well perform for predicting the behaviour of flows that closely follow the Boussinesq hypothesis where the flow is locally isotropic and equilibrium (the production and dissipation terms are approximately equal) where the normal Reynolds stresses are relatively unimportant. They are favoured in engineering applications due to its low computational cost and numerical stability than more complex models such as the Reynolds Stress Model.

However, the two-equation models have shown a poor performance to accurately predict an anisotropy of the normal stresses or to account for streamline curvature effects. These effects are considered a major deficiency of the Boussinesq hypothesis that observed in turbulent flows over curved surface faces, separation points in vortices (Versteeg and Malalasekera, 2007). In addition, the two equation models fail to predict accurately the production rate of the turbulent energy in the vicinity of stagnation points where the strain rate is very high such as in impinging jet flows as reported by Craft *et al.* (1993).

However, there are non-linear eddy viscosity models that assume a non-linear relationship between Reynolds stress and the velocity gradient, i.e. Reynolds Stress Model (RSM), non-linear v^2 - f and non-linear κ - ϵ (Hoffmann and Chiang, 2000).

The limitations of the Boussinesq hypothesis are avoided using the Reynolds Stress Model (RSM) which introduced by Launder *et al.* (1975). The RSM model is a complex model which solves one transport equation for each of the Reynolds stresses, therefore, it is an appropriate model to account the features of anisotropic turbulence flows. A better description of the physics of the turbulent flow can be predicted using the RSM model since the Reynolds stresses are calculated individually. However, the numerical stability and convergence are the most difficulties that obstacle the RSM model in the industrial use, especially in complex natural flows (Wilcox, 1993). In the present study, the model was used to validate the baseline blade in the range of wind speeds 5-13m/s, however, a satisfactory convergence was never obtained.

The RANS models describe the mean flow properties, which require a much coarser mesh than the DNS and LES. They have been considered the mainstay approach to model turbulence in engineering flow applications, including wind turbines, over the last three decades (Irtaza, 2009).

Figure 3-7 illustrates the common turbulence models and their computational complexities.

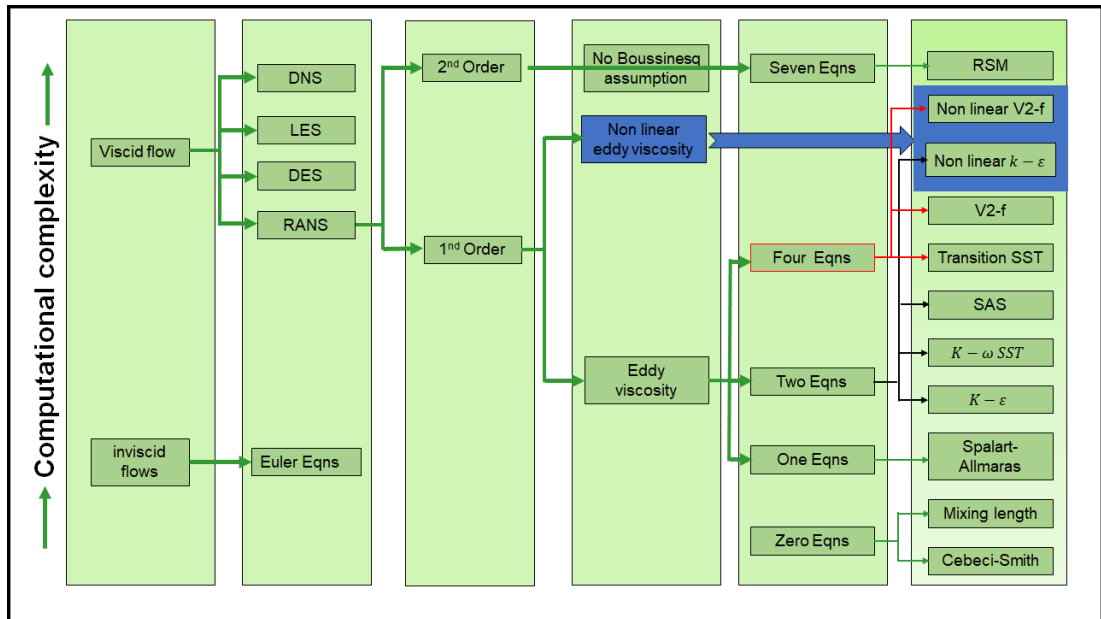


Figure 3-7 Common turbulence models classifications (Almohammadi, 2014).

3.6.4 Concept of the eddy viscosity

The Reynolds stresses are a core closure problem, which appears on the right-hand side of the momentum equations (3.14) to (3.16). This problem was solved by using the Boussinesq assumption, which introduced a new concept to eddy viscosity. In 1877, Boussinesq proposed a pioneering assumption that has opened the way for turbulence models to exist. There is an analogy in action between the viscous stresses and the Reynolds stresses on the mean flow. Both stresses are found on the right-hand side of the momentum equations and the turbulent stresses increase as the rate of deformation increases (Versteeg and Malalasekera, 2007). In a similar manner to Newton's viscosity law, Boussinesq proposed that the Reynolds stresses might be proportional to the mean rates of deformation.

For an incompressible fluid flow, and according to Newton's viscosity law, the relationship between the viscous stresses and the rate of the deformation of the fluid element is expressed in the following equation:

$$\tau_{ij} = \mu s_{ij} = \mu \left(\frac{\partial u_i}{\partial x_j} + \frac{\partial u_j}{\partial x_i} \right) \quad (3.26)$$

Similarly, the Boussinesq assumption is given as follows:

$$\tau_{ij} = -\overline{\rho u'_i u'_j} = \mu_t \left(\frac{\partial U_i}{\partial x_j} + \frac{\partial U_j}{\partial x_i} \right) - \frac{2}{3} \rho k \delta_{ij} \quad (3.27)$$

In both equations (3.26) and (3.27), there is a similarity in their terms, except for μ which is the fluid viscosity and is a function of the fluid properties. On the other hand, the turbulent or eddy viscosity μ_t is a function of the turbulence. In this way, the turbulence models are used for modelling the turbulent viscosity and thus the solution of the RANS equations can be obtained.

The following sections are dedicated only towards the discussion and assessment of the turbulence models that have commonly been used to predict the flow field around wind turbines.

3.6.5 The Spalart–Allmaras model

The Spalart-Allmaras (S-A) model is considered more sophisticated than the zero-equation turbulence models, which use algebraic relations to determine the eddy viscosity parameter (Hoffmann and Chiang, 2000). The S-A model employs one transport equation for kinematic eddy viscosity and the length scale is defined algebraically. Hence, the model is considered more economical than the two-equation turbulence models, and is designed for aerodynamic purpose flows. The eddy viscosity is expressed as follows (Versteeg and Malalasekera, 2007):

$$\mu_t = \rho \tilde{\nu} f_{v1} \quad (3.28)$$

Where,

μ_t = the eddy viscosity.

$\tilde{\nu}$ = the kinematic eddy viscosity parameter.

f_{v1} = the damping function, which tends to zero at the wall and tends to unity for high Reynolds number.

Therefore, the Reynolds stresses are obtained by using the Boussinesq assumption, as follows:

$$\tau_{ij} = -\overline{\rho u'_i u'_j} = \rho \tilde{\nu} f_{v1} \left(\frac{\partial U_i}{\partial x_j} + \frac{\partial U_j}{\partial x_i} \right) \quad (3.29)$$

3.6.6 The $k - \varepsilon$ model

The $k - \varepsilon$ model belongs to the class of two-equation turbulence models, which solve two transport equations that account for two turbulence quantities. This model has been modified in a number of variations to improve its accuracy in different engineering flows. The standard $k - \varepsilon$ model (Launder and Spalding 1974) has two transport equations to calculate the turbulent kinetic energy (k) and dissipation rate (ε) (Launder and Spalding, 1974). In this model, both the velocity scale (v) and length scale (l) are related to k and ε as follows (Versteeg and Malalasekera, 2007):

$$v = k^{1/2} \quad (3.30)$$

$$l = \frac{k^{3/2}}{\varepsilon} \quad (3.31)$$

The eddy viscosity can be defined as the following expression:

$$\mu_t = \rho C_\mu \frac{k^2}{\varepsilon} \quad (3.32)$$

The turbulent kinetic energy and its dissipation rate are calculated using the following transport equations, respectively:

$$\frac{\partial(\rho k)}{\partial t} + \text{div}(\rho k \mathbf{U}) = \text{div} \left[\frac{\mu_t}{\sigma_k} \text{grad } k \right] + 2\mu_t S_{ij} \cdot S_{ij} - \rho \varepsilon \quad (3.33)$$

$$\frac{\partial(\rho \varepsilon)}{\partial t} + \text{div}(\rho \varepsilon \mathbf{U}) = \text{div} \left[\frac{\mu_t}{\sigma_\varepsilon} \text{grad } \varepsilon \right] + C_{1\varepsilon} \frac{\varepsilon}{k} 2\mu_t S_{ij} \cdot S_{ij} - C_{2\varepsilon} \rho \frac{\varepsilon^2}{k} \quad (3.34)$$

I II III IV V

Where,

I= the rate of change of k or ε .

II=Transport of k or ε by convection.

III=Transport of k or ε by diffusion.

IV=Rate of the production of k or ε .

V= Rate of the destruction of k or ε .

The following table shows the k - ε model constants (Versteeg and Malalasekera, 2007).

Table 3-1 k- ε model constants.

Constant name	value
σ_k	1.00
σ_ε	1.30
$C_{1\varepsilon}$	1.44
$C_{2\varepsilon}$	1.92
C_μ	0.09

3.6.7 The $k - \omega$ model

The $k - \omega$ model was introduced by Kolmogorov (Kolmogorov, 1991). It involves two transport equations for k and ω , where ω refers to the rate of the dissipation of energy per unit volume and time (Celik, 1999). The purpose of using ω instead of ε is to overcome a major drawback of the $k - \varepsilon$ model, which shows unsatisfactory performance for the boundary layers' predictions in the case of adverse pressure gradients (Versteeg and Malalasekera, 2007). The $k - \omega$ model has been modified in different forms, the most popular of which was developed by Wilcox (1988). The main advantage of this model is its ability to integrate through the viscous sub-layers region, without the need for logarithmic wall functions (Menter, 1992). However, it shows a high sensitivity with the ω –equation in the free-stream, outside the boundary layers.

The eddy viscosity is given by the following expression:

$$\mu_t = \rho k / \omega \quad (3.35)$$

Where,

$$l = \sqrt{k} / \omega \quad (3.36)$$

$$v = k^{1/2} \quad (3.37)$$

$$\omega = \varepsilon / k \quad (3.38)$$

The model employs two transport equations, as follows:

$$\frac{\partial(\rho k)}{\partial t} + \text{div}(\rho k \mathbf{U}) = \text{div} \left[\left(\mu + \frac{\mu_t}{\sigma_k} \right) \text{grad}(k) \right] + P_k - \beta^* \rho k \omega \quad (3.39)$$

$$\frac{\partial(\rho\omega)}{\partial t} + \text{div}(\rho\omega\mathbf{U}) = \text{div} \left[\left(\mu + \frac{\mu_t}{\sigma_\omega} \right) \text{grad}(\omega) \right] + \gamma_1 \left(2\rho S_{ij} \cdot S_{ij} - \frac{2}{3} \rho \omega \frac{\partial U_i}{\partial x_j} \delta_{ij} \right) - \beta_1 \rho \omega^2$$

I
II
III
IV
V

(3.40)

Where

$$P_k = \left(2\mu_t S_{ij} \cdot S_{ij} - \frac{2}{3} \rho k \frac{\partial U_i}{\partial x_j} \delta_{ij} \right) \quad (3.41)$$

I= Rate of change of K or ω .

II=Transport of K or ω by convection.

III= Transport of K or ω by diffusion.

IV=Rate of the production of K or ω .

V= Rate of the destruction of K or ω .

3.6.8 The SST k- ω (shear stress transport) model

The SST k- ω turbulence model was developed by Menter to overcome the drawbacks that are associated with the k- ϵ model in the near wall and the sensitivity of the k- ω model in the free-stream. Menter (1992) suggested a hybrid turbulence model in which employs the turbulent frequency equation (ω) and the dissipation of turbulent rate (ϵ). The SST k- ω model is grounded by implementing the k- ω model in the boundary layer, and gradually converts to the k- ϵ in the fully turbulent region far from the wall by using a blending function (Versteeg and Malalasekera, 2007). In this model, the same k-equation is used, whereas the ϵ -equation has been modified into a ω -equation, by substituting $\epsilon = k\omega$ as follows:

$$\frac{\partial(\rho\omega)}{\partial t} + \text{div}(\rho\omega\mathbf{U}) = \text{div} \left[\left(\mu + \frac{\mu_t}{\sigma_{\omega,1}} \right) \text{grad}(\omega) \right] + \gamma_2 \left(2\rho S_{ij} \cdot S_{ij} - \frac{2}{3} \rho \omega \frac{\partial U_i}{\partial x_j} \delta_{ij} \right) - \beta_2 \rho \omega^2 + 2 \frac{\rho}{\sigma_{\omega,2}} \frac{\partial k}{\partial x_k} \frac{\partial \omega}{\partial x_k} \quad (3.42)$$

On the right-hand side of equation (3.42), an extra term which is the last one refers to the cross-diffusion term that is activated outside the boundary layer.

It was experimentally found that the ratio of the turbulence production to its dissipation can be greater than one. Therefore, the classical eddy-viscosity models such the $k - \epsilon$ and $k - \omega$ yield an over-prediction of the turbulent shear stress in adverse pressure gradient flows (Menter, 1994). Hence, the SST model involves a new modification of the classical eddy-viscosity to enforce the Bradshaw's assumption that states the turbulent shear stress in a boundary layer is proportional to the turbulent kinetic energy as follows (Woelke, 2007).

$$\tau = \rho a_1 k \quad \dots\dots\dots (3.43)$$

Where,

τ : Turbulent shear stress (N/m²).

ρ : Density (kg/m³).

a_1 : Constant =0.3.

k : Turbulent kinetic energy (m²/s²).

Thus, the new kinematic eddy-viscosity (ν_t) is calculated using the SST model as follows.

$$\nu_t = \frac{a_1 k}{\max(a_1 \omega; \frac{\partial u}{\partial x} F_2)} \dots\dots\dots (3.44)$$

Where, F_2 is a function that equals one for the case of boundary layer flows and zero for free shear layers flows. The new modification in the eddy-viscosity equation results major improvements in a prediction of the separation flow using the SST model over both the original $k - \varepsilon$ and $k - \omega$ models. The advantages of the SST model were shown in a large number of challenging research flows such flows involving adverse pressure gradients, flow over a backward-facing step, NACA 4412 airfoil flow and transonic bump flow as presented by Menter (1994).

However, the SST model suffers the same aforementioned deficiencies of the two-equation turbulence models that presented in section 3.6.3. In addition, the SST model requires a fine mesh towards the boundary layer including the viscous sub-layer yielding relatively expensive when compared to the high Reynolds models such $k - \varepsilon$ model (Fluent, 2013).

Moreover, the SST model fails to capture the effect of laminar-turbulent transition flow since it produces almost fully turbulent flow in the boundary layer (Menter *et al.*, 2006). The SST model has been extended using two extra equations that coupled with the transport equations of the original SST model results the transition SST model which implemented to capture the effect of laminar-turbulent transition flows. One extra equation is dedicated in the transition SST model to account for the intermittency and the second extra equation is used to predict the transition onset based on the principle of momentum thickness (Menter *et al.*, 2006). The transition SST model has the advantages of the SST model and it performs better to account the effect of transition flows in flat plate, turbomachinery machines, turbine and compressor cascade, DLR F-5 wing and helicopter cabin as shown by Menter *et al.* (2006). Moreover, it is claimed that the transition SST model shows better validated predictions than other models when the transition

location plays a crucial role for simulation (Freudenreich *et al.*, 2004; Menter *et al.*, 2004). However, due to two extra transport equations are included, the transition SST model is more time consuming and sensitive to convergence than the SST model.

The different constants for Wilcox's equation and Menter's equation are given in the following table (Versteeg and Malalasekera, 2007).

Table 3-2 Wilcox's and Menter's constants.

Wilcox's constants (k-ω model)		Menter's constants (SST k-ω model)	
constant	value	constant	value
σ_k	2.0	σ_k	1.0
σ_ω	2.0	$\sigma_{\omega,1}$	2.0
γ_1	0.553	$\sigma_{\omega,2}$	1.17
β_1	0.075	γ_2	0.44
β^*	0.09	β_2	0.083
-	-	β^*	0.09

3.7 Assessment of the turbulence models' performance for HAWT applications

As previously discussed in chapter two, wind turbines operate in a complex natural flow field that is associated with a number of phenomena, such as turbulence, stalled flow and vortices. Approved experimental measurements are required to assess the numerical results that are obtained by using the CFD codes. Hence, the NREL rotor VI experiments have been chosen in this study as a baseline case to validate the computational domain and assess the choice of turbulence model performance.

This section is an assessment and review of the previous CFD studies, which frequently employed different RANS equations to model flow around NREL rotor VI. The computational resource requirements, and a reasonable accuracy, provide the basis for dominating the RANS turbulence models in the literature (Bai and Wang, 2016). Hence, different RANS turbulence models were utilized, such as one equation Spalart-Allmaras model, two equation models, including different modifications of the $k - \varepsilon$ models and

the $k - \omega$ models (Lanzafame *et al.*, 2013; Sørensen and Schreck, 2012; Yu *et al.*, 2011; Fu and Farzaneh, 2010).

The Spalart-Allmaras model was developed by the Boeing Company, specifically with a view to predict the flow behaviour of external aerodynamic applications (Spalart and Allmaras, 1994). The S-A model has been utilized to predict the NREL rotor VI performance in different studies (Lee *et al.*, 2016; Derakhsahan and Tavazziani, 2015; Song, 2014; Elfarrar *et al.*, 2014; Aranake *et al.*, 2012; Potsdam and Mavriplis, 2009). The model shows a good performance to match the wind tunnel data in terms of power, torque and pressure coefficient distributions at low wind speeds, between 5 m/s to 8 m/s, where the flow is an attached regime. The discrepancy of the model was a clear occurrence in the range of wind speeds between 10m/s to 25 m/s, where the stall regime exists and involves multiple length scales and three-dimensional separations. The NREL rotor VI is stalled regulated control to limit the peak power at the wind speeds higher than 10m/s. Hence, the poor performance of the Spalart-Allmaras is expected due to one transport equation is used to solve the eddy viscosity and the length scales, which are defined algebraically (Versteeg and Malalasekera, 2007). Furthermore, the model is less sensitive to predicting the effect of adverse pressure gradients accurately (Spalart and Allmaras, 1994). In addition, the model over-predicts the velocity profile in the recirculation region of backward-facing step flow (Menter, 1992).

Alternatively, the standard $k - \varepsilon$ model is the most successful model that is employed by the CFD community in a large variety of engineering applications, including wind turbines (Yu, 2017). Like the Spalart-Allmaras model, the lack of sensitivity to adverse pressure is a known weakness that afflicts the standard $k - \varepsilon$ model (Spalart and Allmaras, 1994; Menter, 1992). As a consequence, the model overpredicts the shear-stress level that delays or prevents the $k - \varepsilon$ model to capture separated flows (Menter, 1992), specifically on the curved wall, as reported by (Peyret and Krause, 2000). Hence, the standard $k - \varepsilon$ model has been modified into a number of versions, such as Renormalization Group (RNG) model (Yakhot *et al.*, 1992), realizable model (Shih *et al.*, 1995) and the low Reynolds $k - \varepsilon$ models (Shih *et al.*, 1995; Launder and Sharma, 1974). The standard model and its modifications have been utilized to resolve the RANS equations to predict the NREL phase VI performance in terms of power, thrust and pressure coefficients in different efforts (Elfarrar *et al.*, 2015; Derakhsahan and Tavazziani, 2015; Elfarrar *et al.*, 2014; Park *et al.*, 2007).

A comparison with the Spalart-Allmaras model shows the predictions of the NREL phase VI performance were improved due to the $k - \varepsilon$ models involving two transport equations to solve the turbulent kinetic energy and its dissipation. Among them, the Launder-Sharma model shows the best performance to match the wind tunnel data in terms of power, thrust and pressure coefficients distributions, with a discrepancy in the stall regime that is less than the Spalart-Allmaras model (Elfarra *et al.*, 2015). However, the $k - \varepsilon$ models suffer from a major drawback associated with the fact that it is not possible to integrate the ε -equation through the viscous sub-layer. Therefore, it is necessary to supplement the $k-\varepsilon$ model with logarithmic wall functions in the cells adjacent to walls. Accordingly, it can seriously compromise the predictive capability of the model towards developing and separating boundary layers (Menter, 1992).

On the other hand, in order to overcome the shortcomings of the $k-\varepsilon$ model, a number of turbulence models have been developed, such as the $k-\omega$ model (WILCOX, 1988). However, the $k-\omega$ model has not been commonly used in the extant literature. It was utilized for predicting the numerical power and thrust in the investigation that conducted by Guo *et al.* (2015). In their study, the model shows strong agreements when compared with the wind tunnel data in terms of the numerical power, thrust, and pressure coefficient distributions. These agreements were found at low wind speeds of 5m/s to 9m/s, where the flow is mostly attached. However, the discrepancy of the model occurs at a higher wind speed of 10m/s, to match the measured power and thrust force.

The SST $k-\omega$ is the most popular model that has been used to resolve the RANS equations around wind turbines, including the NREL rotor VI (Yu, 2017; Bai and Wang, 2016; Gomez and Munduate, 2014). The model shows promising results, which strongly capture the wind tunnel data of the NREL rotor VI in terms of power, thrust force and pressure coefficients distributions in the attached regime at a velocity of 5m/s to 8m/s (Rahimi *et al.*, 2016; Lanzafame *et al.*, 2013; Yelmule and Vsj, 2013; Sagol *et al.*, 2012; Mo and Lee, 2012; Moshfeghi *et al.*, 2012; Stone *et al.*, 2010; Sørensen, 2009; Sørensen *et al.*, 2002). Like the $k-\varepsilon$ model, the SST $k-\omega$ model suffers from discrepancies in matching the wind tunnel data in a stall regime in terms of the power and pressure coefficient distributions at wind speeds up to 10m/s (Chen, 2016; Mo and Lee, 2012; Moshfeghi *et al.*, 2012; Sørensen *et al.*, 2002).

As discussed previously, the RANS turbulence models, particularly the two-equation models, perform well in predicting the wind tunnel data in terms of power, thrust and the pressure coefficient distribution. These agreements were established where the flow is almost attached in a range of 5m/s to 8m/s. However, the turbulence models vary in a discrepancy in matching the measured data in the cases of wind speeds are greater than 10m/s, due to the existence of stalled flow.

In the present study, the SST $k-\omega$ model has been chosen as it combines the features of the $k-\epsilon$ and $k-\omega$ models. Therefore, the SST $k-\omega$ model is an appropriate choice for predicting stalled flow. Furthermore, the ability of the Spalart-Allmaras model has been examined for capturing the wind tunnel data, since it is an economic model.

3.8 Conclusion

The first part of this chapter was dedicated to introducing the main governing equations, including the Navier-Stokes equations and the RANS equations, which have been frequently used in CFD studies. Furthermore, the chapter includes an illustration of the structure of the CFD modelling process, namely, the pre-processor, solver and post-processor. It has shown that the numerical accuracy is significantly affected by setting up both the pre-processor and solver.

In contrast, the physical behaviour of turbulence and a description of the common turbulence models were presented in the second part of the chapter. In addition, the common features of the RANS turbulence models have been introduced, with a view towards choosing the most suitable models in this study. Among the turbulence models, the SST $k-\omega$ model has been chosen for combining the features of the $k-\epsilon$ and $k-\omega$ models. The Spalart-Allmaras model will be tested due to its economical requirements.

Chapter 4 : Validation of Baseline Case (NREL Phase VI Rotor)

4.1 Introduction

The purpose of this chapter is to validate the three-dimensional numerical results that were obtained using Computational Fluid Dynamics. The validation was conducted by comparing the CFD results with experimental measurements, in terms of aerodynamic torque, pressure coefficients distributions, thrust force, and normal force coefficients at five different spanwise sections. Unstructured mesh elements have been used to discretize the computational domain, which was divided into two domains by employing the multi-rotating frame (MRF). The SST $k-\omega$ turbulence and the Spalart-Allmaras models were utilised to solve the RANS equations in the steady-state conditions.

4.2 Experimental Data and Real Rotor Description

The NREL phase VI unsteady aerodynamic experiments were tested in the world's largest wind tunnel, located at the NASA-AMS 24.4m x 36.6m (80ft X 120ft), as shown in Figure 4-1. The effects of different operating conditions on the NREL phase VI performance were considered in this effort, such as the upwind/downwind configurations of rigid and teetered rotors. Further, experiments that include data that considers the full scale-steady/unsteady aerodynamic behaviour of a HAWT and structural dynamic were carried out at a blockage ratio error of less than 2% (Hand *et al.*, 2001). The results were published in order to improve and validate different numerical methods, such as the FAST_AD and CFD codes. The NREL phase VI rotor consists of two blades that were made from the blade root to the blade tip using the S809 airfoil, which was designed and tested for HAWT purposes (Tangler and Somers, 1995). Each blade is linearly tapered and non-linearly twisted, as shown in Figures 4-2 and 4-3, respectively. The stall regulated upwind NREL phase VI rotor was chosen to be the baseline case in the present study for all computations. The stall regulated is a passive control method that employs the aerodynamic behaviour of the stalled flow to limit the peak power with increasing wind speeds (Tangler and Somers, 1995). The specifications of the rotor, local chord and twisted angles distributions along the radial distance of blade are shown in Tables 4-1 and 4-2 (Hand *et al.*, 2001).



Figure 4-1 The NREL phase VI rotor in the NASA – Ames wind tunnel (Hand *et al.*, 2001).

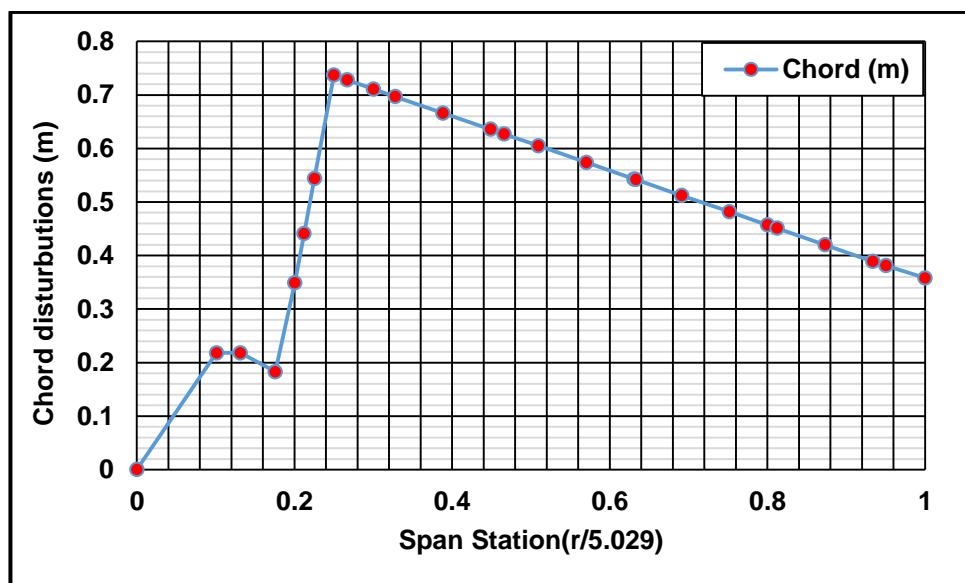


Figure 4-2 Rotor chord distributions (Hand *et al.*, 2001).

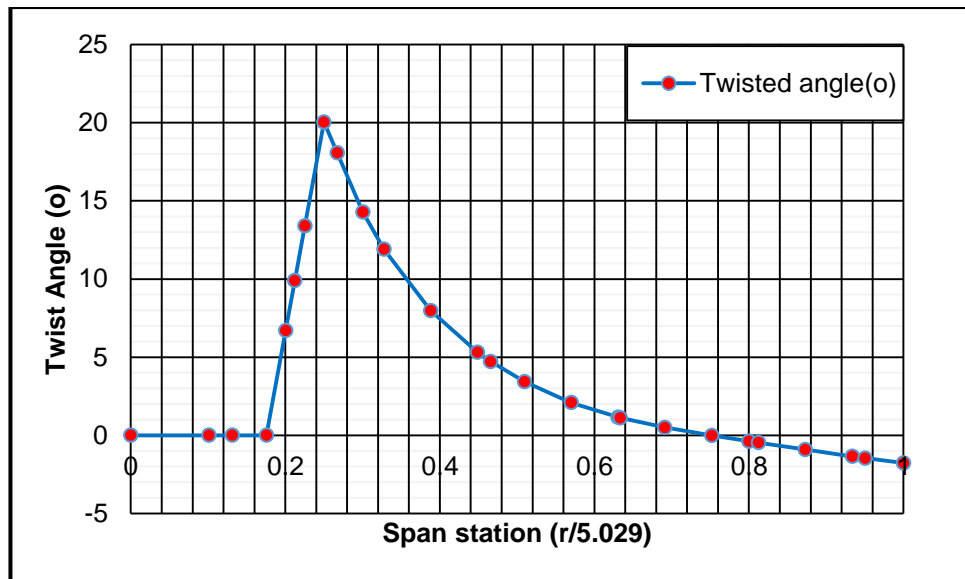


Figure 4-3 Twist angle distributions(Hand *et al.*, 2001).

Table 4-1 NREL phase VI rotor specifications (Hand *et al.*, 2001).

Number of blades	2
Rotor diameter	10.06 m
RPM	72 RPM
Rotor location	Upwind
Rated power	19.8 KW
Power regulation	Stall regulated
Blade tip pitch angle	3 degrees (down)
Blade airfoil	S809
Blade chord length	0.728 m –0.358 m (linearly tapered)
Twist angle	Non – linear twist along the span

Table 4-2 Local chord and twisted angles distributions along the NREL phase VI rotor (Hand et al., 2001).

Section	Radial distance (m)	Span Station (r/5.029)	Chord length (m)	Twist angle (°)
1	0	0	Hub	Hub
2	0.508	0.101	0.218	0
3	0.660	0.131	0.218	0
4	0.883	0.176	0.183	0
5	1.008	0.200	0.349	6.7
6	1.067	0.212	0.441	9.9
7	1.133	0.225	0.544	13.4
8	1.257	0.250	0.737	20.040
9	1.343	0.267	0.728	18.074
10	1.510	0.300	0.711	14.292
11	1.648	0.328	0.697	11.909
12	1.952	0.388	0.666	7.979
13	2.257	0.449	0.636	5.308
14	2.343	0.466	0.627	4.715
15	2.562	0.509	0.605	3.425
16	2.867	0.570	0.574	2.083
17	3.172	0.631	0.543	1.150
18	3.185	0.633	0.542	1.115
19	3.476	0.691	0.512	0.494
20	3.781	0.752	0.482	-0.015
21	4.023	0.800	0.457	-0.381
22	4.086	0.812	0.451	-0.475
23	4.391	0.873	0.420	-0.920
24	4.696	0.934	0.389	-1.352
25	4.780	0.950	0.381	-1.469
26	5.029	1.000	0.358	-1.775

4.3 Rotor geometry

The SpaceClaim (ANSYS) application was utilised to create a 3D model of the NREL phase VI rotor, as shown in Figure 4-4, corresponding to the local chord and twisted angles distributions, which are shown in Table 4-2 and Figure 4-5. The rotor blade is divided into a blade root and the main blade body, as shown in Figure 4-6. The blade root consists of cylindrical and transition sections. The cylindrical section starts from a radial distance of 0.508m to 0.883m, and then the transition airfoil extends to a radial distance at 1.257m. The construction of the main blade body begins using the S809 airfoil from 1.257m to the end of the blade. This is due to the S809 airfoil having a sharp trailing edge, theoretically. A slight modification was done on the blade trailing edge by reducing the chord length of a blade by 1% in order to avoid the non-orthogonal cell faces, which would be difficult to handle during in the meshing process, as shown in Figure 4-7.

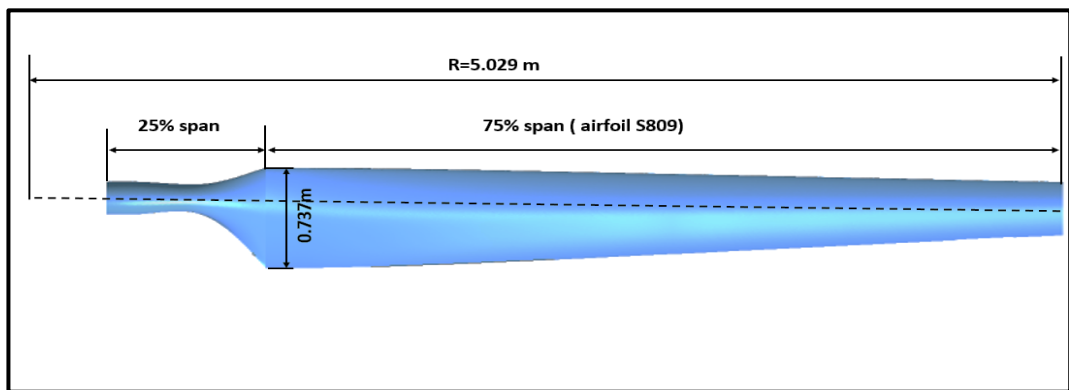


Figure 4-4 View of the NREL Phase VI blade.

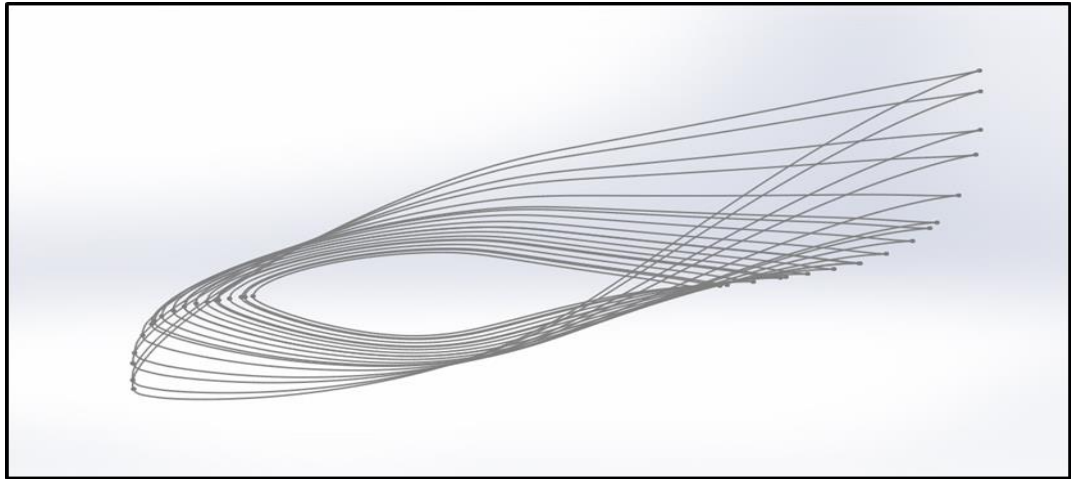


Figure 4-5 Airfoil cross sections of the baseline blade.

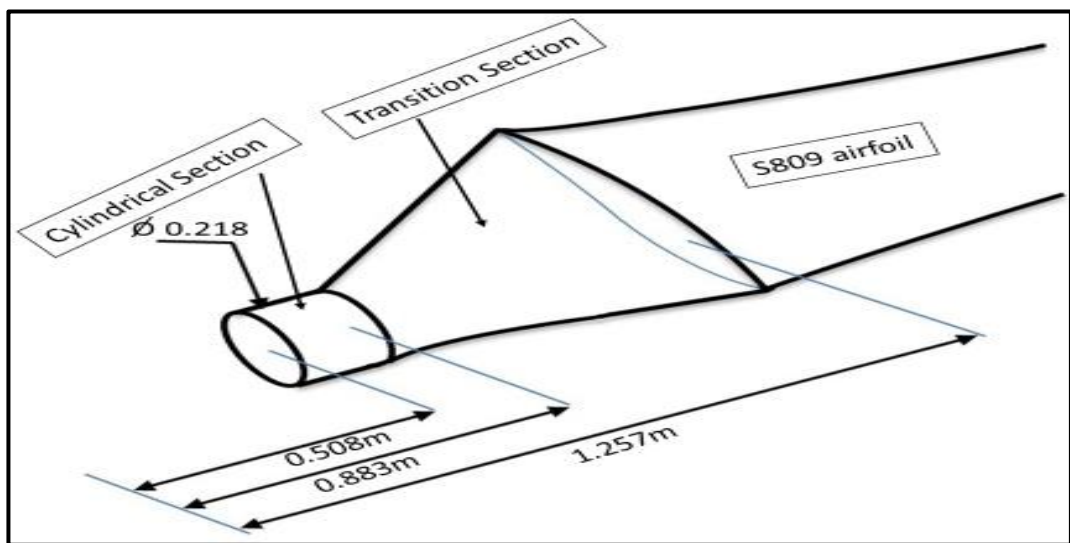


Figure 4-6 Rotor blade parts (Hand et al., 2001).

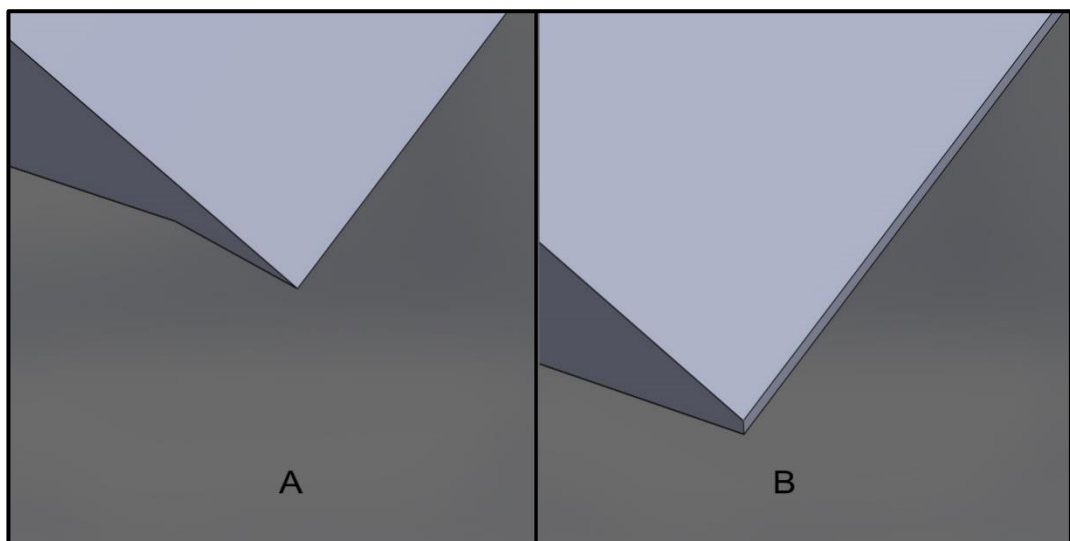


Figure 4-7 Illustration of: A- Original Blade, B- Modified blade.

In the NREL phase VI experiments, the surface pressure distributions were measured using twenty-two pressure transducers that were installed at 30%, 46.6%, 63.3%, 80% and 95% span of the blade. Further, a couple of pressure taps were also installed at 4% and 36% of the blade chord. The local effective angle of attack and dynamic pressure were measured by using five hole-probes that were mounted at 34%, 51%, 67%, 84% and 91% spanwise of the blade, as shown in Figure 4-8.

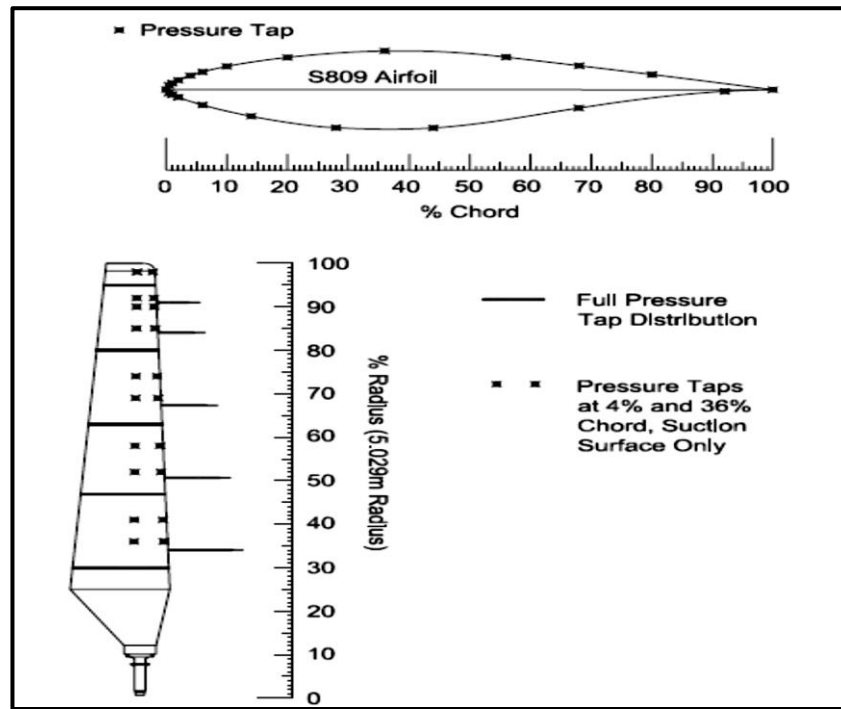


Figure 4-8 Pressure taps and five-hole probe locations (Hand et al., 2001).

4.4 Calculations of the aerodynamic force coefficients

Aerodynamic torque and thrust are considered the most important loads that indicate wind turbine performance. Throughout the NREL phase VI experiments, both torque and thrust coefficients were integrated along the rotor blade and then multiplied by the number of blades to give the total aerodynamic torque and thrust. The following equations were used to calculate the thrust and torque coefficients, respectively:

$$C_{TH} = (C_N \cos(\phi + \beta) - C_T \sin(\phi + \beta)) \quad (4.1)$$

$$C_{TQ} = (C_N \sin(\phi + \beta) + C_T \cos(\phi + \beta)) \quad (4.2)$$

Where, C_{TH} is a thrust coefficient and C_{TQ} is a torque coefficient. The C_N and C_T represent the normal and tangential force coefficients respectively and are illustrated in Figure 4-9.

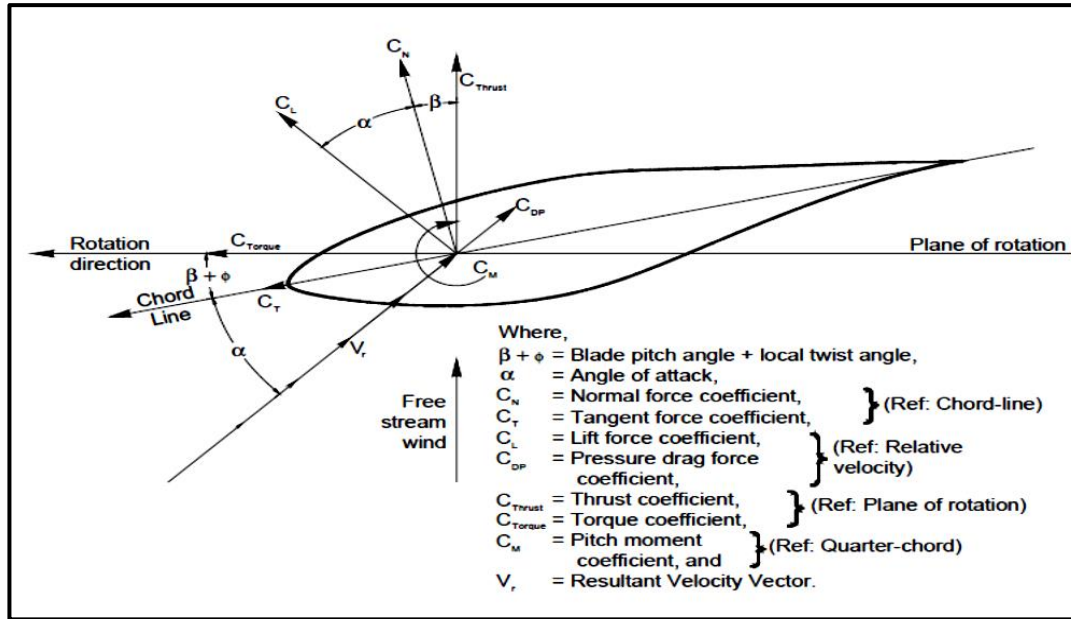


Figure 4-9 Schematic of aerodynamic force coefficients (Hand et al., 2001).

Both coefficients (C_N and C_T) can be determined by integrating a pressure coefficient along the blade chord. Thus, the normalised pressure coefficient C_{pi} can be calculated as follows:

$$C_{pi} = \frac{p - p_{\infty}}{\frac{1}{2} \rho_{\infty} (U_{\infty}^2 + (\Omega r)^2)} \quad (4.3)$$

Where,

p : computed local static pressure (Pa).

p_{∞} : Free stream static pressure (Pa).

ρ_{∞} : Free stream density (Kg/m^3).

U : Wind speed (m/s).

Ω : Rotating speed (rad/s).

r : The radial distance from the rotor hub to the blade section (m).

And, the following equations are employed to calculate C_N and C_T .

$$C_N = \sum_i \left(\frac{C_{pi} + C_{pi+1}}{2} \right) (x_{i+1} - x_i) \quad (4.4)$$

$$C_T = \sum_i \left(\frac{C_{pi} + C_{pi+1}}{2} \right) (y_{i+1} - y_i) \quad (4.5)$$

Where,

x_i : is a normalised distance along the blade chord.

y_i : is a normalised distance orthogonal along the blade chord.

The value of x or y in equations (4.4) and (4.5) starts from $x=1$ at the trailing edge and continue over the upper blade surface until it reaches the leading edge, then continues over the lower blade surface until the trailing edge.

4.5 Computational fluid domain

In the present study, the Multiple Moving Reference Frame (MRF) approach was chosen to model the flow field around the NREL phase VI. The MRF technique has been widely used in CFD studies to model the flow field around the rotating turbomachinery blades, including wind turbines. The MRF is a steady-state approximation model that allows an unsteady stationary frame to be steady with respect to the moving frame, where different rotational and/or translational speeds can be specified for different zones (Fluent, 2009). Hence in the present study, the computational domain was divided into a stationary frame (located away from blades) and rotating frame (located close to the blades), while the interface boundary condition was used to merge the separated frames, as shown in Figures 4-10 and 4-11.

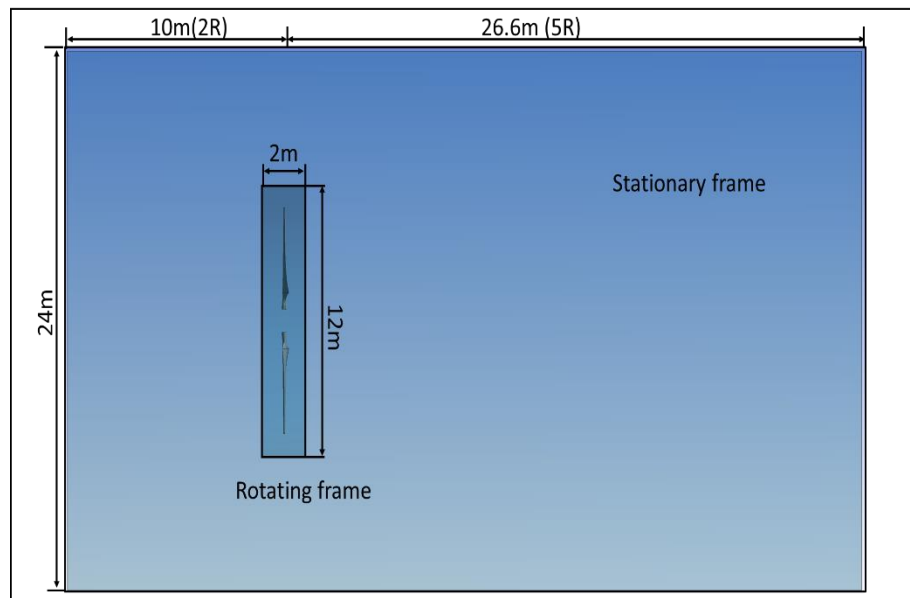


Figure 4-10 Side view of the computational domain.

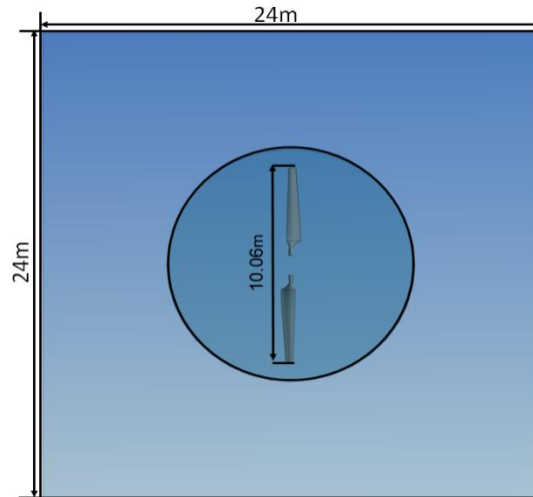


Figure 4-11 Front view of the computational domain.

4.6 Mesh generation

A big challenge for turbulence models is to capture the boundary flow around the wind turbine blade, due to the separated flow and generating vortices that are associated with wind turbine operations. The NREL phase VI rotor has a complicated blade geometry and is a stall regulated, therefore, significant efforts were made to create an acceptable quality mesh, given that it significantly affects the convergence and accuracy of the numerical results (Hirsch, 2007).

ANSYS Meshing (version 17.0) was employed to generate an unstructured mesh within the stationary and rotating domain, separately. An accepted mesh quality was obtained by increasing the mesh density around the rotor blades and the mean flow field, which is included in the stationary domain. Therefore, two influence bodies were employed. The first body was created in the stationary domain, as shown in Figure 4-12 and the second influence body was used to refine elements around the rotor blades, as shown in Figure 4-13. The mesh specifications of the stationary domain are summarised in Table 4-3. Unlike the stationary domain, the rotating domain includes the rotor blades, which are considered the main parts that generate the wind turbine's power. Therefore, greater attention has been paid to studying the mesh quality and the grid-independence effect on the numerical results. Three different element sizes of the blade surface have been examined to study the grid-independence effect, as shown in Table 4-4.

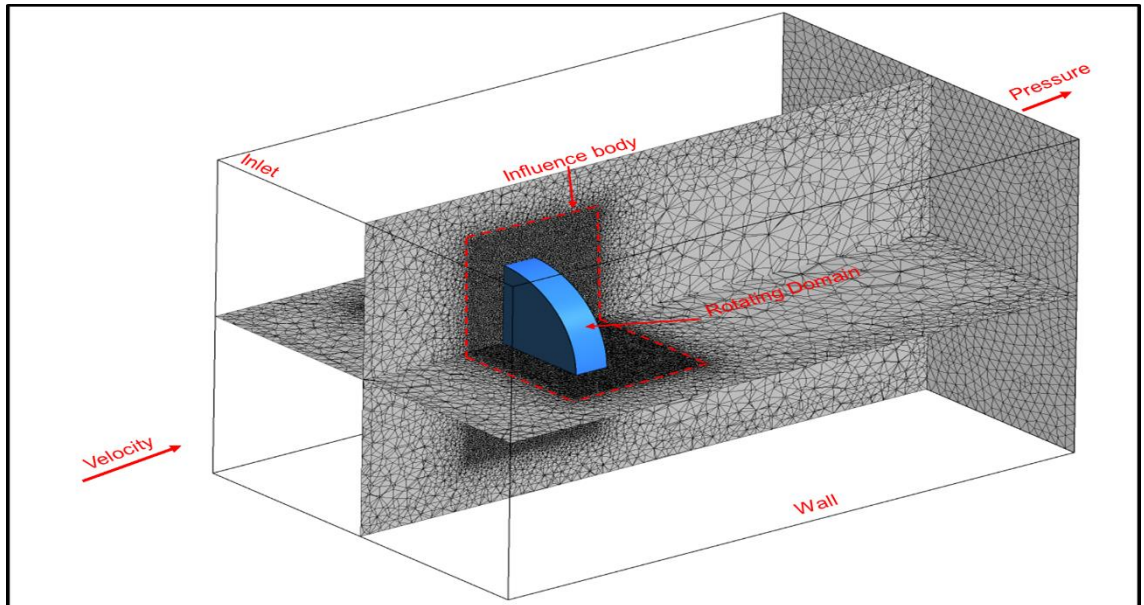


Figure 4-12 View of the unstructured mesh of the stationary domain.

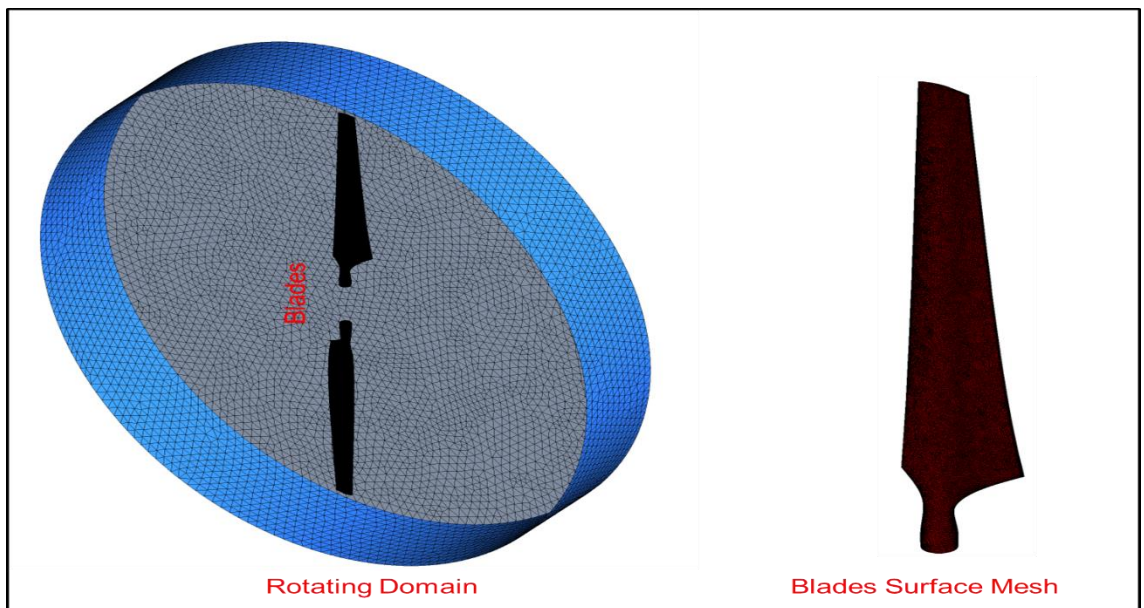


Figure 4-13 View of the unstructured mesh of the rotating domain and blade.

Table 4-3 Mesh specification of the stationary domain.

Mesh Parameter	Value
Influence body sizing	300mm
Interface surface 1 sizing	200mm
Interface surface 2 sizing	200mm
Interface surface 3 sizing	200mm

Table 4-4 Mesh specification of the rotating domain.

Mesh parameter	Mesh type 1	Mesh type 2	Mesh type 3
Influence body sizing	150 mm	150 mm	150 mm
Interface surface 1 sizing	200 mm	200 mm	200 mm
Interface surface 2 sizing	200 mm	200 mm	200 mm
Interface surface 3 sizing	200 mm	200 mm	200 mm
Blade face sizing	10 mm	9 mm	7 mm
Inflation layers number	10 layers	10 layers	10 layers
Number of elements	8,405,297	9,422,292	11,021,521

4.7 Reynolds Number calculations

Considering whether the flow behaviour around the blade is turbulent or laminar, the Reynolds number was calculated at the root and blade tip. As the NREL phase VI rotor blade is an irregular plate (twisted and tapered), the Reynolds number should be calculated using v_{rel} (relative velocity) and c (airfoil chord section), as follows:

$$Re = \frac{\rho v_{rel} c}{\mu} \quad (4.6)$$

Where

ρ : Air density (Kg/m³).

v_{rel} : Blade relative velocity (m/s).

$$v_{rel} = \sqrt{v_o^2 + (\omega r)^2} \quad (4.7)$$

v_o : Wind speed velocity (m/s)

ω : Angular velocity (rad/s).

r : Radial distance from the root blade to the airfoil section (m).

c : The airfoil chord section (m).

μ : Dynamic viscosity [kg/m.s].

The Reynolds numbers of the blade root and tip according to wind speed are listed in the following table.

Table 4-5 Reynolds numbers at the root and blade tip blade.

Wind speed (m/s)	Reynolds number at the r=1.252 m. (root airfoil)	Reynolds number at the r=5.029 m. (tip airfoil)
5	540,655.5	937,363.1
7	594,477.2	945,021.3
9	659,441.2	955,136.7
11	732,589.4	967,632.2
13	811,712.1	982,417.2
15	895,226.7	999,389.8
17	982,013.3	1,018,441.0
19	1,071,277.0	1,039,456.0

Based on Table 4-5, the flow around the whole blade is turbulent, since the minimum value of speed 5 m/s is more than 5×10^5 (Fluent, 2006).

4.8 Boundary conditions

In all CFD applications, the appropriate initial and boundary conditions of the physical problem are required to solve the RANS equations. In this study, the boundary conditions are considered according to the NREL phase VI rotor experiments, which were performed at the NASA-AMS wind tunnel, as shown in Figure 4-14. The numerical solutions were conducted using ANSYS FLUENT version 17.0 in order to solve an incompressible flow in steady-state conditions. The following diagram is an illustration of the used boundary conditions in this study.

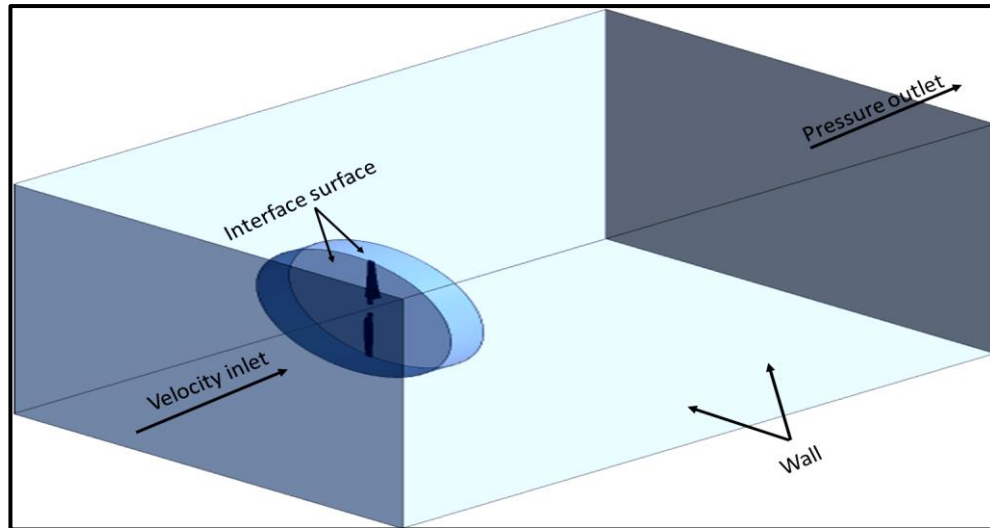


Figure 4-14 View of the boundary conditions of the problem.

4.8.1 Inlet boundary conditions

In all numerical computations, the air was taken as a working fluid. Since the fluid flow was considered incompressible, the velocity inlet boundary condition was used to specify the flow velocity at the entrance of the computational domain. Hence, wind speeds from 5 m/s to 25 m/s have been applied to specify the flow velocity at the computational domain inlet, which corresponds to the NREL phase VI experiments. The temperature and the air density were used corresponding to the measured values, which are listed in Table 4-6. Further, the turbulence intensity and length scale were used to specify the kinetic turbulent energy (k) and its specific dissipation rate (ω) at the inlet. The turbulent intensity was chosen to be 0.5%, corresponding to the wind tunnel value (Simms *et al.*, 2001). The following equations are employed in the ANSYS FLUENT in order to estimate the turbulence quantities k and ω (Fluent, 2009).

The turbulent kinetic is calculated as follows:

$$K = \frac{3}{2} (u_{avg} I)^2 \quad (4.8)$$

And, the following equation is utilised to estimate the turbulent dissipation:

$$\omega = \frac{k^{1/2}}{C_{\mu} l} \quad (4.9)$$

Where,

u_{avg} : is the mean flow velocity.

I : is the turbulence intensity.

C_{μ} : is an empirical constant equal to 0.09.

l : is the turbulence length scale.

Table 4-6 Measured rotating velocity of the rotor and air properties.

Wind Velocity (m/s)	RPM	Temperature (°C)	Density (kg/m ³)
5	71.67	13.45	1.224
6	71.76	13.08	1.226
7	71.87	13.11	1.226
8	71.99	12.60	1.228
9	72.11	12.49	1.228
11	72.14	11.46	1.235
13	72.09	11.68	1.233
15	72.06	11.91	1.232
17	72.02	12.49	1.228
19	72.02	13.23	1.224
23	72.12	15.53	1.213
25	72.19	15.48	1.212

4.8.2 Outlet boundary conditions

This boundary condition was used to define the pressure of the outlet of the computational domain. An outlet pressure of zero was applied to this boundary, which means no pressure differential is occurred at the domain exit, when compared to the atmospheric pressure.

4.8.3 No-slip wall conditions

A no-slip condition is used to set the tangential and normal velocity components to zero at the walls. The no-slip condition and rotating wall were imposed to define the rotor blades, as it is included in the rotating domain. The wall of the computational domain was defined as a no-slip condition and stationary wall.

4.9 Solver settings

In this study, all the numerical computations were conducted in steady-state conditions. The RANS equations and two different turbulence models, including the Spalart-Allmaras and Shear Stress Transport SST k- ω models, were implemented to solve the governing flow equations using Ansys Fluent 17.0. The SIMPLE Pressure-Based Solver was chosen, since it

has been developed to be an appropriate approach for low-speed incompressible applications and it requires less memory than the Density – Based Solver. In addition, the density is constant and there is no linking between pressure and density in the case of incompressible flows (Versteeg and Malalasekera, 2007).

Considering the spatial discretization, the second order upwind schemes were utilised to discretize the convection terms for all transport equations, except the standard interpolation was used for pressure. The solution convergence was established by monitoring the residual history, moment coefficient and lift coefficient over cycle of 2000 iterations. However, an adequate convergence was noticed after 1200 iterations, when the convergence criteria were chosen to be 10^{-6} for all variables.

4.10 Effect of the normal wall distance

As previously discussed, the non-dimensional wall distance y^+ plays a significant role in the correct prediction of the numerical results, compared to experimental data. This importance of the y^+ is considered due to accounting for the viscosity-affected region in accurately obtaining the effects of the stalled flow, which is employed in the NREL phase VI.

Several studies have employed different values of y^+ for estimating the effects of the near wall, using the low Reynolds turbulence models, such as the Spalart-Allmaras and the SST $k-\omega$ models. It has been observed that at y^+ values greater than 150, there is an inability to predict the flow behaviour at the near wall conditions accurately (Lee *et al.*, 2017). However, it seems that an acceptable prediction of the aerodynamic performance of the NREL phase VI requires a refinement mesh near the wall blade with a y^+ value around 5.

A good validation in terms of the output power and pressure coefficients has been reported at an average value of y^+ equal 7, which is between the viscous sub-layer and buffer layers (Mo and Lee, 2012). Interestingly, at an average value of y^+ equals of 5.2, the same validation was found in the numerical results in terms of output power, thrust force and pressure coefficient distributions (Sudhamshu *et al.*, 2016). In their study, the maximum value of y^+ was found to be 50, which means some parts of the near wall on the blade surface were calculated from the buffer layers.

In contrast, numerous researchers have employed a y^+ value in the range of 1 to 5, in order to account for the whole viscous sub-layer effects along the entire blade (Langer - Moller *et al.*, 2017; Rahimi *et al.*, 2016; Moshfeghi *et al.*, 2012; Tang, 2012). However, an accurate prediction of the CFD results

for the viscosity-wall affected regions can be obtained if the overall resolution of the near wall effect is sufficient. This target is more significant than a mesh refinement in the normal wall direction, towards achieving a certain value of y^+ . Using an unstructured mesh is recommended when creating 10-20 or more prism layers around a wall, in order to obtain an accurate estimation of the near wall effects (Fluent, 2013).

Hence, the requirements of the computational resources and an acceptable accuracy are considered in the present study. Therefore, ten layers of prismatic cells were generated around the blades, with a growth rate of 1.25. Consequentially, a maximum value of y^+ less than 2 was obtained along the entire blade, except for near the blade tip. Figure 4-15 shows the y^+ contour along the entire blade for the suction and pressure side of a blade, which was obtained using the ANSYS CFD-post at wind speeds of 5m/s and 25 m/s.

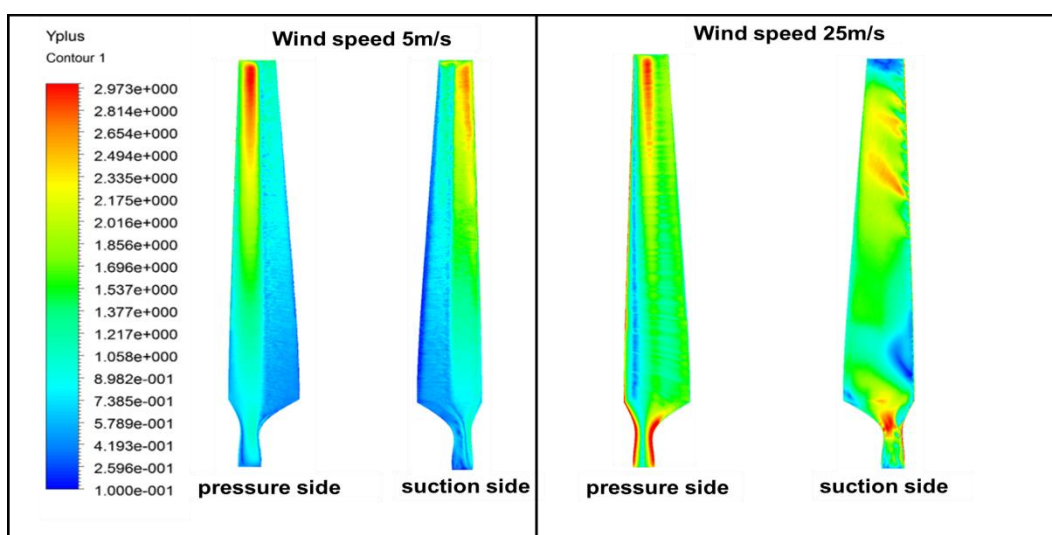


Figure 4-15 y^+ contours for pressure and suction sides.

4.11 Grid independence study

The independency on the numerical solution was tested by generating three different levels of a mesh refinement. The grid volume of the stationary domain was gradually coarsened, since the far field effects were not important. The rotating frame is the most important part of the computational domain, due to including blades that are responsible for generating an aerodynamic torque. Therefore, the mesh refinement was focused on the rotor blades, particularly the blades' surfaces, by reducing the mesh element size from 10mm to 7mm gradually, as shown in Table 4-4. The solution convergence was established by monitoring the residual history, moment coefficient and lift coefficient over a cycle of 2000 iterations. The grid

independence analysis was carried out on the numerical torque values at wind speeds of 5m/s and 7m/s. It was found that the values of the CFD torque vary less than 0.34% at wind speed of 5 m/s and 7m/s for grid numbers greater than 11 million cells, as shown in Figure 4-16.

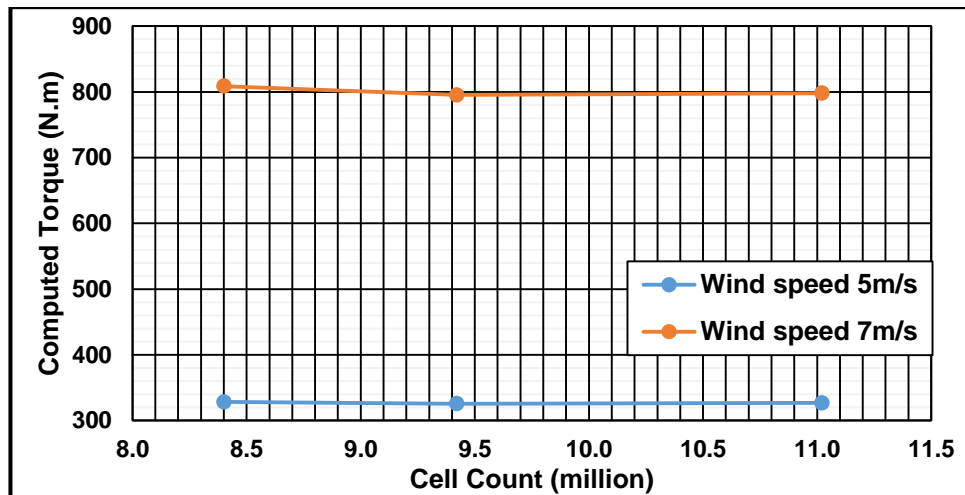


Figure 4-16 Effect of grid refinement on the computed torque.

4.12 Numerical results

The CFD results are divided into two parts. The first part is the validation of the numerical results that were obtained using the Spalart-Allmaras and SST $k-\omega$ models, with a view to match the experimental measurements of the NREL phase VI rotor. The second part involves the results on the improvements of wind turbine performance as a result of winglet functionality, which will be discussed in the next chapters.

The validation was done by comparing the predicted aerodynamic performance of the NREL phase VI rotor and the measured data. Hence, the comparisons were conducted in terms of the computed torque, thrust force, pressure and normal force coefficients.

Table 4-7 and Figure 4-17 show a comparison between the experimental and numerical torque results, which were obtained for different wind speeds according to the wind tunnel tests.

Table 4-7 Comparison of measured and computed torque.

Wind speed (m/s)	Exp. Torque (N.m) ¹	SST k-w model		S-A model	
		Computed Torque (N.m)	Error (%)	Computed Torque (N.m)	Error (%)
5	311.18	326.76	5.0	293.55	-5.6
6	536.39	552.72	3.0	513.71	-4.2
7	782.21	798.07	2.0	772.05	-1.2
8	1023.56	1020.77	-0.2	1037.65	1.3
9	1282.04	1130.62	-11.8	1252.12	-2.3
11	1482.04	1314.36	-11.3	1416.95	-4.4
13	1220.10	1273.40	4.3	1475.48	20.9
15	1188.30	1069.44	-10.0	1419.23	19.4
17	898.45	923.53	2.7	1229.02	36.7
19	882.15	860.39	-2.4	1095.54	24.1
23	1016.03	1005.28	-1.0	1102.03	8.4
25	1205.58	1083.90	-10.0	1199.55	-0.5

¹ The experimental torque values were taken from (Elfarra, 2011).

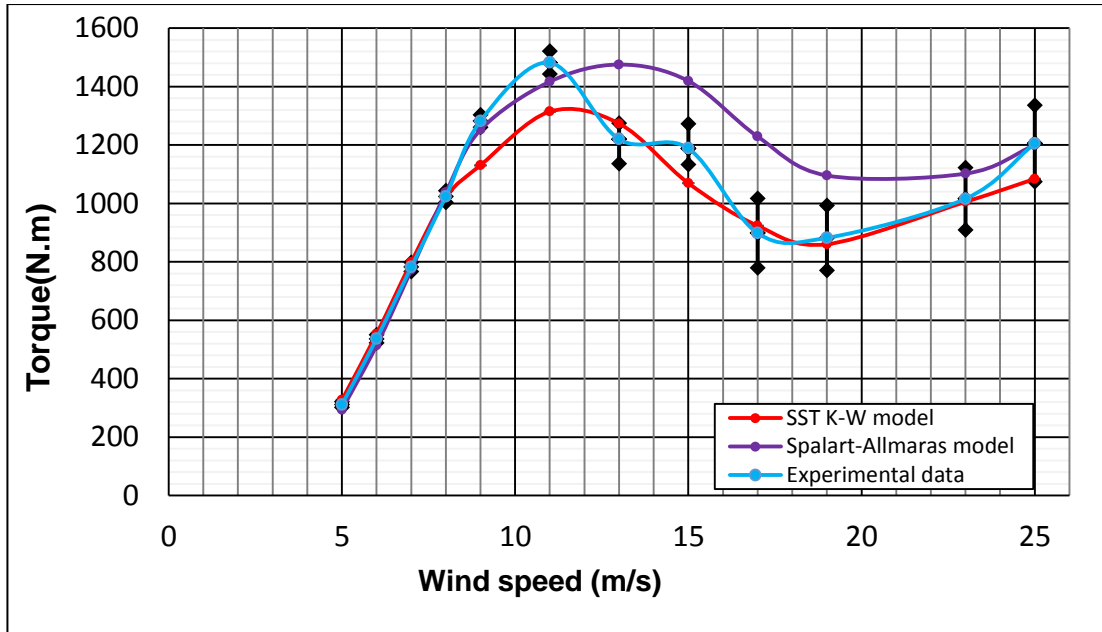


Figure 4-17 Comparison of measured and computed torque values.

Based on Figure 4-17, it can be observed that at low wind speeds of 5m/s to 8m/s, where the flow is almost considered an attached regime, as shown in Figures 4-18 and 4-19, both the turbulence models show a good prediction of the numerical torque results, when compared with the measured data. However, the Spalart-Allmaras model shows an over-prediction of the computed torque values at the higher wind speeds of 9m/s, due to the stalled flow existing at section 47% on the span location of the blade, as shown in Figure 4-20.

In contrast, the SST k- ω model demonstrates superior performance in computing the numerical torque values of the pre-stall and post-stall regime, as shown in Figures 4-19, 4-21 and 4-22. The different performances of both turbulence models occurred due to different techniques that are followed by each model to predict the effects of the turbulence. The Spalart-Allmaras model is an economic model, which solves a single transport equation to compute the kinematic eddy viscosity. The turbulence length scale is modelled using an algebraic equation. The main weakness of the Spalart-Allmaras model is that it predicts high backflow velocities in the recirculation region, due to its insensitivity to the effect of adverse pressure gradients (Menter, 1992). This could explain why the Spalart-Allmaras model was less sensitive in accurately capturing the effect of the stalled flow at higher wind speeds of 11m/s.

Therefore, the SST k- ω model has been employed in this study to predict the flow field around the NREL rotor VI as a baseline case, along with all the CFD modifications, which will be discussed in the next chapters.

Thus, a comparison between the computed thrust force values and the measured data was done using the SST k- ω model, as shown in Figure 4-23. This comparison shows a good agreement between the numerical thrust results and wind tunnel data. However, the SST k- ω model slightly over-predicts the thrust force at low wind speeds, where the flow is almost attached. Furthermore, there is a slight under-prediction of the computed thrust force at the higher wind speeds of 17m/s, when the stalled flow occurs. Similar behaviour when predicting thrust force using the SST k- ω model was found in the efforts of various scholars (Lee *et al.*, 2017; Yelmule and Vsj, 2013; Sørensen *et al.*, 2002).

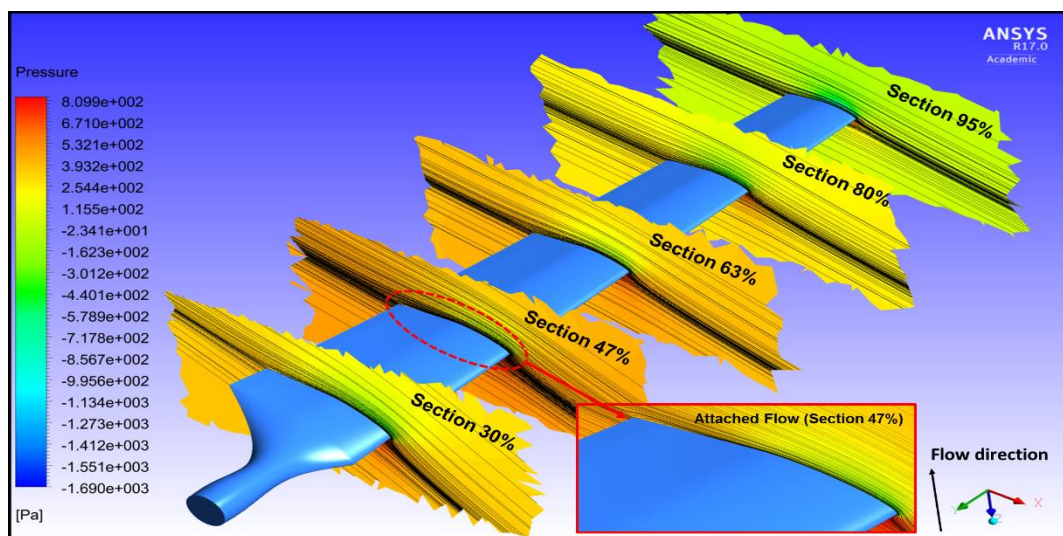


Figure 4-18 Pressure contours and streamlines predicted by the Spalart-Allmaras model at 8m/s.

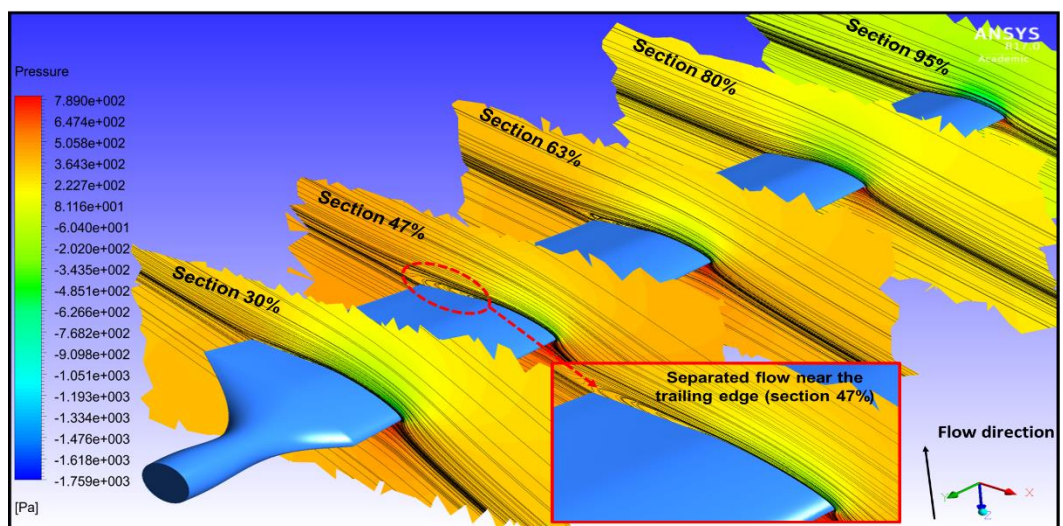


Figure 4-19 Pressure contours and streamlines predicted by the SST k- ω model at 8 m/s.

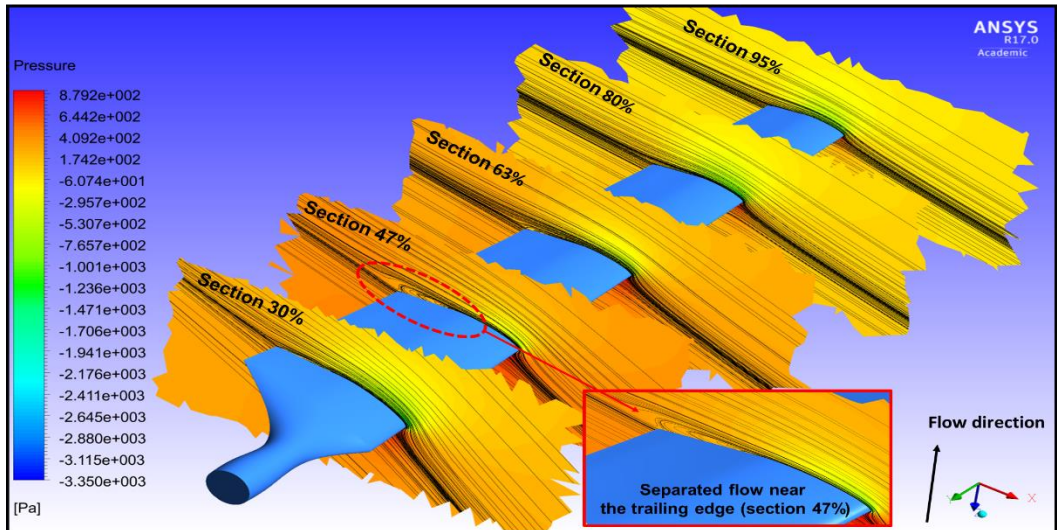


Figure 4-20 Pressure contours and streamlines predicted by the Spalart-Allmaras model at 9 m/s.

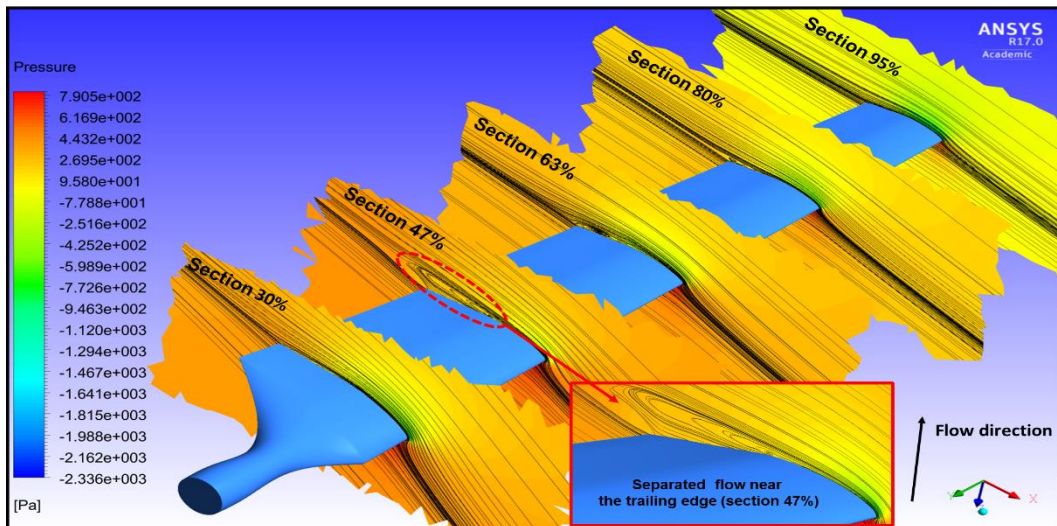


Figure 4-21 Pressure contours and streamlines predicted by the SST k- ω model at 9m/s.

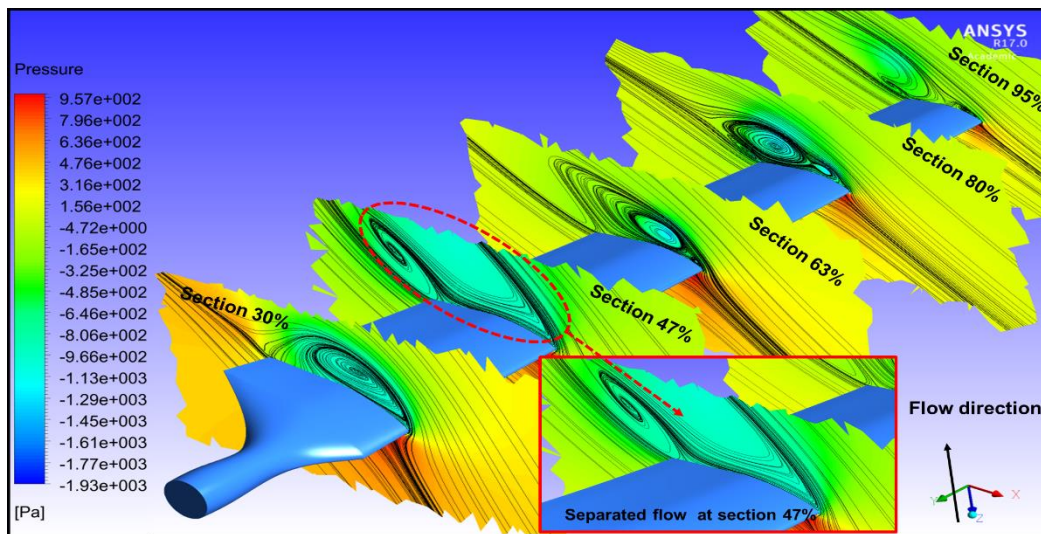


Figure 4-22 Pressure contours and streamlines predicted by the SST k- ω model at 19m/s.

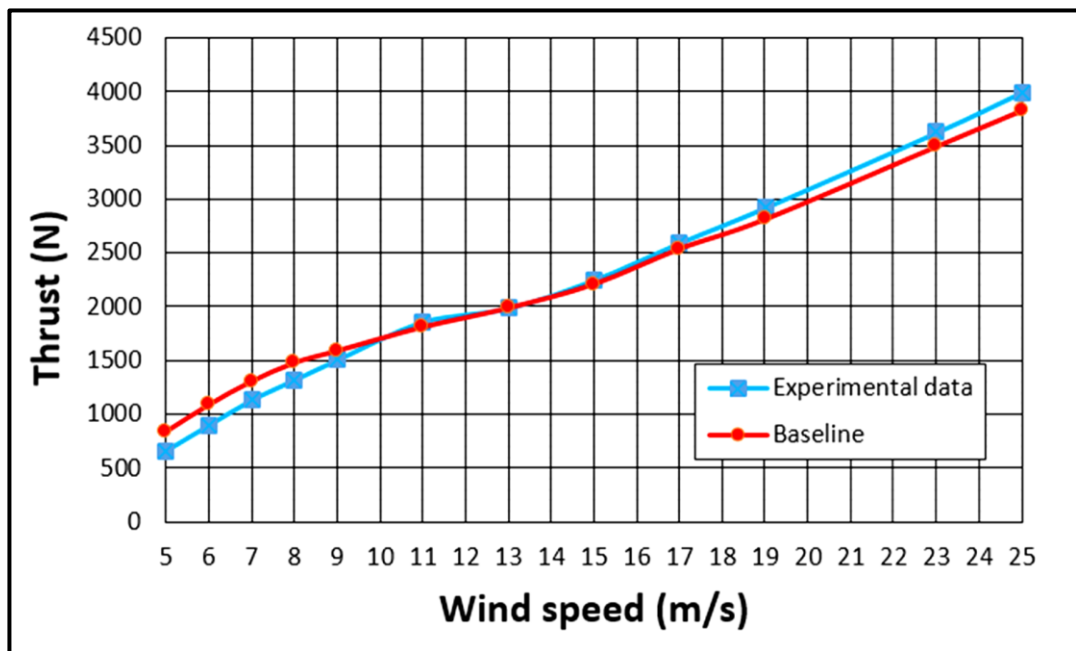


Figure 4-23 Comparison of measured and computed thrust force.

4.13 Pressure and normal force coefficients

Figures 4-24 to 4-31 demonstrate the comparisons of measured and calculated pressure coefficients and normal force coefficients for different wind speeds of 5, 7, 15 and 25 m/s at 30%, 47%, 63%, 80% and 95% span location of the blade. The pressure coefficients and normal force coefficients were calculated using equations (4.3) and (4.4), respectively. The pressure coefficients were plotted as a non-dimensional distribution along the chord

direction of a blade. The pressure coefficient figures were plotted upside-down with negative suction values on the top part of the figures.

At low wind speeds, the flow is mostly attached at 5m/s and 7m/s along the span-wise of the blade as shown in the streamlines plots in Figures 4-32 and 4-33, respectively. It can be noted that good agreements were obtained in computed pressure coefficients, when compared to the measured results of all spanwise sections at wind speeds of 5m/s and 7m/s, as shown in Figures 4-24 and 4-25, respectively. However, it is clearly shown in Figures 4-26 and 4-27 that, there is a discrepancy between measured and computed pressure coefficient distributions at wind speeds of 15m/s and 25m/s, particularly in the suction side. The discrepancy occurs at high wind speeds due to the effect of the stall regulated control method, which is employed to limit the peak power of the NREL phase VI with increasing wind speeds, as shown in the streamline plots at wind speeds of 15m/s and 25m/s in Figures 4-34 and 4-35 , respectively.

According to the stall regulated control, the streamlines flow is developed along the suction side of the blade from an attached flow to a stalled flow, with increasing wind speeds as shown in Figure 4-36. Hence, the SST k- ω model demonstrates an inability to match the measured pressure coefficients of the suction sides. Similar behaviour was observed in different previous studies, which use the RANS turbulence models to compute pressure coefficients (Elfarra *et al.*, 2014; Gomez and Munduate, 2014; Mo and Lee, 2012).

Furthermore, the same discrepancy was noticed with unsteady state studies, which employed the RANS, DES and LES turbulence models to match the measured pressure coefficients distributions on the suction sides at higher wind speeds of 15m/s (Quon, 2014; Li, 2014; Sezer-Uzol, 2006; Johansen *et al.*, 2002).

The computed normal force coefficients comprising of the measured data are shown in Figures 4-28 to 4-31. According to the equation (4.4), the sectional normal force coefficient is directly influenced by the sectional pressure coefficient distribution along the chord-wise of a blade. Hence, the discrepancy of the SST k- ω model was observed in order to match wind tunnel data at high wind speeds due to the existence of stalled flow.

At low wind speeds of 5m/s and 7m/s, the attached flow is mostly dominant along the entire blade. Despite this, there is an observed transition and separated flow at wind speeds of 7m/s, which starts from the blade hub and increases to the 63% spanwise location of the blade, as shown in

Figure 4-36. The SST $k-\omega$ model shows a good agreement in computing the normal force coefficients at low wind speeds, when compared to the experimental data as shown in Figures 4-28 and 4-29.

In contrast, the discrepancy occurred when computing the normal force coefficients at high wind speeds of 15m/s and 25m/s due to the influence of the stalled flow. Figures 4-30 and 4-31 show the predicted values of the normal force coefficients when compared to the measured data of wind speeds of 15m/s and 25m/s. The streamlined behaviour of the flow field interprets the discrepancy of matching the experimental data at high wind speeds. Figure 4-36 shows that the flow is almost separated on the suction side, at a wind speed of 15m/s, except at the blade tip. Meanwhile, the blade is entirely under the separation condition flow, at a wind speed of 25m/s.

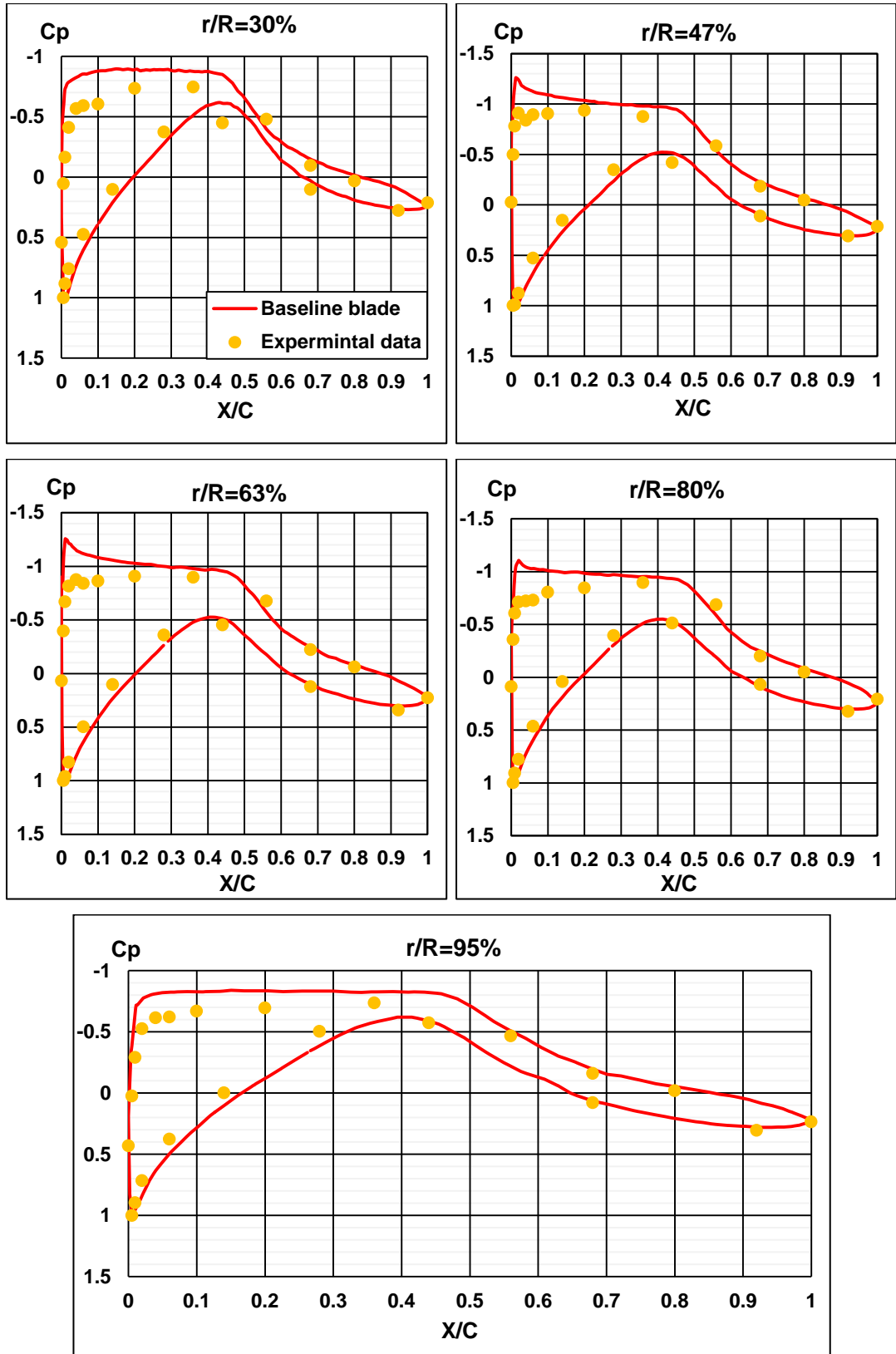


Figure 4-24 Comparisons of measured and computed pressure coefficients at 5m/s.

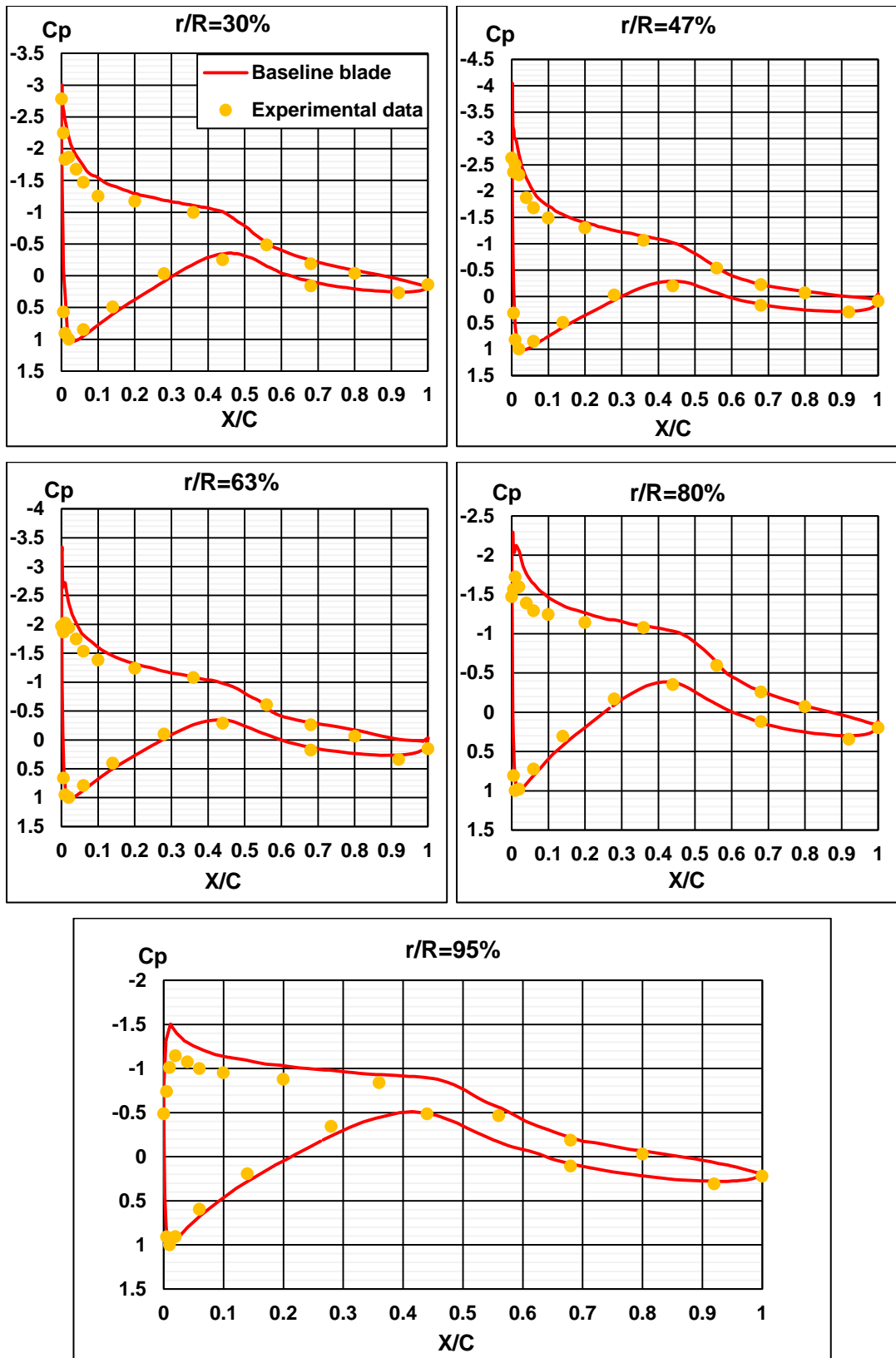


Figure 4-25 Comparisons of measured and computed pressure coefficients at 7m/s.

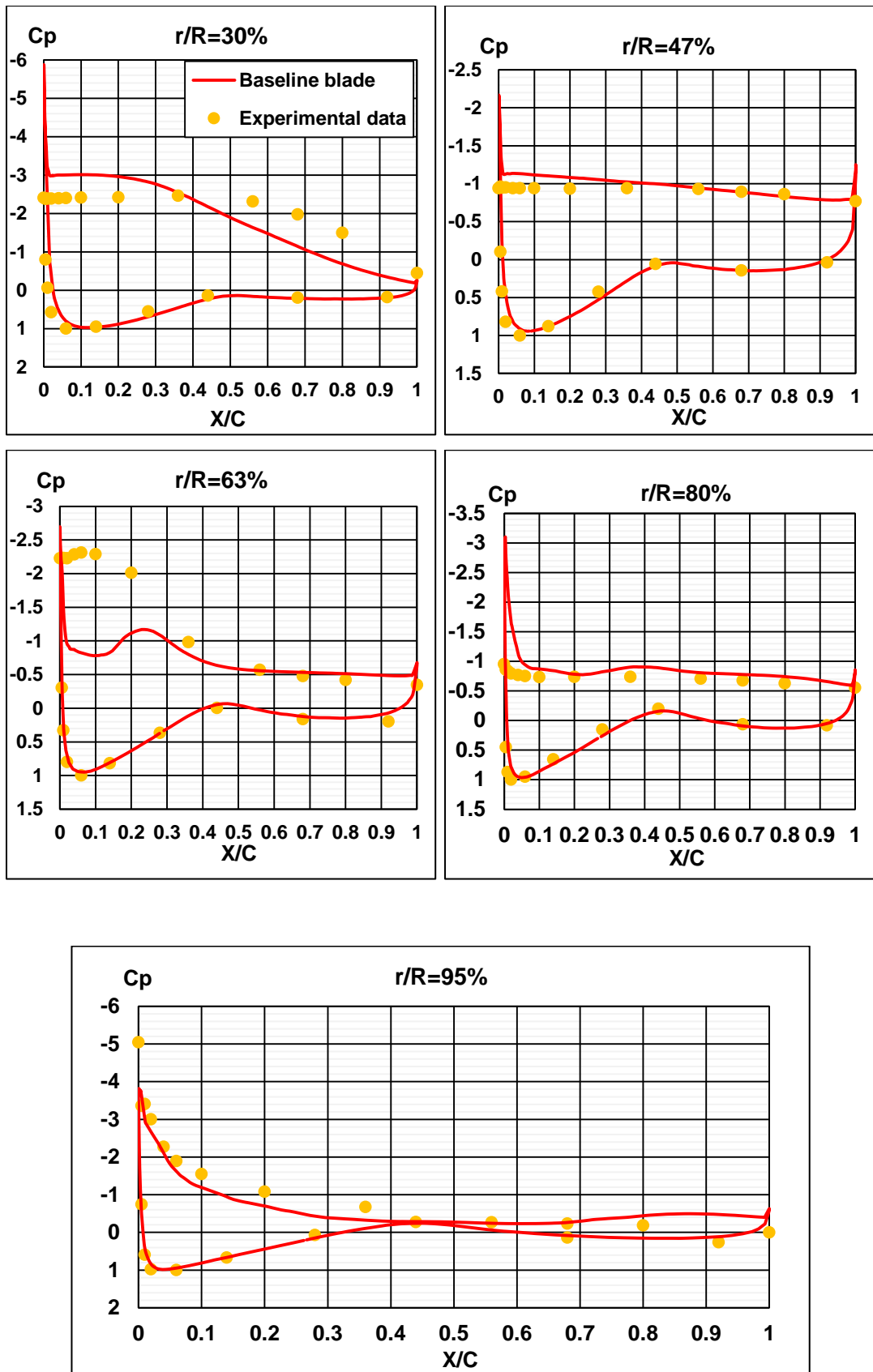


Figure 4-26 Comparisons of measured and computed pressure coefficients at 15m/s.

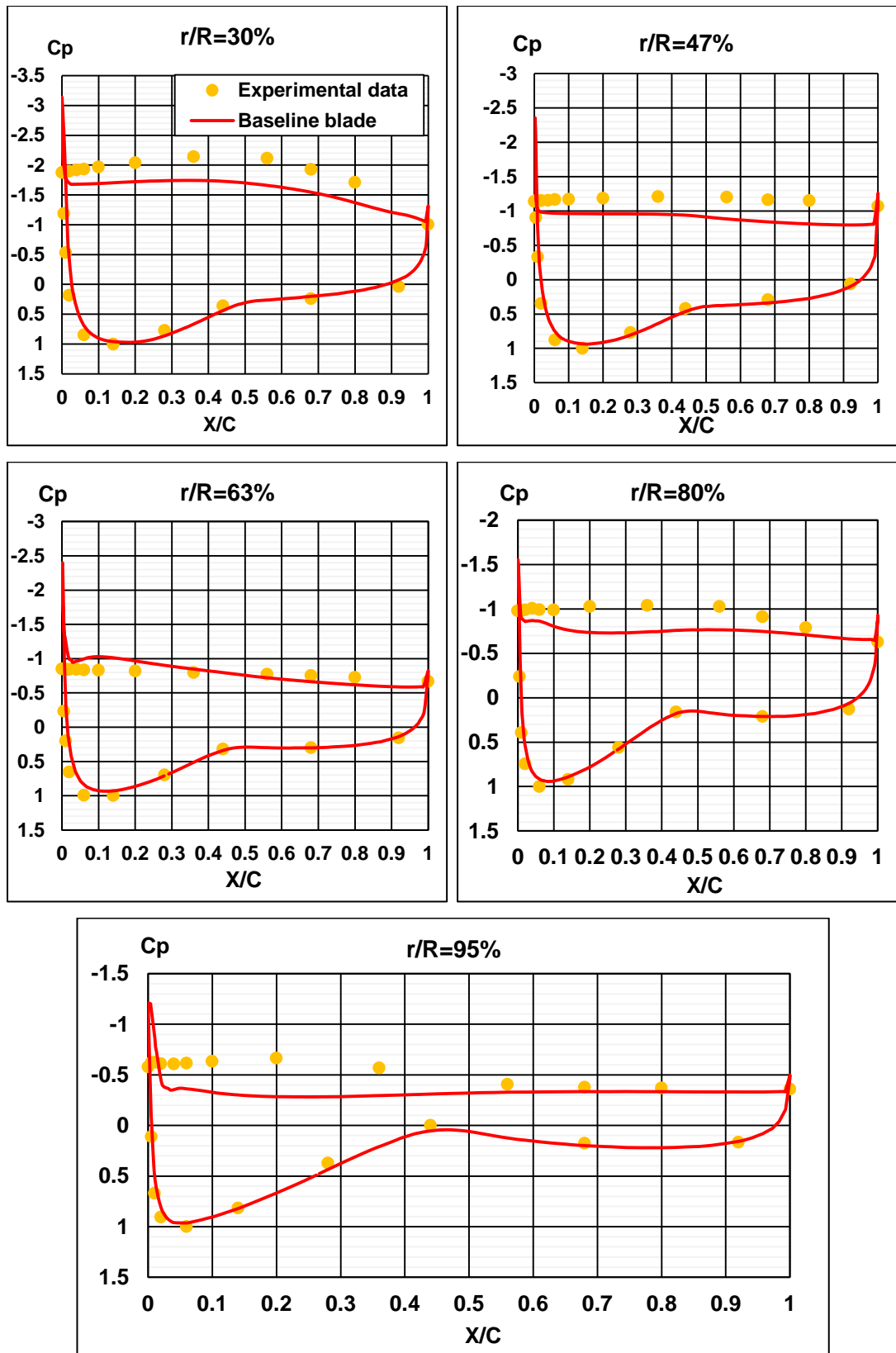


Figure 4-27 Comparisons of measured and computed pressure coefficients at 25m/s.

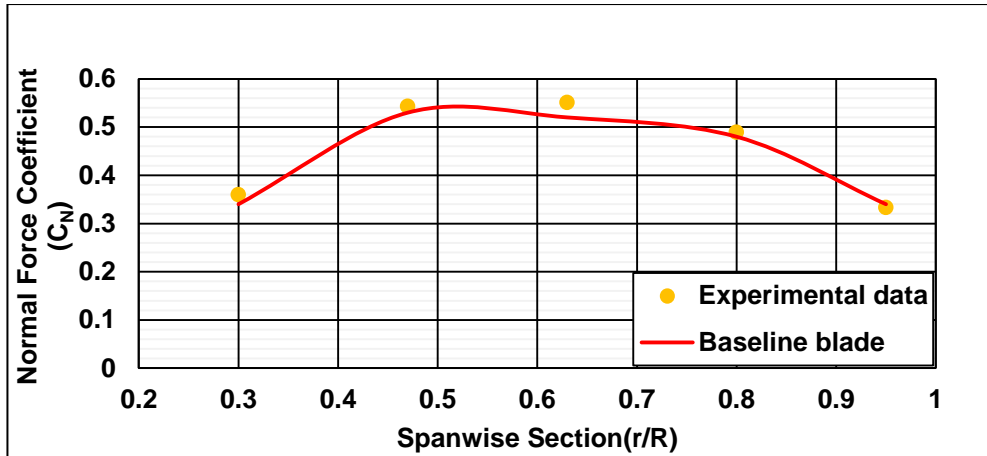


Figure 4-28 Comparison of measured and computed normal force coefficients at 5m/s.

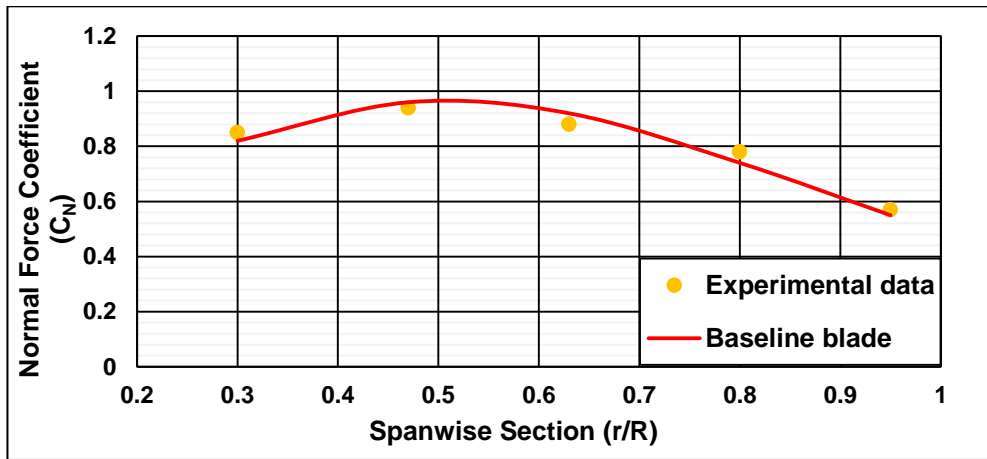


Figure 4-29 Comparison of measured and computed normal force coefficients at 7m/s.

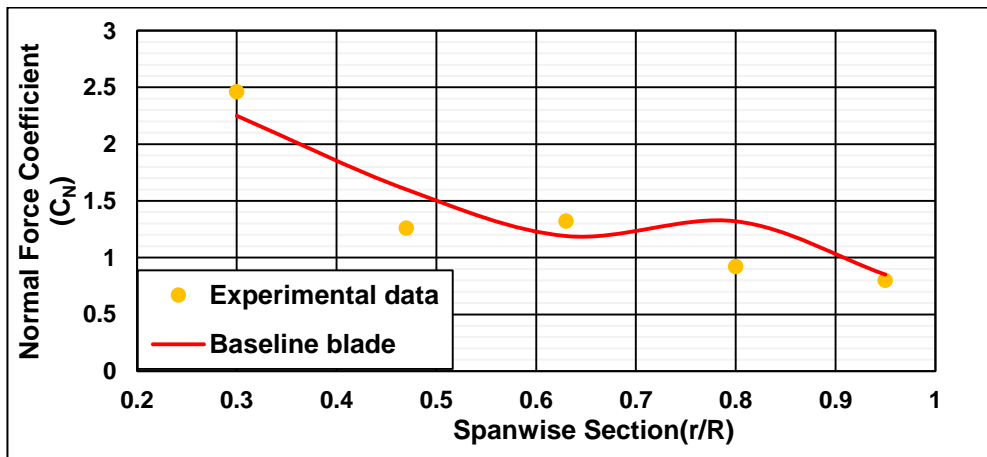


Figure 4-30 Comparison of measured and computed normal force coefficients at 15m/s.

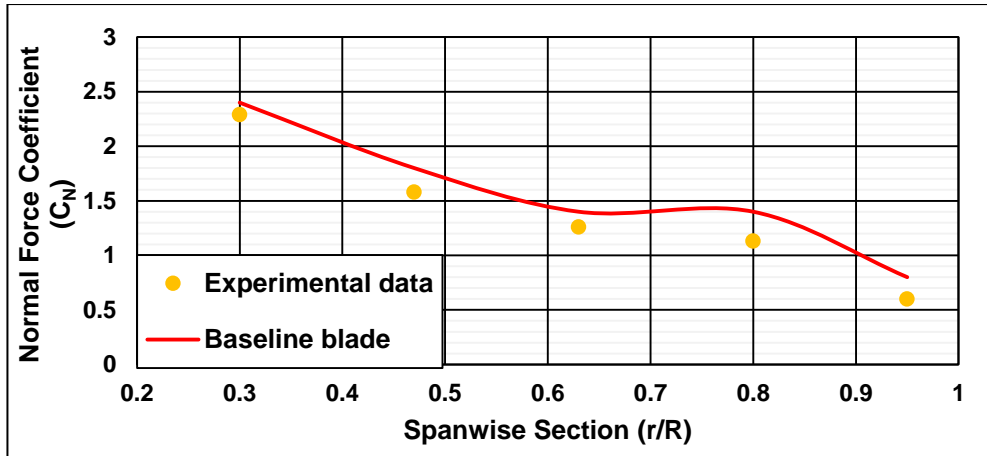


Figure 4-31 Comparison of measured and computed normal force coefficients at 25m/s.

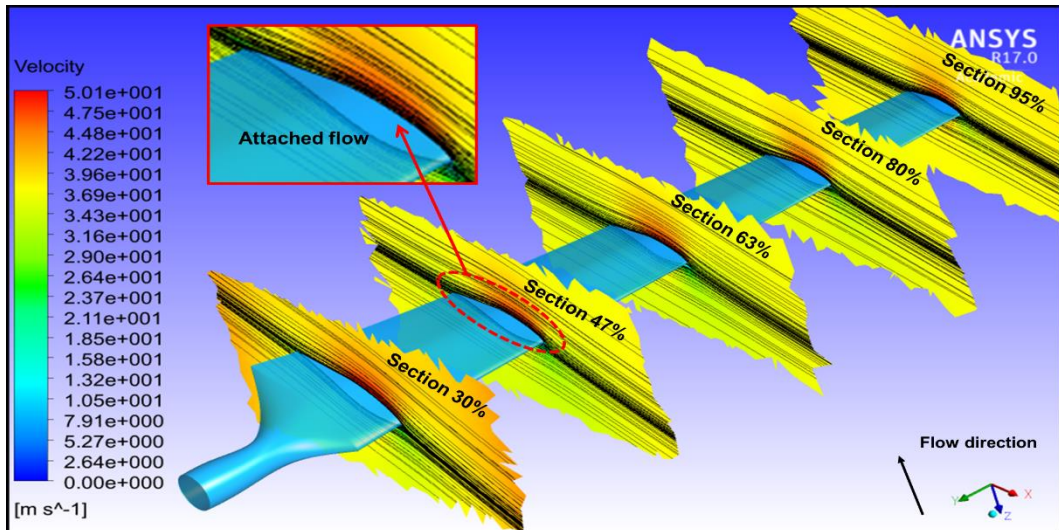


Figure 4-32 Velocity contours and streamlines at 5m/s.

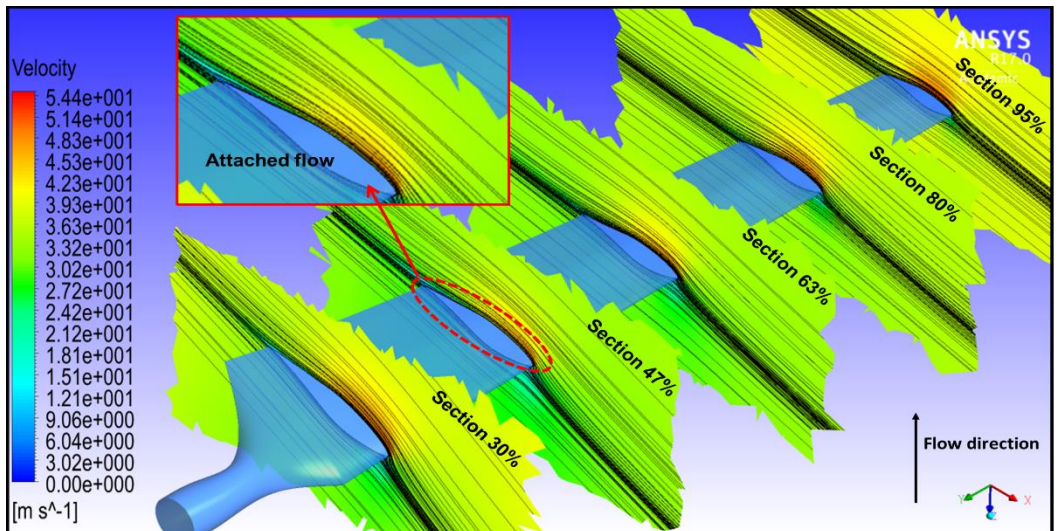


Figure 4-33 Velocity contours and streamlines at 7m/s.

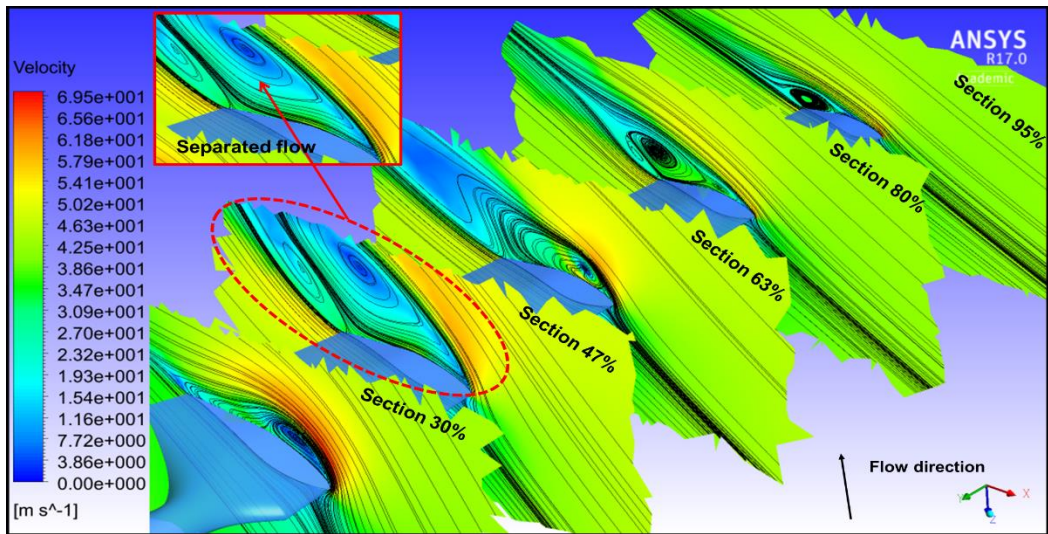


Figure 4-34 Velocity contours and streamlines at 15m/s.

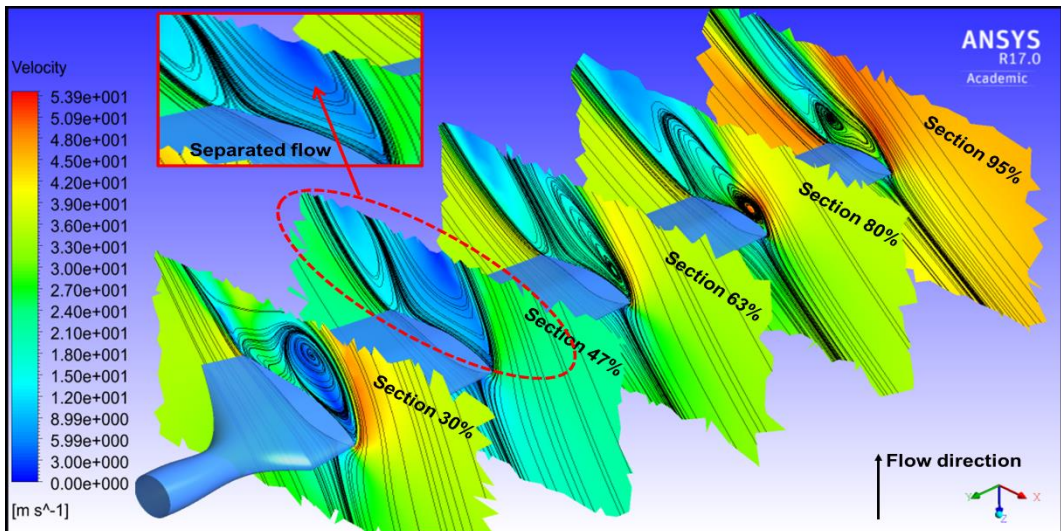


Figure 4-35 Velocity contours and streamlines at 25m/s.

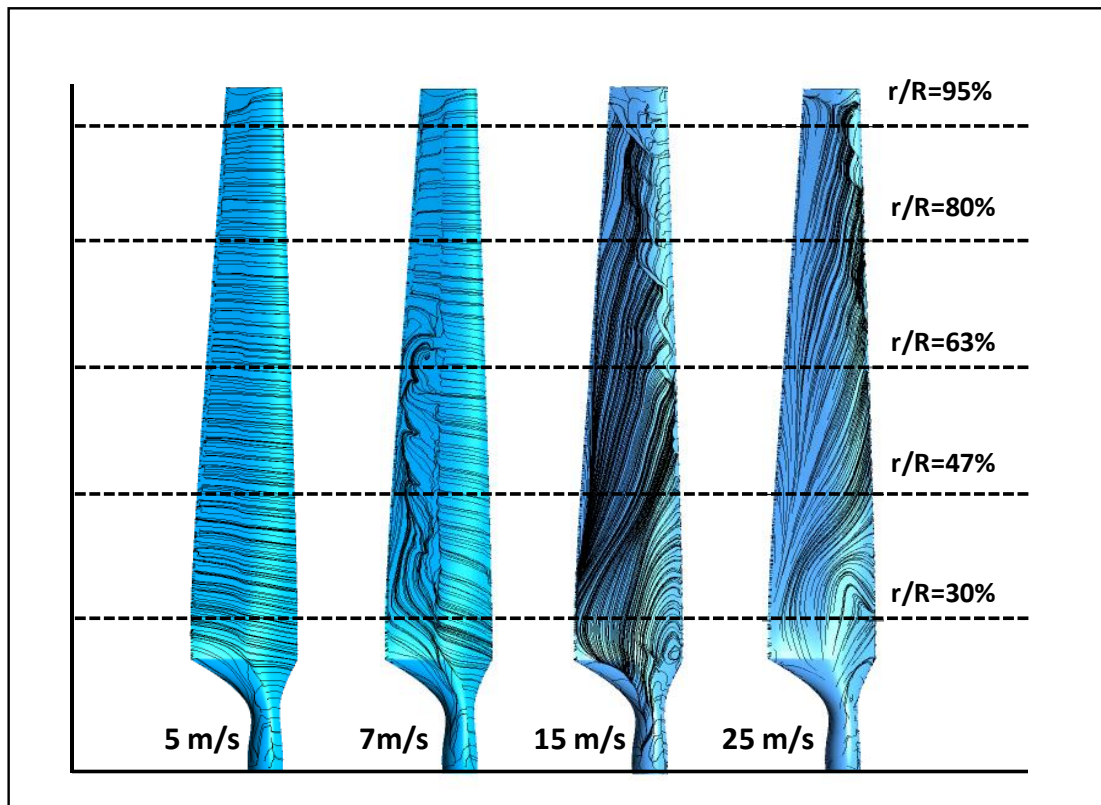


Figure 4-36 Surface streamlines along the suction side of the baseline blade.

4.14 Conclusions

In this chapter, the 3D geometry of the NREL phase VI rotor has been introduced as a baseline case to assess the ability of the CFD models to match the experimental data. The validation of the numerical results was done by comparing wind tunnel measurements in terms of numerical torque, pressure coefficients distributions and normal force coefficients with those obtained from CFD calculations.

The mesh refinement for the grid independence study was focused on the rotating frame, as it includes blades. Three different levels of the element size were utilised and the solution convergence was obtained by monitoring the residual history, moment coefficient and lift coefficient over a cycle of 2000 iterations.

The numerical results were obtained using two turbulence models, namely, the Spalart-Allmaras and SST $k-\omega$ models. The comparisons of the numerical torque with wind tunnel data demonstrate the superiority of the SST $k-\omega$ model. This superiority was particularly observed at high wind speeds for matching the experimental data, where the Spalart-Allmaras over-predicted measured torque values.

However, the SST $k-\omega$ model shows a discrepancy in accurately predicting the pressure coefficient distributions and normal force coefficients at higher wind speeds of 10m/s. The discrepancy occurred due to the stalled flow that is implemented in the NREL phase VI to limit the peak power at high wind speeds. More precisely, at the wind speed of 15m/s, the discrepancy was observed at the suction side for 30% and 63% sections in spanwise direction of the blade. Similarly, the model under-predicted the pressure coefficient distributions at 30%, 47%, 80% and 95% sections of the spanwise direction of the blade at the wind speed of 25m/s.

Chapter 5 : The Effect of Winglet Planform on the Performance of Wind Turbine

5.1 Introduction

The purpose of this chapter is to present the numerical results that were obtained using two different winglet planforms: the rectangular and elliptical winglets. Four winglet configurations were created using the S809 and PSU 94-097 airfoils, and subsequently examined to investigate the NREL phase VI performance. Among the winglet parameters, the influences of the winglet height and cant angle were investigated, because they have the potential to improve winglet performance. The assessments of the four winglet configurations are presented in terms of their ability to increase/decrease the NREL phase VI power.

5.2 Winglet function

The function of a winglet is to improve wind turbine performance by reducing total drag forces, i.e. the profile drag and induced drag, which are generated along the wind turbine blades. The profile drag is defined as the energy that is transferred from the rotating blade to the moving air, due to the viscosity of the moving air, as well the pressure drag. The profile drag depends on the airfoil shape, angle of attack and the blade surface area (the wetted area), whereas, the induced drag is the drag that is created due when generating the spanwise flow along the wind turbine blades (Maughmer, 2002).

Unlike the infinite blade, the spanwise flow is produced because of the pressure difference between the two blade sides. Thereby, the flow moves from the high-pressure side of a blade to meet at the blade tip and trailing edge with the opposite direction flow, which moves from the low-pressure side. Consequently, they give rise to three swirling motions, known as the blade tip, trailing edge and root vortices. In general, the generation of vortices requires energy that is transferred from blade to the air; this wasted energy is represented by the induced drag(Maughmer, 2002).

According to the aforementioned discussion, a winglet provides a flow field that weakens the spanwise flow, and then reduces the amount of induced drag. In this way, a winglet diffuses the wingtip vortices from a blade tip towards a winglet tip by carrying the aerodynamic loading. Hence, an efficient winglet should be designed with the least wetted area in order to avoid the effect of the profile drag, which has a significant impact on winglet

performance. In this regard, an efficient winglet design requires the least wetted area.

5.3 Winglet configurations

In this study, the tip of the baseline blade was modified by attaching four winglet configurations, as shown in Figure 5-1. To study the effect of winglet height (h), the winglet configurations were obtained by extending the winglet root airfoil by 5cm, 10cm and 15cm. All configurations were tilted by two cant angles, which are 90° and 45° in order to study the influence of the cant angle.

The configurations include two winglet planforms (rectangular and elliptical), with a view to investigate the influence of the winglet planform on the aerodynamic characteristics of the blade. For each extension, the rectangular planform is obtained by equalling the root chord of the winglet ($C1$) and the tip chord ($C2$). In contrast, the elliptical winglet was created by reducing the tip chord ($C2$) by 75% when compared to $C1$, as shown in Figure 5-2. In addition, the S809 and PSU 94-097 airfoils are chosen to create the winglet profiles in order to study the effect of the airfoil on the winglet performance. The four winglet configurations' parameters are listed in Table 5-1.

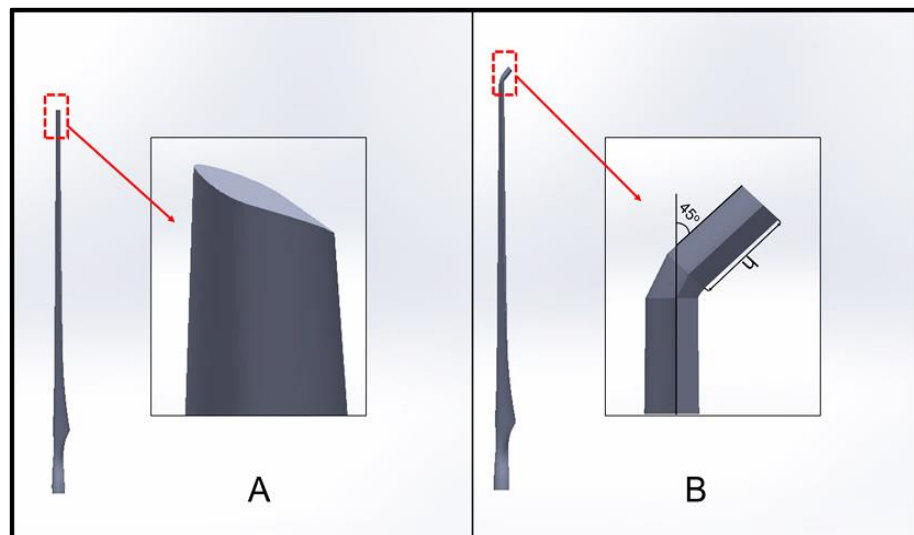


Figure 5-1 View of: A- Baseline blade, B- Baseline blade with winglet.

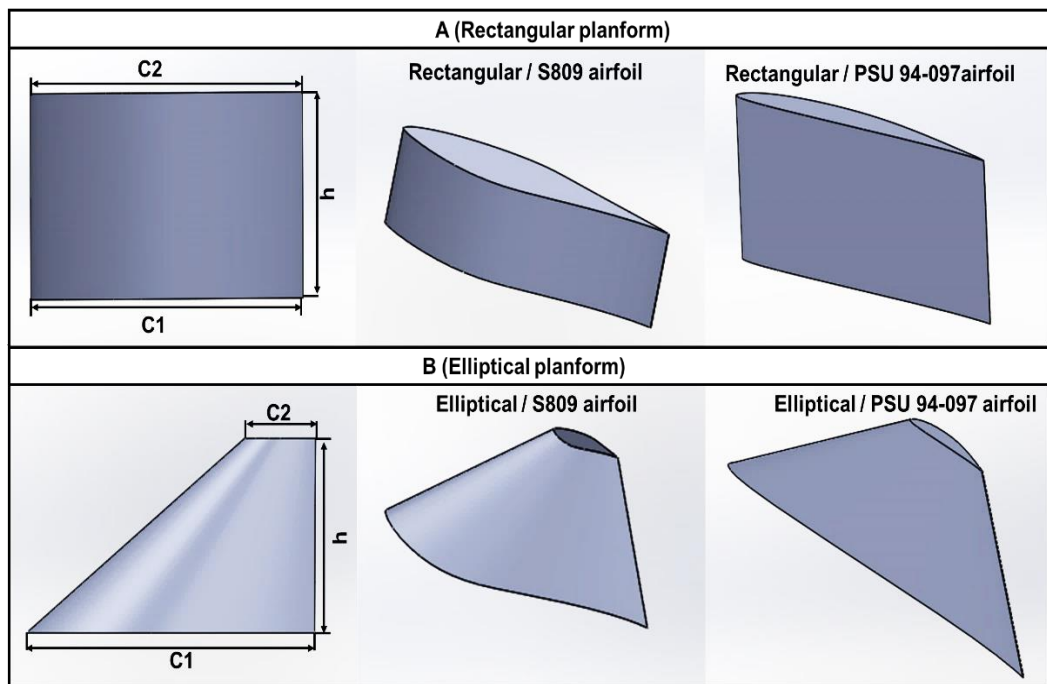


Figure 5-2 View of: A- Rectangular planform, B- Elliptical planform.

Table 5-1 Winglet configurations parameters.

Configuration No.	Winglet Planform	Winglet airfoil
1	Rectangular	S809
2	Rectangular	PSU 94-097
3	Elliptical	S809
4	Elliptical	PSU 94-097

The S809 airfoil as shown in Figure 5-3A was designed theoretically and was verified experimentally for the NREL by the Airfoils and Incorporated State College (Tangler and Somers, 1995). The S809 airfoil was tested at the Reynolds numbers of 1.0×10^6 to 3.0×10^6 (see Figure A-1 in Appendix-A). The fluid flow characteristics, such as the aerodynamic coefficients, transitional flow and stall regime on the upper and lower of the S809 airfoil surfaces, were investigated to fulfil the requirements of a HAWT.

In contrast, the PSU 94-097 airfoil, as shown in Figure 5-3B, was designed experimentally at Reynolds numbers of 1.0×10^5 to 1.0×10^6 as a winglet airfoil, with a view to improve the performance of sailplanes (see Figure A-2 in Appendix-A) (Maughmer, 2002). In addition, the requirements that satisfy

winglet airfoil performance in a wide range of low speed applications were considered for a HAWT (Gertz, 2011).

Therefore, the S809 airfoil was chosen to construct a winglet profile due to it has similar aerodynamic characteristics of the baseline tip airfoil such lift, drag and moment coefficients. In contrast, the function of winglet is diffusing of the wingtip vortices, which is different than the baseline blade. Consequently, choosing a wind turbine airfoil to create the winglet profile might be affecting its performance. For this reason, the PSU 94-097 airfoil was chosen as it is used as a winglet airfoil for low-speed applications including a wind turbine.

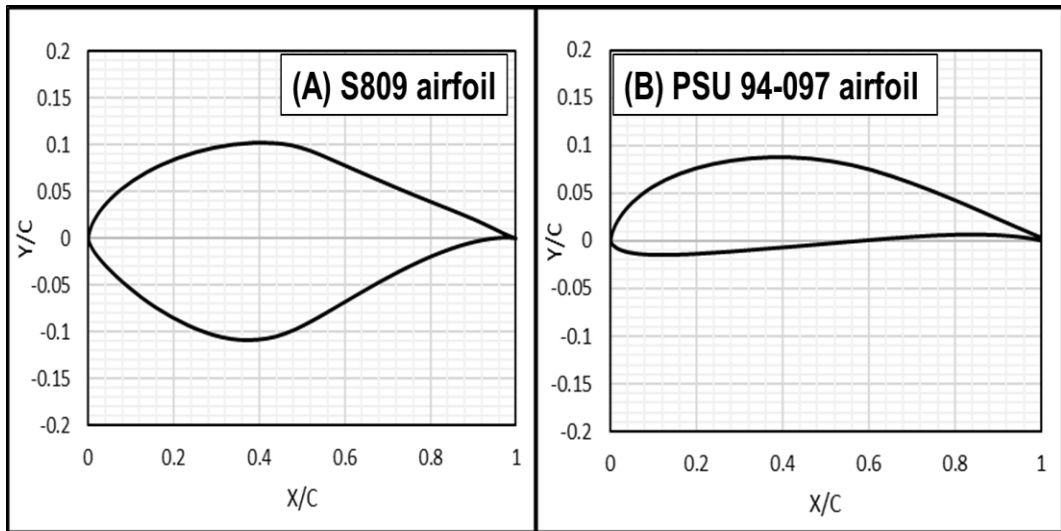


Figure 5-3 Illustration of: A-Schematic of the S809 airfoil, B- Schematic of the PSU 94-097 airfoil.

5.4 Winglet numerical results

The calculations were carried out using a similar numerical method followed for validating the baseline case. Thereby, the performances of all winglet cases are predicted in steady-state conditions and the governing flow equations are solved by employing the SST $k-\omega$ turbulence model at wind speeds of 5, 7, 10, 15, 20 and 25m/s. Both the measured and computed power of the baseline case are calculated using the following equation:

$$P = T x \omega \quad (5.1)$$

A comparison of the measured and computed power is shown in the following graph.

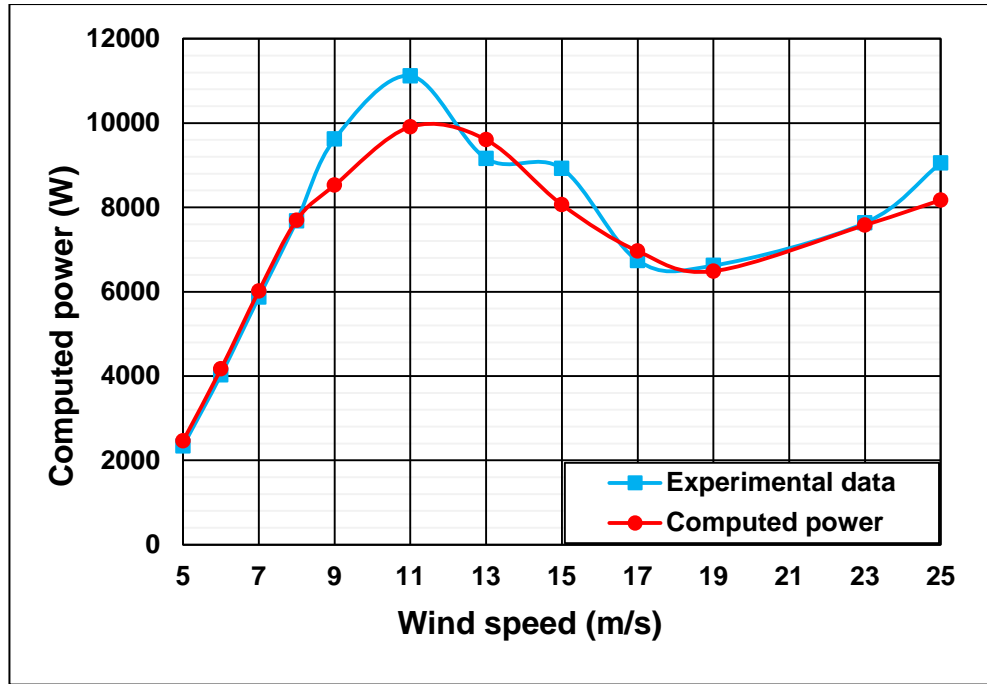


Figure 5-4 Comparison of measured and predicted power.

The following tables show the percentages of increases/decreases in power and thrust forces that are obtained by attaching the four winglet configurations. The four winglet configurations are examined at cant angles of 90° and 45°. Additionally, the computations include the influence of the varying of winglet height: 5cm, 10cm and 15cm. Furthermore, all configuration performances are tested at the pre-stall and post-stall region.

Table 5-2 Percentage of increase/decrease in power and thrust force for the configuration 1 (Rectangular/S809) at a cant angle of 90°.

Wind Speed (m/s)	Baseline Power (W)	h=5 cm		h=10 cm		h=15 cm	
		Power %	Thrust %	Power %	Thrust %	Power %	Thrust %
5	2463.77	3.5	5.3	5.0	7.8	5.4	8.7
7	6017.44	3.8	4.7	6.3	7.1	6.7	7.7
10	9402.48	5.3	3.6	9.5	6.5	7.1	5.9
15	8063.57	-0.34	2.7	7.9	3.3	-2.0	1.4
20	6705.38	-5.5	-0.2	-5.1	-1.6	-6.0	-1.6
25	8172.60	-0.88	0.5	-3.3	-1.4	-4.3	-1.8

Table 5-3 Percentage of increase/decrease in power and thrust force for the configuration 1 (Rectangular/S809) at a cant angle of 45°.

Wind speed (m/s)	Baseline Power (W)	h=5 cm		h=10 cm		h=15 cm	
		Power %	Thrust %	Power %	Thrust %	Power %	Thrust %
5	2463.77	5.1	5.4	7.0	8.0	9.1	10.3
7	6017.44	5.1	5.0	6.8	7.0	9.4	9.5
10	9402.48	5.4	3.7	7.4	5.6	9.8	6.9
15	8063.57	2.0	4.6	0.29	5.5	6.1	5.9
20	6705.38	-2.6	0.5	-3.5	0.9	1.7	3.1
25	8172.60	0.5	1.0	-3.9	0.3	9.1	3.3

Table 5-4 Percentage of increase/decrease in power and thrust force for the configuration 2 (Rectangular/PSU 94-097) at a cant angle of 90°.

Wind speed (m/s)	Baseline Power (W)	h=5 cm		h=10 cm		h=15 cm	
		Power %	Thrust %	Power %	Thrust %	Power %	Thrust %
5	2463.77	-2.5	1.7	-1.9	3.8	0.3	6.1
7	6017.44	-2.6	0.6	-1.3	2.3	-3.2	1.2
10	9402.48	-4.6	-0.9	-4.1	0.2	-4.3	0.6
15	8063.57	-4.2	1.9	-9.1	0.9	-9.7	1.8
20	6705.38	-4.0	-0.6	-6.4	-2.3	-7.4	-1.4
25	8172.60	-2.0	-0.7	-1.6	-1.5	-7.9	-3.4

Table 5-5 Percentage of increase/decrease in power and thrust force for the configuration 2 (Rectangular/PSU 94-097) at a cant angle of 45°.

Wind speed (m/s)	Baseline Power (W)	h=5 cm		h=10 cm		h=15 cm	
		Power %	Thrust %	Power %	Thrust %	Power %	Thrust %
5	2463.77	0.43	2.4	2.7	6.2	5.6	9.6
7	6017.44	-1.4	0.6	0.9	3.5	3.6	6.5
10	9402.48	-4.9	-0.6	-3.7	1.2	0.55	3.9
15	8063.57	-1.6	5.0	-4.5	2.5	-7.2	4.9
20	6705.38	-0.5	0.6	-3.0	1.1	4.2	2.4
25	8172.60	-3.8	-1.0	-1.0	1.2	5.8	1.8

Table 5-6 Percentage of increase/decrease in power and thrust force for the configuration 3 (Elliptical/S809) at a cant angle of 90°.

Wind speed (m/s)	Baseline Power (W)	h=5 cm		h=10 cm		h=15 cm	
		Power %	Thrust %	Power %	Thrust %	Power %	Thrust %
5	2463.77	1.6	2.2	2.6	5.9	3.6	4.9
7	6017.44	-0.1	0.8	0.6	2.0	1.5	2.8
10	9402.48	-3.7	-0.9	-3.0	-0.2	-2.0	0.3
15	8063.57	-3.8	4.8	-6.0	1.5	-10.4	-0.1
20	6705.38	3.7	2.2	-3.2	0.6	8.2	-0.04
25	8172.60	-0.05	0.3	-2.1	-0.7	2.2	-0.008

Table 5-7 Percentage of increase/decrease in power and thrust force for the configuration 3 (Elliptical/S809) at a cant angle of 45°.

Wind speed (m/s)	Baseline Power (W)	h=5 cm		h=10 cm		h=15 cm	
		Power %	Thrust %	Power %	Thrust %	Power %	Thrust %
5	2463.77	0.8	1.1	3.7	3.7	6.2	6.0
7	6017.44	-0.9	-0.04	1.6	2.2	3.4	3.9
10	9402.48	-4.8	-1.7	-2.2	0.1	0.09	1.4
15	8063.57	-3.5	-1.6	-5.2	2.4	-11.1	1.6
20	6705.38	-3.3	0.8	1.19	0.1	-1.11	0.7
25	8172.60	-3.5	0.2	0.55	1.0	-1.85	-0.4

Table 5-8 Percentage of increase/decrease in power and thrust force for the configuration 4 (Elliptical/ PSU 94-097) at a cant angle of 90°.

Wind speed (m/s)	Baseline Power (W)	h=5 cm		h=10 cm		h=15 cm	
		Power %	Thrust %	Power %	Thrust %	Power %	Thrust %
5	2463.77	0.7	2.2	2.0	4.2	3.3	6.0
7	6017.44	-1.2	0.5	0.06	1.9	1.3	3.2
10	9402.48	-5.3	-1.4	-4.2	-0.3	-2.5	0.58
15	8063.57	-8.2	1.6	-13.4	0.6	-8.4	0.50
20	6705.38	-8.0	-1.1	-5.7	-0.7	2.8	-1.0
25	8172.60	-4.4	-1.6	-2.6	-1.0	-3.0	-1.2

Table 5-9 Percentage of increase/decrease in power and thrust force for the configuration 4 (Elliptical/ PSU 94-097) at a cant angle of 45°.

Wind speed (m/s)	Baseline Power (W)	h=5 cm		h=10 cm		h=15 cm	
		Power %	Thrust %	Power %	Thrust %	Power %	Thrust %
5	2463.77	1.0	2.0	3.7	4.9	6.0	7.7
7	6017.44	-1.1	0.4	1.5	2.9	3.0	4.7
10	9402.48	-4.5	-0.9	-2.6	0.6	-1.7	1.7
15	8063.57	-9.1	1.0	-8.5	2.1	-9.8	2.7
20	6705.38	-5.6	-1.0	4.7	0.9	-4.8	0.2
25	8172.60	4.0	1.2	-5.6	-1.0	-1.9	0.04

Based on the tables above, the four winglet configurations show different performances. The configurations' performances vary depending on the wind speeds, cant angle, winglet height, winglet airfoil and, the winglet planform. Further, each factor affects winglet performance based on his different role, which will be discussed in detail in this section. All configurations were tilted towards the suction side of the baseline blade, since they result in better performance than the other sides (Elfarra *et al.*, 2015; Johansen and Sørensen, 2007).

The configurations' performances are assessed by comparing the percentages of the power increase or decrease in the NREL phase VI power. This is expanded on below.

5.4.1 Assessment of configuration 1

A rectangular planform was chosen to generate configuration 1, using the S809 airfoil. The performance of configuration 1 was examined by varying the cant angle, winglet height and wind speed, as shown in Tables 5-2 and 5-3.

At a cant angle of 90° and winglet height of 5cm, configuration 1 shows a slight percentage in power increase by the average value, which equals 4.2%, as shown in Table 5-2. This improvement in output power was obtained at the range of wind speeds between 5m/s and 10m/s, where the flow is mostly attached, as discussed in section 4.12. More improvements in the percentage of the power increase are obtained due to increases in the configuration height. Accordingly, the percentage of power increase was

raised by the average of 6.9% and 6.4% in the case of 10cm and 15cm, respectively, as shown in Figure 5-5.

However, at a cant angle of 90° , the performance of configuration 1 decreased at higher wind speeds of 10m/s, due to the stalled flow as shown in the streamlines plot in Figure 5-6. Further, the penalty of the profile drag increases with increasing wind speed (see Equation 2.60). Thereby, at a cant angle of 90° , the greatest gain in configuration 1 is obtained at wind speeds of 5m/s to 10m/s, since the flow is mostly attached.

In contrast, at a cant angle of 45° , the performance of configuration 1 clearly improves at moderate and high wind speeds, where the stalled flow exists, as shown in Table 5-3.

At low wind speeds (5-10m/s), configuration 1 increases the percentage of power increase by the average of 5.2%, 7.0% and 9.4%, corresponding to the heights 5cm, 10cm and 15cm, respectively. However, there is a reduction in the performance of configuration 1 at a range of speeds from 15m/s to 25m/s, particularly, in the case of 5cm and 10cm. This reduction is overcome by increasing the height of configuration 1 to 15cm as shown in Figure 5-7.

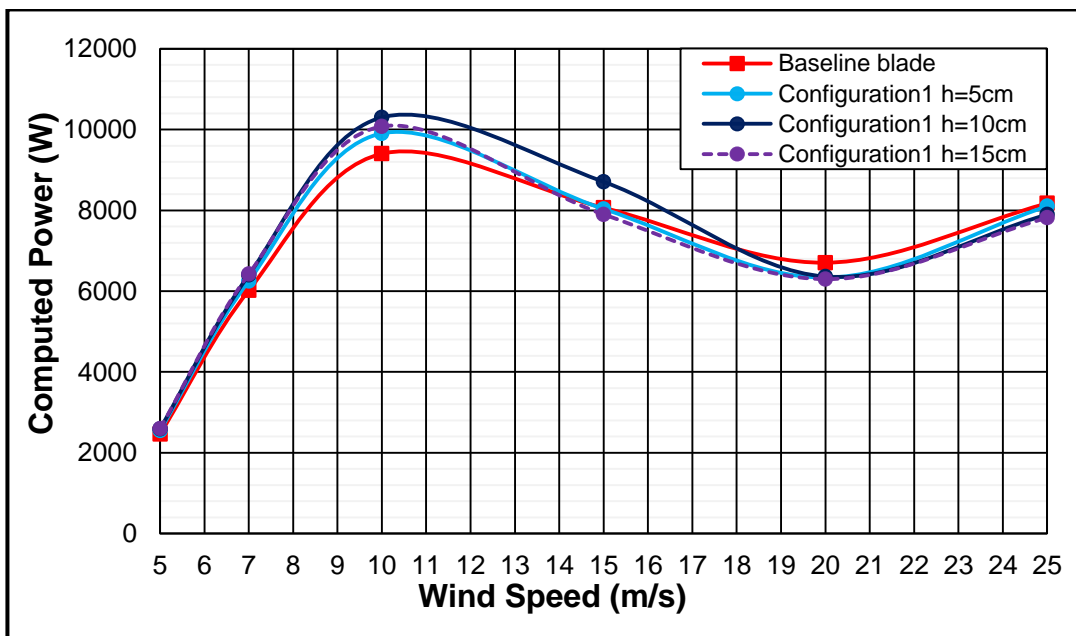


Figure 5-5 Comparison of calculated power using configuration 1 (cant angle of 90°).

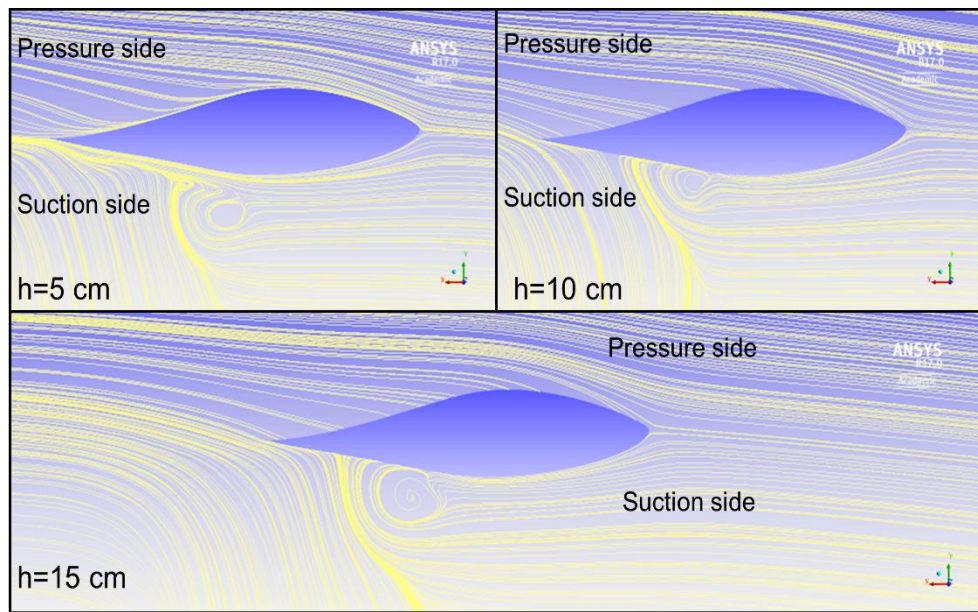


Figure 5-6 Streamlines around configuration 1 at a wind speed of 15m/s.

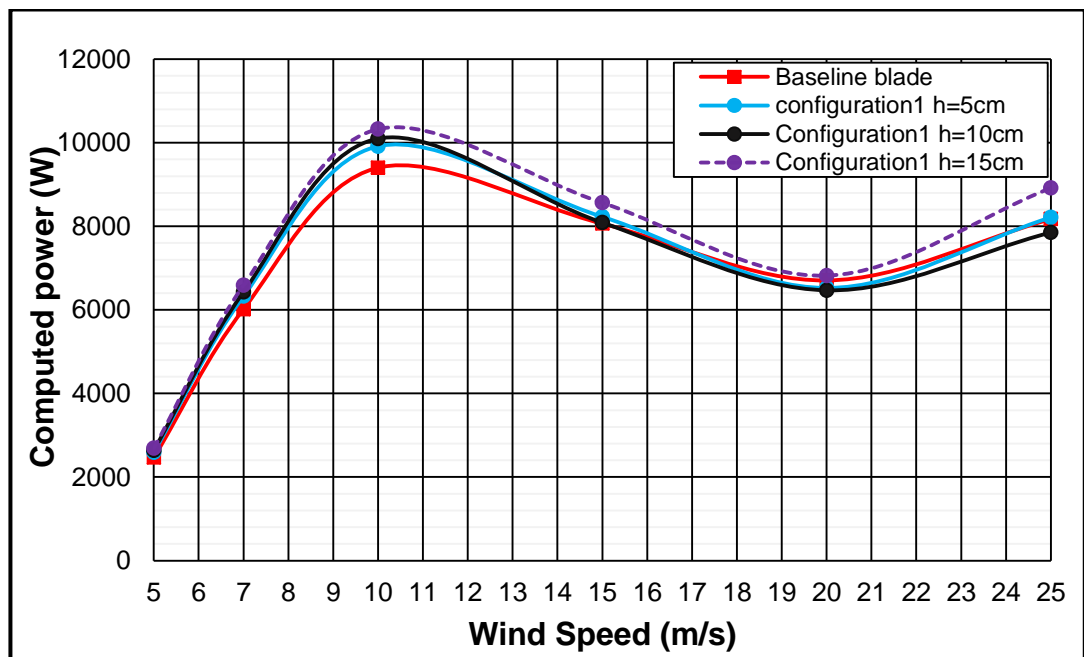


Figure 5-7 Comparison of calculated power using configuration 1 (cant angle of 45°).

Two winglet parameters (cant angle and winglet height) have been examined, with a view to study configuration 1. At a cant angle of 90°, the configuration demonstrates good performance where the flow is almost attached. However, this performance deteriorates under the stalled flow condition and an increase in the configuration height results in a reduction in the NREL phase VI performance.

The advantage of the cant angle of 45° enables the baseline blade to increase the projection area of a wind turbine. Thereby, there exists more available kinetic energy in the moving air that could be extracted by a turbine rotor, according to equations (2.2) and (2.5). Consequentially, at a cant angle of 45° and height equalling 15cm, configuration 1 achieves the greatest percentage in power increase, despite whether the flow is attached or stalled.

Figures 5-8 to 5-10 show a comparison between the pressure contours of the baseline blade and the cases of 5cm, 10cm and 15cm at speeds of 7m/s and cant angle of 45° . Figure 5-8 presents the improvements that occurred in the pressure suction (more reduction) near the blade top, particularly, on the suction side where the configurations are tilted by 45° . These improvements increased as the configuration height increased, as can be clearly observed at the sections of 95% and 98% on the span of the blade, as shown in Figures 5-9 and 5-10 respectively.

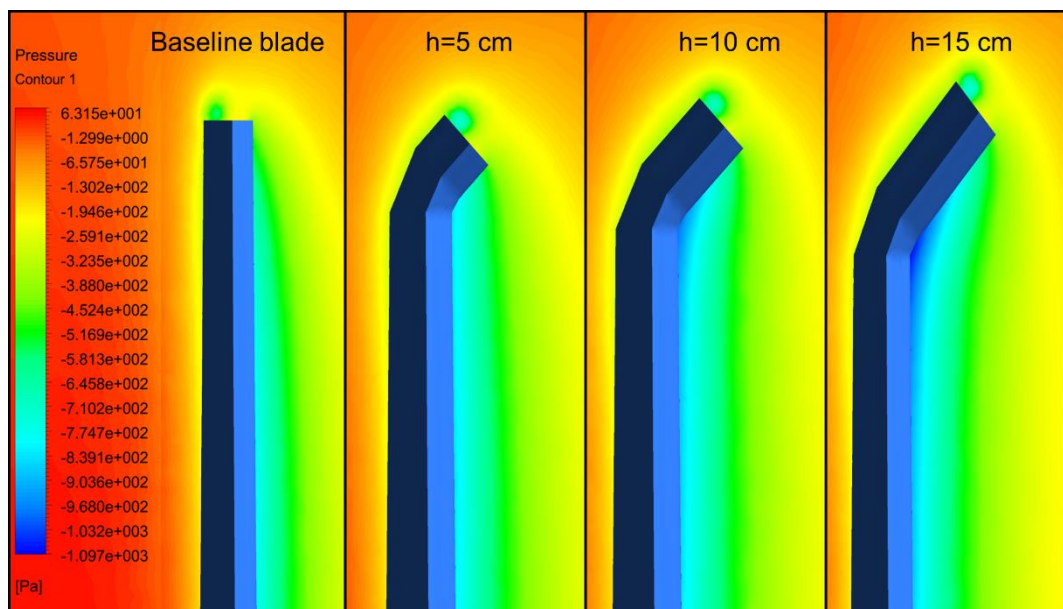


Figure 5-8 Comparison of pressure contours between baseline blade and configuration 1.

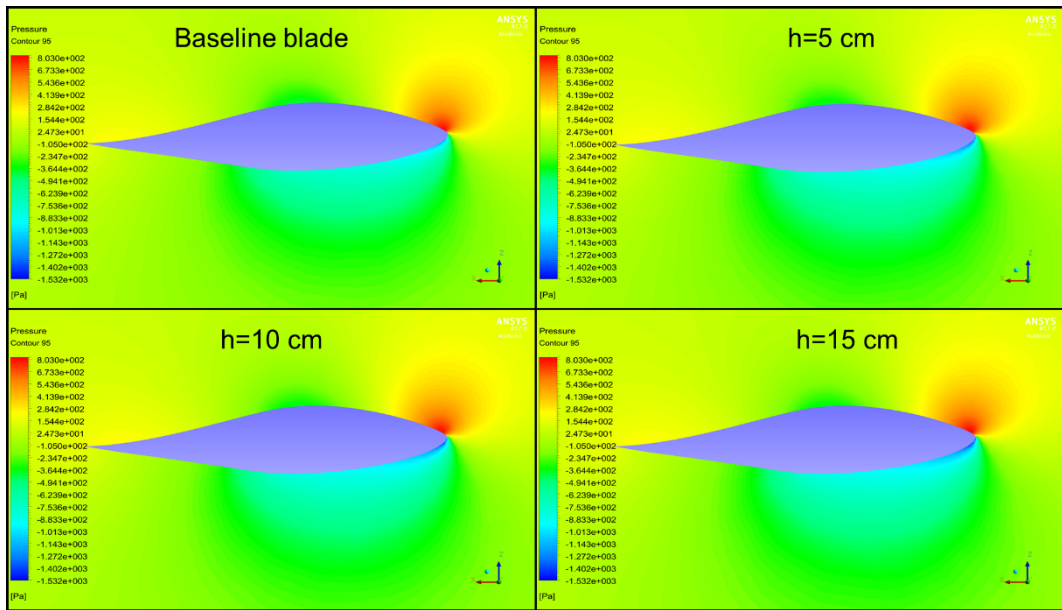


Figure 5-9 Comparison of pressure contours between baseline blade and configuration 1, at the spanwise section of 95%.

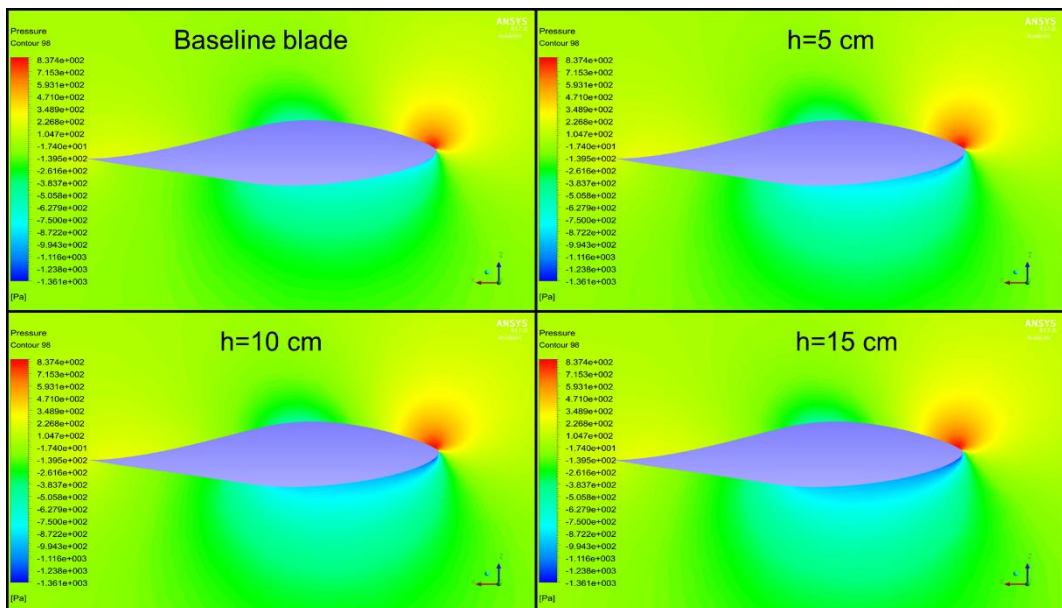


Figure 5-10 Comparison of pressure contours between baseline blade and configuration 1, at the spanwise section of 98%.

5.4.2 Assessment of configuration 2

Configuration 2 was examined under the same conditions of configuration 1, except using the PSU 94-097 airfoil to generate the winglet profile. Tables 5-4 and 5-5 show the percentages of the power increase/decrease that were obtained by attaching this configuration at cant angles of 90° and 45° , respectively.

At a cant angle of 90° , the poor performance of this configuration is clearly observed using the PSU 94-097 airfoil, when compared to the performance of configuration 1 for all wind speeds. Unlike configuration 1, an increase in the height of configuration 2 from 5cm to 15cm resulted in greater deterioration in the baseline power, as the penalty of the profile drag increases.

In contrast, at a cant angle of 45° , the performance is slightly improved, particularly in the case of 15cm. This improvement occurs due to employing the feature of the cant angle of 45° , which enables configuration 2 to perform as a winglet function that reduces the impact of the wingtip vortices. Additionally, more available kinetic energy could be extracted from the moving air due to increasing the projection area of the turbine rotor.

In short, configuration 2 shows inefficient performance results a reduction in wind turbine power when compared to configuration 1. Figure 5-11 shows the comparison of power increases that have been obtained due to attaching configuration 1 and 2, which were tilted by a cant angle of 45° and height of 15cm. This figure depicts a reduction in the winglet performance that resulted from employing the PSU 94-097 airfoil. This reduction was obtained due to changing the aerodynamic characteristics of the selected airfoil. Thereby, the effect of the aerodynamic winglet airfoil should be considered to improve its performance. However, the aerodynamic effect of the winglet airfoil will be discussed in the next chapter.

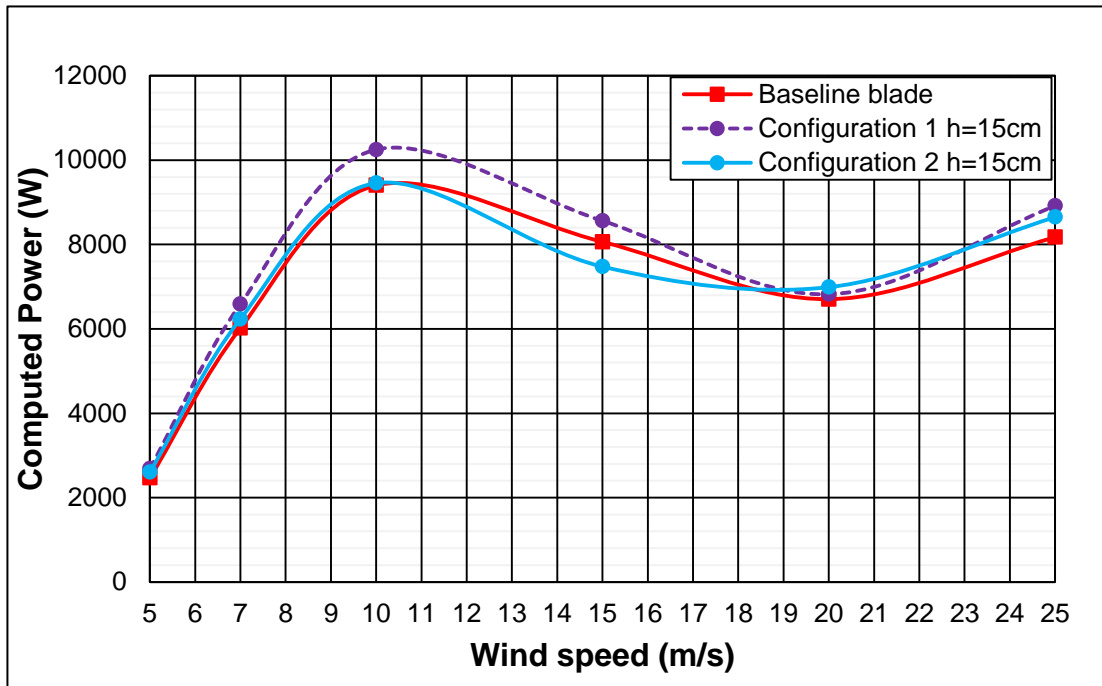


Figure 5-11 Comparison of calculated power between configuration1 and 2, at a cant angle of 45° and height of 15cm.

5.4.3 Assessment of configuration 3

The elliptical shape was chosen to create winglet configuration 3 using the S809 airfoil. The numerical performance of configuration 3 at the cant angles of 90° and 45° are listed in Tables 5-6 and 5-7.

At a cant angle of 90°, configuration 3 shows slight improvements in the percentage of power increase at low wind speeds (5m/s and 7m/s) for the cases 10cm and 15cm. In contrast, tilting the same cases by cant angle of 45°, results in further improvements in power increase. However, the wind turbine power is deteriorated at the wind speeds (over 10m/s) for configurations 3 as the stalled flow exists and the increase in profile drag.

Figure 5-12 shows a comparison between the performance of configuration 1 and 3 at a cant angle of 45° and height of 15cm. Unlike configuration 1, configuration 3 results in a slight improvement in output power at low wind speeds. Further, the wind turbine power is significantly reduced at the wind speeds (over 10m/s) for configuration 3. Hence, it could be concluded that the winglet planform plays a significant role in increasing or decreasing the wind turbine performance, since both of configurations (1 and 3) have the same winglet parameters, such the cant angle, airfoil and winglet height.

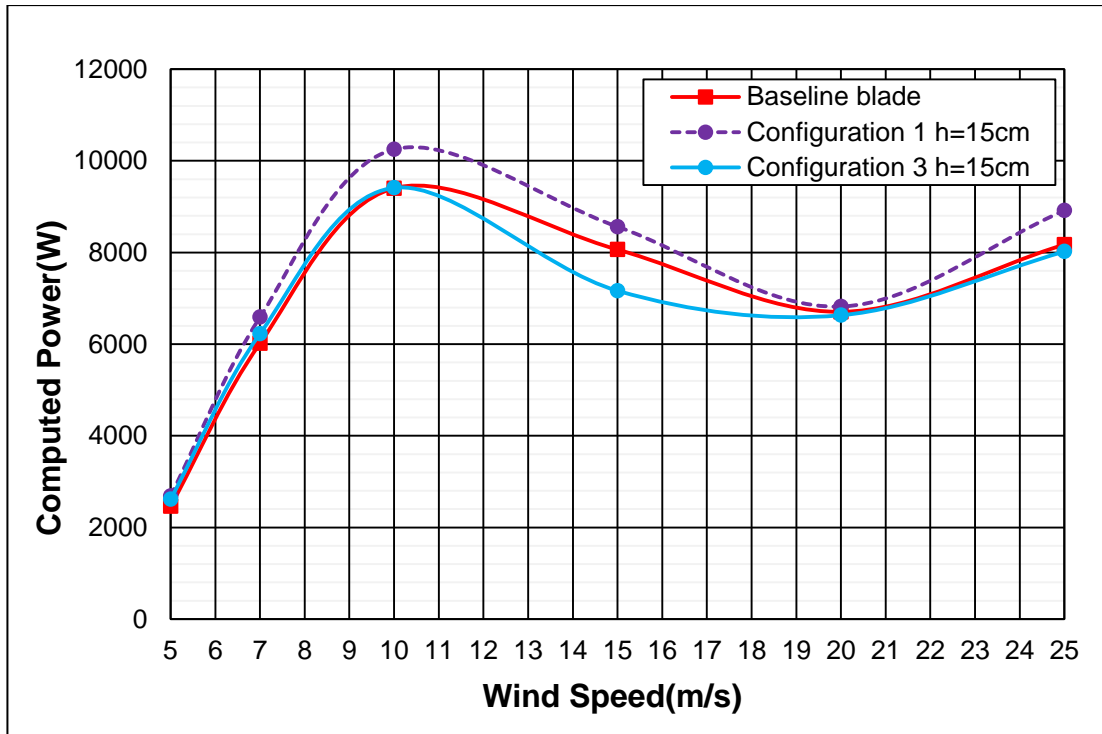


Figure 5-12 Comparison of calculated power between configuration 1 and configuration 3.

At a wind speed of 7m/s and ($h=15\text{cm}$, cant angle= 45°), Figure 5-13 shows the different role of configuration 1 and 3 in the improvement of pressure distribution towards the span of the blade. Unlike configuration 3, further improvement is obtained in the pressure distribution (pressure reduction at the suction side) near the blade top, due to attaching configuration 1. This improvement is clearly observed at the span section of 95% and 98% of the baseline blade, as shown in Figures 5-14 and 5-15, respectively.

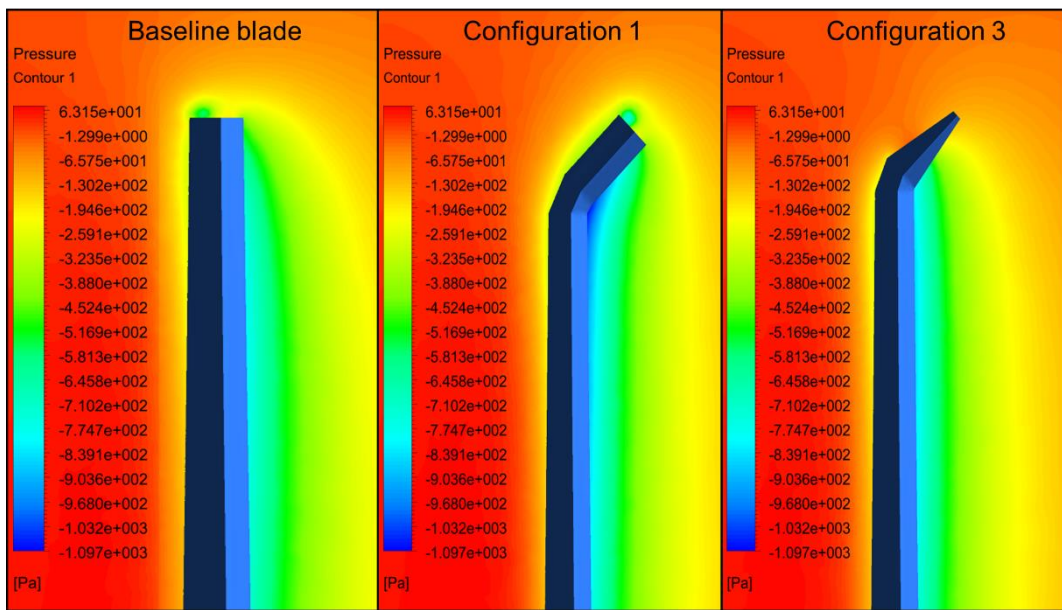


Figure 5-13 Comparison of pressure contours between baseline blade and the configurations (1, 3).

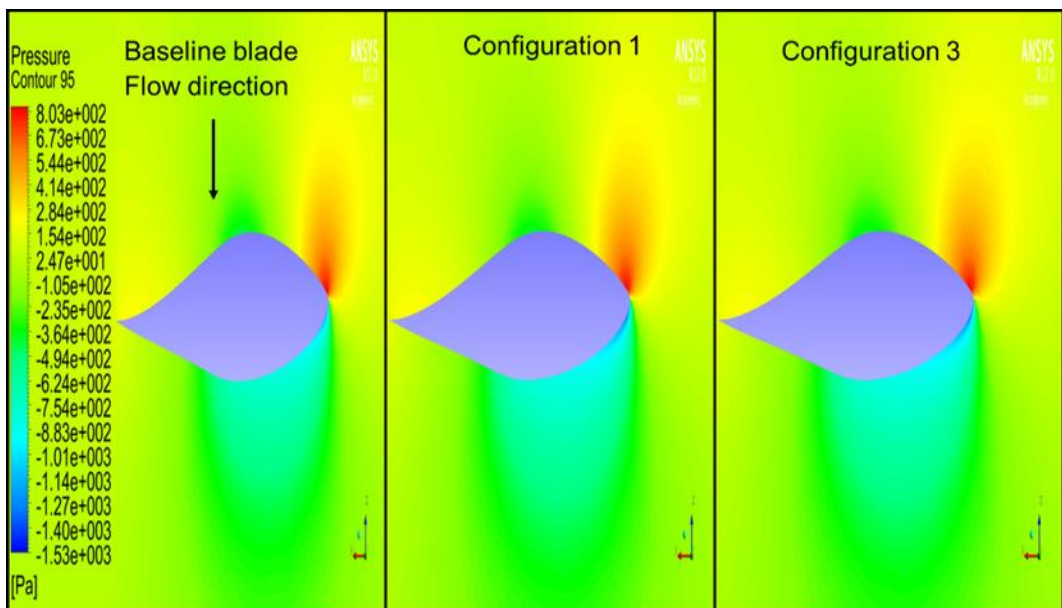


Figure 5-14 Comparison of pressure contours between baseline blade and the configurations (1, 3).

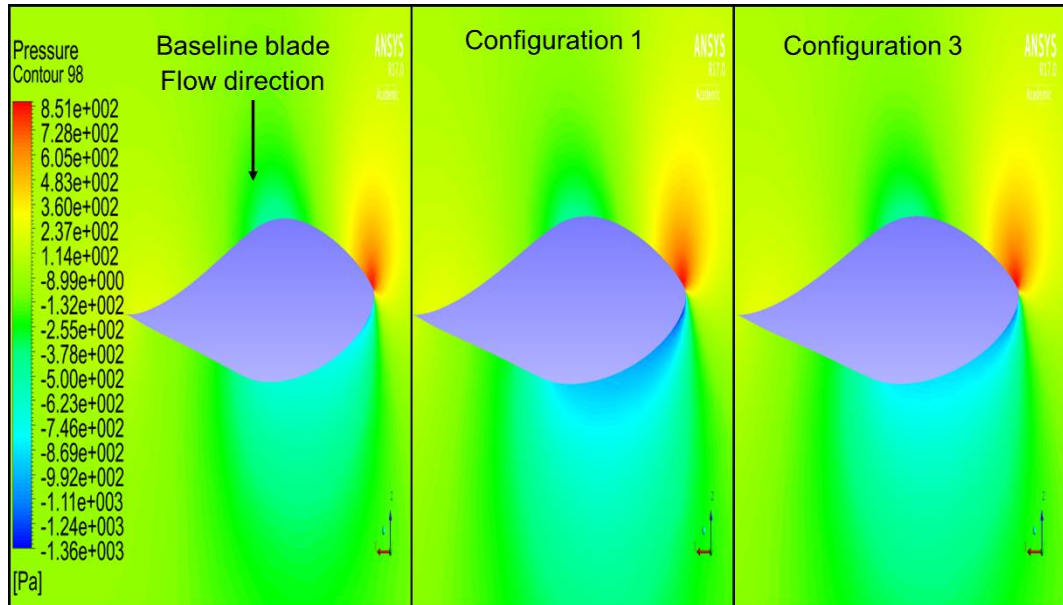


Figure 5-15 comparison of pressure contours between baseline blade and the configurations (1, 3).

5.4.4 Assessment of configuration 4

The elliptical planform was implemented by creating configuration 4 using the PSU 94-097 airfoil. The numerical percentages of the power increase are shown at the cant angles of 90° and 45° in Tables 5-8 and 5-9.

Like configuration 3, the performance of configuration 4 shows a slight increase in the wind turbine power at low wind speeds. This improvement is obtained by implementing a cant angle of 45° and height of 15cm. At wind speeds up to 10m/s, the wind turbine power deteriorates for configuration 4, which reveals dominating the profile drag against its gain, when compared to the performance of configuration 1, as shown in Figure 5-16.

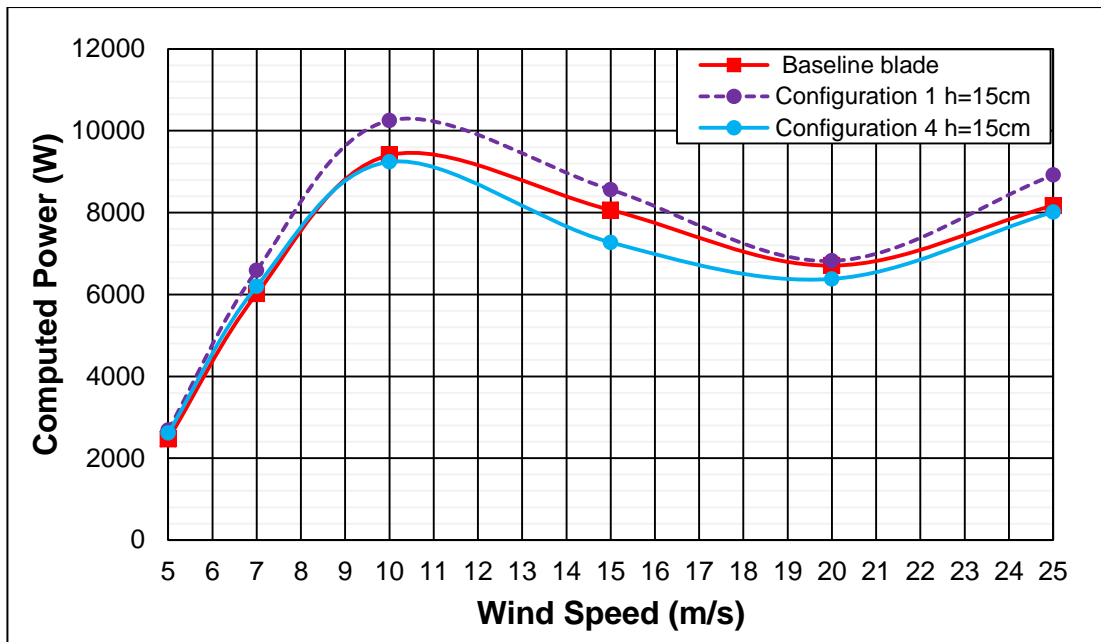


Figure 5-16 Comparison of calculated power between configuration 1 and 4 at a cant angle of 45° and height of =15cm.

Based on the assessments above, the best percentage of power increase is obtained by attaching configuration 1, which is extended by 15cm and tilted by a cant angle of 45°. Accordingly, this configuration will be taken as a reference design in the following discussion and will be referred as configuration 1.

5.5 Aerodynamic influences of the winglet parameters on its performance

Chapter five investigates the influence of winglet planform, airfoil, winglet height and cant angle on the wind turbine performance in the range of wind speeds 5-25m/s. Each parameter has a different role in increase/decrease of the enhancement of winglet performance.

Tables 5-2 to 5-9 show that, the most gain of winglet was resulted due to an increase in the projection area of the turbine rotor. For this reason, winglet supplements the baseline blade to capture more kinetic energy from moving air in addition to diffusing the wingtip vortices away from a blade tip. The greatest additional projection area of the rotor was achieved in case of rectangular planform, 45° cant angle and 15 cm winglet height which represented by the configurations 1 and 2 as shown in Tables 5-3 and 5-5, respectively.

From Tables 5-3 and 5-5, although the same additional projection area was added to the wind turbine rotor due to attaching configurations 1 and 2. Configuration 1 caused more percentage in the power increase of the NREL phase VI rotor when compared to configuration 2 as result to configuration 1 was created using the S809 airfoil. Unlike the PSU 94-097 airfoil, the S809 airfoil was designed as a wind turbine airfoil to convert the kinetic energy from the moving air into pressure difference around wind turbine blade. Hence, the superiority of configuration 1 is resulted due to employing the S809 airfoil in its profile as a comparison to the PSU 94-097 airfoil that used to generate configuration 2.

Additionally, the best winglet performance was achieved at the range of wind speeds 5-10m/s where the flow is almost attached as shown in Tables 5-2 and 5-3. However, this performance was clearly decreased due to the effect of separation flow and the penalty of profile drag at wind speeds greater than 10m/s.

5.6 Sectional flow and surface wall shear streamlines

Figures 5-17 to 5-23 show the effect of configurations 1 and 3 on the cross-sectional flow and the surface wall streamlines, at wind speeds of 7m/s and 15m/s. Considering the spanwise direction, there is no significant effect observed on the flow behaviour at the five spanwise sections of the baseline blade, for configurations 1 or 3 in the case of 7m/s and 15m/s, as shown in Figures 5-17 and 5-18, respectively. In contrast, the function of configurations 1 and 3 can be clearly observed by presenting the streamlines of the skin friction at wind speeds of 7m/s and 15m/s, as shown in Figures 5-19 and 5-20, respectively.

At 7m/s, where the flow is mostly attached, Figure 5-19 shows the spanwise flow in two opposite directions, which meet at the tip and trailing edge of the baseline blade. Additionally, similar behaviour to the spanwise flow is observed on the original blade surfaces, when compared to configurations 1 and 3, except at the blade tip.

At the blade tip, Figure 5-19 shows that the streamlines of the skin friction are diffused from the baseline tip towards the trailing edge on the pressure and suction sides, for configurations 1 or 3. In this way, the configurations (1 or 3) eliminate the main reason responsible for generating the wingtip vortices at the baseline tip, as discussed in section of 2.10. Accordingly, the wingtip vortices are generated on the tip of configuration 1 or 3, instead of the baseline tip, as shown in Figure 5-21.

Figure 5-22 shows the streamlines flow of the baseline tip compared to the tip, which is attached by configuration 1 and 3. The comparison shows the ability of configuration 3 to decrease the effect of the wingtip vortices more than configuration 1. This ability is obtained due to a reduction in the tip of configuration 3 by 75% of the baseline tip. However, this feature is not sufficient to make configuration 3 better at performing than configuration 1 in improving the NREL phase VI performance, as it will be discussed in the section of the pressure coefficient distributions.

A similar conclusion can be drawn at 15m/s, where the suction side of the blade is dominated by the stalled flow, as shown in Figures 5-20 and 5-23.

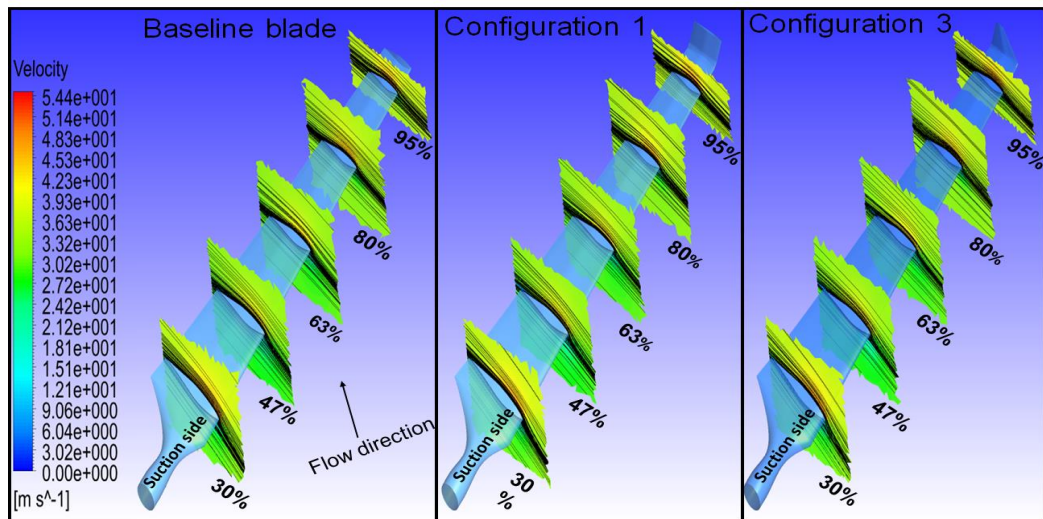


Figure 5-17 Comparison of velocity contours and sectional flow streamlines between baseline blade and configurations 1 and 3 at 7m/s.

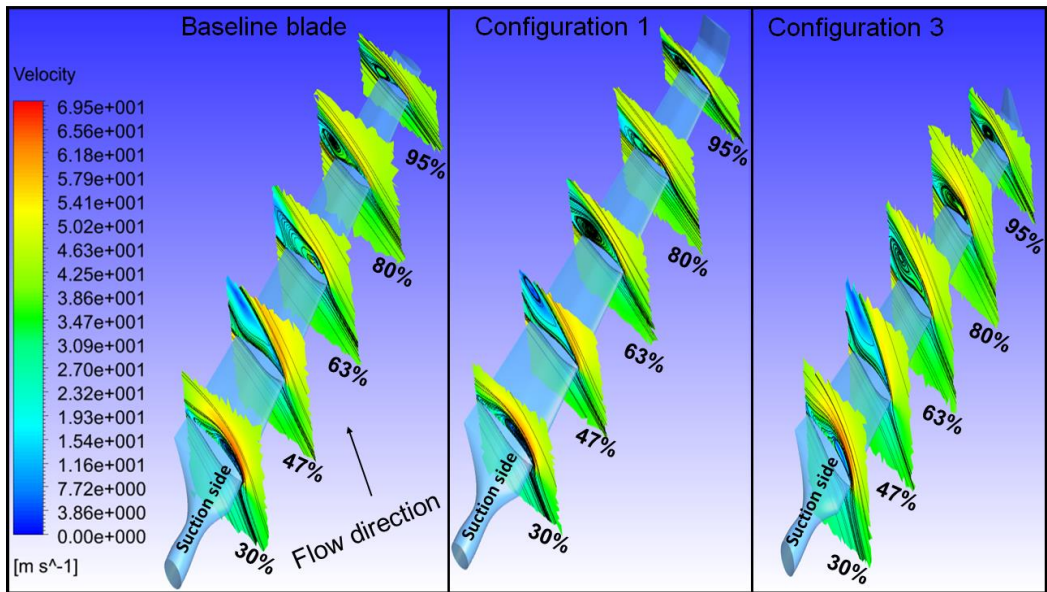


Figure 5-18 Comparison of velocity contours and sectional flow streamlines between baseline blade and configurations 1 and 3 at 15m/s.

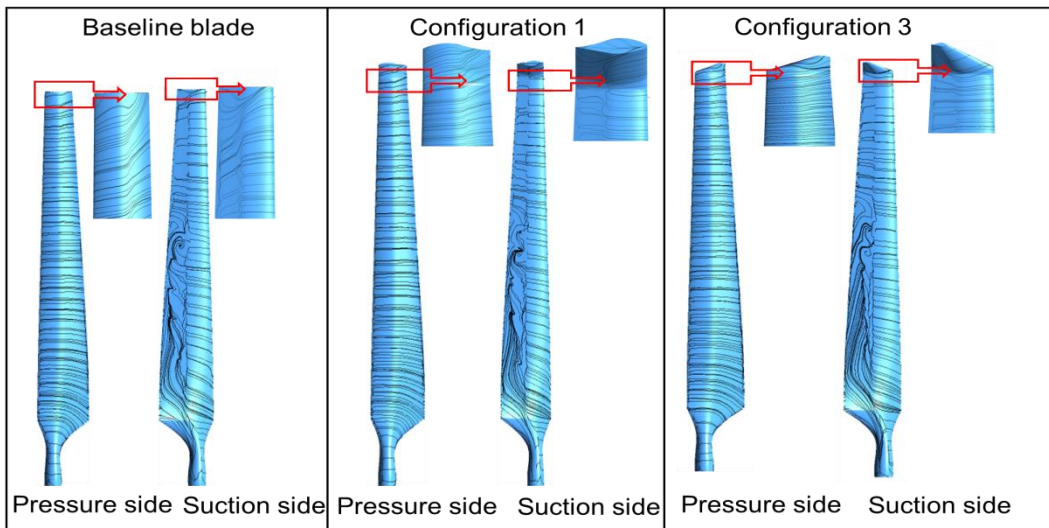


Figure 5-19 Comparison of surface wall shear streamlines between the baseline blade and configurations 1 and 3 at 7m/s.

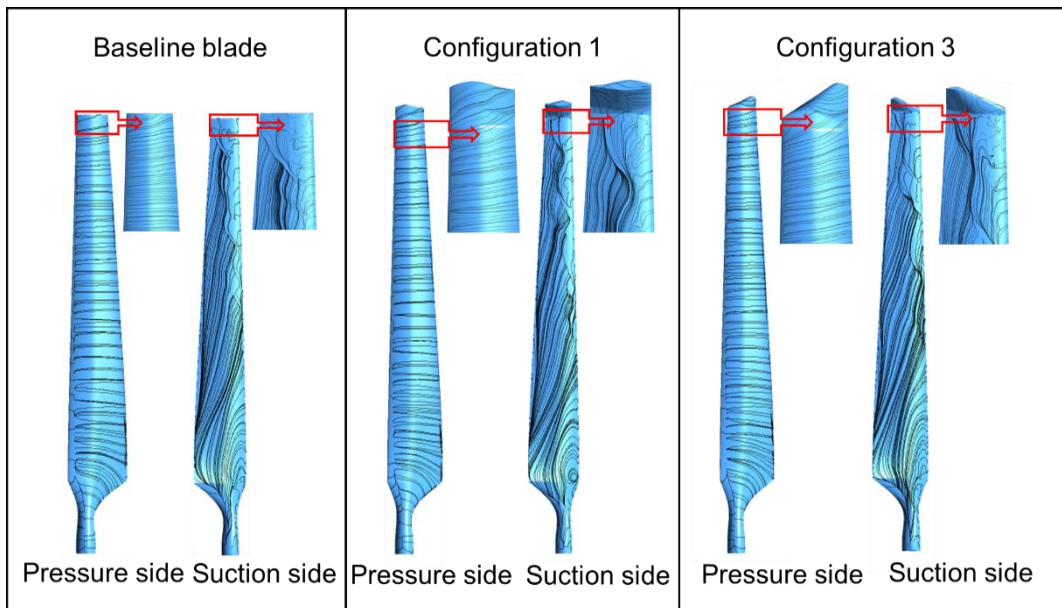


Figure 5-20 Comparison of surface wall shear streamlines between the baseline blade and configurations 1 and 3 at 15 m/s.

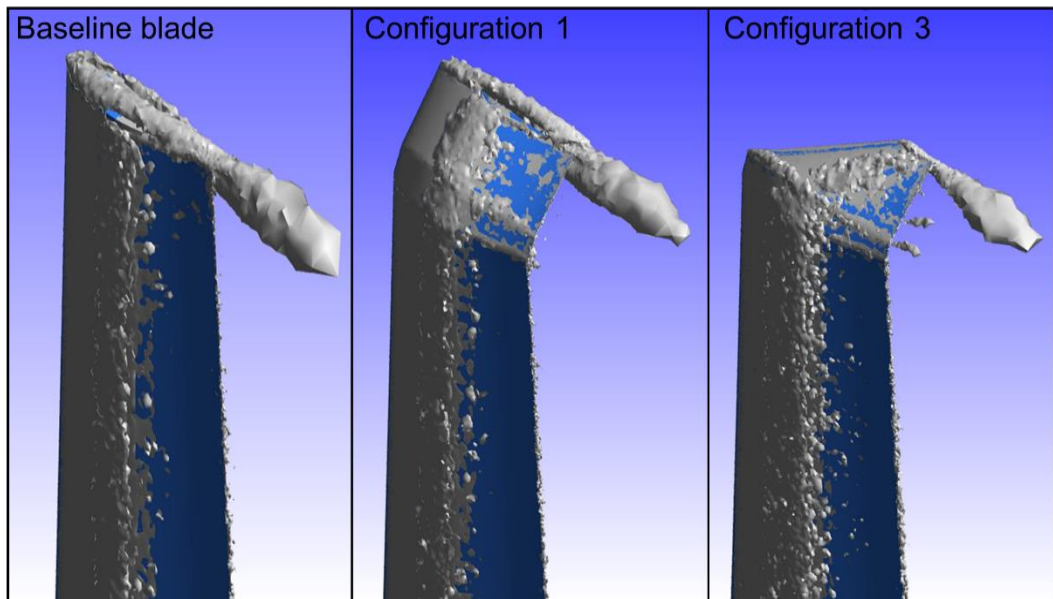


Figure 5-21 View of the tip vorticities of the baseline blade and configurations (1, 3) at 7m/s.

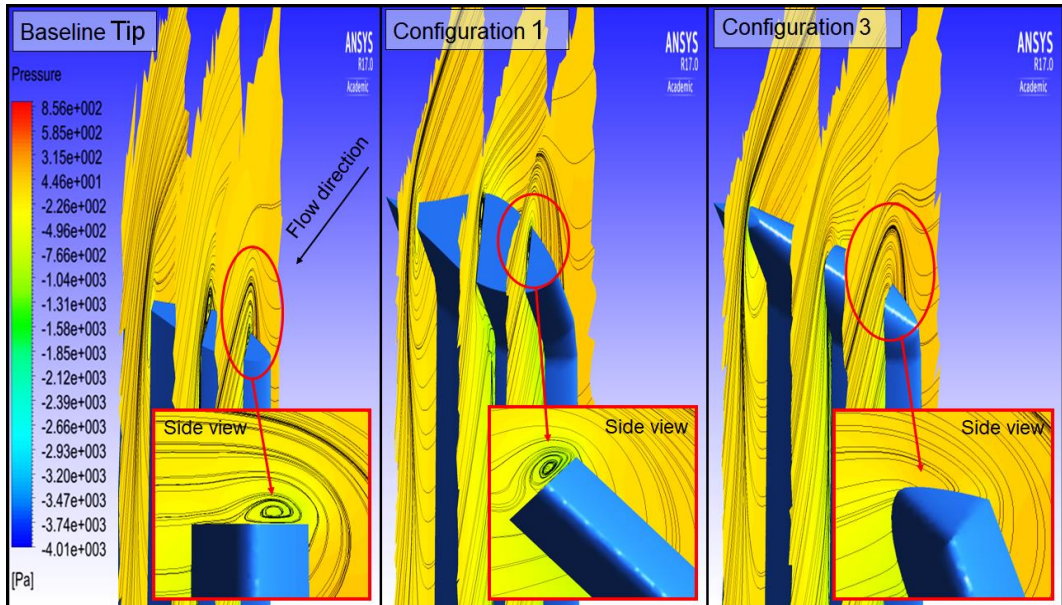


Figure 5-22 Comparison of tip flow streamlines between baseline blade and configurations 1 and 3 at 7m/s.

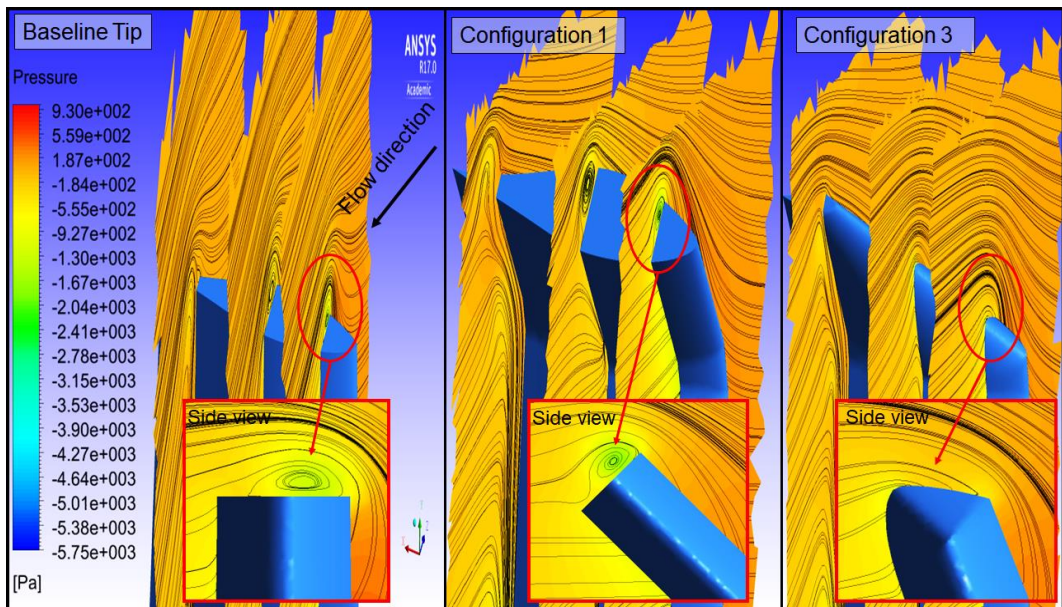


Figure 5-23 Comparison of sectional flow streamlines between baseline blade and configurations 1 and 3 at 15m/s.

5.7 Pressure coefficient distributions

To understand the aerodynamic effect of the winglet function on the NREL phase VI performance, comparisons between the calculated pressure coefficients were conducted between the baseline blade and those of configurations 1 and 3, which are tilted towards the suction side by an angle of 45° and height of 15cm. The comparisons are shown in Figures 5-24, 5-25 and 5-26 at wind speeds of 7m/s, 10m/s and 25m/s, respectively.

Figure 5-24 shows improvements in the pressure coefficients at a wind speed of 7m/s, where the flow is mostly attached. The improvements (increasing the pressure coefficients values) are observed at the suction side of the blade, where the configurations are tilted by an angle of 45° . These improvements are clearly observed at the spanwise sections of 95% and 98%. The improvements of the pressure coefficients suggest that additional energy is extracted from the fluid flow by the rotor due to attaching the winglets.

When considering the effect of the winglet planform, Figure 5-24 shows that configuration 1, results in more improvement in the pressure coefficients than configuration 3, particularly, at sections 95% and 98% span of the blade. Different improvements have been actioned because of the different surface areas that were added to the rotor. However, there were no significant improvements in the pressure coefficient distributions at the suction and pressure sides for the spanwise sections at 30%, 47% and 63%.

Similar conclusions can be drawn at 10m/s and 25m/s, as shown in Figures 5-25 and 5-26, respectively.

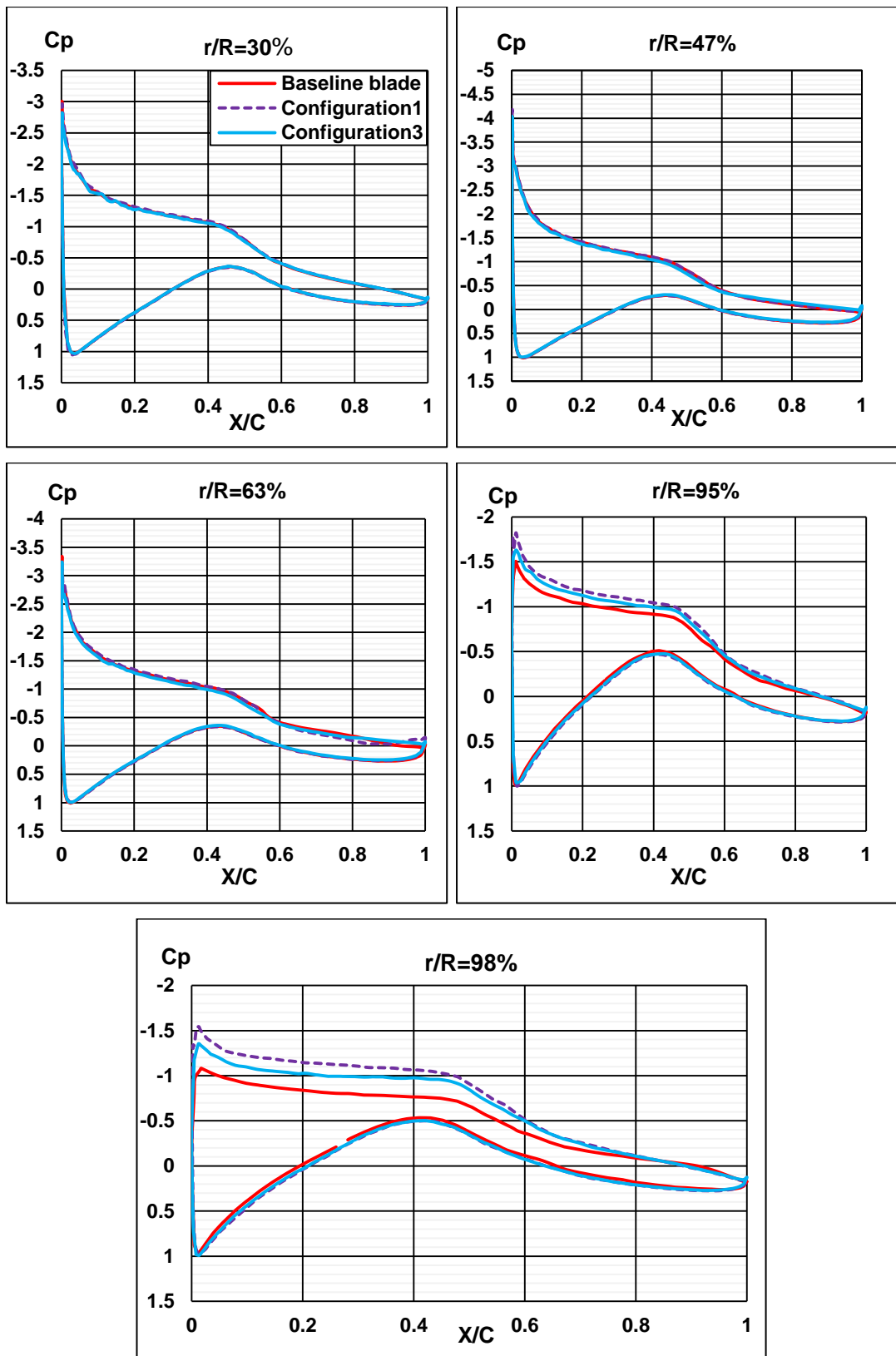


Figure 5-24 Comparisons of computed pressure coefficients at 7m/s between the baseline and configurations 1 and 3.

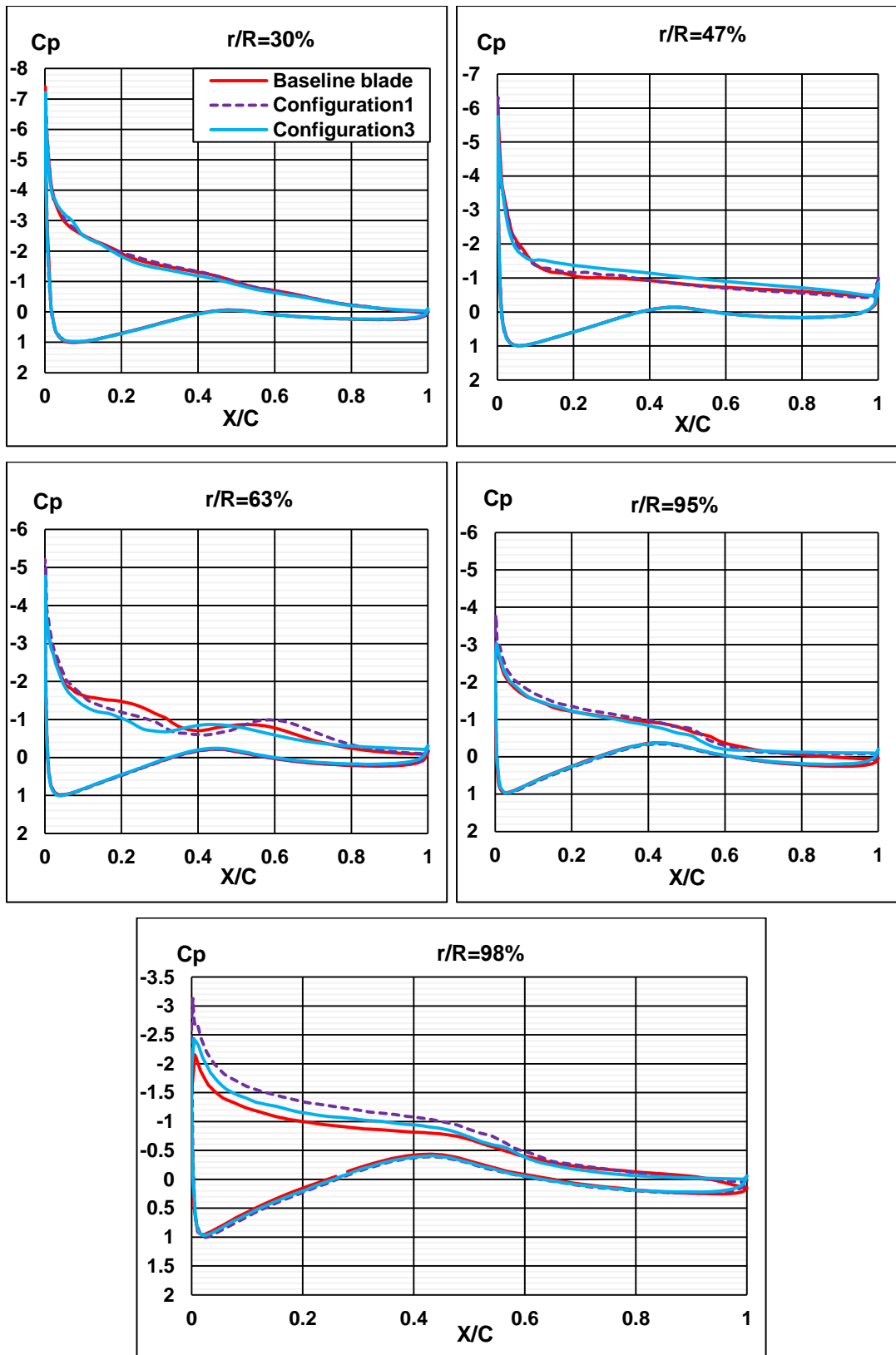


Figure 5-25 Comparisons of computed pressure coefficients at 10 m/s between baseline and configurations 1 and 3.

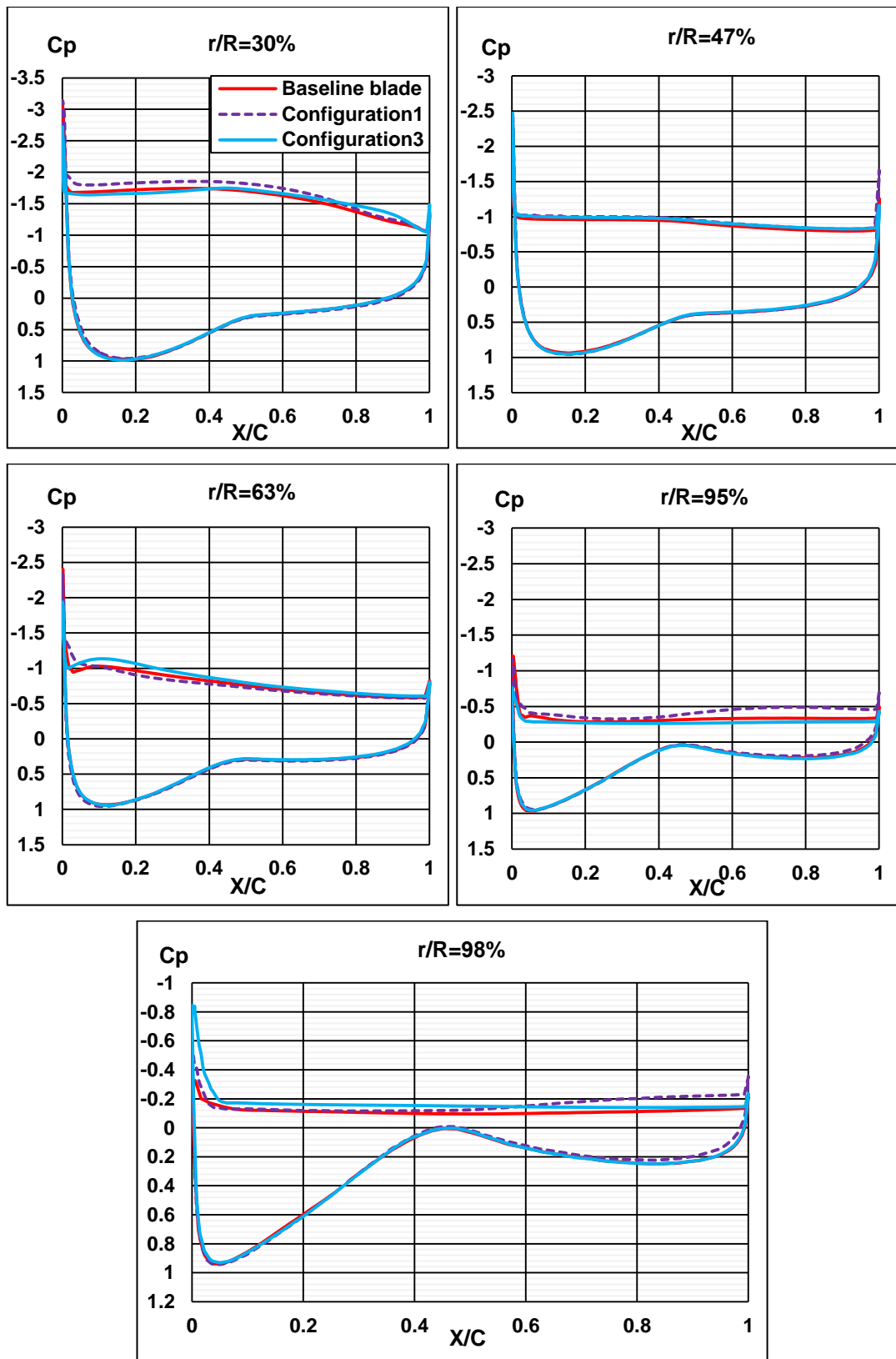


Figure 5-26 Comparisons of computed pressure coefficients at 25m/s between baseline and configurations 1 and 3.

5.8 Normal force coefficients and thrust force.

Regarding the thrust force, in most of the winglet configurations, the thrust force is increased when compared to the baseline case, as shown in Tables 5-2 to 5-9.

In short, the thrust force increases due to an increase in the extended area that is added to the baseline blade. A similar conclusion can be observed by employing the rectangular configurations, since they result in greater thrust force than the elliptical configurations. In addition, the configurations that are tilted by a cant angle of 45° results in a greater increase in thrust force than that when they are tilted by a cant angle of 90° , due to an increase in the projection area of the baseline blade. Further, the S809 airfoil causes greater increase in the thrust force than the PSU 94-097 airfoil in cases that have similar parameters, such as the cant angle, height and the winglet planform.

However, configuration 1, which is extended by 15cm and tilted by a cant angle of 45° results in the greatest increase in thrust force. This is due to the extension of the baseline blade toward the suction side, which results in improvements in the pressure coefficients, particularly near the blade top, as shown in Figures 5-24 to 5-26. Thereby, the normal force coefficients are increased due to integrating improvements in the pressure coefficients (see Equation 4.4).

Figures 5-27 to 5-29 show sectional increases in the normal force coefficients (C_N), which occurred for configurations 1 and 3 at wind speeds of 7m/s, 10m/s and 25m/s. The aforementioned figures show that the maximum increase in the normal force coefficients is obtained by attaching configuration 1 (cant angle of 45° and height of 15cm), due to the greatest additional area added to the rotor. Generally, the increase in the C_N becomes greater near the blade top, particularly at 95% span of the blade due to the influence of configuration 1. The overall thrust force of configuration 1 compared to the baseline blade is shown in Figure 5-30.

In contrast, winglet configurations 2, 3 and 4 caused increases in the thrust force, which is less than the thrust force for configuration 1. The main disadvantage of the rise in thrust force is potentially tip deflection due to an increase in the flap-wise bending moment. Nevertheless, the maximum percentage of the increases in the computed thrust force is calculated at a wind speed of 5m/s, which is lower than the measured safe value that equals 3994.56 N at a wind speed of 25m/s as shown in Figure 4-23.

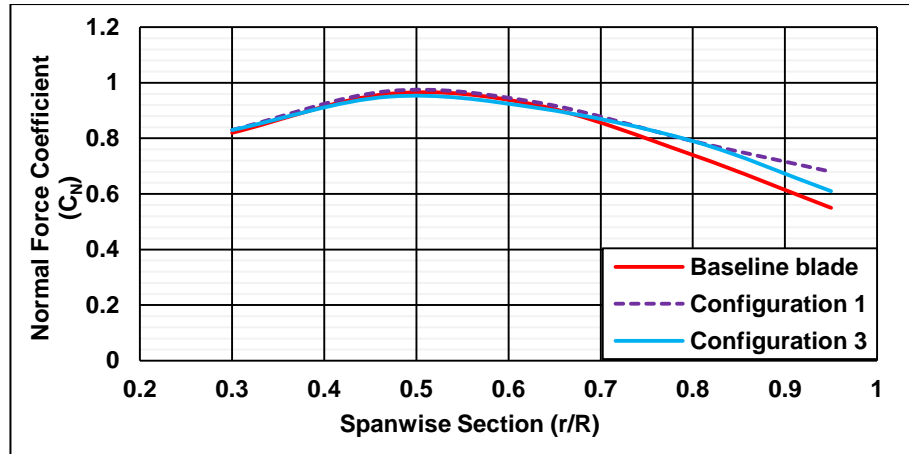


Figure 5-27 Comparison of normal force coefficients between baseline blade and configurations (1, 3) at 7m/s.

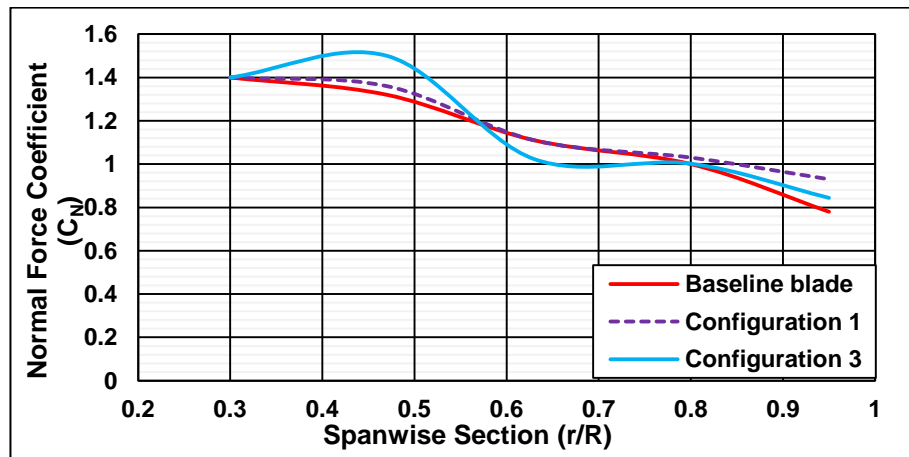


Figure 5-28 Comparison of normal force coefficients between baseline blade and configurations (1, 3) at 10m/s.

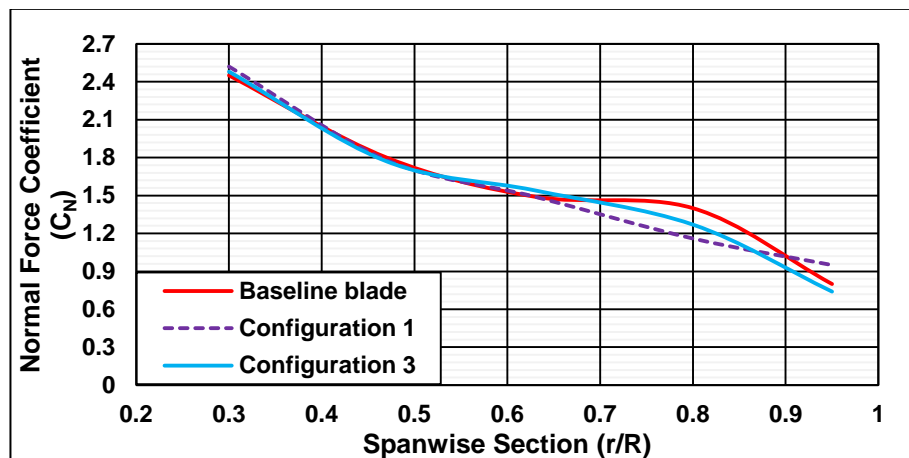


Figure 5-29 Comparison of normal force coefficients between baseline blade and configurations (1, 3) at 25m/s.

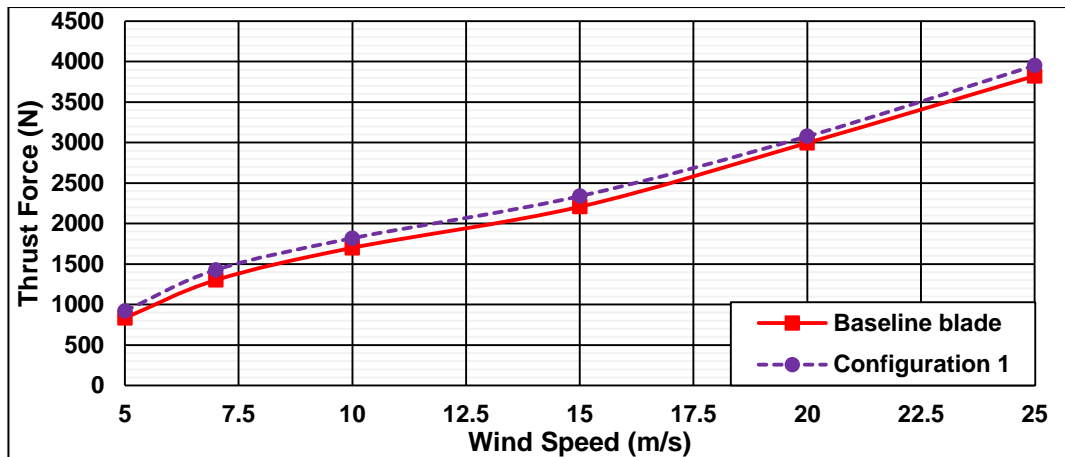


Figure 5-30 Comparison of baseline blade thrust force and configuration 1.

In summary, configuration 1 (cant angle of 45° and height of 15cm) shows the greatest improvement in output power. The greatest gain of configuration 1 occurs at wind speeds ranging from 5-10m/s, where the flow is mostly attached, as shown in Figure 5-31. In this region, configuration 1 shows an improvement in the power increase of around 9% before a reduction in the performance of configuration 1, which is observed at wind speeds greater than 10m/s. However, considering the experimental data presented in Figure 5-4, since the rotor power increases beyond the wind speed of 19 m/s, the percentage of power increase improves to 9% for configuration 1 at the cut-out speed of 25 m/s.

It seems that the reduction in the percentage of performance for configuration 1 occurs due to the stalled flow and the penalty of the profile drag. However, the configuration 1 causes an increase in the normal force coefficients at the spanwise direction of the blade. Accordingly, the overall percentages of the thrust increase are occurred as shown in Figure 5-31.

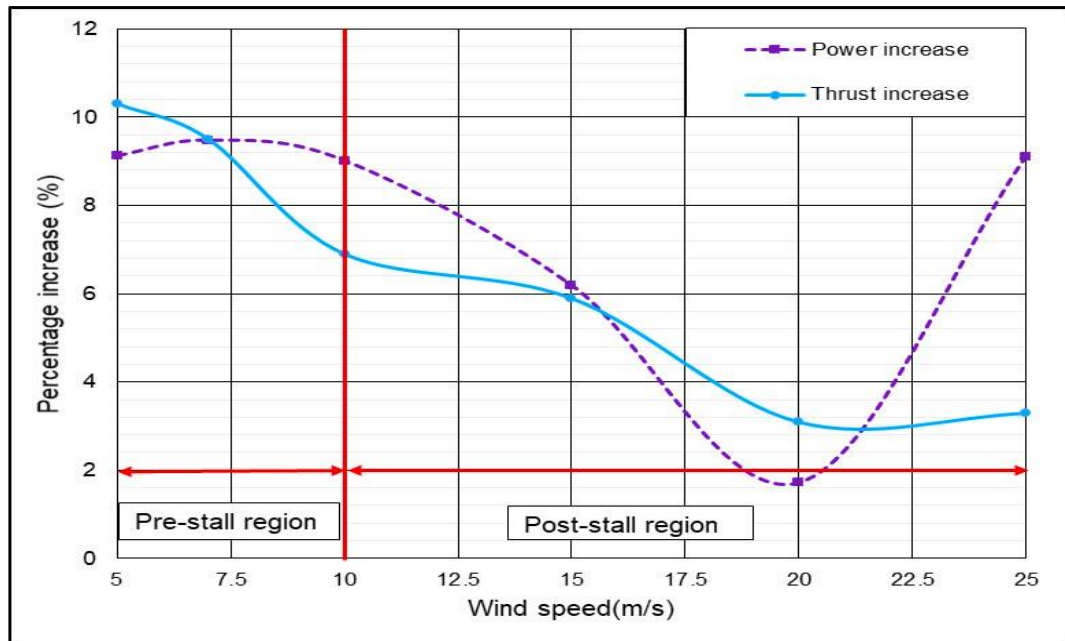


Figure 5-31 Percentage of increase in power and thrust force of configuration1.

5.9 Conclusions

In this chapter, four winglet configurations have been examined with a view towards improving the NREL phase VI productions. The configurations were categorised corresponding to the winglet planform and airfoil. Each configuration was tested by varying the configuration height and cant angle at a range of 5-25 m/s.

This chapter involved studying the effect of four winglet parameters on winglet performance: winglet planform, airfoil, cant angle and winglet height. The rectangular planform demonstrates better performance than its elliptical counterpart, due to attaching a greater extension area, which enables the baseline blade to capture more kinetic energy from the moving air. A similar conclusion can be drawn in the case of the rectangular winglet, which extended towards the suction side by a cant angle of 45° against using 90° . Unlike the elliptical planform, the performance of the rectangular planform improved due to increasing the winglet height. Additionally, the S809 airfoil shows improvements in power increases that are greater than the PSU 94-097 airfoil.

This chapter has presented the sectional distributions of the pressure coefficients that were obtained for configurations 1 and 3 at sections 30%, 47%, 63%, 95% and 98% of the blade span. The improvements in the pressure coefficients are occurred at the suction side where the winglets are

tilted. These improvements are clearly observed near the blade top, particularly at section 95% and 98% of blade span.

The streamlines of skin friction show the function of the winglet, which diffuses the meeting region of the two opposite spanwise flows towards the winglet tip, instead of the baseline tip. In this way, the effect of wingtip vortices is weakened on the baseline blade, by moving the generating vortices away from the baseline tip.

Considering the winglet planform, configuration 3 (elliptical planform) causes a reduction in the effect of the wingtip vortices that is greater than configuration 1, as result of a reduction in the tip area of configuration 3 by 75% of the baseline tip. However, the improvements of the pressure coefficients near the blade top reveal the superiority of configuration 1 in extracting more energy than configuration 3.

Further, this chapter has dealt with the aerodynamic influence of the winglet configurations on the thrust increases that are achieved due to increases in the normal force coefficients. The highest percentage of thrust increase is observed by attaching configuration 1 (cant angle of 45° and height of 15cm) as a result of increasing the wetted area of the baseline blade.

In conclusion, among the winglet configurations, configuration 1 (cant angle of 45° and height of 15cm) resulted in the highest overall percentage of power increase.

Chapter 6 : The Effect of Winglet Airfoil on the Wind Turbine Performance

6.1 Introduction

Chapter five presented the effects of a number of winglet parameters on the NREL phase VI performance, including the winglet airfoil. The assessments of the winglet configurations reveal that the S809 airfoil performs better than the PSU 94-097 for improving the NREL phase VI performance. Accordingly, this chapter investigates the aerodynamic characteristics of a winglet airfoil, which are required to increase wind turbine performance.

For this purpose, the S801, S803, S805A and S806A airfoils were preliminarily analysed using Xfoil code to calculate their aerodynamic coefficients at Reynolds number 1×10^6 and Mach number 0.02. Numerical comparisons in 2D were carried out between the selected airfoils' coefficients and the NREL phase VI blade tip airfoil (S809).

A rectangular planform that is extended by 15cm and canted 45° towards the suction side is chosen for 3D winglet calculations, as it had the best percentage of power increase.

6.2 Requirements of the winglet airfoil design

Designing an airfoil needs a good understanding of the operating conditions under which the airfoil function is required. The most important factors that are addressed in the literature to design any airfoil are the specified range of aerodynamic coefficients, Reynolds number, Mach numbers, stall characteristics, thickness, and their insensitivity to surface roughness (Tangler and Somers, 1995). It is noteworthy that for each operating condition, there are optimum airfoil characteristics, which secure the best wing/winglet combination performance. Hence, it is most important to fully determine the operating conditions of the winglet and how they aerodynamically impact the wind turbine blades to avoid poor performance (Maughmer *et al.*, 2002).

Accordingly, the operating conditions of the NREL phase VI rotor were taken as reference conditions to design or choose a suitable winglet airfoil. The NREL phase VI rotor is a stall regulated wind turbine as presented in chapter four (see section 4.2). The lift coefficient of the S809 airfoil was measured at the Reynolds numbers, ranging from 3×10^5 to 1×10^6 at the Colorado State University (CSU), Ohio State University (OSU), and Delft University of Technology (DUT) (Jonkman, 2003), as shown in Figure 6-1.

Figure 6-1 shows the flow around the S809 airfoil is categorised by 3 different zones, namely, the attached flow regime (zone A), the stalled development regime (zone B), and the fully stalled regime (zone C). Different flow regimes are applied to impose on the performance of the NREL phase VI, as a stall regulated wind turbine. This means if a wind speed varies between 10 and 25m/s, the output power will be stall limited to approximately 10kW due to the existing stall regime at zone B and C.

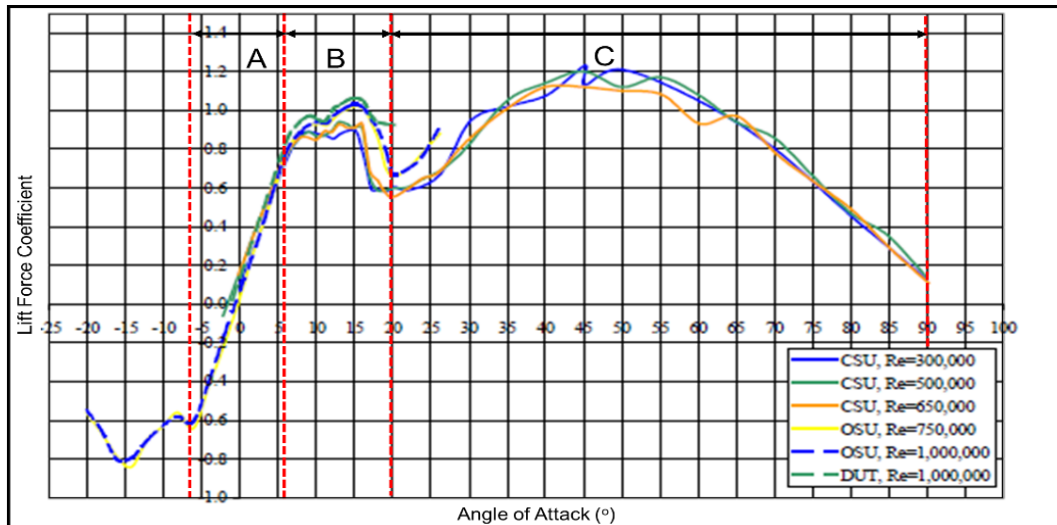


Figure 6-1 Experimental lift coefficient for the S809 airfoil (Jonkman, 2003).

6.3 Aerodynamic solver

The Xfoil flow solver was used to calculate the lift, drag and moment coefficients (C_l , C_d , and C_m) of the S809 airfoil. The Xfoil is an interactive and open source code written in the FORTRAN language, created by Drela (1989) for the design and analysis of subsonic isolated airfoils. The Xfoil uses an inviscid two-dimensional panel method, which is coupled with an integral boundary layer method to obtain a viscous solution for the fluid flow around an airfoil. The objective of using the Xfoil solver is to reduce the computational time required to calculate the aerodynamic coefficients of selected or designed airfoils.

The panel convergence was considered by using 250 panel nodes ($N=250$) to reduce a fluctuation of the aerodynamic coefficient values due to changes in the transition location. Considering the free transition, a critical number value was chosen equal to 9 ($N_{crit}=9$), as an indication of the ambient disturbance level in the average wind tunnel, as recommended in the Xfoil documentation as shown in Table 6-1 (Drela and Youngren, 2001).

Table 6-1 Values of n_{crit} for different applications.

Situation	n_{crit}
Sailplane	12-14
Motor glider	11-13
Clean wind tunnel	10-12
Average wind tunnel	9
Dirty wind tunnel	4-8

The capability of the Xfoil code to match the experimental data has already been presented in a number of studies (Zhu *et al.*, 2014; Batten *et al.*, 2007). Nevertheless, a validation study is conducted in the present work, as shown in Figures 6-2 to 6-4. The aerodynamic coefficients of the S809 were calculated using the Xfoil solver at the operational conditions of the NREL phase VI, where the Reynolds and Mach numbers are 1×10^6 and 0.02, respectively, and the range of the Angle of Attack (AOA) is 0° to 20° .

Figure 6-2 shows the lift coefficient values of the S809 airfoil varying from 0.1569 to 0.8676 at the range of 0° to 6° AOA as 6° is a stalled angle (see Table B-1 in Appendix-B), where the flow corresponds to zone A, as shown in Figure 6-1. Along the same lines, Figure 6-3 shows the variation of the C_d value varies between 0.0093 and 0.00864 (see Table B-1 in Appendix-B). Additionally, the same figure shows that the C_d has significantly increased at the angles are greater than 6° AOA due to the laminar separation bubbles. The variation of the C_m versus the AOA is shown in Figure 6-4, which is limited to a range of -0.04 to -0.06.

Figure 6-5 shows the maximum computed performance ratio (C_l / C_d) is 100.41 at the 6° AOA, before a remarkable decrease is observed due to the laminar separation bubbles.

As a result of the numerical validation of the S809 airfoil, the preliminary 2D analysis of the S809 coefficients in zone (A) were taken as the operating conditions to design or choosing a suitable winglet airfoil which can improve the performance of the NREL phase VI rotor.

It should be noted that the winglet airfoil should be designed in a way that the maximum lift force is generated with the lowest possible drag in order to avoid the penalty of the profile drag. Accordingly, the winglet airfoil must have a performance ratio (C_l / C_d) that is relatively greater than the S809 airfoil at 0°

to 6° AOA. In addition, to maintain the longitudinal static stability and torsional moment of the blades, the C_m of the winglet airfoil should be varied within the same range of the S809 airfoil. Furthermore, it is important to consider the roughness factor, which contributes to the annual energy loss by 20-30% for stall regulated rotors, i.e. NREL phase VI (Tangler and Somers, 1995).

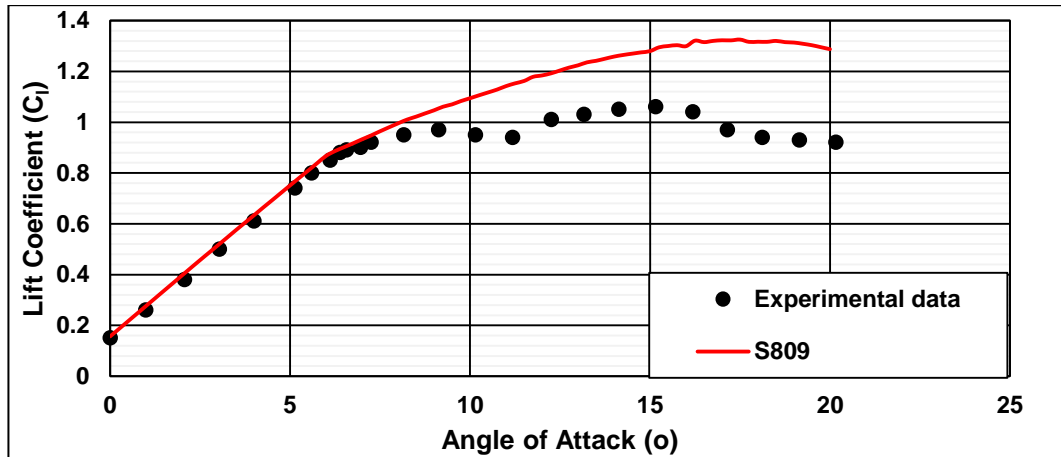


Figure 6-2 Comparison of measured and calculated lift coefficients of the S809 airfoil.

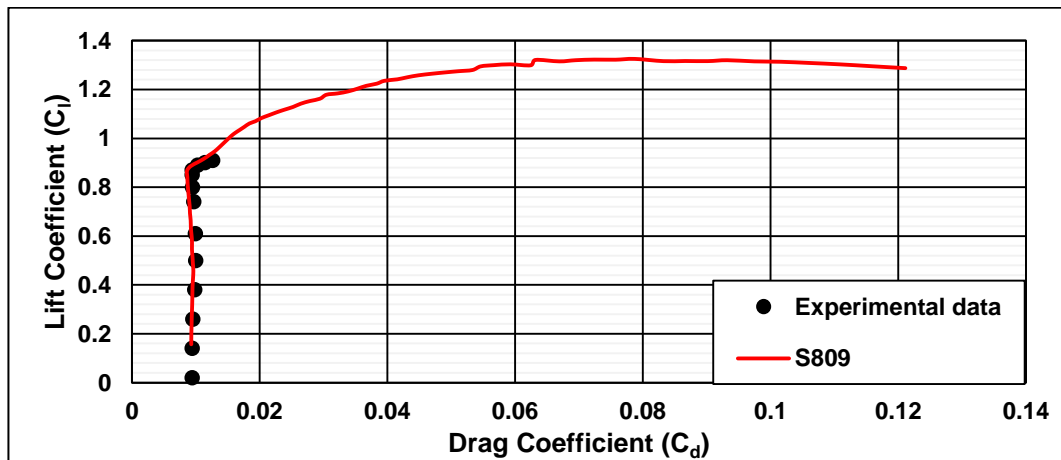


Figure 6-3 Comparison of measured and calculated lift and drag coefficients of the S809 airfoil.

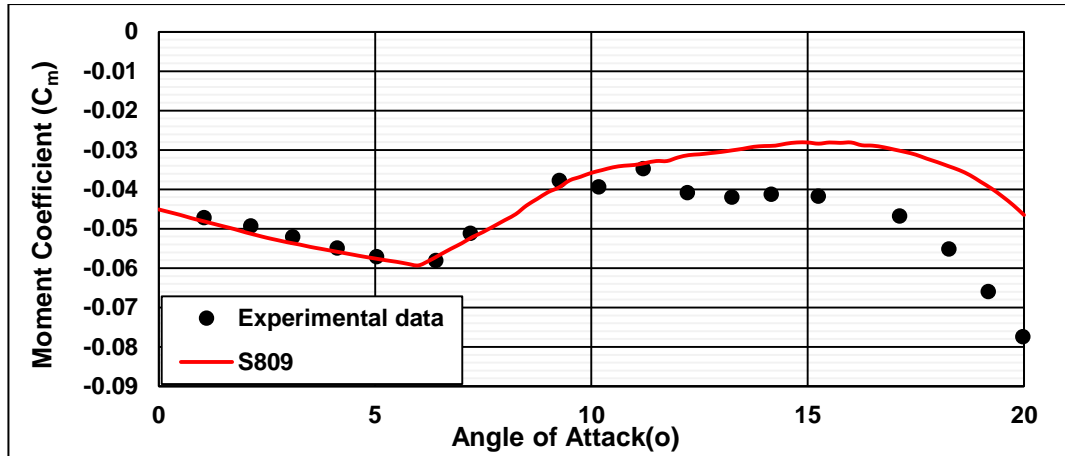


Figure 6-4 Comparison of measured and calculated moment coefficients of the S809 airfoil.

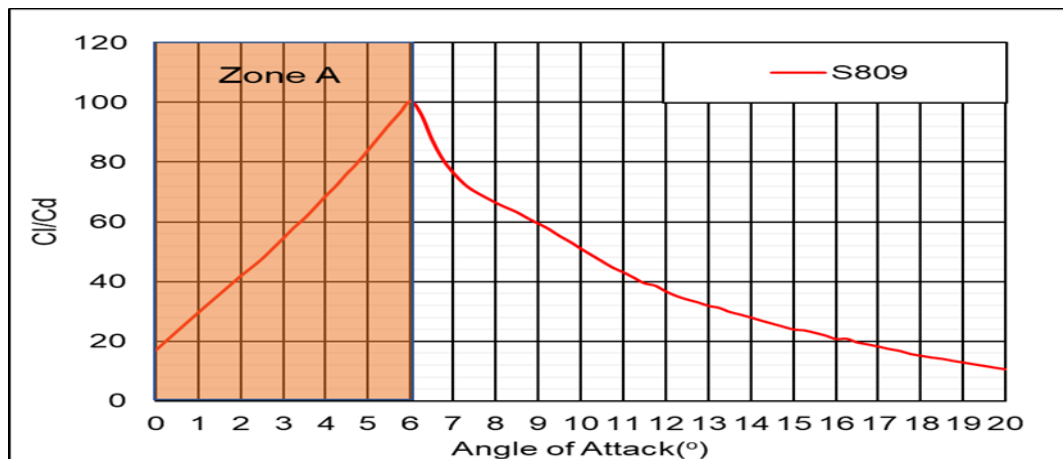


Figure 6-5 Calculated performance ratios (C_l / C_d) of the S809 airfoil.

Considering the choice of a winglet airfoil, different airfoils were experimentally tested and designed for horizontal axis wind turbines (HAWTS) in a cooperative effort that was conducted between the NREL and Airfoil Incorporation (see section 2.9) (Tangler and Somers, 1995).

Among the 25 airfoils, 4 thin airfoils, namely, S801, S803, S805A, and S806A were designed as appropriate primary and blade tip airfoils for the requirements of a blade length of 5-10m and generator size of 20-150KW. These features correspond to the blade length and output power of the NREL phase VI as shown in Table 4-1 (see section 4.2). The S801, S803, S805A and S806A airfoils are chosen in this work as winglet airfoils to improve the performance of the NREL phase VI. The aerodynamic performance of the selected airfoils was assessed using the Xfoil and CFD was used to model the 3D flow field around the rotor-winglet system.

6.4 Preliminary analysis of the selective airfoils

Figures 6-6 to 6-9 show the preliminary aerodynamic analysis of the selected airfoils, which were calculated at the operating conditions of the NREL phase VI. As shown in Figure 6-6, the lift coefficients of the S805A and S806A airfoils are slightly higher than that of the S809 airfoil, at various AOA, whereas the difference in the C_l between the S809 airfoil and both the S803, S801 airfoils are remarkably high.

Among the selected airfoils shown in Figure 6-7, the S806A airfoil shows the lowest drag coefficient, which varies between 0.00562 and 0.00568 in the range of 0° - 4.5° AOA (see Table B-5 in Appendix-B). Further, Figure 6-8 shows the variations of the C_m for the selected airfoils at differing AOA. Unlike the S801 and S803 airfoils, the C_m for both S805A and S806A airfoils varies in the same range of the C_m of S809 airfoil. Furthermore, the performance ratios of the selected airfoils (C_l/C_d) are greater than that of the S809 airfoil, as shown in Figure 6-9.

Considering the penalty of profile drag, both S806A and S805A have the lowest drag coefficients, and have values of the C_m , which vary within the C_m of the S809 airfoil. Accordingly, both of the S805A and S806A airfoils are chosen to construct two winglet configurations. Winglet configuration A1 was created using the S806A airfoil, whereas, the S805A airfoil was used for constructing the winglet configuration B1.

The CFD method was employed to predict the performance of the NREL phase VI, which is obtained by attaching configurations A1 and B1.

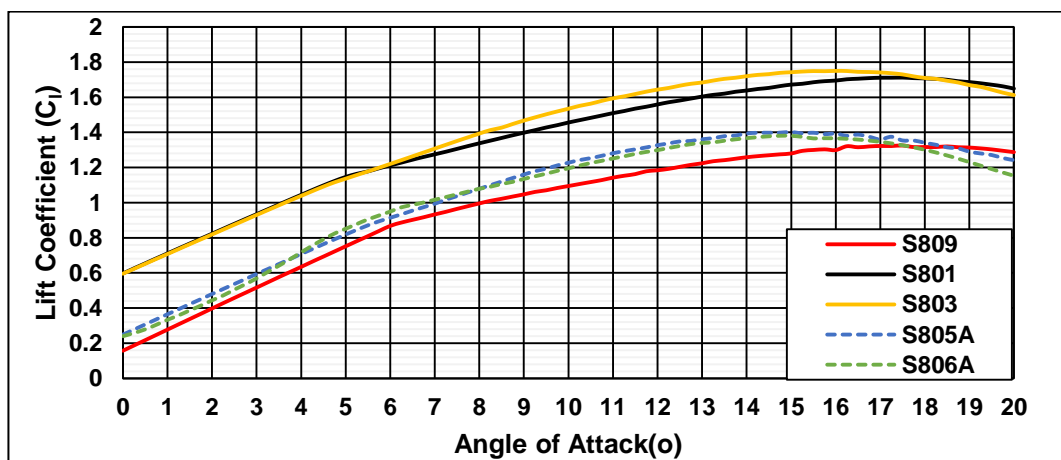


Figure 6-6 Comparison of lift coefficients between S809 and selected airfoils.

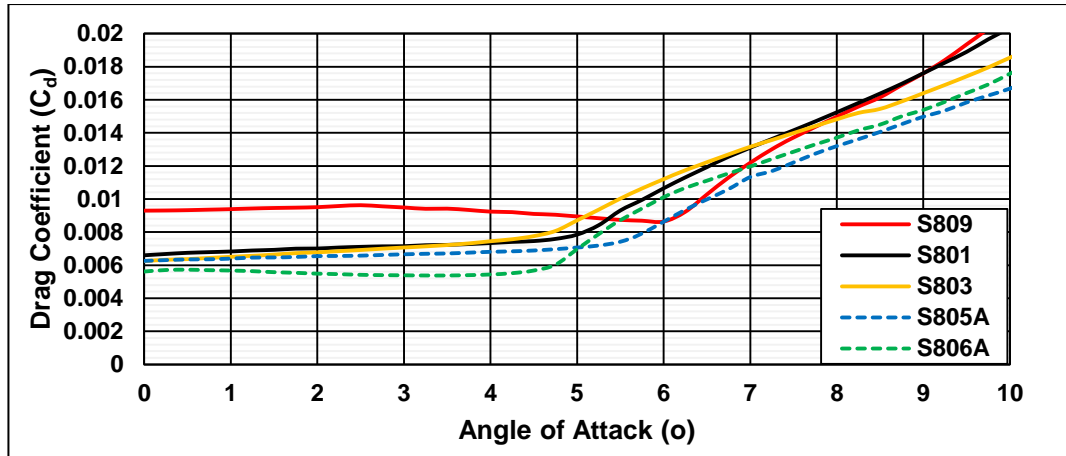


Figure 6-7 Comparison of drag coefficients between S809 and selected airfoils.

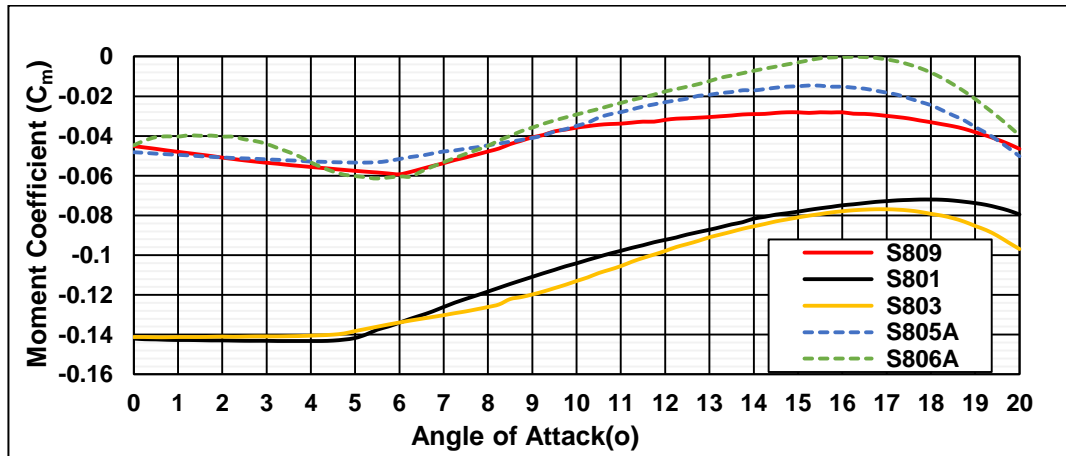


Figure 6-8 Comparison of moment coefficients between S809 and selected airfoils.

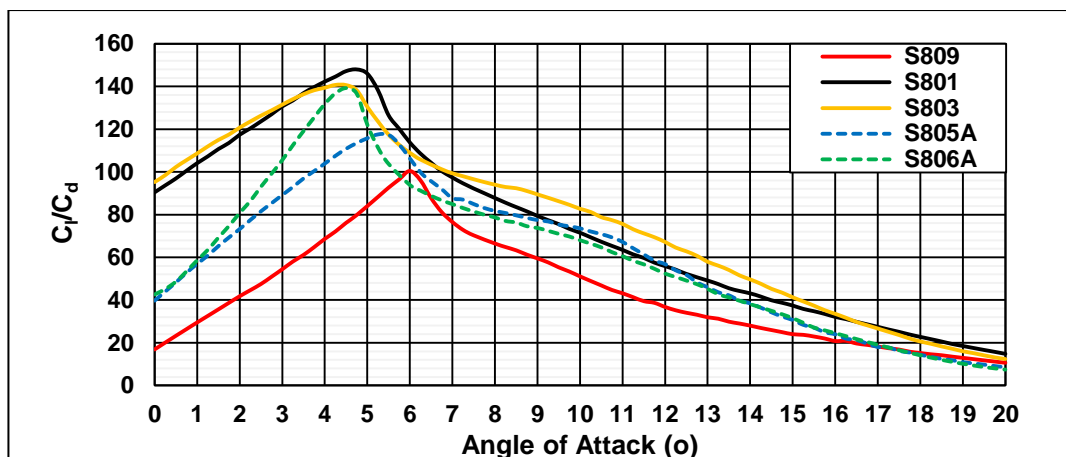


Figure 6-9 Comparison of performance ratio (C_l / C_d) between S809 and selected airfoils.

6.5 Winglet configurations

The 3D fluid flow around the rotor-winglet companion is predicted by implementing similar numerical methodology followed when calculating the fluid flow around the baseline blade. The computed winglet performance is estimated for the range of the wind speeds of 5m/s to 20m/s, where 25m/s is the cut-out speed.

Figure 6-10 shows a schematic of the S805A and S806A airfoils, which are used to create two winglet configurations. Configuration A1 is created by extending the S806A airfoil by 15cm. The same method is followed to construct configuration B1 by implementing the S805A airfoil. The baseline tip is modified by attaching the two configurations that are tilted towards the suction side of the blade by a cant angle of 45° as shown in Figure 6-11.

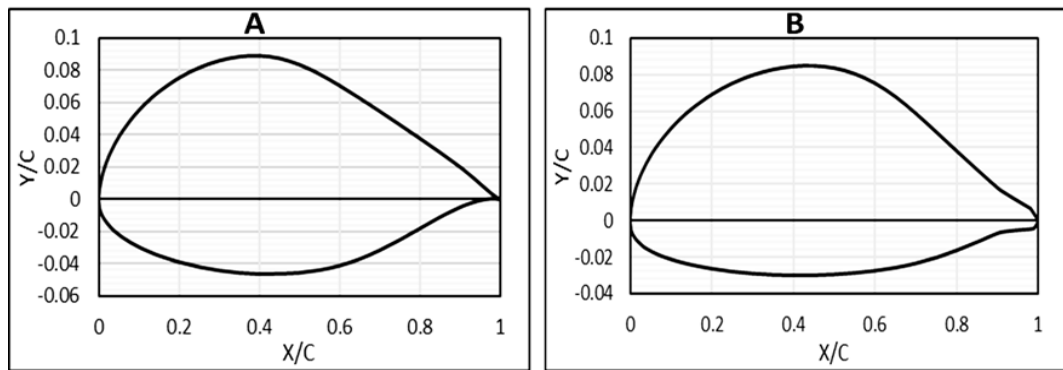


Figure 6-10 Schematic of: A- S805A airfoil, B- S806A airfoil.

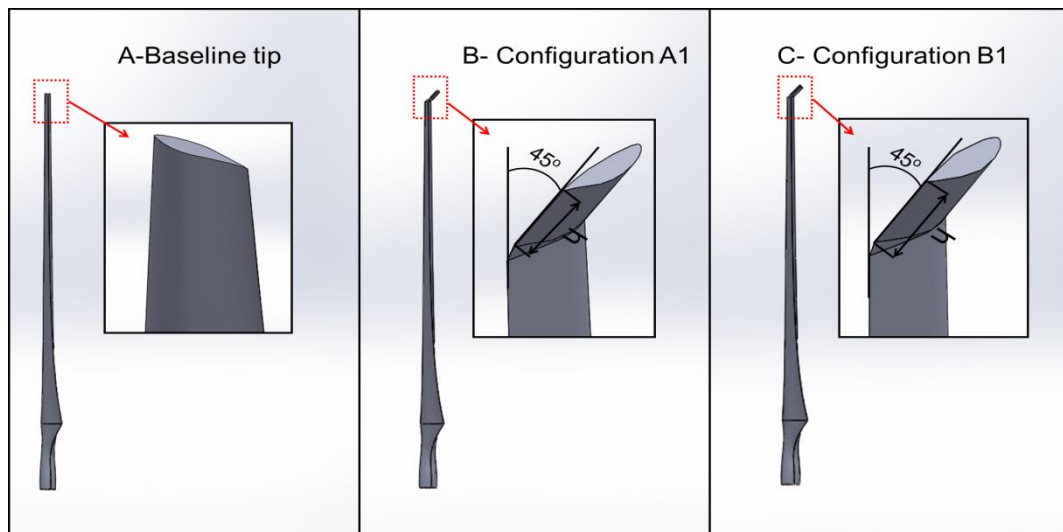


Figure 6-11 View of: A- Baseline tip, B- Configuration of A1 and C- Configuration of B1.

6.6 Pressure and normal force coefficient distributions

To understand the aerodynamic influence of the winglet airfoil on the NREL phase VI performance, comparisons of the predicted surface pressure coefficients are presented between the baseline blade and the two configurations, at wind speeds of 7m/s, 10m/s, and 15m/s, as illustrated in Figures 6-12 to 6-14.

Figure 6-12 shows how the pressure coefficient distributions are improved at the spanwise suction side, particularly on the sections that are located near the blade top, since the configurations are tilted toward the suction side. This improvement is clearly observed in the spanwise sections at 95% and 98% of the blade length. The improvements of the pressure coefficients indicate that additional energy is extracted from the fluid flow by the rotor, due to attaching winglets.

Considering the effect of S805A and S806A airfoils, at wind speed of 7m/s, there are no improvements in the pressure coefficients at the spanwise sections of 30%, 47% and 63%, as shown in Figure 6-12. In contrast, improvements in the pressure coefficients are clearly shown at the near of the blade top, particularly at the spanwise sections of 95% and 98%. However, at 95% and 98% span of the blade, the same improvements are observed in the pressure coefficients for both configurations A1 and B1.

At 10m/s and 15m/s, the stalled flow exists, as shown in Figures 6-13 and 6-14, respectively. Attaching both configurations is clearly shown to improve the pressure coefficient distributions at the spanwise sections of 95% and 98% span of the blade. Furthermore, an increase of wind speed above 10m/s shows a feature of the S806A airfoil, which has less drag coefficient compared with the S805A airfoil. This feature is clearly observed by comparing improvements in the pressure coefficients, which resulted from attaching configurations A1 and B1.

At 10m/s, Figure 6-13 shows at the spanwise section of 98%, that configuration A1 results in an improvement in pressure coefficients, which is slightly greater than configuration B1. At a wind speed of 15m/s, a similar observation can be made at the spanwise sections of 95% and 98%, as shown in Figure 6-14.

However, the effect of both airfoils on wind turbine performance can be clearly observed by integrating the computed torque, which is generated along the whole blade.

Figures 6-15 to 6-17 show sectional increases in the normal force coefficients (C_N), which occur for configurations A1, B1 at wind speeds of 7m/s, 10m/s and 15m/s.

At a low wind speed of 7m/s, there is no increase in the normal force coefficient at the spanwise section of 30%, 47% and 63% for configurations A1 and B1. However, the increase in the C_N becomes more at near the blade top, particular at the 80% and 95% span of the blade. This result agrees with the effect of both configurations on the pressure coefficient distributions, as shown in Figure 6-12. Nevertheless, there is no significant difference in the increase of the C_N due to employing the S806A or S805A airfoil.

In contrast, the stalled flow that exists at wind speeds of 10m/s and 15m/s results in a fluctuation in the prediction of the C_N values, due to the deficiency of the SST $k-\omega$ model, as shown in Figures 6-16 and 6-17. However, these figures show increases in the C_N at the blade top, particularly at the 95% span of the blade.

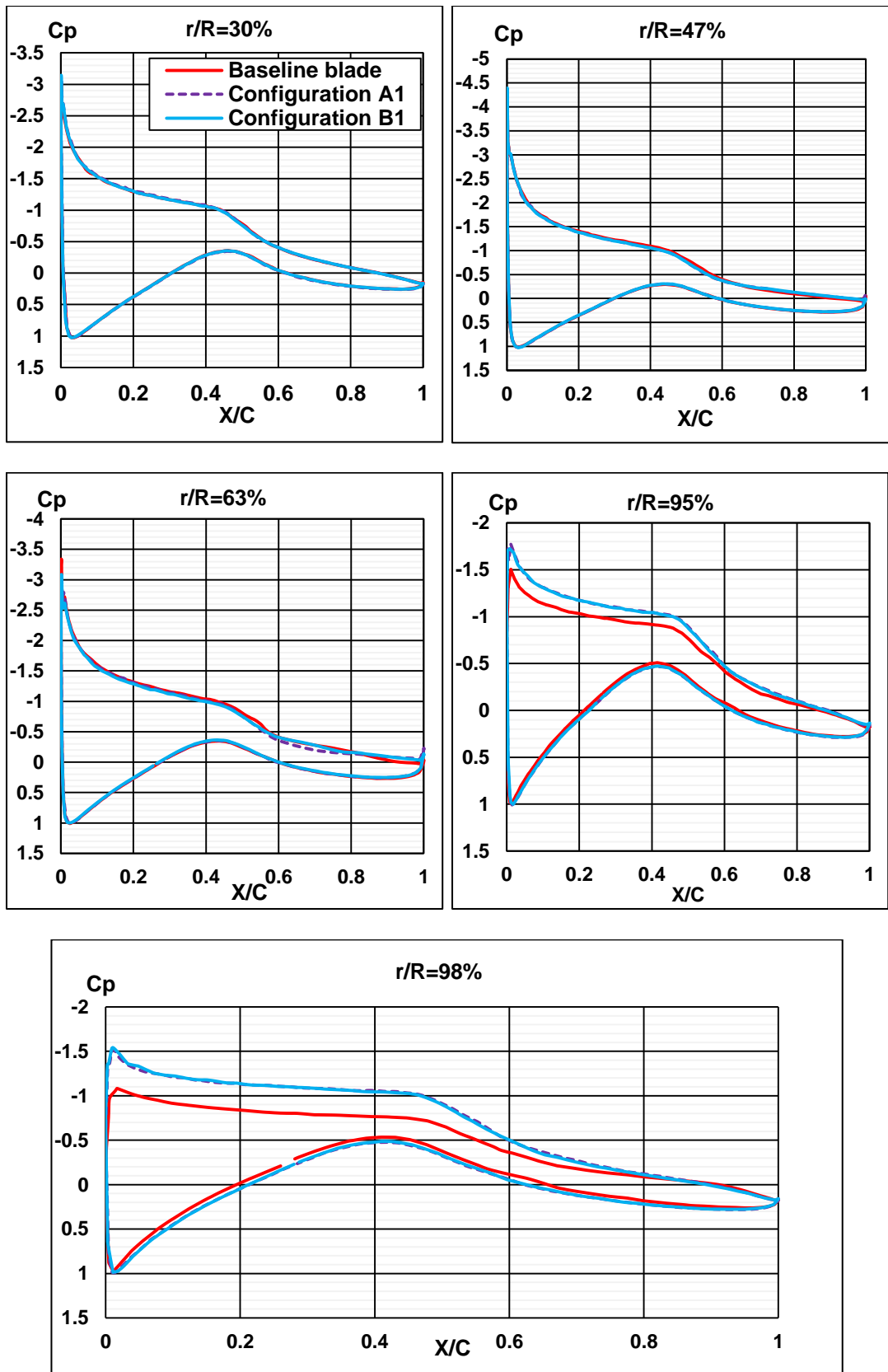


Figure 6-12 Comparisons of computed pressure coefficients between the baseline blade and configurations (A1 and B1) at 7m/s.

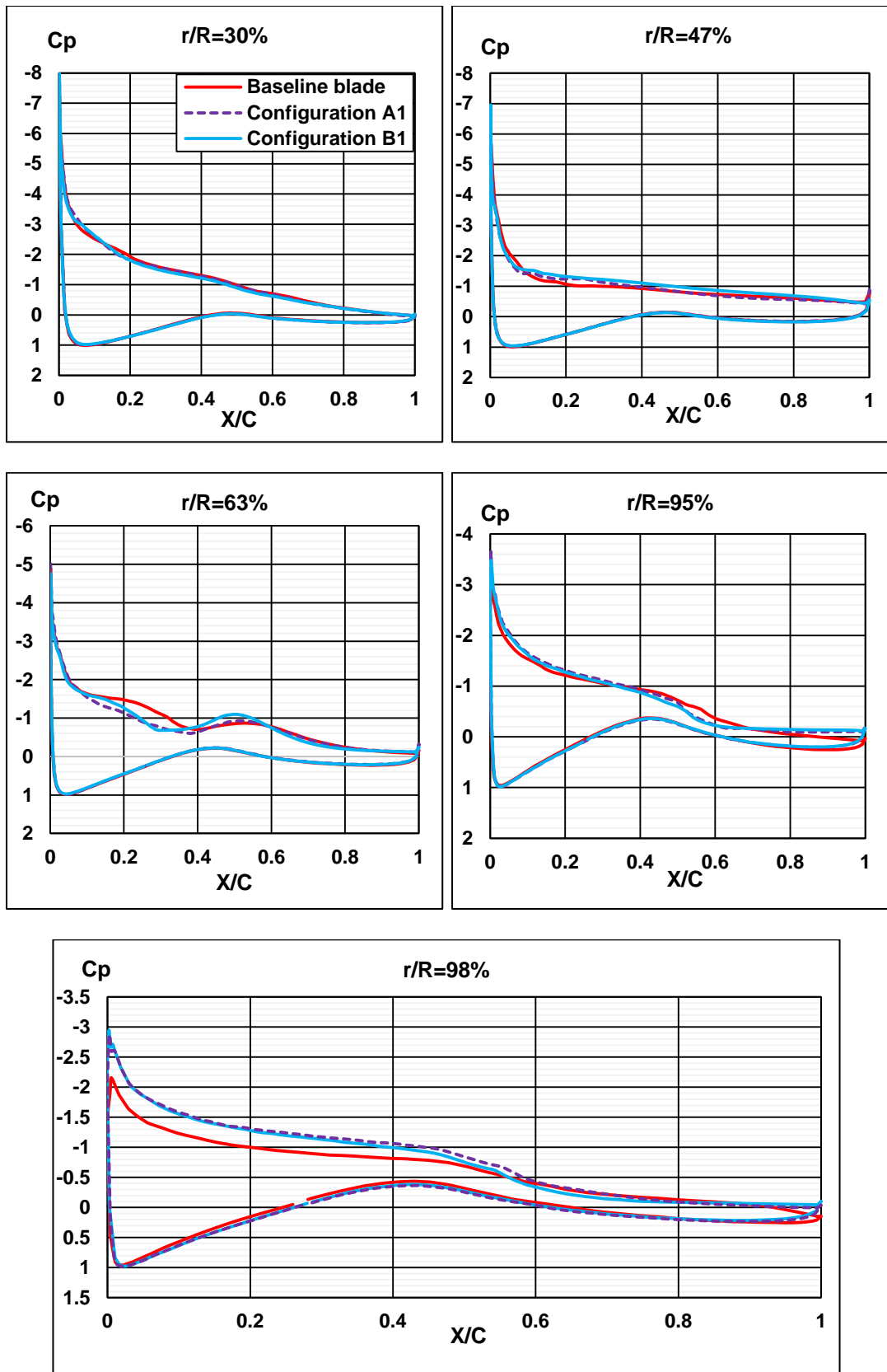


Figure 6-13 Comparisons of computed pressure coefficients between the baseline blade and configurations (A1 and B1) at 10m/s.

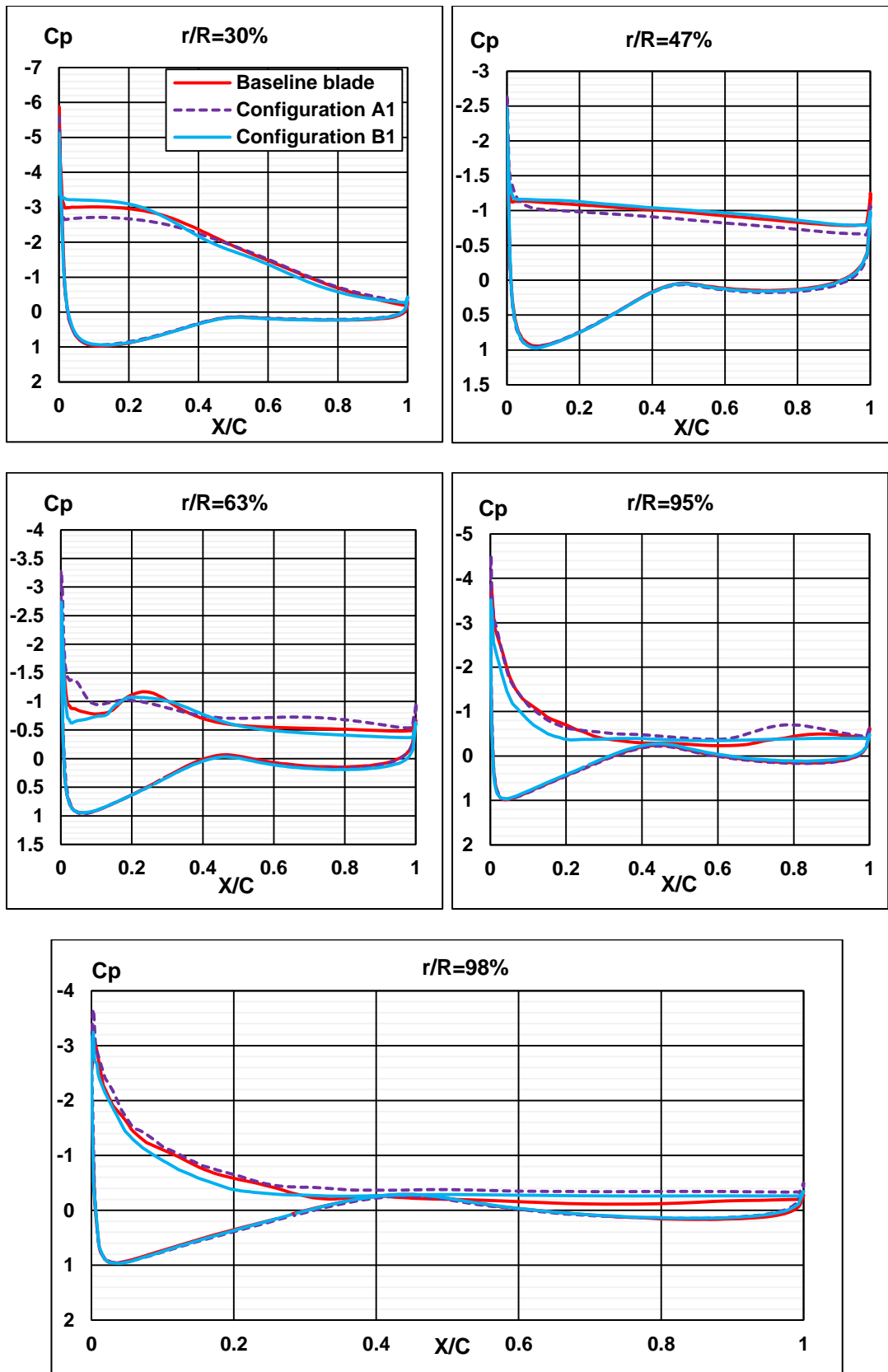


Figure 6-14 Comparisons of computed pressure coefficients between the baseline blade and configurations (A1 and B1) at 15m/s.

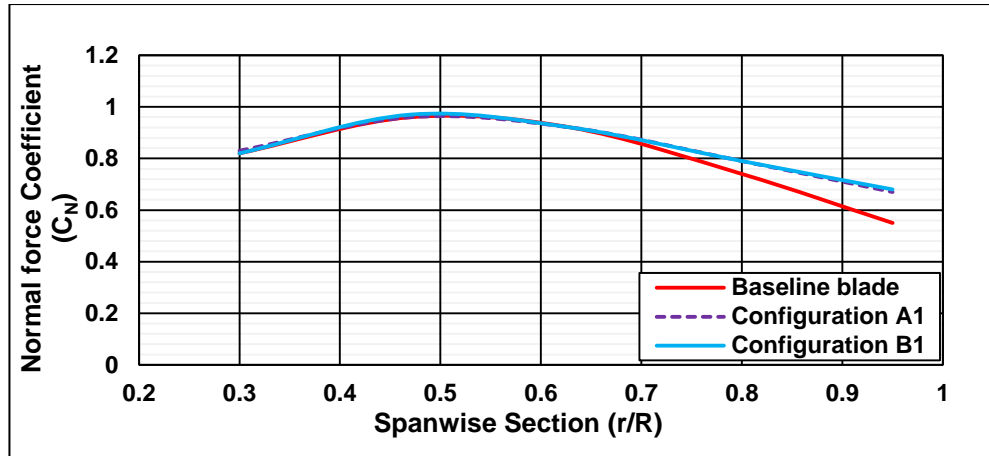


Figure 6-15 Comparison of normal force coefficients between the baseline blade and configurations (A1, B1) at 7m/s.

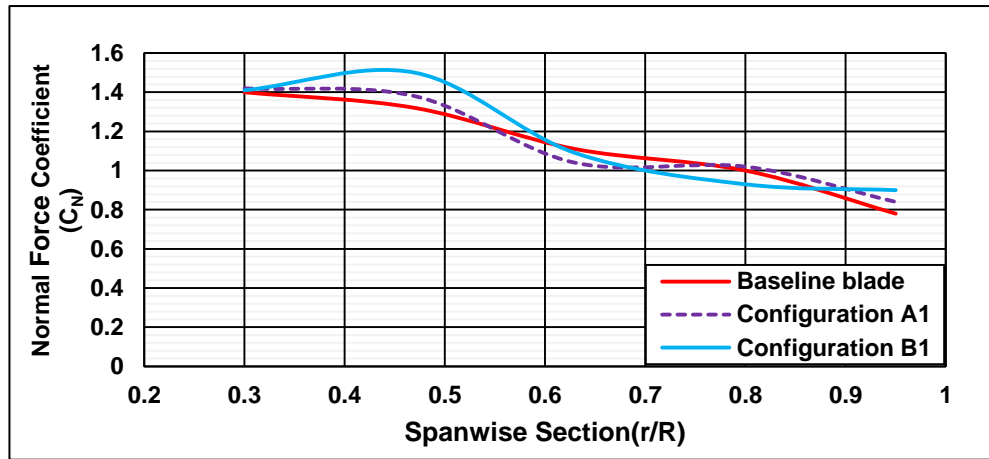


Figure 6-16 Comparison of normal force coefficients between the baseline blade and configurations (A1, B1) at 10m/s.

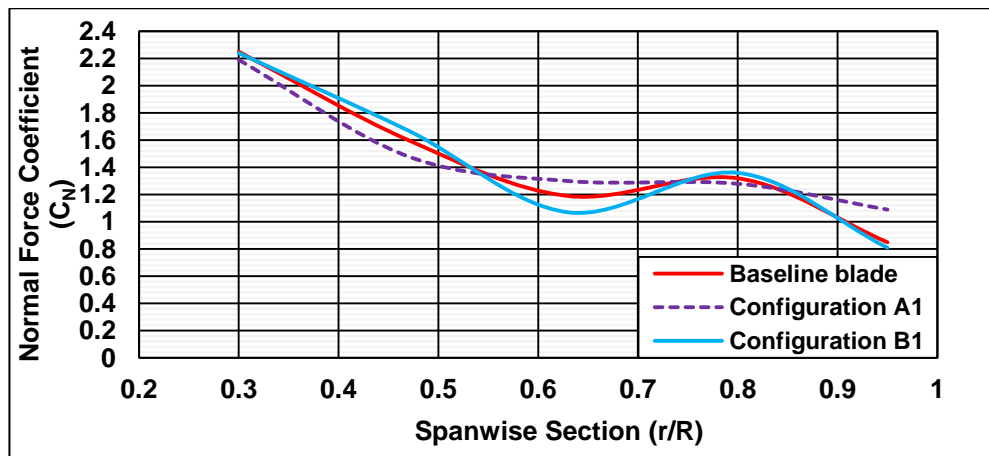


Figure 6-17 Comparison of normal force coefficients between the baseline blade and configurations (A1, B1) at 15m/s.

6.7 Sectional flow and surface wall shear streamlines

This section presents the aerodynamic influence of the configurations (A1 and B1) on the flow field of the NREL phase VI at wind speeds of 7m/s and 15 m/s, as shown in Figures 6-18 to 6-29.

At wind speeds of 7m/s and 15m/s, due to the location of the winglet where it is attached at the blade tip. There is no significant effect resulting from using both configurations (A1, B1) on the chordwise direction flow at the blade sections of 30%, 47%, 63%, 80% and 95%, as shown in Figures 6-18 and 6-19, respectively.

Meanwhile, the gain of the winglet is clearly displayed by presenting the pressure contours, as shown in Figures 6-20 to 6-25. At 7m/s, where the flow is almost attached, both configurations improve the pressure field near the blade top, particularly at the suction side where the configurations are tilted, as shown in Figure 6-20. When comparing it to the baseline blade, this improvement increases towards the top of the baseline blade at the sections of 95% and 98% span of the blade, as shown in Figures 6-22 and 6-23 respectively. This result agrees with the pressure coefficient distributions that are shown in similar sections in Figure 6-12.

In contrast, at 15m/s, the suction side of the blade is dominated by the separation flow, as shown in Figure 6-19. There is no significant improvement observed in the pressure field at the suction side of the blade, as shown in Figure 6-21. However, improvements in the difference of pressure contours can be observed at the section of 95% and 98% span of the blade, as shown in Figures 6-24 and 6-25, respectively. The gains in the pressure contours have occurred as a result of slight improvements in the pressure coefficients that are obtained at section 95% and 98% for both configurations (A1 and B1), as illustrated in Figure 6-14.

Figures 6-26 and 6-27 show the effect of configurations A1 and B1 on the skin friction streamlines that are observed in speeds of 7m/s and 15m/s, respectively. These figures show the skin friction lines are removed away from the baseline tip towards the trailing edge on the pressure and suction sides, for configurations A1 or B1. Accordingly, the wingtip vortices are generated at the winglet tip of configurations A1 or B1, instead of the baseline tip, as shown in Figures 6-28 and 6-29.

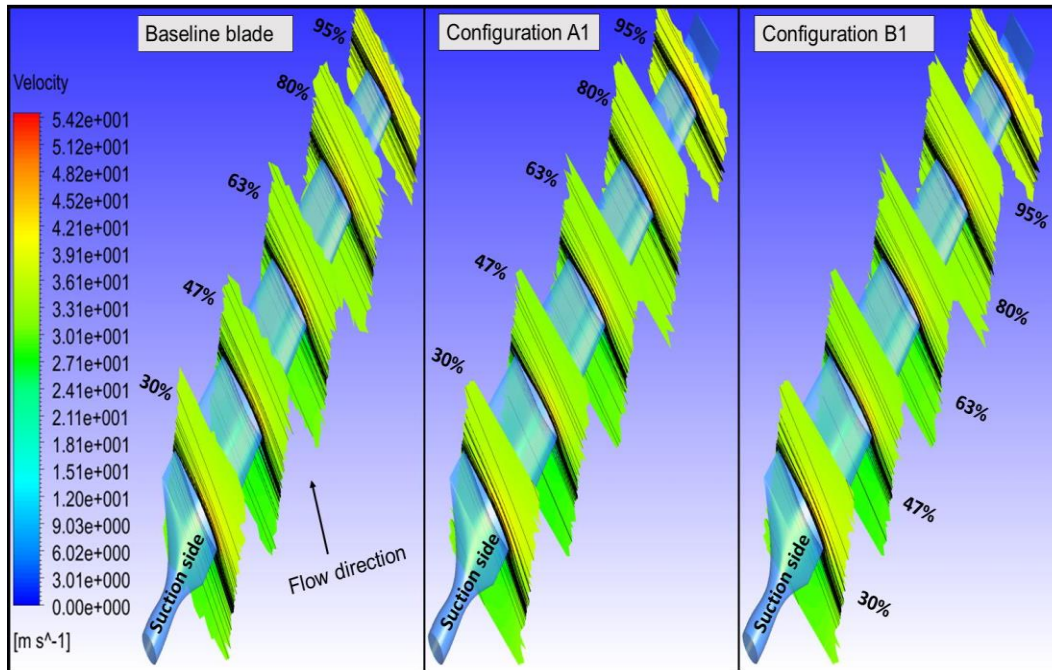


Figure 6-18 Comparison of velocity contours and sectional flow streamlines between the baseline blade and configurations (A1, B1) at 7m/s.

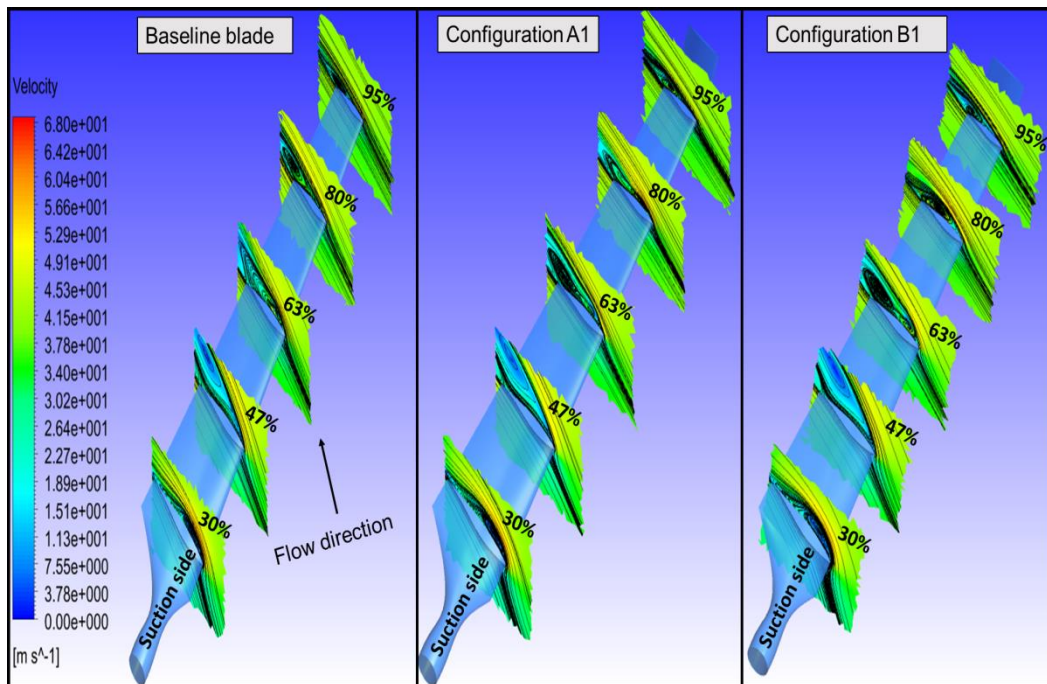


Figure 6-19 Comparison of velocity contours and sectional flow streamlines between the baseline blade and configurations (A1, B1) at 15m/s.

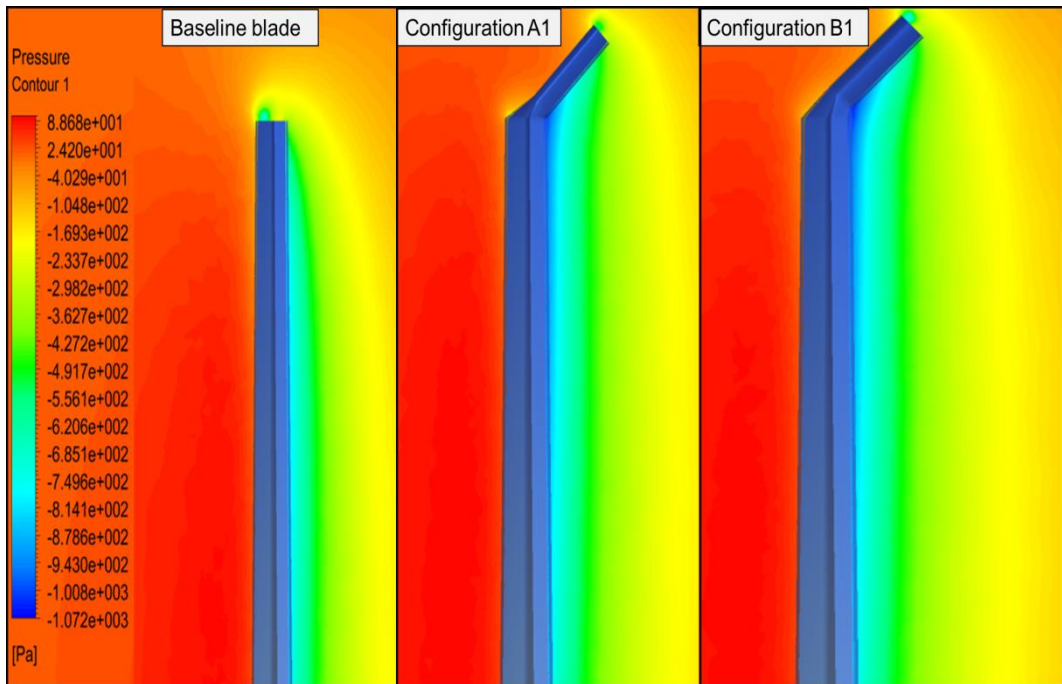


Figure 6-20 Comparison of pressure contours between baseline blade and configurations (A1 and B1) at 7m/s.

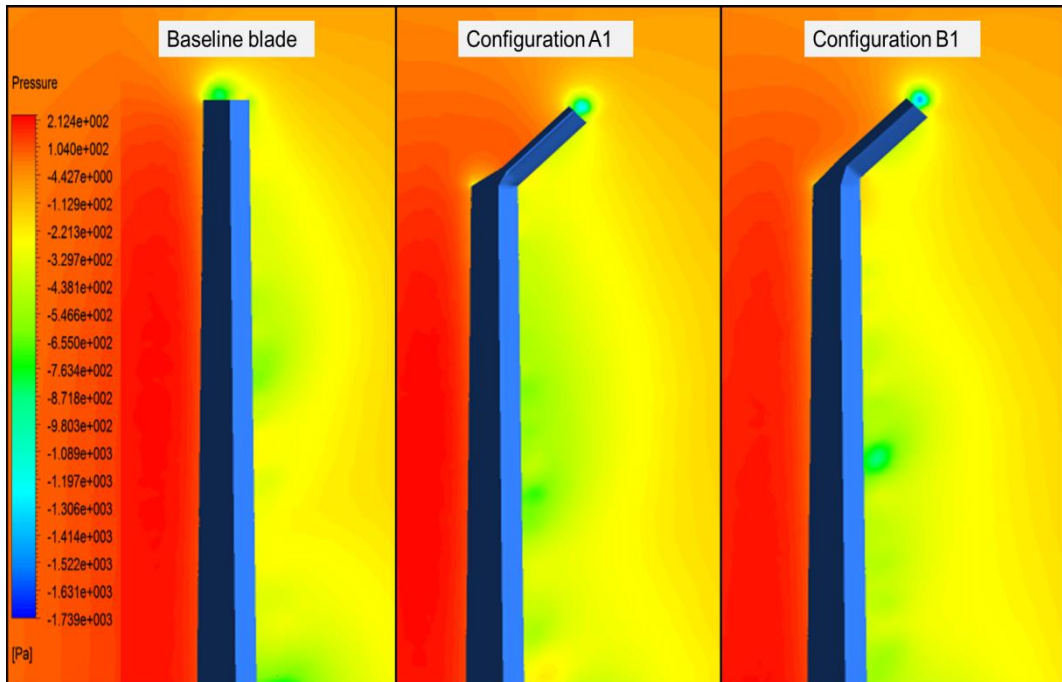


Figure 6-21 Comparison of pressure contours between baseline blade and configurations (A1 and B1) at 15m/s.

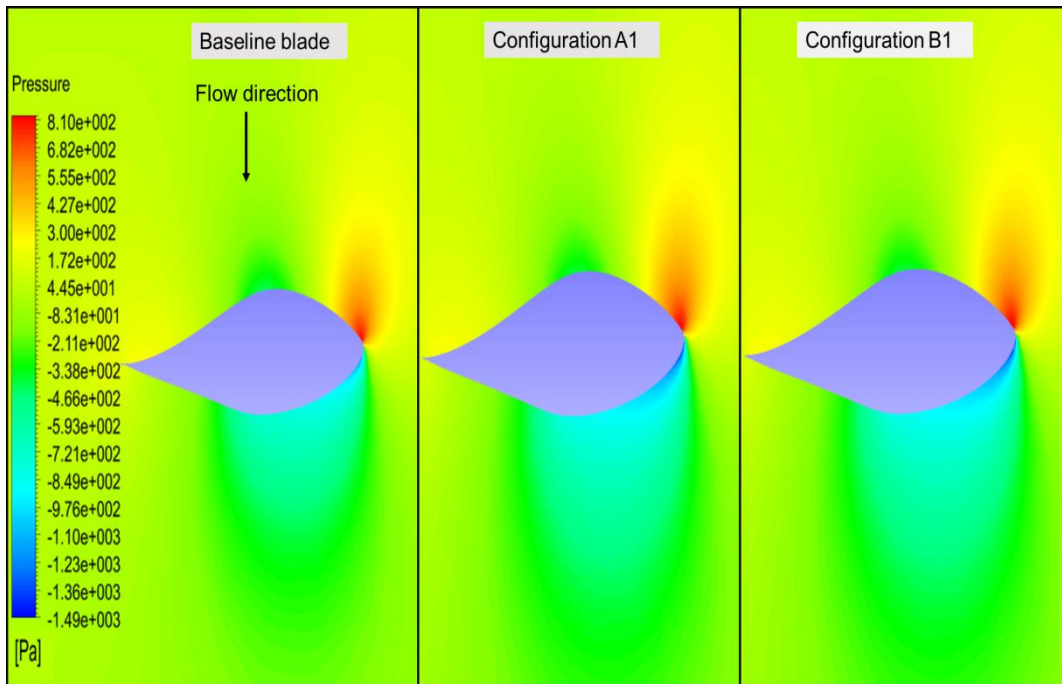


Figure 6-22 Comparison of pressure contours between baseline blade and configurations (A1 and B1 at section of 95%) at 7m/s.

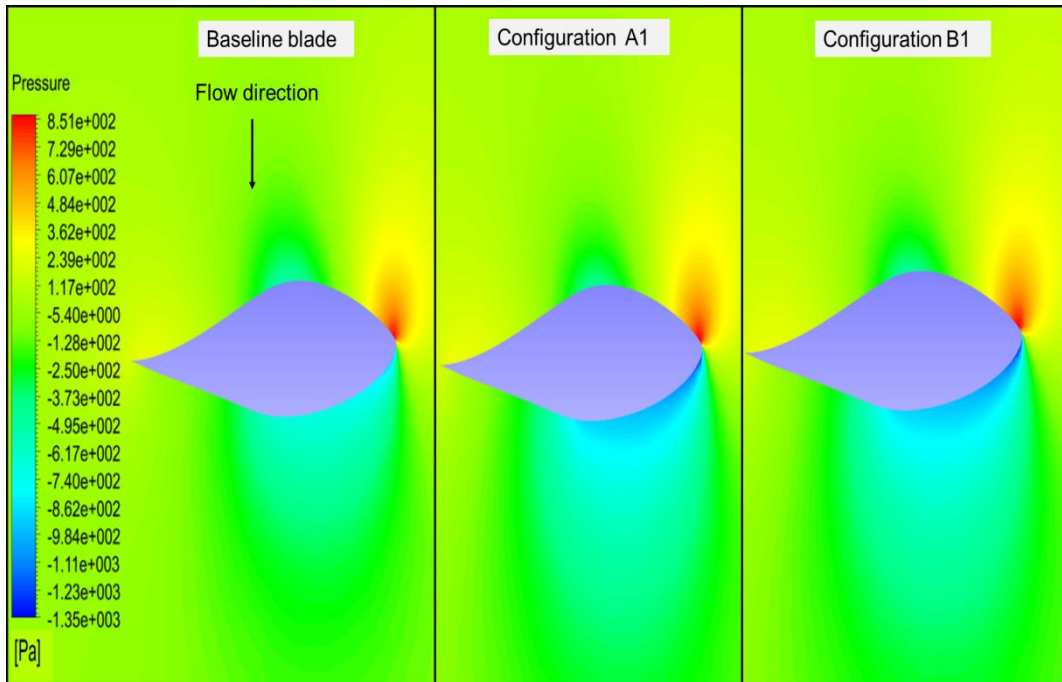


Figure 6-23 Comparison of pressure contours between baseline blade and configurations (A1 and B1 at section of 98%) at 7m/s.

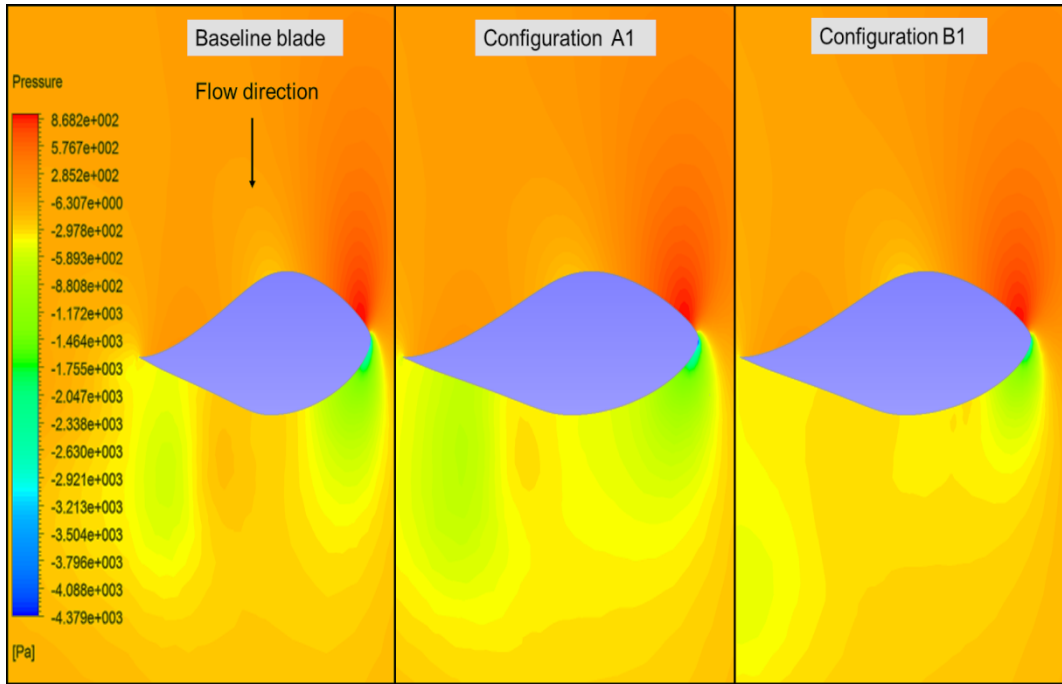


Figure 6-24 Comparison of pressure contours between baseline blade and configurations (A1 and B1 at section of 95%) at 15m/s.

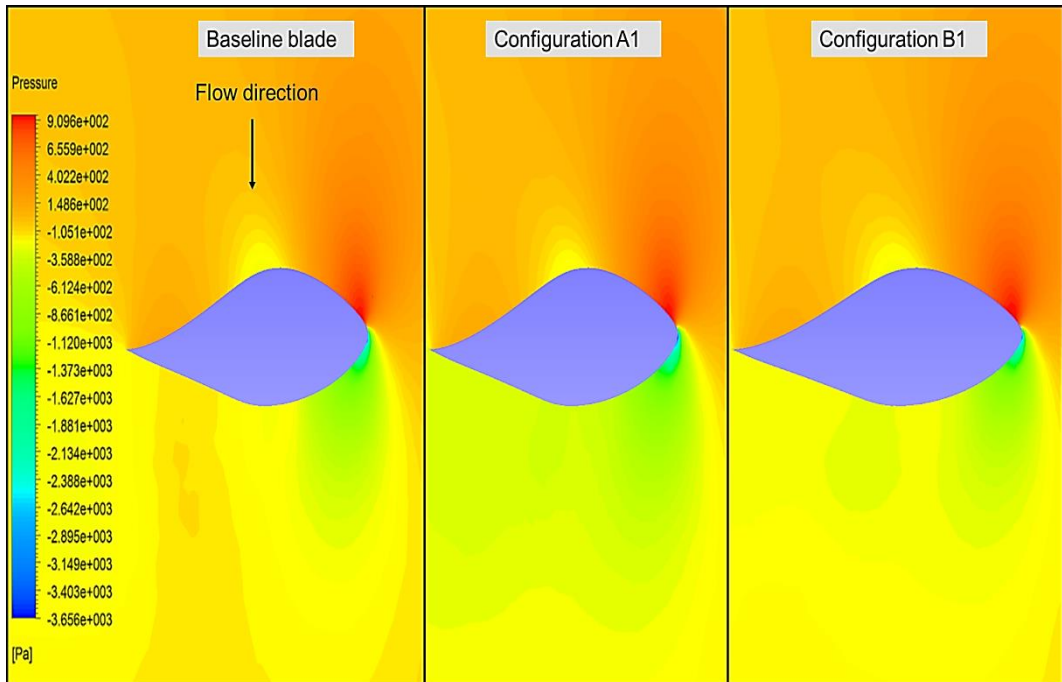


Figure 6-25 Comparison of pressure contours between baseline blade and configurations (A1 and B1 at section of 98%) at 15m/s.

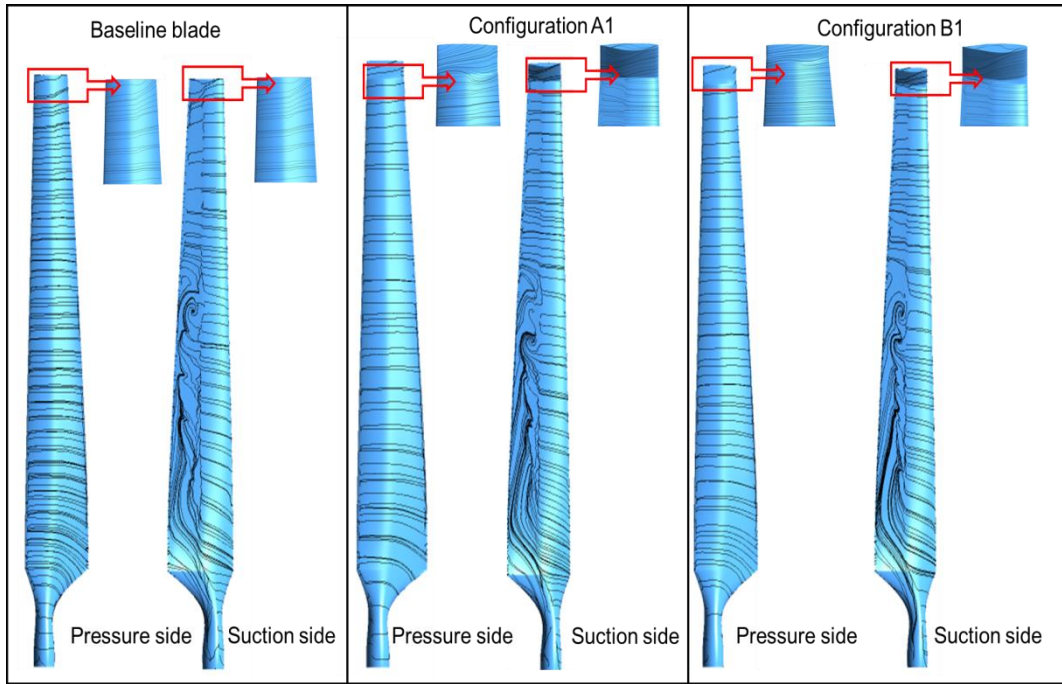


Figure 6-26 Comparison of surface wall shear streamlines between the baseline blade and configurations (A1 and B1) at 7m/s.

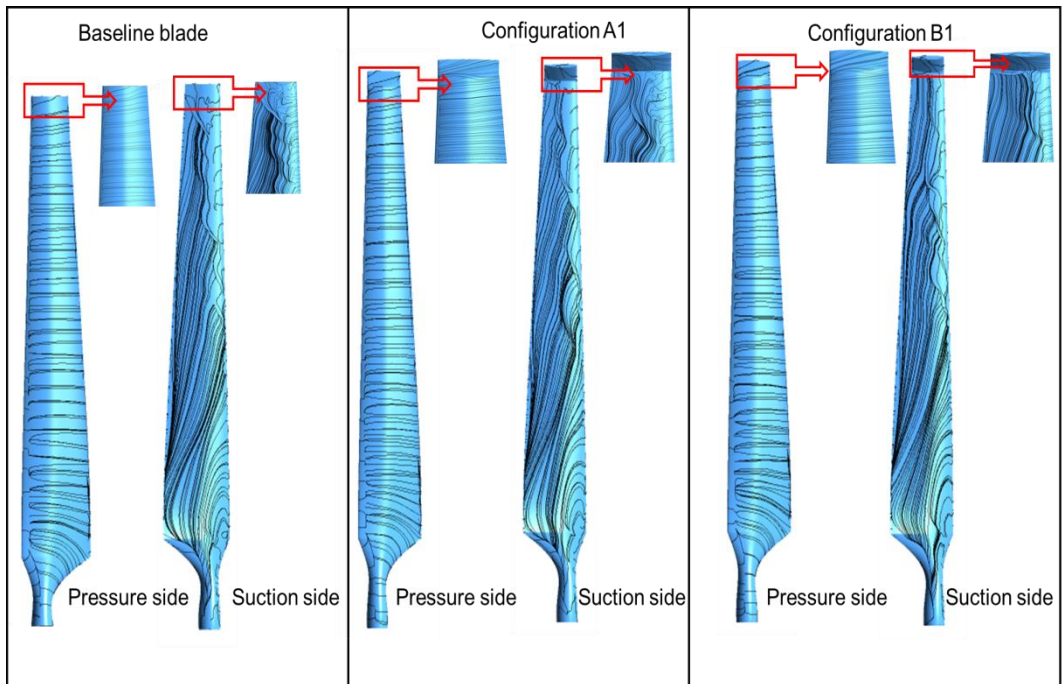


Figure 6-27 Comparison of surface wall shear streamlines between baseline blade and configurations (A1 and B1) at 15m/s.

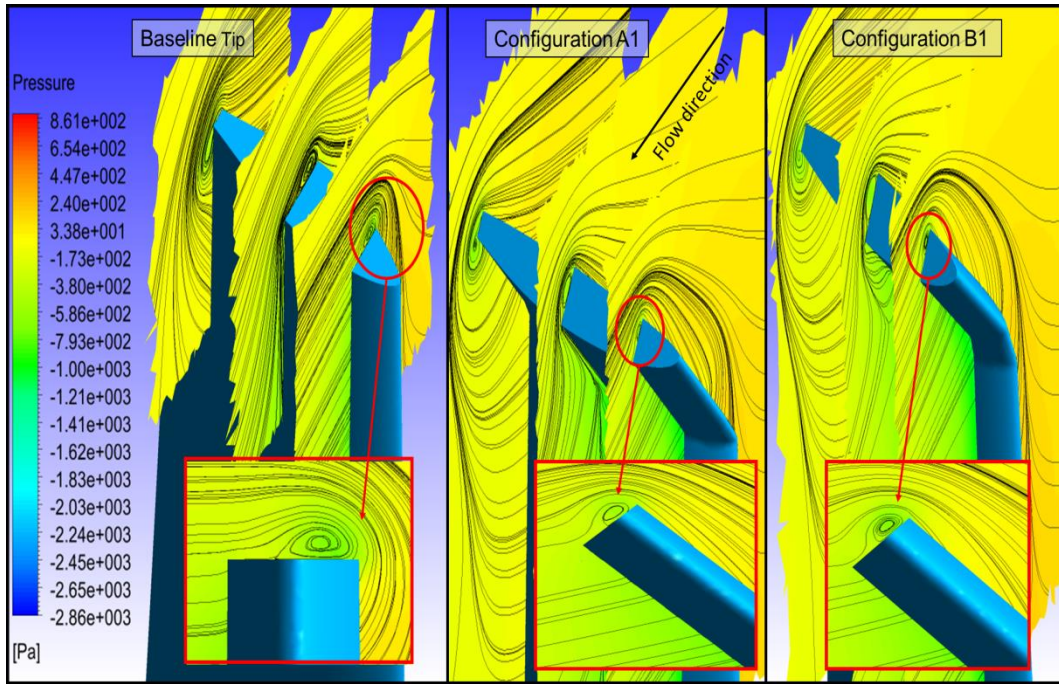


Figure 6-28 Comparison of pressure contours and sectional flow streamlines between baseline blade and configurations (A1 and B1) at 7 m/s.

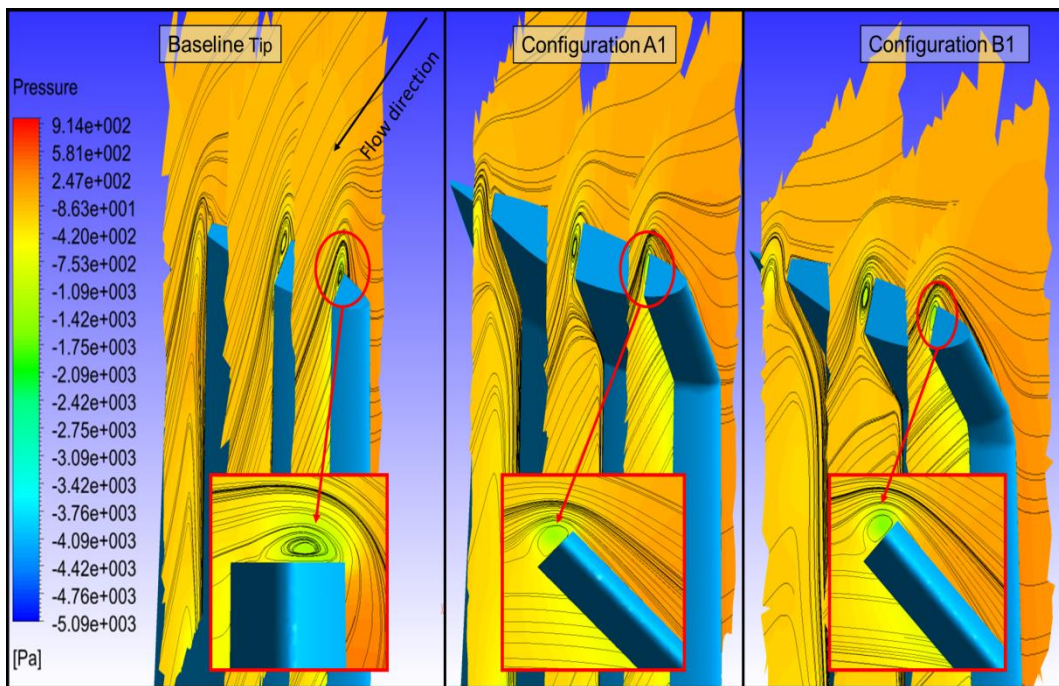


Figure 6-29 Comparison of the pressure contours and sectional flow streamlines between baseline blade and configurations (A1 and B1) at 15m/s.

6.8 Power and Thrust Force

Both configurations (A1 and B1) were created using the S806A and S805A airfoils, respectively, whilst keeping the same winglet parameters, including height, planform and cant angle. Consequently, the aerodynamic performance (C_l/C_d) of both airfoils is the only factor that affects the function of configurations A1 and B1. The importance of the C_l/C_d is given as a drag coefficient (C_d) significantly affects the penalty of the profile drag, which is obtained due to attaching a winglet. In addition, the lift coefficient (C_l) is influenced by the stalled flow, which exists at a range of 10m/s to 20m/s.

Hence, from Figure 6-9 and (Tables B-5 and B-4 Appendix-B) at 0° AOA, the S806A airfoil has $C_l/C_d= 42.61$, which is higher than the C_l/C_d of the S805A airfoil, which equals 39.72. Additionally, the drag coefficient of the S806A is 0.00562 and is less than the drag coefficient of the S805A (0.00626). Consequentially, the penalty of profile drag that resulted from using the S806A for creating configuration A1 is less than that of configuration B1.

Table 6-2 and Figure 6-30 show the percentages of increase in power that were obtained for configurations A1 and B1 comparing to the improvements achieved using the configuration 1 (S809 airfoil).

Regarding the Configurations A1 and B1, The maximum increase in the output power was achieved by attaching configuration A1. The best improvements in the output power, due to attaching configuration A1 are 8.34% and 7.39 % at low wind speeds of 5m/s and 7m/s, respectively, where the flow regime is almost attached. These improvements are due to the absence of the effect of stalled flow and when the profile drag is not significantly affected by low wind speed. However, the performance enhancement of configuration A1 is decreased when the wind speed increases above 10m/s, as a result of existence of the stall regime to limit the peak power and increase the effect of profile drag.

Unlike configuration A1, the configuration B1 shows less performance enhancement in the power increase of the rotor at wind speeds of 5m/s and 7m/s, as shown in Table 6-2. In addition, there is a significant reduction in the performance enhancement of configuration B1 at wind speeds greater than 10m/s, where the stalled flow is dominated along the blades, and the profile drag increases with the square of wind speed.

Figure 6-33 and Table 6-2 show that the thrust force was increased for both configurations (A1 and B1). The increase in the thrust force occurs due to the extension of the baseline blade towards the suction side by 15cm, which

results in improvements in the pressure coefficients, particularly near the blade top. Thereby, normal force coefficients increased, as explained and illustrated in Figures 6-15 to 6-17. Accordingly, configuration A1 causes a percentage increase in thrust force that is slightly greater than configuration B1 as a result of further increases in the C_N value. Table 6-2 shows the maximum percentage of increase in thrust force was obtained at 5m/s by 8.81%, and then decreased with increasing wind speed to the minimum value of 0.19% at 20m/s.

Table 6-2 Percentages of the power increase and thrust force using the configurations (1, A1 and B1).

Wind Speed (m/s)	Configuration A1 (S806A airfoil)		Configuration B1 (S805A airfoil)		Configuration 1 (S809 airfoil)	
	Power %	Thrust %	Power %	Thrust %	Power %	Thrust %
5	8.34	8.81	7.36	8.00	9.1	10.3
7	7.39	7.55	5.55	6.44	9.4	9.5
10	4.91	3.88	1.55	3.71	9.8	6.9
15	3.37	3.05	1.02	3.61	6.1	5.9
20	6.78	0.19	0.34	-0.23	1.7	3.1

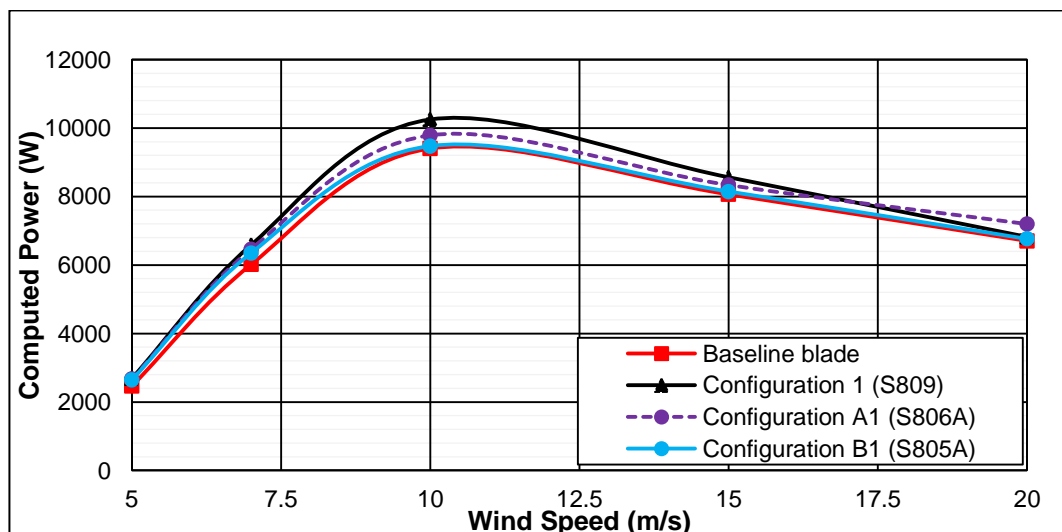


Figure 6-30 Comparison of calculated power between baseline blade and configurations (1, A1 and B1).

However, from Table 6-2 and Figure 6-30, both the configurations (A1 and B1) show less percentages of increase in power than that obtained for the configuration 1 (S809 airfoil). Configuration 1 results in more improvements in pressure coefficients near the blade top at the suction sides. These improvements are observed, particularly, at suction 95% and 98% span of the blade, for instance, at 10 m/s as shown in Figures 6-31 and 6-32, respectively. Accordingly, more increase in the thrust force is obtained due to attaching configuration 1 than that resulted for configurations A1 and B1 as shown in Figure 6-33.

The superiority of the configuration 1 might be rising due to the S809 airfoil is thicker than both S806A and S805A airfoils since the max thickness of S809 airfoil is 21% of chord length when compared to 11.5% and 13.5% of chord length for the S806A and S805A airfoils, respectively (Tangler and Somers, 1995). Accordingly, more kinetic energy could be extracted by the baseline blade in case of configuration 1 which results greater percentage of increase in power than that obtained for the configurations A1 and B1. However, the performance enhancement of configuration 1 is more affected than configuration A1 at high wind speed, particularly, at 20 m/s due to the stalled flow and penalty of the profile drag as shown in Table 6-2.

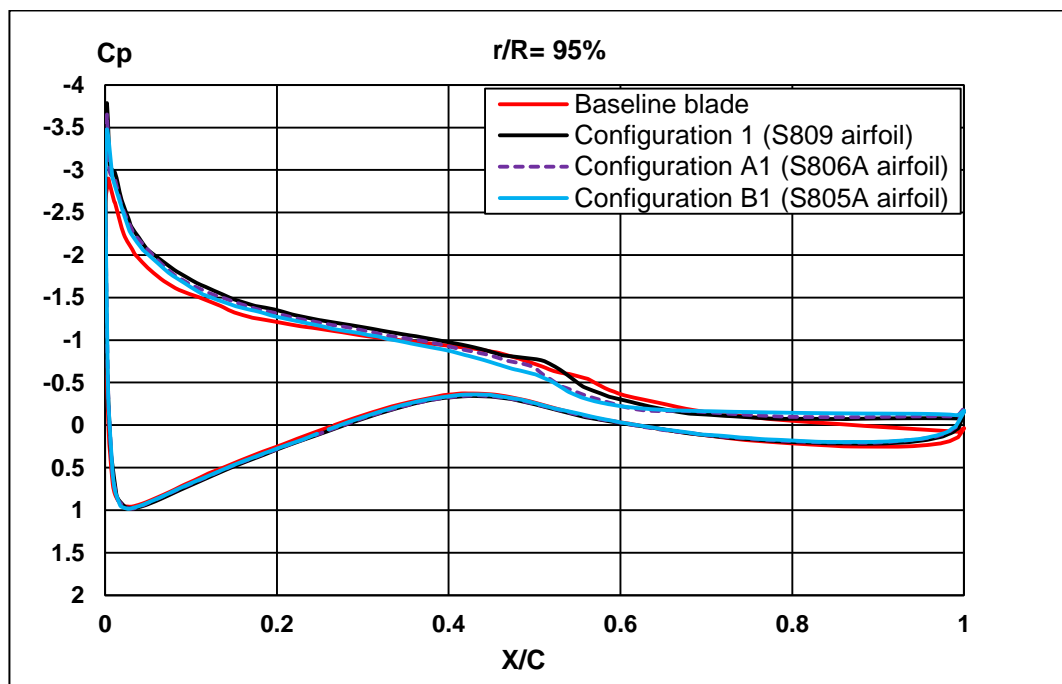


Figure 6-31 Comparison of pressure coefficients between baseline and configurations (1, A1, B1) at section of 95%.

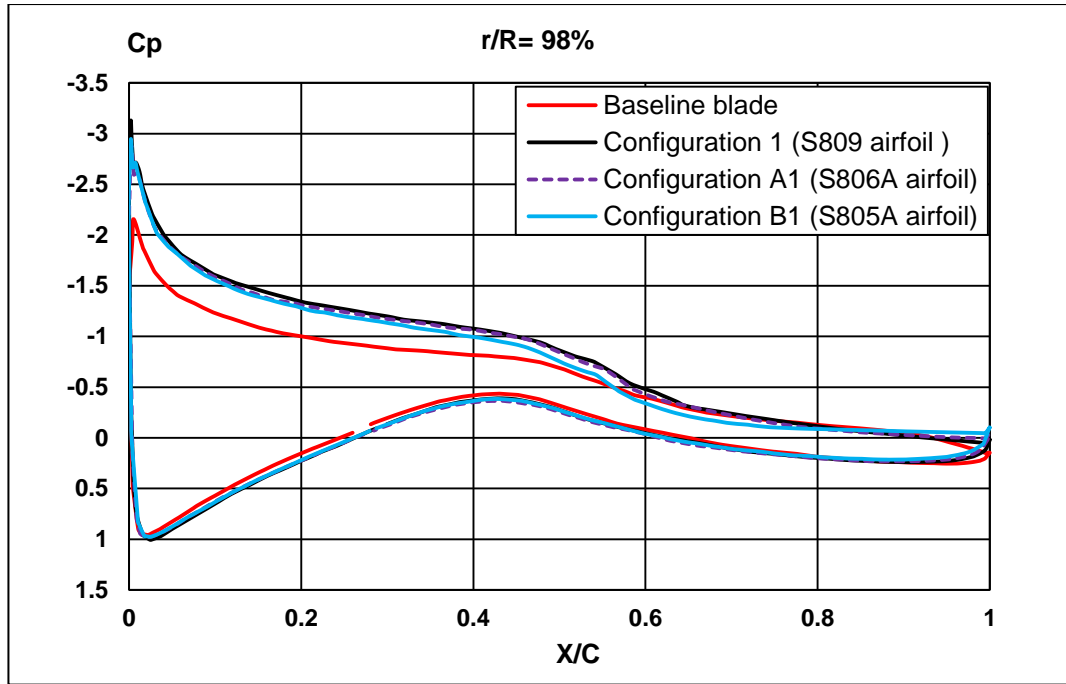


Figure 6-32 Comparison of pressure coefficients between baseline blade and configurations (1, A1, B1) at section of 98%.

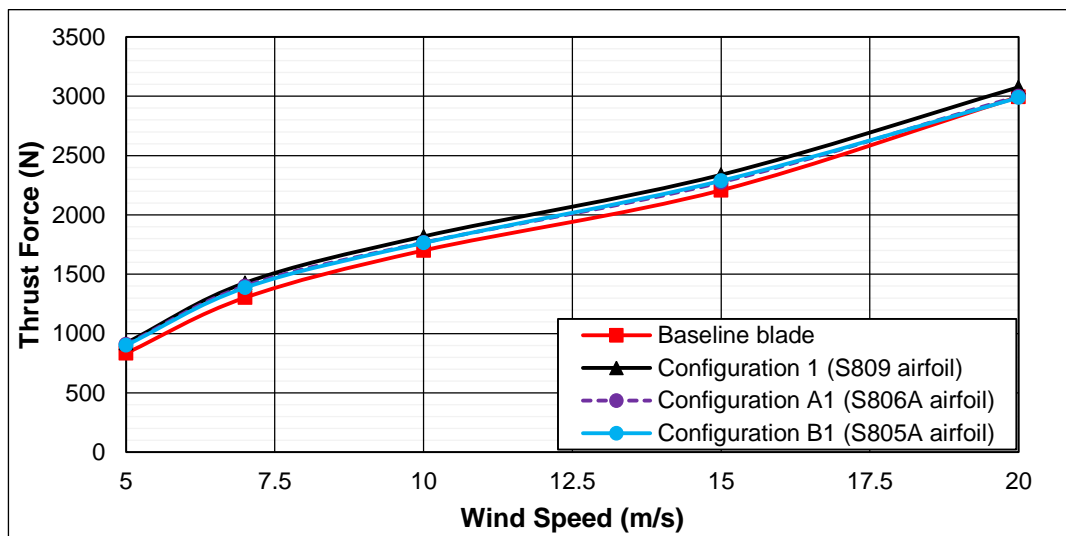


Figure 6-33 Comparison of calculated thrust force between baseline blade and configurations (1, A1 and B1).

6.9 Winglet airfoil requirements

The winglet airfoil requirements have been investigated in this chapter aerodynamically. An efficient winglet design needs an airfoil that generates the lift required with the lowest possible drag to avoid the penalty of profile drag at high wind speeds. Hence, the winglet airfoil should be designed to avoid generating the laminar separation bubbles that increase significantly the drag coefficient against a remarkably decrease in the lift coefficient resulting in deterioration of the winglet performance.

In addition, it is noteworthy that the operating conditions of the blade tip airfoil play a vital role to determine the optimum coefficients of winglet airfoil to secure the best winglet performance. Thus, it is most important to fully understand the mechanism of winglet function and how it aerodynamically impact the wind turbine performance to avoid the poor design.

Hence, the operating conditions of the S809 airfoil (tip airfoil of the NREL phase VI rotor) at Reynolds number 1×10^6 was taken as reference conditions to choose an effective winglet airfoil. In order to test the influence of new winglet airfoil on the NREL phase VI rotor performance. The range of wind speeds 5-10 m/s was chosen where the flow is almost attached and it is expected to obtain the best winglet performance as shown in the comparative analysis of the winglet configurations in chapter five (see Tables 5-2 and 5-3).

Preliminary calculations in 2D were carried out using Xfoil code to predict the aerodynamic coefficients of four NREL airfoils (S801, S803, S805A and S806A) which designed as blade tip airfoils (see Table 2-2). Considering the less drag coefficients, the S805A and S806A airfoils were chosen to generate two rectangular winglet planforms that attached at the tip of the baseline blade. The CFD results show the greatest percentage in power increase was obtained in case of employing the S806A due to it has lower C_d when compared to the S805A airfoil.

6.10 Conclusions

This chapter studied the effects of the aerodynamic behaviour of the winglet airfoil on its performance, since it is significantly affected by a drag coefficient. A preliminary analysis of 4 airfoils, namely, S801, S803, S805A and S806A has been presented.

The preliminary analysis was carried out using the Xfoil code towards predicting the aerodynamic performance of the selected airfoils by calculating the aerodynamic coefficients, such as the lift, drag and moment coefficients. In choosing a suitable winglet airfoil, the S806A and S805A airfoils were selected due to the fact that they have the less drag coefficients. The reason behind choosing the less drag coefficient is to reduce the effect of the penalty of profile drag, which affects a winglet performance.

3D CFD calculations are used to predict the performance of the winglet configurations (A1 and B1), that are created by implementing the S806A and S805A airfoils. In order to examine the effect of the winglet airfoil, both configurations are generated by keeping the same winglet parameters, including height, planform, tilting direction, and cant angle.

At low wind speeds of 5m/s and 7m/s where the flow is almost attached, it was found that winglet configuration A1 yields the greatest improvement in terms of power by 8.34% and 7.39%, respectively, as compared to the baseline. The S806A airfoil performs better than S805A to increase the wind turbine power as it has a greater aerodynamic performance ratio and less drag coefficient than the S805A airfoil.

In contrast, at wind speeds above 10m/s, the performance of both configurations is affected by the stalled flow and by increasing the effect of the profile drag. Consequently, configuration A1 shows a performance that is better than configuration B1 due to implementing the S806A airfoil, which has a drag coefficient that is less than the S805A airfoil.

In addition, a comparison was carried out between the performances of the configurations 1, A1 and B1. The configuration 1 shows greater percentages of increase in power than configurations A1 and B1.

Chapter 7 : Conclusions and Recommended Future Work

7.1 Conclusions

The main objective of this study was to investigate the aerodynamic effect of the winglet on wind turbine performance, using the CFD method. The following issues have been considered and studied:

- Choosing the turbulence model to predict the performance of the NREL phase VI, with and without attaching a winglet.
- A numerical study of the aerodynamic effect of the winglet planform on the overall performance of the wind turbine.
- A numerical study of the aerodynamic effect of the winglet airfoil on the overall performance of the wind turbine.

According to this study, the following points can be drawn:

- In this study, the SST k- ω and the Spalart-Allmaras turbulence models have been used for the simulation of aerodynamic behaviour of wind turbine. Both models show a good agreement with the experimental data, at a range of low wind speeds between 5m/s and 8m/s, due to the absence of stalled flow. At wind speeds higher than 10m/s, the Spalart-Allmaras model over-predicts the calculated torque due to the separation flow, while the SST k- ω shows a reasonable match between the calculated torque and the experimental data. Consequentially, the SST k- ω model is implemented to predict the properties of fluid flow in all the CFD calculations in the present study.
- The aerodynamic behaviour of two winglet planforms, i.e. rectangular and elliptical winglets, attached to the NREL phase VI has been investigated. The streamlines of skin friction show both winglet planforms diffuse the wingtip vortices from the baseline tip towards the winglet tip. In this regard, the elliptical planform caused more reduction in the wingtip vortices, as compared with the rectangular planform, due to the reduction of the elliptical tip by 75% when compared to the rectangular tip.
- A rectangular planform shows better performance enhancement than an elliptical planform for the power increase, despite less reduction in the wingtip vortices, as compared with the elliptical planform. The rectangular planform increases the NREL phase VI performance to more than 9%, at the range of low wind speeds from 5m/s to 10m/s, since the flow is almost

attached. However, this performance significantly decreases at higher wind speeds than 10m/s due to the presence of stalled flow and penalty of the profile drag.

- The pressure coefficient distributions reveal the aerodynamic gain of attaching winglets is limited near the blade top. The numerical results show that there are no significant improvements in the pressure coefficients at 30%, 47%, and 63% span wise section of the baseline blade. In contrast, improvements in the pressure coefficients are clearly observed toward the suction side of the blade, where the winglet is canted, particularly at 95% and 98% span wise section of the blade.
- The numerical results show that greater increase in the output power is achieved using the configurations that are tilted by the cant angle of 45° against the angle of 90° . A major advantage of using the cant angle of 45° is to capture more available energy from the moving air by extending the span of the baseline blade. The same reason causes improvements in the NREL phase VI performance, due to an increase the winglet height. Accordingly, the highest percentage of the power increase is achieved by attaching configuration 1, which extended and canted by 15cm and 45° , respectively.
- A suitable winglet airfoil is mainly dependent on the aerodynamic coefficients of the selected airfoil, such as C_l , C_d and C_m . For this purpose, a preliminarily analysis was conducted using the Xfoil code to predict the aerodynamic coefficients of selected airfoils (S801, S803, S805A and S806A airfoils). The S806A and S805A airfoils were chosen to create configuration A1 and B1, respectively, since they have less drag coefficients than other airfoils. The full calculations by CFD simulations show that configuration A1 leads to further increase in the power for NREL phase VI, as compared to configuration B1, presumably due to a lower C_d for S806A airfoil.
- An efficient winglet should be designed to increase the frontal projection area of the wind turbine rotor with the least winglet wetted area in order to avoid the effect of the profile drag. Hence, the winglet height, cant angle and the profile drag are the most important parameters that should be optimised to achieve the greatest wind turbine performance. In addition, this optimisation should be carried out where the flow is attached since the stalled flow significantly increases the penalty of profile drag resulting in deterioration of the winglet performance.

7.2 Future work

The recommended future work based on this thesis is as follows:

- All winglet calculations are conducted to improve the performance of the NREL phase VI, which is a stall regulated wind turbine. Consequentially, winglet performance is affected by the separation flow that exists at the wind speeds more than 10m/s.

Future work is required to investigate the aerodynamic effects of attaching winglets on wind turbine performance, with the absence of the stalled flow. For this purpose, the variable-pitch wind turbine can be recommended to use as a baseline case.

- In the current study, the highest percentage of power increase was slightly more than 9%, which is achieved by attaching configuration 1, using the S809 airfoil at the low range of wind speeds from 5m/s to 10m/s.

Further work is needed to reduce the penalty of the profile drag for configuration 1, by optimising the S809 airfoil.

- The current study focused on the aerodynamic effect of winglets to improve the power of a wind turbine, using different winglet configurations that are obtained by changing the winglet planform and airfoil.

Future work is recommended to investigate the aerodynamic effect of the winglet planform and airfoil on the aerodynamic properties of wingtip vortices, such the strength of the tip vortices, propagation speed and their travelling time.

- Improving the performance of wind turbines by attaching winglets results in an increase in thrust force which leads to more rise in a flapwise bending moment compared with the baseline blade. Accordingly, more increase in tip deflection is expected in case of attaching winglets.

Consequently, future work requires a structured analysis using CFD tools to study the effects of attaching winglets on the wind turbine tip deflection to ensure the operation of wind turbines in safe conditions.

References

- Abedi, H. 2016. "*Development of Vortex Filament Method for Wind Power Aerodynamics*". PhD thesis, Dept. of Applied Mechanics, Chalmers University of Technology, Göteborg, Sweden.
- Abedi, H. 2011. "*Aerodynamic loads on rotor blades*". Master thesis, Chalmers University of Technology.
- Abedi, H., Davidson, L. and Voutsinas, S. 2013. "Vortex method application for aerodynamic loads on rotor blades". *EWEA 2013: Europe's Premier Wind Energy Event, 4-7 February Vienna*.
- Al-Abadi, A. 2014. "*Novel Strategies for Aerodynamic Performance Improvement of Wind Turbines in Turbulent Flow*". PhD thesis, Friedrich-Alexander-Universität Erlangen-Nürnberg (FAU).
- Alfredsson, P.H. and Dahlberg, J. 1979. "*A preliminary wind tunnel study of windmill wake dispersion in various flow conditions*", 198024, NASA.
- Ali, A. 2014. "*Aerodynamic optimisation of small scale horizontal axis wind turbine blades*". Master thesis, RMIT University, Melbourne, Australia.
- Almohammadi, K.M. 2014. "*Optimization of a CFD based design of a straight blade vertical axis wind turbine (SB-VAWT)*". PhD thesis, University of Leeds.
- Anderson, J. 2001. "Incompressible Flow over Finite Wings: Prandtl's Classical Lifting-Line Theory". *Fundamentals of Aerodynamics*. **3**, pp.360-387.
- Anderson, J.D. 2010. "*Fundamentals of aerodynamics*". Third ed., Tata McGraw-Hill Education, New York.
- Aranake, A.C., Lakshminarayan, V.K. and Duraisamy, K. 2012. "Assessment of transition model and CFD methodology for wind turbine flows". *42nd AIAA Fluid Dynamics Conference and Exhibit, 25-28 June, New Orleans, Louisiana*.
- Ariffudin, M.H., Zawawi, F.M., Kamar, H.M. and Kamsah, N. 2016. "Effectiveness of blade tip on low speed horizontal axis wind turbine performance". *JURNAL TEKNOLOGI*. **78**(8-4), pp.31-39.
- Arndt, R.E. 2002. "Cavitation in vortical flows". *Annual Review of Fluid Mechanics*. **34**(1), pp.143-175.
- Bai, C. and Wang, W. 2016. "Review of computational and experimental approaches to analysis of aerodynamic performance in horizontal-axis wind turbines (HAWTs)". *Renewable and Sustainable Energy Reviews*. **63**, pp.506-519.
- Batten, W., Bahaj, A., Molland, A., Chaplin, J. and Group, S.E.R. 2007. "Experimentally validated numerical method for the hydrodynamic design of horizontal axis tidal turbines". *Ocean engineering*. **34**(7), pp.1013-1020.

- Berens, M. 2008. "*Potential of multi-winglet systems to improve aircraft performance*". PhD thesis, Technical University of Berlin.
- Branlard, E. 2011. "*Wind turbine tip-loss corrections: review, implementation and investigation of new models*". Master thesis, Technical University of Denmark, Denmark.
- Buhl Jr, M.L. 2005. "*New Empirical Relationship between Thrust Coefficient and Induction Factor for the Turbulent Windmill State*", NREL/TP-500-36834, USA, NREL.
- Burton, T., Sharpe, D., Jenkins, N. and Bossanyi, E. 2001. "*Wind energy handbook*". John Wiley & Sons Ltd, West Sussex, England.
- Carcangiu, C.E. 2008. "*CFD-RANS study of horizontal axis wind turbines*". PhD thesis, Università degli Studi di Cagliari.
- Celik, I.B. 1999. "*Introductory turbulence modeling*". West Virginia University, USA.
- Chen, H. 2016. "*Numerical Study of Trailing Edge Flow Control for Horizontal Axis Wind Turbines*". PhD thesis, University of Sheffield.
- Coleman, G.N. and Sandberg, R.D. 2010. "*A primer on direct numerical simulation of turbulence-methods, procedures and guidelines*". University of Southampton, UK.
- Congedo, P.M. and De Giorgi, M.G. 2008. Optimizing of a wind turbine rotor by CFD modeling. *ANSYS Italy Conference, 16-17 October, Mestre, Italy*.
- Craft, T., Graham, L. and Launder, B.E. 1993. "Impinging jet studies for turbulence model assessment—II. An examination of the performance of four turbulence models". *International Journal of Heat and Mass Transfer*. **36**(10), pp.2685-2697.
- Derakhsahan, S. and Tavazziani, A. 2015. "Study of wind turbine aerodynamic performance using numerical methods". *Clean Energy Technol.* **3**(2), pp.83-90.
- Drela, M. 1989. "XFOIL: An analysis and design system for low Reynolds number airfoils". *Low Reynolds number aerodynamics*. Springer, pp.1-12.
- Drela, M. and Youngren, H. 2001. *XFOIL 6.94 user guide*. Secondary" XFOIL 6.94 user guide". MIT Aero & Astro.
- Elfarrar, M.A. 2011. "*Horizontal axis wind turbine rotor blade: winglet and twist aerodynamic design and optimization using CFD*". PhD thesis, Middle East Technical University

- Elfarrar, M.A., Sezer - Uzol, N. and Akmandor, I.S. 2014. "NREL VI rotor blade: numerical investigation and winglet design and optimization using CFD". *Wind energy*. **17**(4), pp.605-626.
- Elfarrar, M.A., Sezer Uzol, N. and Akmandor, I.S. 2015. "Investigations on Blade Tip Tilting for Hawt Rotor Blades Using CFD". *International Journal of Green Energy*. **12**(2), pp.125-138.
- Elfarrar, M.A., Sezer Uzol, N. and Akmandor, I.S. 2014. "Investigations on Blade Tip Tilting for Hawt Rotor Blades Using CFD". *International Journal of Green Energy*. **12**(2), pp.125-138.
- Fluent. 2006. "*FLUENT v6. 3*", ANSYS.
- Fluent. 2009. "*ANSYS FLUENT 12.0 User's Guide*", USA, ANSYS.
- Fluent, A. 2013. "*Release 15.0*", USA, ANSYS.
- Freudenreich, K., Kaiser, K., Schaffarczyk, A., Winkler, H. and Stahl, B. 2004. "Reynolds number and roughness effects on thick airfoils for wind turbines". *Wind Engineering*. **28**(5), pp.529-546.
- Fu, P. and Farzaneh, M. 2010. "A CFD approach for modeling the rime-ice accretion process on a horizontal-axis wind turbine". *Journal of Wind Engineering and Industrial Aerodynamics*. **98**(4), pp.181-188.
- Gall, P.D. and Smith, H.C. 1987. "Aerodynamic characteristics of biplanes with winglets". *Journal of Aircraft*. **24**(8), pp.518-522.
- Gatski, T.B., Hussaini, M.Y. and Lumley, J.L. 1996. "*Simulation and modeling of turbulent flows*". Oxford University Press, New York.
- Gaunaa, M. and Johansen, J. 2007. "Determination of the maximum aerodynamic efficiency of wind turbine rotors with winglets". *Journal of Physics: Conference Series 75 (2007) 012006*: IOP Publishing.
- Gertz, D.P. 2011. "*An evaluation testbed for alternative wind turbine blade tip designs*". Master thesis, University of Waterloo.
- Giuni, M. 2013. "*Formation and early development of wingtip vortices*". PhD thesis, University of Glasgow.
- Gomez and Munduate, X. 2014. "Zig-zag tape influence in NREL Phase VI wind turbine". *Journal of Physics: Conference Series 524 (2014) 012096*: IOP Publishing, p.012096.
- Guo, H., Wen, S. and Ping, D. 2015. "Research on Dynamic Stall and Aerodynamic Characteristics of Wind Turbine 3D Rotational Blade". *International Journal of Simulation-Systems, Science & Technology*. **16**.
- Gupta, A. and Amano, R. 2012. "CFD Analysis of Wind Turbine Blade With Winglets". *ASME 2012 International Design Engineering Technical*

Conferences and Computers, 12–15 August, Chicago, USA. American Society of Mechanical Engineers, pp.843-849.

Gupta, S. 2006. "*Development of a time-accurate viscous Lagrangian vortex wake model for wind turbine applications*". PhD thesis, University of Maryland.

GWEC. 2017. "*Global Wind Energy Council (GWEC)*", 5 May 2017, Brussels, Belgium, GWEC.

Hand, M., Simms, D., Fingersh, L., Jager, D., Cotrell, J., Schreck, S. and Larwood, S. 2001. "*Unsteady aerodynamics experiment phase VI: wind tunnel test configurations and available data campaigns*", 2001 December, NREL/TP-500-29955, USA, NREL.

Hansen, M.O. 2015. "*Aerodynamics of wind turbines*". Second ed., Earthscan, London.

Hau, E. 2013. "*Wind Turbines: Fundamentals, Technologies, Application, Economics*". Springer Science & Business Media, Germany.

Heyson, H.H., Riebe, G.D. and Fulton, C.L. 1977. "*Theoretical parametric study of the relative advantages of winglets and wing-tip extensions*", SEPTEMBER 1977 NASA Technical Paper 1020, USA, NASA.

Hirsch, C. 2007. "*Numerical computation of internal and external flows: The fundamentals of computational fluid dynamics*". Volume 1, Second ed., Butterworth-Heinemann, USA.

Hoffmann, K.A. and Chiang, S.T. 2000. "*Computational Fluid Dynamics*". Volume III, Fourth ed., EES, Kan, USA.

Ingram, G. 2005. "*Wind turbine blade analysis using the blade element momentum method*". Durham University, UK.

Irtaza, H. 2009. "*Experimental and computational determination of wind loads on netted/sheeted scaffolds*". PhD thesis, Oxford University, UK.

James, F., Manwell, J., McGowan, A. and Rogers, L. 2009. "*Wind Energy Explained: Theory, Design and Application*". Second ed., John Wiley & Sons, UK.

Jasinski, W.J., Noe, S.C., Selig, M.S. and Bragg, M.B. 1998. "Wind turbine performance under icing conditions". *Transactions-American society of mechanical engineers journal of solar energy engineering*. **120**, pp.60-65.

Johansen, J., Sorensen, N., Michelsen, J. and Schreck, S. 2002. "Detached-eddy simulation of flow around the NREL phase-VI blade". *ASME 2002 Wind Energy Symposium: American Society of Mechanical Engineers*, pp.106-114.

Johansen, J. and Sørensen, N.N. 2006. "*Aerodynamic investigation of winglets on wind turbine blades using CFD*", Risø-R-1543(EN), Denmark, Laboratory, R.N.

- Johansen, J. and Sørensen, N.N. 2007. "Numerical analysis of winglets on wind turbine blades using CFD". *European Wind Energy Congress*: Citeseer.
- Jonkman, J.M. 2003. "Modeling of the UAE wind turbine for refinement of FAST_AD", NREL/TP-500-34755, NREL.
- Kim, H. and Patel, V. 2000. "Test of turbulence models for wind flow over terrain with separation and recirculation". *Boundary-Layer Meteorology*. **94**(1), pp.5-21.
- Kocurek, J.D. and Tangler, J.L. 1977. "A prescribed wake lifting surface hover performance analysis". *Journal of the American Helicopter Society*. **22**(1), pp.24-35.
- Kolmogorov, A.N. 1991. "The local structure of turbulence in incompressible viscous fluid for very large Reynolds numbers". *Proceedings: Mathematical and Physical Sciences*. **434**(1890), pp.9-13.
- Landgrebe, A.J. 1972. "The wake geometry of a hovering helicopter rotor and its influence on rotor performance". *Journal of the American Helicopter Society*. **17**(4), pp.3-15.
- Länger - Möller, A., Löwe, J. and Kessler, R. 2017. "Investigation of the NREL phase VI experiment with the incompressible CFD solver THETA". *Wind Energy*. **20**(9), pp.1529-1549.
- Lanzafame, R., Mauro, S. and Messina, M. 2013. "Wind turbine CFD modeling using a correlation-based transitional model". *Renewable energy*. **52**, pp.31-39.
- Lanzafame, R. and Messina, M. 2007. "Fluid dynamics wind turbine design: Critical analysis, optimization and application of BEM theory". *Renewable energy*. **32**(14), pp.2291-2305.
- Lauder, B. and Sharma, B. 1974. "Application of the energy-dissipation model of turbulence to the calculation of flow near a spinning disc". *Letters in heat and mass transfer*. **1**(2), pp.131-137.
- Lauder, B.E., Reece, G.J. and Rodi, W. 1975. "Progress in the development of a Reynolds-stress turbulence closure". *Journal of fluid mechanics*. **68**(3), pp.537-566.
- Lauder, B.E. and Spalding, D.B. 1974. "The numerical computation of turbulent flows". *Computer methods in applied mechanics and engineering*. **3**(2), pp.269-289.
- Lee, K., Roy, S., Huque, Z., Kommalapati, R. and Han, S. 2017. "Effect on Torque and Thrust of the Pointed Tip Shape of a Wind Turbine Blade". *Energies*. **10**(1), p79.
- Lee, K., Roy, S., Huque, Z., Kommalapati, R., Sui, C. and Munir, N. 2016. "Pointed Tip Shape Effect on Aerodynamic Load for NREL Phase VI Wind Turbine Blade". *Journal of Clean Energy Technologies*. **4**(4).

- Leishman, J.G. 2002. "Challenges in modelling the unsteady aerodynamics of wind turbines". *Wind energy*. **5**, pp.85-132.
- Li, Y. 2014. "*Coupled computational fluid dynamics/multibody dynamics method with application to wind turbine simulations*". PhD thesis, University of Iowa.
- Lindenburg, C. 2003. "*Investigation into rotor blade aerodynamics*", ECN 74112, NOVEM.
- Maniaci, D. 2013. "*Wind turbine design using a free-wake vortex method with winglet application*". PhD thesis, Pennsylvania State University.
- Manwell, J.F., McGowan, J.G. and Rogers, A.L. 2010. "*Wind energy explained: theory, design and application*". John Wiley & Sons, USA.
- Mathew, S. 2006. "*Wind energy: fundamentals, resource analysis and economics*". Springer, India.
- Maughmer, M. 2006. "The design of winglets for low-speed aircraft". *Technical Soaring*. **30**(3), p6173.
- Maughmer, M. and Kunz, P. 1998. "Sailplane winglet design". *Technical Soaring*. **22**(4), pp.116-123.
- Maughmer, M.D. 2002. "About Winglets". *Soaring Magazine*. **26**(3), p18.
- Maughmer, M.D. 2003. "Design of winglets for high-performance sailplanes". *Journal of Aircraft*. **40**(6), pp.1099-1106.
- Maughmer, M.D., Swan, T.S. and Willits, S.M. 2002. "Design and testing of a winglet airfoil for low-speed aircraft". *Journal of Aircraft*. **39**(4), pp.654-661.
- Menter, F., Langtry, R. and Likki, S. 2004. "*A correlation based transition model using local variables part I—model formulation*". ASME Paper No".
- Menter, F., Langtry, R. and Völker, S. 2006. "Transition modelling for general purpose CFD codes". *Flow, turbulence and combustion*. **77**(1-4), pp.277-303.
- Menter, F.R. 1992. "Performance of popular turbulence model for attached and separated adverse pressure gradient flows". *AIAA journal*. **30**(8), pp.2066-2072.
- Menter, F.R. 1994. "Two-equation eddy-viscosity turbulence models for engineering applications". *AIAA journal*. **32**(8), pp.1598-1605.
- Menter, F.R. 1992. "*Improved two-equation k-omega turbulence models for aerodynamic flows*", NASA Technical Memorandum 103975, California, NASA.
- Mo, J. and Lee, Y. 2012. "CFD Investigation on the aerodynamic characteristics of a small-sized wind turbine of NREL PHASE VI operating

with a stall-regulated method". *Journal of mechanical science and technology*. **26**(1), pp.81-92.

Moriarty, P.J. and Hansen, A.C. 2005. "AeroDyn theory manual", No. NREL/TP-500-36881, NREL.

Moshfeghi, M., Song, Y.J. and Xie, Y.H. 2012. "Effects of near-wall grid spacing on SST K-W model using NREL Phase VI horizontal axis wind turbine". *Journal of Wind Engineering and Industrial Aerodynamics*. **107**, pp.94-105.

Nilsson, K. 2015. "Numerical computations of wind turbine wakes and wake interaction", SE-100 44 Stockholm, Sweden, Technology, R.I.o.

NREL. 2016. "NREL's S809 Airfoil Graphic and Coordinates". [Online] National Renewable Energy Laboratory. [Accessed 10/5/2016]. Available from: http://wind.nrel.gov/airfoils/Shapes/S809_Shape.html.

Park, K., Seol, H., Choi, W. and Lee, S. 2009. "Numerical prediction of tip vortex cavitation behavior and noise considering nuclei size and distribution". *Applied Acoustics*. **70**(5), pp.674-680.

Park, Y.M., Chang, B. and Cho, T. 2007. "Numerical simulation of wind turbine scale effects by using CFD". *Proceedings of the 45th Aerospace Sciences Meeting and Exhibition., 8-11 January, Reno, USA*.

Peyret, R. and Krause, E. 2000. "Advanced turbulent flow computations". Springer, USA.

Pope, S.B. 2001. "Turbulent flows". Cornell University, UK.

Potsdam, M.A. and Mavriplis, D.J. 2009. "Unstructured mesh CFD aerodynamic analysis of the NREL Phase VI rotor". *AIAA paper*. **1221**, p2009.

Prabhakar, A. and Ohri, A. 2014. "Application of CFD Simulation in the Design of a Parabolic Winglet on NACA 2412 ". *Proceedings of the World Congress on Engineering 2014, July 2 - 4, London, UK*.

Pratumnopharat, P. 2012. "Novel methods for fatigue data editing for horizontal axis wind turbine blades". thesis, Northumbria University.

Quon, E. 2014. "Data transfer strategies for overset and hybrid computational methods". PhD thesis, Georgia Institute of Technology.

Rahimi, H., Daniele, E., Stoevesandt, B. and Peinke, J. 2016. "Development and application of a grid generation tool for aerodynamic simulations of wind turbines". *Wind Engineering*. **40**(2), pp.148-172.

Robison, D., Coton, F., Galbraith, R.M. and Vezza, M. 1995. "Application of a prescribed wake aerodynamic prediction scheme to horizontal axis wind turbines in axial flow". *Wind Engineering*. pp.41-51.

- Sagol, E., Reggio, M. and Ilinca, A. 2012. "Assessment of two-equation turbulence models and validation of the performance characteristics of an experimental wind turbine by CFD". *ISRN Mechanical Engineering*. **2012**.
- Sant, T. 2007. "*Improving BEM-based aerodynamic models in wind turbine design codes*". PhD thesis, Delft University.
- Saravanan, P. 2013. "*Aerodynamic analysis of small horizontal axis wind turbine blades with winglets*". PhD thesis, ANNA University.
- Saravanan, P., Parammasivam, K. and Selvi Rajan, S. 2013. "Experimental Investigation on Small Horizontal Axis Wind Turbine Rotor Using Winglets". *Journal of Applied Science and Engineering*. **16**(2), p159 to 164.
- Sezer-Uzol, N. 2006. "*Unsteady flow simulations around complex geometries using stationary or rotating unstructured grids*". PhD thesis, Pennsylvania State University.
- Shih, T., Liou, W.W., Shabbir, A., Yang, Z. and Zhu, J. 1995. "A new k- ϵ eddy viscosity model for high reynolds number turbulent flows". *Computers & Fluids*. **24**(3), pp.227-238.
- Simms, D., Schreck, S., Hand, M. and Fingersh, L. 2001. "NREL unsteady aerodynamics experiment in the NASA-Ames wind tunnel: a comparison of predictions to measurements". *National Renewable Energy Laboratory, Golden, CO, Report No. NREL/TP-500-29494*.
- Smith, M., Komerath, N., Ames, R., Wong, O. and Pearson, J. 2001. "Performance analysis of a wing with multiple winglets". *19th AIAA Applied Aerodynamics Conference, 11- 14 June USA*. p.2407.
- Snel, H., Houwink, R., Bosschers, J., Piers, W., Van Bussel, G. and Bruining, A. 1993. "*Sectional prediction of 3D effects for stalled flow on rotating blades and comparison with measurements*", 199421, *Organizations, N.P.*
- Somers, D.M. 1997. "*Design and experimental results for the S809 airfoil*", *United States, Lab, N.R.E.*
- Song, Y. 2014. "*CFD Simulation of the Flow around NREL Phase VI Wind Turbine*". Master thesis, Massachusetts University.
- Sørensen, N.N. 2009. "CFD Modelling of Laminar-turbulent Transition for Airfoils and Rotors Using the γ -Re model". *Wind energy*. **12**(8), pp.715-733.
- Sørensen, N.N., Michelsen, J. and Schreck, S. 2002. "Navier–Stokes predictions of the NREL phase VI rotor in the NASA Ames 80 ft \times 120 ft wind tunnel". *Wind energy*. **5**(2 - 3), pp.151-169.
- Sørensen, N.N. and Schreck, S. 2012. "Computation of the National Renewable Energy Laboratory Phase - VI rotor in pitch motion during standstill". *Wind energy*. **15**(3), pp.425-442.

- Spalart, P.R. and Allmaras, S.R. 1994. "A one equation turbulence model for aerodynamic flows". *30th aerospace sciences meeting and exhibit, 6-9 Januray, Reno, USA*.
- Stone, C., Lynch, C.E. and Smith, M.J. 2010. "Hybrid RANS/LES simulations of a horizontal axis wind turbine". *48th AIAA Aerospace Sciences Meeting Florida, USA*.
- Sudhamshu, A., Pandey, M.C., Sunil, N., Satish, N., Mugundhan, V. and Velamati, R.K. 2016. "Numerical study of effect of pitch angle on performance characteristics of a HAWT". *Engineering Science and Technology*. **19**(1), pp.632-641.
- Tang, X. 2012. "*Aerodynamic design and analysis of small horizontal axis wind turbine blades*". PhD thesis, University of Central Lancashire, UK.
- Tangler, J. 1990. "Atmospheric performance of the special-purpose SERI thin-airfoil family: Final results". *European Wind Energy Conference 10-14 September Madrid, Spain* Solar Energy Research Institute.
- Tangler, J.L. and Somers, D.M. 1995. "*NREL airfoil families for HAWTs*", *NREL/TP-442-7109, NREL*.
- Thomson, L. 1966. "*Theoretical Aerodynamics... Revised and Enlarged*". Macmillan; St. Martin's Press, USA.
- Tu, J., Yeoh, G.H. and Liu, C. 2012. "*Computational fluid dynamics: a practical approach*". Second ed., Butterworth-Heinemann, UK.
- Van, A. 2001. "*Requirements for a Wind Turbine Aerodynamics Simulation Module*", *ECN-C-01-099, ECN*.
- Vandam, C.P. and Roskam, J. 1983. "*Analysis of Nonplanar Wing-tip mounted Lifting Surfaces on Low-speed Airplanes*", *NASA Report 3684, NASA*.
- Vermeer, L. 1994. Measurements on the properties of the tip vortex of a rotor model. *European Wind Energy Conference, July 1995*.
- Vermeer, L., Sørensen, J.N. and Crespo, A. 2003. "Wind turbine wake aerodynamics". *Progress in aerospace sciences*. **39**(6), pp.467-510.
- Versteeg, H.K. and Malalasekera, W. 2007. "*An introduction to computational fluid dynamics: the finite volume method*". Second ed., Pearson Education, England.
- Whale, J., Anderson, C., Bareiss, R. and Wagner, S. 2000. "An experimental and numerical study of the vortex structure in the wake of a wind turbine". *Journal of Wind Engineering and Industrial Aerodynamics*. **84**(1), pp.1-21.
- Whitcomb, R.T. 1976. "*A design approach and selected wind tunnel results at high subsonic speeds for wing-tip mounted winglets*", *NASA TN D-8260, NASA*.

- White, E.B., Kutz, D., Freels, J., Hidore, J.P., Grife, R., Sun, Y. and Chao, D. 2011. "Leading-edge roughness effects on 633-418 airfoil performance". *AIAA paper*. **352**(2011), p9.
- WILCOX, D. 1988. "Reassessment of the scale-determining equation for advanced turbulence models". *AIAA journal*. **26**(11), pp.1299-1310.
- Wilcox, D.C. 1993. "*Turbulence modeling for CFD*". Second ed., DCW industries La Canada,USA.
- Woelke, M. 2007. "Eddy Viscosity Turbulence Models employed by Computational Fluid Dynamic". *Prace Instytutu Lotnictwa*. pp.92-113.
- Wood, D. 1991. "A three-dimensional analysis of stall-delay on a horizontal-axis wind turbine". *Journal of Wind Engineering and Industrial Aerodynamics*. **37**(1), pp.1-14.
- Xu, G. and Sankar, L.N. 2000. "Effects of transition, turbulence and yaw on the performance of horizontal axis wind turbines". *AIAA paper*. **48**, p2000.
- Yakhot, V., Orszag, S., Thangam, S., Gatski, T. and Speziale, C. 1992. "Development of turbulence models for shear flows by a double expansion technique". *Physics of Fluids A: Fluid Dynamics*. **4**(7), pp.1510-1520.
- Yelmule, M.M. and Vsj, E.A. 2013. "CFD predictions of NREL phase VI rotor experiments in NASA/AMES wind tunnel". *International Journal of Renewable Energy Research (IJRER)*. **3**(2), pp.261-269.
- Yu, G., Shen, X., Zhu, X. and Du, Z. 2011. "An insight into the separate flow and stall delay for HAWT". *Renewable energy*. **36**(1), pp.69-76.
- Yu, H. 2017. "A critical review on the simulations of wind turbine aerodynamics focusing on hybrid RANS-LES methods". *Energy*. **138**, pp.257-289.
- Zhang, C. 2013. "*Aerodynamic, structural and aero-elasticity modelling of large composite wind turbine blades*". PhD thesis, Loughborough University.
- Zhu, W.J., Shen, W.Z. and Sørensen, J.N. 2014. "Integrated airfoil and blade design method for large wind turbines". *Renewable energy*. **70**, pp.172-183.

Appendix-A

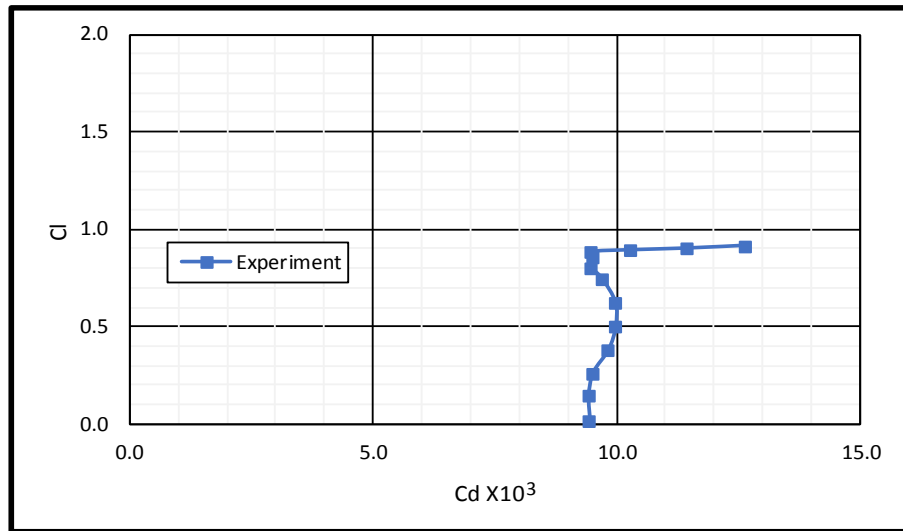


Figure A-1 Aerodynamic characteristics of the S809 airfoil for $Re = 1,000,000$ (Somers, 1997).

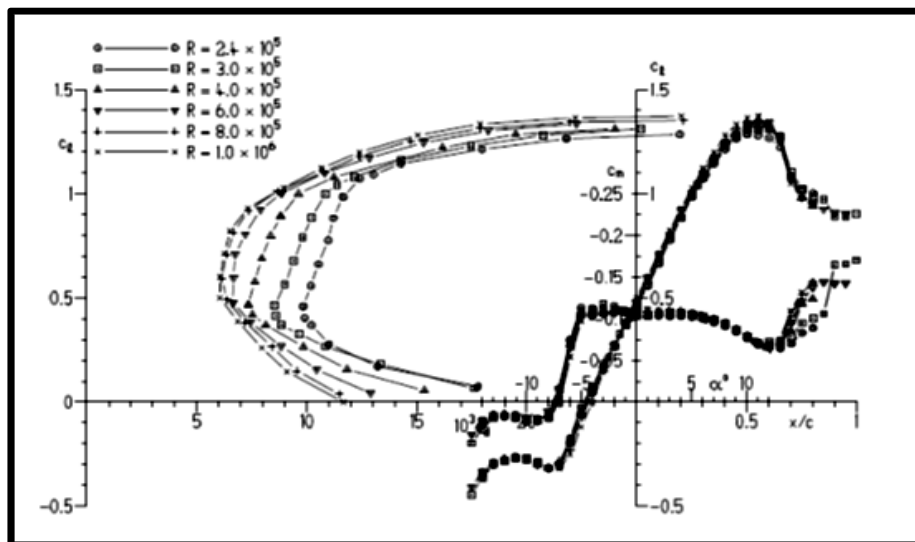


Figure A-2 Aerodynamic characteristics of the PSU 94-09 (Maughmer et al., 2002).

Table A-1 S809 airfoil coordinates (NREL, 2016).

UPPER SURFACE		LOWER SURRFACE	
x/c	y/c	x/c	y/c
1	0	0.000213	-0.00179
0.996203	0.000487	0.001045	-0.00348
0.98519	0.002373	0.001208	-0.00372
0.967844	0.00596	0.002398	-0.00527
0.945073	0.011024	0.009313	-0.0115
0.917488	0.017033	0.02323	-0.0204
0.885293	0.023458	0.04232	-0.03027
0.848455	0.03028	0.065877	-0.04082
0.80747	0.037766	0.093426	-0.05192
0.763042	0.045974	0.124111	-0.06308
0.715952	0.054872	0.157653	-0.07373
0.667064	0.064353	0.193738	-0.08357
0.617331	0.074214	0.231914	-0.09244
0.56783	0.084095	0.271438	-0.09991
0.519832	0.093268	0.311968	-0.10528
0.474243	0.099392	0.35337	-0.10818
0.428461	0.10176	0.395329	-0.10801
0.382612	0.10184	0.438273	-0.10455
0.33726	0.10007	0.48192	-0.09735
0.29297	0.096703	0.527928	-0.08657
0.250247	0.091908	0.576211	-0.07398
0.209576	0.085851	0.626092	-0.06064
0.171409	0.078687	0.676744	-0.04744
0.136174	0.07058	0.727211	-0.0351
0.104263	0.061697	0.776432	-0.0242
0.076035	0.052224	0.823285	-0.01516
0.051823	0.042352	0.86663	-0.0082
0.03191	0.032299	0.905365	-0.00336
0.01659	0.02229	0.938474	-0.00049
0.006026	0.012615	0.965086	0.000743
0.000658	0.003723	0.984478	0.000775
0.000204	0.001942	0.996141	0.00029
0	-0.00002	1	0

Table A-2 PSU 94-097 airfoil coordinates(Maughmer *et al.*, 2002).

UPPER SURFACE		LOWER SURRFACE	
x/c	y/c	x/c	y/c
0.00008	0.00099	0	0
0.00164	0.00566	0.00002	-0.00044
0.00747	0.01362	0.00031	-0.00162
0.01749	0.02237	0.00109	-0.00264
0.03163	0.03144	0.00237	-0.00363
0.04983	0.04046	0.0045	-0.00484
0.072	0.04913	0.01504	-0.00843
0.09803	0.05723	0.03099	-0.01135
0.12778	0.06457	0.05223	-0.01344
0.16104	0.07103	0.07861	-0.01473
0.19757	0.07655	0.10991	-0.01527
0.23701	0.08108	0.1458	-0.01515
0.27899	0.08456	0.18595	-0.01443
0.32302	0.08696	0.22994	-0.01325
0.36876	0.08819	0.27724	-0.01174
0.41564	0.08819	0.32729	-0.00998
0.46324	0.08687	0.37951	-0.00805
0.51121	0.08417	0.43325	-0.00602
0.55916	0.08011	0.48785	-0.00394
0.60678	0.07468	0.54273	-0.00177
0.65387	0.06808	0.59735	0.00039
0.70009	0.06072	0.6511	0.00238
0.7449	0.05297	0.70331	0.00407
0.78772	0.0451	0.75332	0.00535
0.828	0.03739	0.80042	0.00612
0.86517	0.03004	0.84394	0.00635
0.89868	0.02324	0.88321	0.00603
0.92886	0.0172	0.9176	0.00522
0.95406	0.01223	0.94656	0.00405
0.97398	0.00834	0.96959	0.0027
0.98838	0.00554	0.98635	0.00141
0.99709	0.00385	0.99656	0.00041
1	0.00328	1	0

Appendix-B

Table B-1 Polar file for the S809 airfoil.

alpha	C _l	C _d	C _{dp}	C _m	Top_Xtr	Bot_Xtr	C _l /C _d
0	0.1569	0.0093	0.00344	-0.0451	0.5841	0.5203	16.87097
0.25	0.1869	0.00931	0.00347	-0.0458	0.5835	0.521	20.07519
0.5	0.2169	0.00933	0.00352	-0.0465	0.583	0.5219	23.24759
0.75	0.247	0.00936	0.00357	-0.0473	0.5825	0.5228	26.38889
1	0.2771	0.00939	0.00362	-0.048	0.582	0.5237	29.51012
1.25	0.3071	0.00943	0.00368	-0.0487	0.5815	0.5248	32.56628
1.5	0.3372	0.00946	0.00372	-0.0494	0.5808	0.5257	35.64482
1.75	0.3671	0.00948	0.00374	-0.0501	0.5796	0.5266	38.72363
2	0.3974	0.00951	0.00378	-0.0509	0.5787	0.5275	41.78759
2.25	0.4275	0.00958	0.00384	-0.0516	0.5777	0.5283	44.62422
2.5	0.4574	0.00963	0.00391	-0.0523	0.5764	0.5294	47.4974
2.75	0.4868	0.00956	0.00391	-0.0529	0.5748	0.5302	50.9205
3	0.5163	0.00949	0.00391	-0.0535	0.5723	0.5312	54.40464
3.25	0.546	0.00941	0.00386	-0.054	0.5691	0.532	58.02338
3.5	0.5758	0.00942	0.00386	-0.0546	0.5664	0.533	61.12527
3.75	0.6049	0.00934	0.00386	-0.0551	0.5632	0.5339	64.76445
4	0.6341	0.00924	0.0038	-0.0556	0.5593	0.5349	68.62554
4.25	0.6639	0.00921	0.00376	-0.0561	0.5554	0.5361	72.08469
4.5	0.6928	0.0091	0.00374	-0.0566	0.5512	0.537	76.13187
4.75	0.7221	0.00905	0.00372	-0.0571	0.548	0.5379	79.79006
5.25	0.7805	0.00884	0.00363	-0.058	0.5372	0.5398	88.29186
5.5	0.8094	0.00874	0.00361	-0.0584	0.5293	0.5409	92.6087
5.75	0.8387	0.00869	0.00363	-0.0589	0.5214	0.5418	96.51323
6	0.8676	0.00864	0.00364	-0.0593	0.5073	0.5429	100.4167
6.25	0.8866	0.00923	0.00384	-0.0581	0.417	0.5438	96.05634
6.5	0.9018	0.01028	0.00452	-0.0566	0.3357	0.5448	87.72374

Table B-2 Polar file for the S801 airfoil.

alpha	C_l	C_d	C_{dp}	C_m	Top_Xtr	Bot_Xtr	C_l/C_d
0	0.5968	0.0066	0.00213	-0.142	0.685	0.7331	90.42424
0.25	0.6258	0.00668	0.00218	-0.1423	0.6825	0.7382	93.68263
0.5	0.6542	0.00675	0.00225	-0.1424	0.6796	0.7422	96.91852
0.75	0.6827	0.00679	0.0023	-0.1426	0.6761	0.7465	100.5449
1	0.7109	0.00683	0.00233	-0.1427	0.6724	0.7498	104.0849
1.25	0.739	0.00689	0.0024	-0.1427	0.6683	0.7533	107.2569
1.5	0.7671	0.00693	0.00243	-0.1428	0.6635	0.7573	110.6926
1.75	0.7952	0.007	0.00249	-0.1429	0.6598	0.7607	113.6
2	0.823	0.00701	0.00254	-0.1429	0.6551	0.7633	117.4037
2.25	0.8511	0.00707	0.00259	-0.143	0.651	0.7662	120.3819
2.5	0.8791	0.00711	0.00263	-0.1431	0.6452	0.7689	123.6428
2.75	0.9067	0.00714	0.00267	-0.1431	0.64	0.7707	126.9888
3	0.9342	0.00715	0.00272	-0.1431	0.634	0.7722	130.6573
3.25	0.9619	0.00721	0.00277	-0.1432	0.6293	0.7737	133.4119
3.5	0.9896	0.00723	0.00282	-0.1432	0.6223	0.7753	136.8741
3.75	1.017	0.00728	0.00287	-0.1432	0.6147	0.7769	139.6978
4	1.0443	0.00734	0.00293	-0.1432	0.6061	0.7784	142.2752
4.25	1.0715	0.00741	0.003	-0.1432	0.5965	0.7798	144.6019
4.5	1.0979	0.00746	0.00307	-0.143	0.5845	0.781	147.1716
4.75	1.1231	0.00759	0.00316	-0.1425	0.562	0.7824	147.971
5	1.1461	0.00785	0.00331	-0.1417	0.5289	0.7838	146
5.25	1.164	0.00842	0.00362	-0.1399	0.4734	0.7853	138.2423
5.5	1.1778	0.00931	0.00413	-0.1375	0.4012	0.787	126.5091
5.75	1.1956	0.00995	0.00454	-0.1359	0.3548	0.7887	120.1608
6	1.2118	0.01065	0.00499	-0.134	0.3059	0.7903	113.784
6.25	1.2278	0.01131	0.00545	-0.132	0.2624	0.7917	108.5588
6.5	1.2444	0.01193	0.0059	-0.1302	0.2268	0.7931	104.3085

Table B-3 Polar file for the S803 airfoil.

alpha	C_l	C_d	C_{dp}	C_m	Top_Xtr	Bot_Xtr	C_l/C_d
0	0.5952	0.00625	0.00158	-0.1412	0.6482	0.6736	95.232
0.25	0.6232	0.00633	0.00162	-0.1412	0.6423	0.6801	98.45182
0.5	0.6515	0.00637	0.00166	-0.1413	0.6357	0.6857	102.2763
0.75	0.6795	0.00644	0.00171	-0.1413	0.6288	0.6916	105.5124
1	0.7073	0.00651	0.00175	-0.1412	0.6221	0.6965	108.6482
1.25	0.7353	0.00657	0.00181	-0.1412	0.6143	0.702	111.9178
1.5	0.7633	0.00664	0.00187	-0.1412	0.6077	0.708	114.9548
1.75	0.7909	0.00673	0.00193	-0.1411	0.6001	0.7141	117.5186
2	0.8186	0.00678	0.00199	-0.141	0.5926	0.7188	120.7375
2.25	0.8466	0.00685	0.00206	-0.1411	0.5854	0.7234	123.5912
2.5	0.8742	0.00692	0.00212	-0.141	0.5784	0.7267	126.3295
2.75	0.9017	0.007	0.00219	-0.1409	0.5698	0.73	128.8143
3	0.9296	0.00707	0.00227	-0.1409	0.5619	0.7334	131.4851
3.25	0.9571	0.00714	0.00234	-0.1409	0.5525	0.7366	134.0476
3.5	0.9845	0.00722	0.00244	-0.1408	0.5442	0.7398	136.3573
3.75	1.0118	0.00732	0.00253	-0.1407	0.5325	0.7433	138.224
4	1.0384	0.00745	0.00263	-0.1405	0.5176	0.7469	139.3826
4.25	1.0652	0.00757	0.00274	-0.1403	0.5023	0.7505	140.7133
4.5	1.0913	0.00776	0.00287	-0.14	0.4805	0.7546	140.6314
4.75	1.1157	0.00807	0.00306	-0.1394	0.4439	0.7585	138.2528
5	1.1363	0.00871	0.0034	-0.1382	0.3803	0.763	130.4592
5.25	1.1572	0.00936	0.0038	-0.1371	0.3266	0.7677	123.6325
5.5	1.1777	0.01003	0.00422	-0.136	0.2729	0.7725	117.4177
5.75	1.1988	0.01064	0.00463	-0.1349	0.2297	0.7778	112.6692
6	1.2203	0.0112	0.00503	-0.1339	0.1941	0.7835	108.9554
6.25	1.2418	0.01174	0.00542	-0.1329	0.1635	0.7896	105.7751
6.75	1.2854	0.0127	0.00621	-0.1311	0.1206	0.8039	101.2126

Table B-4 Polar file for the S805A airfoil.

alpha	C_l	C_d	C_{dp}	C_m	Top_Xtr	Bot_Xtr	C_l/C_d
0.00	0.24870	0.00626	0.0017	-0.0482	0.6107	0.7867	39.72843
0.25	0.27740	0.00631	0.00171	-0.0485	0.6081	0.7899	43.96197
0.50	0.30660	0.00635	0.00173	-0.0489	0.6054	0.7931	48.28346
0.75	0.33560	0.00636	0.00175	-0.0492	0.6027	0.7954	52.7673
1.00	0.36440	0.0064	0.00178	-0.0495	0.5998	0.7981	56.9375
1.25	0.39310	0.00646	0.00181	-0.0498	0.597	0.8013	60.85139
1.50	0.42220	0.00647	0.00184	-0.0502	0.5934	0.804	65.25502
1.75	0.45070	0.0065	0.00186	-0.0505	0.5894	0.8065	69.33846
2.00	0.47960	0.00655	0.00191	-0.0508	0.5857	0.8097	73.22137
2.25	0.50820	0.00656	0.00192	-0.0511	0.5799	0.8127	77.46951
2.50	0.53660	0.00658	0.00196	-0.0513	0.5746	0.8151	81.55015
2.75	0.56500	0.00662	0.002	-0.0515	0.5699	0.818	85.34743
3.00	0.59380	0.00666	0.00206	-0.0518	0.5655	0.8209	89.15916
3.25	0.62160	0.00669	0.00208	-0.052	0.5577	0.8233	92.9148
3.50	0.65030	0.00671	0.00215	-0.0523	0.5525	0.8257	96.91505
3.75	0.67850	0.00676	0.0022	-0.0525	0.5467	0.8284	100.3698
4.00	0.70740	0.00681	0.00227	-0.0529	0.5411	0.8313	103.8767
4.25	0.73530	0.00684	0.00233	-0.053	0.5338	0.8336	107.5
4.50	0.76340	0.00689	0.00241	-0.0532	0.5248	0.8362	110.7983
4.75	0.79100	0.00697	0.00249	-0.0533	0.5131	0.839	113.4864
5.00	0.81830	0.00707	0.00256	-0.0534	0.4955	0.8419	115.7426
5.25	0.84510	0.00719	0.00267	-0.0534	0.4764	0.8443	117.5382
5.50	0.87080	0.00742	0.00282	-0.0532	0.4457	0.8472	117.3585
5.75	0.89380	0.00792	0.00309	-0.0526	0.3912	0.8507	112.8535
6.25	0.93340	0.00935	0.00396	-0.0506	0.2658	0.8569	99.82888
6.50	0.95460	0.00998	0.00438	-0.0499	0.2189	0.8605	95.6513

Table B-5 Polar file for the S806A airfoil.

alpha	C_l	C_d	C_{dp}	C_m	TopXtr	BotXtr	C_l/C_d
0	0.2395	0.00562	0.00171	-0.0447	0.7173	0.863	42.61566
0.25	0.2578	0.00571	0.00184	-0.0423	0.7152	0.8843	45.14886
0.5	0.2786	0.00573	0.00187	-0.0406	0.7128	0.8971	48.62129
0.75	0.3046	0.0057	0.00185	-0.0402	0.7105	0.9052	53.4386
1	0.3328	0.00568	0.00181	-0.0403	0.7081	0.9112	58.59155
1.25	0.358	0.00564	0.00178	-0.0397	0.7046	0.9167	63.47518
1.5	0.3864	0.00558	0.00173	-0.0399	0.7002	0.9214	69.24731
1.75	0.4139	0.00554	0.00168	-0.0398	0.696	0.9263	74.71119
2	0.4436	0.00549	0.00165	-0.0403	0.6913	0.9304	80.80146
2.25	0.4714	0.00546	0.00162	-0.0404	0.6867	0.9347	86.337
2.5	0.5044	0.00542	0.0016	-0.0417	0.6808	0.9377	93.06273
2.75	0.5356	0.0054	0.0016	-0.0426	0.6755	0.9415	99.18519
3	0.5687	0.00539	0.00159	-0.044	0.6699	0.9448	105.5102
3.25	0.6051	0.00538	0.00162	-0.0461	0.6628	0.9475	112.4721
3.5	0.6408	0.00538	0.00164	-0.0481	0.6541	0.9506	119.1078
3.75	0.6776	0.0054	0.00168	-0.0504	0.6457	0.9532	125.4815
4	0.717	0.00544	0.00173	-0.0533	0.635	0.9547	131.8015
4.25	0.755	0.00552	0.0018	-0.0558	0.6165	0.9566	136.7754
4.5	0.7909	0.00568	0.00189	-0.0579	0.5868	0.9588	139.243
4.75	0.8241	0.00603	0.00207	-0.0595	0.5366	0.9612	136.6667
5	0.8511	0.00697	0.00255	-0.0602	0.4322	0.964	122.109
5.25	0.8778	0.00788	0.00308	-0.0608	0.3441	0.9669	111.3959
5.5	0.9047	0.00872	0.00357	-0.0614	0.2707	0.9703	103.75
6	0.9489	0.01011	0.00449	-0.0604	0.1711	0.9984	93.85757
6.25	0.9734	0.01067	0.00488	-0.0605	0.136	1	91.22774
6.5	0.9866	0.01111	0.0052	-0.0578	0.1134	1	88.80288